MICROSTRUCTURE-SENSITIVE STRUCTURE-PROPERTY MODELING TOOLS FOR TRIPLEX Mo-Si-B ALLOYS

A Dissertation
Presented to
The Academic Faculty

by

Kyle Andrew Brindley

In Partial Fulfillment
of the Requirements for the Degree
Doctor of Philosophy in the
George W. Woodruff School of Mechanical Engineering

Georgia Institute of Technology
May 2017

MICROSTRUCTURE-SENSITIVE STRUCTURE-PROPERTY MODELING TOOLS FOR TRIPLEX Mo-Si-B ALLOYS

Approved by:

Dr. Richard W. Neu, Advisor
George W. Woodruff School of Mechanical Engineering
School of Materials Science and Engineering
Georgia Institute of Technology

Dr. Surya Kalidindi
George W. Woodruff School of Mechanical Engineering
School of Materials Science and Engineering
School of Civil and Environmental Engineering
Georgia Institute of Technology

Dr. Antonia Antoniou
George W. Woodruff School of Mechanical Engineering
Georgia Institute of Technology

Dr. David L. McDowell
George W. Woodruff School of Mechanical Engineering
School of Materials Science and Engineering
Georgia Institute of Technology

Dr. Arun Gokhale
School of Materials Science and Engineering
Georgia Institute of Technology

Date Approved: March 09, 2017

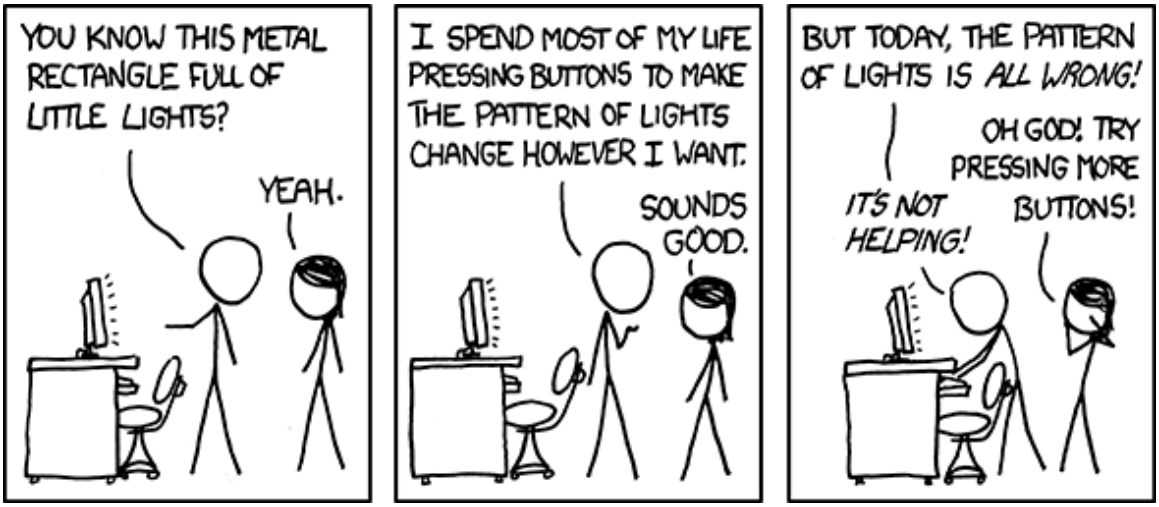

Figure 0.1: xkcd 722: Computer Problems [1]
Title Text: *This is how I explain computer problems to my cat. My cat usually seems happier than me.*

ACKNOWLEDGEMENTS

This work would not have been possible without the guidance and support of many people. Their support greatly improved the quality of this work, guided my growth as a researcher, and helped me ride the emotional roller coaster known as grad school.

I would like to thank my advisor, Dr. Richard Neu, for his guidance and advice throughout this project. He has helped shape the big picture value of this project without sacrificing the many details for a thorough research project. Without his support, this project would not have been as complete or meaningful a contribution to the modeling of Mo-Si-B alloys or as clearly applicable to similar material systems. I would also like to thank my committee members Dr. Antonia Antoniou, Dr. Arun Gokhal, Dr. Surya Kalidindi, and Dr. David McDowell who have helped scale the work to something achievable in a three year project and who have taught many courses directly applicable to my research.

In addition to my advisor and committee, I received significant technical support and guidance from fellow graduate students and friends. I would like to thank Dr. Jordan Weaver and Ali Khosravani for providing all of the training and troubleshooting support for the SEM imaging. None of the imaging I conducted would have been possible without the help of Dr. Ashley Goulding for developing and troubleshooting polishing and etching procedures and for conducting light microscopy. The development of a useful microstructure generator and efficient post-processing algorithms were supported by many discussions with Paul Kern and Dr. Matthew Priddy. Both Paul and Dr. Priddy also helped place the α-Mo CVP calibration in context and develop a reasonable approach to the parametric study of triplex Mo-Si-B. Dr. Matthew Priddy and Dr. Anirban Patra were instrumental in the development and validation

of a reduced order damage parameter to model relative ductility without the need of conducting cohesive simulations in 3D, eliminating the need for weeks long simulations.

Of course, none of this work would have been possible without the sponsor of this project, Pratt & Whitney. I would like to thank the points of contact over the duration of this project: Dr. Gopal Das, Rick Montero, and Dr. Sheila Woodard. Dr. David Furrer helped shape the big picture goals and applicability of this research. Important technical support in characterizing the α-Mo calibration material was provided by Greg Levan of Pratt & Whitney. Additional support was provided through discussions with Erik Mikalsen, Mark Ucasz, Brendan Lenz, and Tania Kashyap.

Without the support and friendship of my group mates and fellow graduate students I could not have completed this work in one piece. I would not have had any free time without the help of my co-lab managers for MPRL, Ashley Goulding and Sanam Gorgannejad, and our research engineer, JD Huggins. It has been a pleasure working with my friends and fellow grad students: Ashley, Sanam, Ernesto Estrada, Andy Radzicki, Anirudh Bhat, Jonathan Leung, Chuchu Zhang, Morris Satin, Aaron Tallman, Paul Kern, Matt Priddy, Adrienne Muth, Paxti Fernandez-Zelaia, and Arkadeep Kumar. Patxi Fernandez-Zelaia and Arkadeep Kumar have been good friends throughout grad school and were part of a fantastic study group through qualifying exams. I would like to thank Adrienne Muth for her friendship, especially through long hours of dissertation writing and job hunting. I would especially like to thank both Ashley and Sean Goulding for their friendship throughout grad school. They have become two of my closest friends and the smiles and laughs we've shared will remain my favorite moments from my time in grad school.

Finally, I would like to thank my family for their continued love and support. I can always rely on my parents, my brother Dan, and my sister Emmie to cheer me up when I'm down, provide a wonderful distraction from work, and laugh (or at least

roll their eyes) at all my bad jokes. I could always look forward to visiting with all of you during difficult semesters of research and studying.

TABLE OF CONTENTS

LIST OF TABLES

LIST OF FIGURES

SUMMARY

Refractory metals and their alloys offer higher temperature alternatives to Ni-base superalloys. In particular, Mo-Si and Mo-Si-B intermetallics offer excellent oxidation and creep resistance at temperatures up to 1400°C. However, these intermetallics present a significant design challenge due to their low ductility and low fracture toughness at room temperature. A balance of high temperature and low temperature mechanical properties may be achieved in Mo-Si-B alloys by including the α-Mo phase in addition to the intermetallic phases.

Balancing the mechanical properties requires proper microstructure optimization. Through the use of finite element simulations, microstructure-sensitive structure-property modeling allows for this optimization to be done faster and less expensively than traditional methods. Three modeling tools are required for microstructural modeling: microstructure generators to re-create statistically realistic microstructures, crystal viscoplasticity constitutive equations implemented for use with finite element solvers, and post-processing tools to evaluate important mechanical properties.

This work presents the development and application of these tools for triplex Mo-Si-B alloys by first developing these tools for the α-Mo phase and calibrating the constitutive equations for the α-Mo phase as a function of Si content, temperature, and strain rate. Following the calibration of the α-Mo phase constitutive equations, an initial model for the fully triplex microstructure is achieved by treating the intermetallic phases as purely elastic. Finally, the triplex microstructure is evaluated for an optimized microstructure balancing strength, fatigue, and ductility.

CHAPTER I

INTRODUCTION

1.1 Motivation

Gas turbine engines are used for power generation in many industries, including the energy and aerospace industries. Whatever the use for a gas turbine engine, increased efficiency is always a goal requiring more research. The performance and efficiency of a gas turbine engine is closely related to the peak operating temperature [2–4]; however, the operating temperatures of gas turbine engines have reached and even surpassed the melting temperatures of the materials that come into direct contact with the hot gases in the engine [4–8]. These high operating temperatures can be achieved only by the use of advanced alloys and coatings that can withstand the harsh environment coupled with specially designed turbine blades that are internally cooled [7,8]. However, introducing internal cooling significantly reduces the efficiency gained by a higher operating temperature as seen in the increasing deviation from ideal performance of engines with higher turbine inlet temperature in Figure 1.1 [4]. When operating at these high temperatures, the turbine blades in the hot section of the engine undergo a complicated load history including cyclic temperature and stress.

Traditionally, turbine blades have been made from Ni-base superalloys, but the temperatures of hot gases in gas turbine engines have been pushed up to and beyond the melting temperature of these alloys [4, 6, 8]. Research into alternative materials is an ongoing effort to increase gas turbine operating temperatures. Some possible alternatives include refractory alloys, ceramics, and ceramic-matrix composites [4, 6, 8–10].

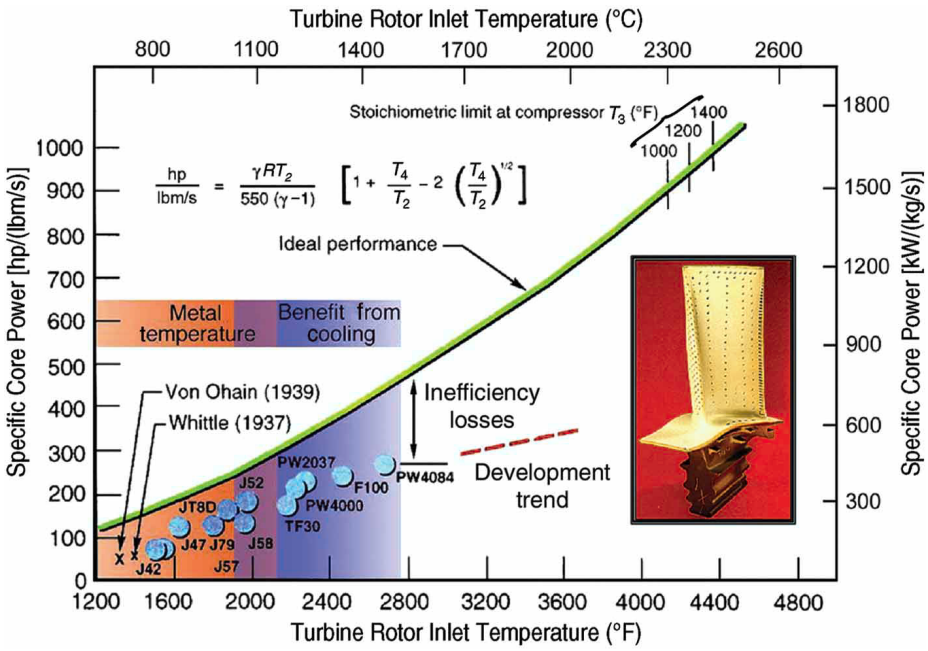

Figure 1.1: Specific power plotted against turbine inlet temperature for selected gas turbine engines [4]

Refractory metals and their alloys offer higher temperature alternatives to Ni-base superalloys [4, 6, 8, 10, 11]. In particular, Mo-Si and Mo-Si-B intermetallics offer oxidation and creep resistance at temperatures up to 1300°C (approximately 2400°F) without the need for internal cooling [8, 12, 13]. However, these intermetallics present a significant design challenge due to their low ductility and low fracture toughness at room temperature [8]. A balance of high temperature and low temperature mechanical properties may be achieved in Mo-Si-B alloys by including the α-Mo phase in addition to the intermetallic phases [8, 12, 13].

Balancing the mechanical properties requires proper microstructure optimization. However, microstructure optimization through traditional methods is a time consuming and expensive exercise [11]. A promising new approach to microstructure optimization can be found in the relatively new field of study referred to as Integrated Computational Materials Engineering (ICME). ICME research seeks to reduce the time and cost of bringing new materials from concept to implementation through

the use of computational material models. ICME efforts focus on developing material models that quantitatively describe the relationship of a material's processing, structure, and properties [14, 15]. Generally, these relationships are described in two stages. First, processing is related to a material structure, and then the material structure can be related to properties.

Through the use of finite element simulations, microstructure-sensitive structure-property modeling allows for microstructure optimization to be done faster and less expensively than traditional methods. Three modeling tools are required for microstructural modeling: microstructure generators to re-create statistically realistic microstructures, crystal viscoplasticity constitutive equations implemented for use with finite element solvers, and post-processing tools to evaluate important mechanical properties and fatigue for a variety of microstructural features.

1.2 Objectives

The goal of the presented work is to build, calibrate, and exercise the modeling tools required to optimize triplex Mo-Si-B alloys following an ICME approach. The immediate goal of the this work is to demonstrate the capabilities of these modeling tools in optimizing the microstructure of triplex Mo-Si-B alloys for better room temperature damage tolerance, high temperature strength, and fatigue life under conditions found in aerospace gas turbine engines. The effects of α-Mo volume fraction and Si content are explored for room temperature and high temperature yield strength, damage tolerance, and fatigue life. The overall goal of the this work is to develop the framework to rapidly deploy these modeling tools for the optimization of new alloy systems beyond that of Mo-Si-B alloys.

1.3 Significance

The novel modeling tools developed in this work include a microstructure generator capable of seamlessly capturing material inhomogeneity with regions of distinct microstructures and up to three separate phases, a crystal-viscoplastic constitutive law calibrated for α-Mo that captures the effects of Si content and temperature, and a quantitative reduced order damage indicator parameter for estimating susceptibility to microcracking as a function of microstructure.

The α-Mo experimental study conducted to calibrate the α-Mo CVP law contains additional evidence of changing deformation mechanisms between pure Mo and α-Mo with even small additions of Si. This change in deformation mechanisms is observed in the changing strain rate sensitivity behavior as a function of temperature.

The novel reduced order damage indicator parameter (DIP) is introduced as a surrogate for cohesive zone models in order to evaluate microstructure-sensitive changes in relative ductility related to susceptibility to widespread brittle microcrack formation in quasi-brittle materials without the need for computationally expensive cohesive zone elements. This reduced order modeling approach facilitates the design of fully 3D microstructures using a quantitative measure for relative interface average damage indicator as one of the targeted design objectives.

The parametric study exercising these modeling tools provides insight into the relationship between α-Mo Si content and α-Mo volume fraction and the mechanical properties of yield strength, fatigue resistance, and susceptibility to microcracking at both room temperature and 1400°C. A short study on the effects of grain size demonstrates the need for high resolution FE models in order to capture grains sizes spanning several orders of magnitude at the same absolute length scales. The parametric study examining these properties also helps build a database of microstructure-property relationships capable of guiding the optimization process for Mo-Si-B alloys for many different applications including for use in gas turbine engines.

In addition to the advances in understanding Mo-Si-B alloys, this research builds the modeling tools and establishes the workflow required to optimize similar material systems including both ductile and quasi-brittle phases for a variety of applications. This helps further establish a framework to rapidly deploy Integrated Computational Materials Engineering (ICME) modeling tools for the optimization of new alloy systems beyond that of Mo-Si-B alloys.

1.4 Overview

Chapter 2 is a literature review of the material and phases modeled in this work, methods for synthetic microstructure reconstruction, crystal-viscoplasticity, fatigue indicator parameters, and modeling damage and micro-crack formation in quasi-brittle solids. Chapter 3 reviews characteristics of triplex Mo-Si-B alloys targeted by the parametric study of this work and the α-Mo material used in the calibration of the constitutive law for this phase. Chapters 4 through 7 present the development and use of the modeling tools comprising the microstructure-sensitive mechanical property modeling workflow shown in Figure 1.2. Chapter 4 presents the microstructure generator modifications required for modeling the α-Mo calibration material and the final synthetic volume elements used in calibration of the α-Mo phase and the triplex Mo-Si-B parametric study. Chapter 5 introduces the constitutive law, the calibration of that law for the α-Mo phase, and the elastic and thermal properties of all three phases in the triplex Mo-Si-B material simulations. Chapter 6 develops and validates a reduced order damage indicator parameter for modeling susceptibility to micro-crack formation without using computationally expensive cohesive zone elements in a 3D FE simulation. Chapter 7 presents the triplex Mo-Si-B parametric study and the results. Finally, Chapter 8 summarizes the work presented in this dissertation, its significance, and the recommendations for future work.

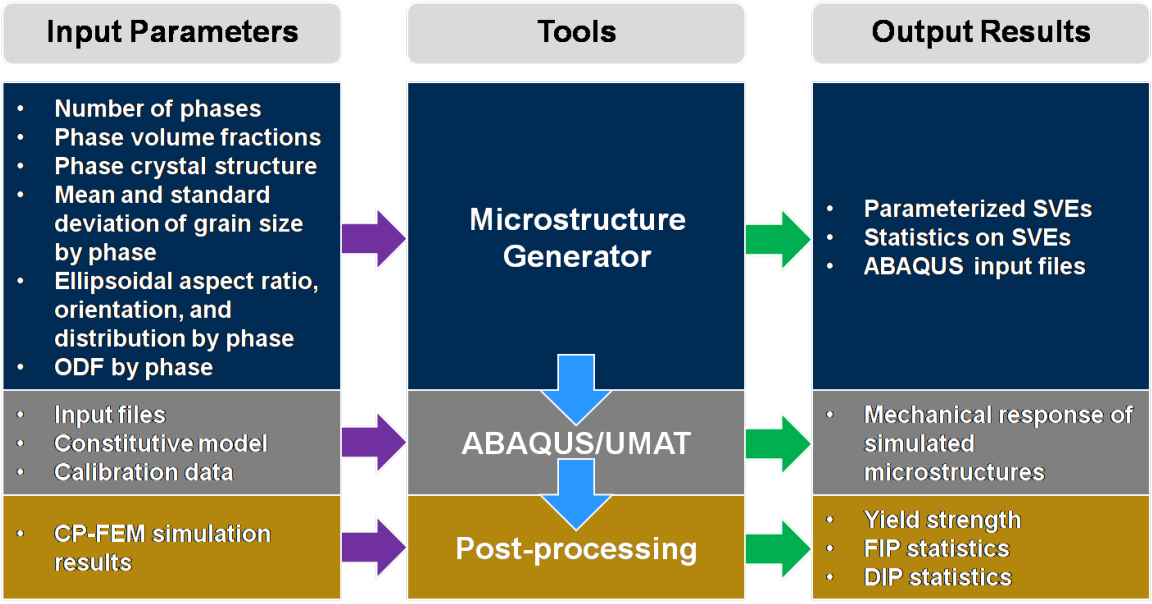

Figure 1.2: Microstructure-sensitive mechanical property modeling workflow

CHAPTER II

BACKGROUND

2.1 Mo-Si-B System

The study of Mo-Si-B alloys started with the work of Nowotny *et al.*, who developed the first phase diagram for the Mo-Si-B ternary system [16], and Aronsson, who determined the body-centered tetragonal crystal structure of Mo_5SiB_2 and related it to the T2 structures of Nb_5Si_3 and Ta_5Si_3 [17]. The ternary phase diagram was later refined by Nunes *et al.* [18]. The Mo rich corner of the Mo-Si-B phase diagram has been especially promising and is shown in Figure 2.1 [19]. The elastic properties of Mo were explored in the 1960s by Featherstone and Neighbours [20] and by Dickinson and Armstrong [21]. More recently, Mo with Si in solid solution and the intermetallic phases of the Mo-Si-B system have been studied to determine mechanical properties of common individual phases of the Mo-Si-B system [22, 23].

There have been numerous studies into the microstructure-property relationships for a variety of duplex and triplex Mo-Si-B alloys [9, 12, 19, 24–33]. Perhaps the most promising of these alloys is a three phase triplex microstructure consisting of the intermetallic Mo_3Si (A15) and Mo_5SiB_2 (T2) phases in a continuous α-Mo matrix [19, 26, 32, 34, 35]. Triplex alloys with these phases correspond to the blue region in Figure 2.1 [19]. Materials with such microstructures are typically created using powder metallurgy because it has proven difficult to create the desired α-Mo matrix using melt-based processing and hot working [12, 36]. This section discusses the individual phases, followed by a discussion of the role of each phase in a balanced triplex Mo-Si-B alloy.

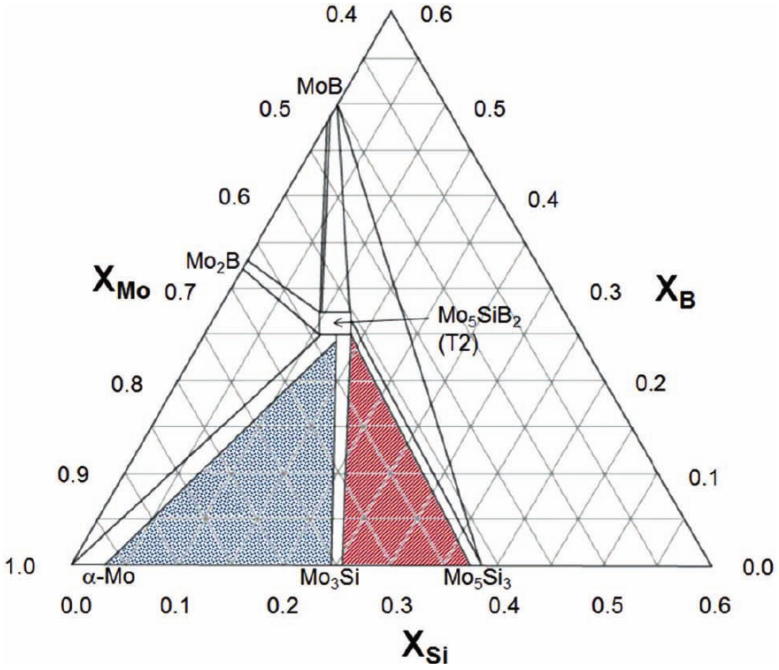

Figure 2.1: Mo-rich portion of the 1600°C isotherm of the Mo-Si-B phase diagram. α-Mo-Mo_3Si-Mo_5SiB_2 in blue region. Mo_3Si-Mo_5Si_3-Mo_5SiB_2 in red region. [19]

2.1.1 Molybdenum and α-Mo

The α-Mo phase is a solid solution of Si in Mo. The BCC crystal structure of Mo is shown in Figure 2.2 [4] and the Mo-Si phase diagram is shown in Figure 2.3 [37]. In Figure 2.3, α-Mo is shown on the far left with a maximum solubility of approximately 1.2 wt% Si at 2025°C [37]. The high melting temperature, low thermal expansion, and high thermal conductivity make Mo a desirable refractory metal for high temperature structural applications [4]. Table 2.1 shows the properties of Mo in comparison to the A15 and T2 intermetallic phases.

The α-Mo phase provides the ductility and fracture toughness for triplex Mo-Si-B alloys; however, it oxidizes readily above 600°C and has poor creep resistance at high temperatures [8, 13, 38, 39]. In the range of 500°C to 600°C, Mo exhibits parabolic weight gain through the formation of a MoO_3 scale; however, at temperatures over

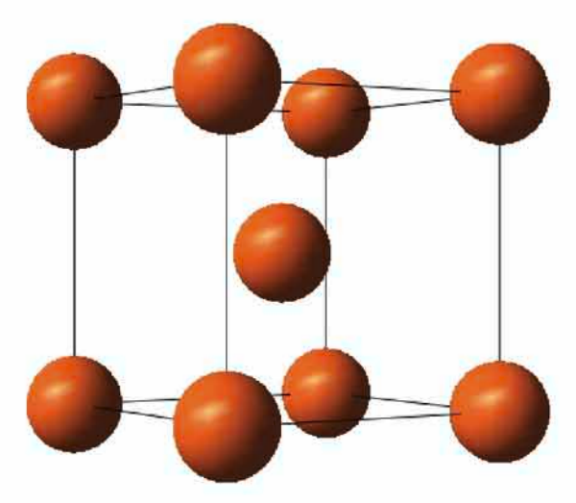

Figure 2.2: Crystal structure of Mo [4]

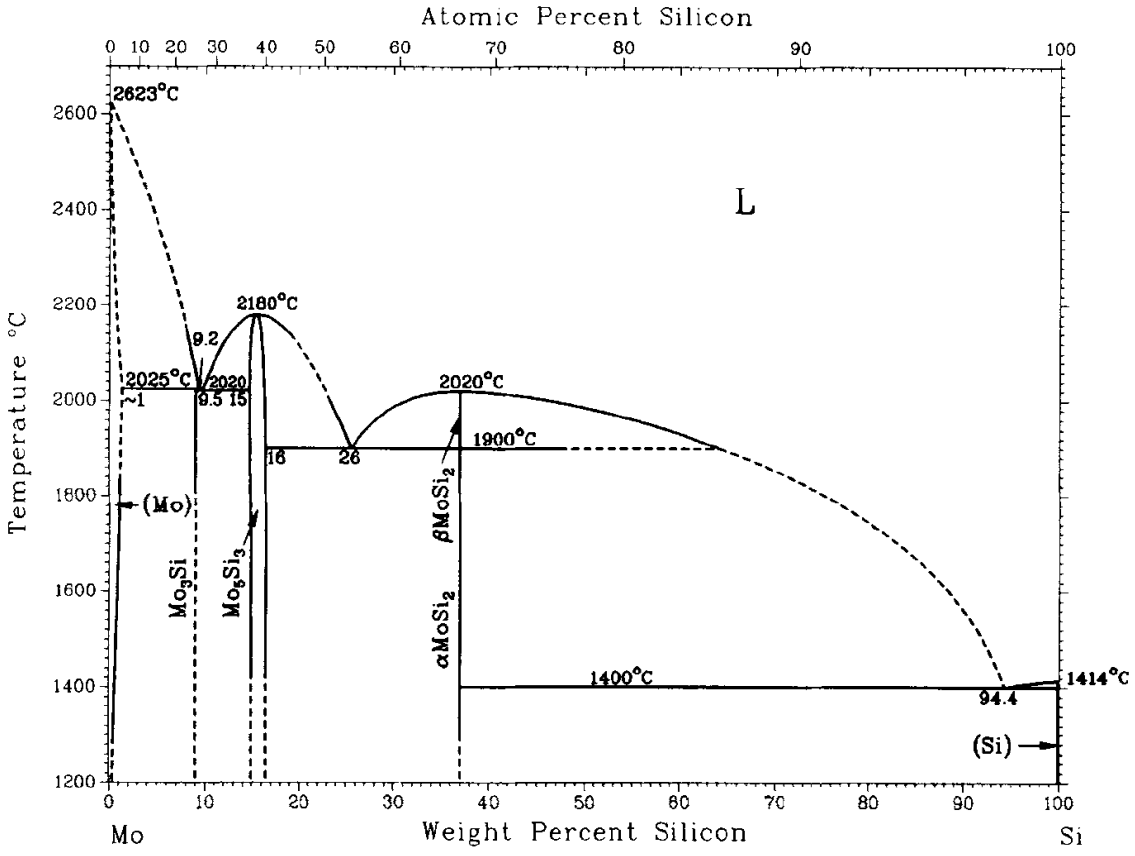

Figure 2.3: Mo-Si phase diagram [37]

700°C Mo suffers from linear weight loss at increasing rates with increasing temperature due to the evaporation of MoO_3, as shown in Figure 2.4 [13].

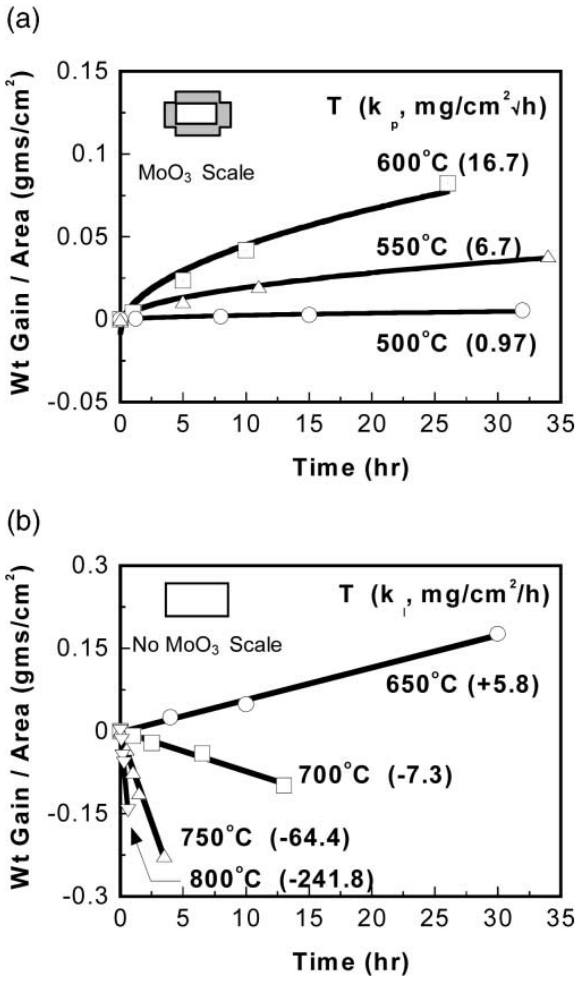

Figure 2.4: Oxidation kinetics of pure Mo [13]

The strength of the α-Mo phase is highly dependent on Si content, where small additions of Si can dramatically increase the yield strength, as seen in Figure 2.5, where as little as 1 wt.% Si can increase the yield strength approximately six times over that of pure Mo [38]. Figure 2.5 also shows the effect of temperature on yield strength. At low temperatures, the yield strength drops off quite quickly, but at temperatures above room temperature yield strength is a relatively shallow function of temperature, especially at low Si contents.

Figure 2.5 also shows a fairly unique property of α-Mo. For very small additions of Si and at temperatures below room temperature, α-Mo shows solid solution softening. Solid solution softening can occur in BCC metals and has been shown to occur in

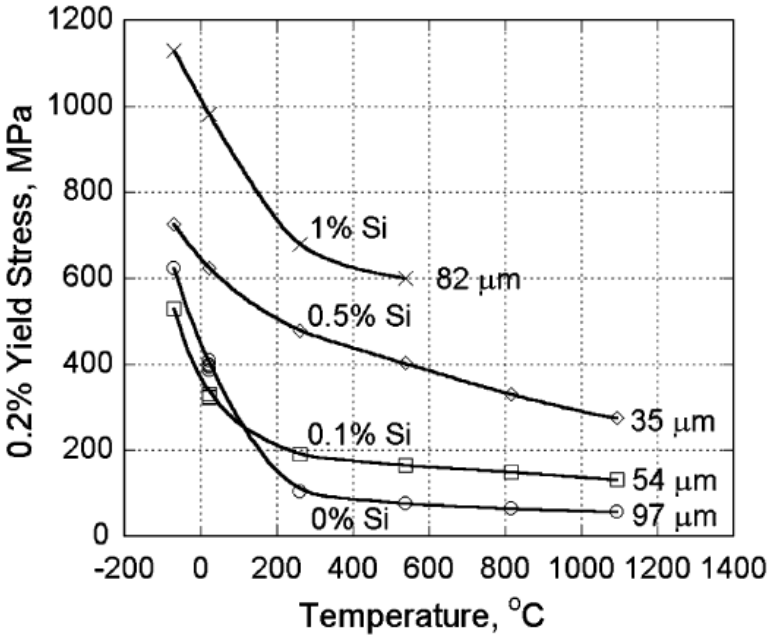

Figure 2.5: α-Mo yield strength as a function of temperature and Si content [38]

Mo-Re and Mo-Pt [40], but there are only two reports of solid solution softening in the Mo-Si system [38,41]. Solid solution softening of BCC metals is related to the thermal activation for formation and propagation of double kinks along screw dislocations [38,42]. As temperatures increases above a critical temperature, T_{dk}, double kinks no longer dominate screw dislocation motion and solid solution softening is no longer observed [38]. The transition temperature from the nucleation and migration of double kinks to similar mobilities of screw and edge dislocations is approximately 20% of the melting temperature, or around 306°C for Mo [38]. a schematic of this transition with temperature for pure Mo and small additions of Si in α-Mo is shown in Figure 2.6 [38].

The thermal activation required for nucleation and migration of double kinks causes the yield strength of Mo to be strain rate sensitive at low temperatures [38]. However, as temperature increases and the mobility of screw and edge dislocations becomes similar, the strain rate sensitivity of yield strength in Mo decreases sufficiently to be almost negligible [38]. The effects of double kink formation diminish

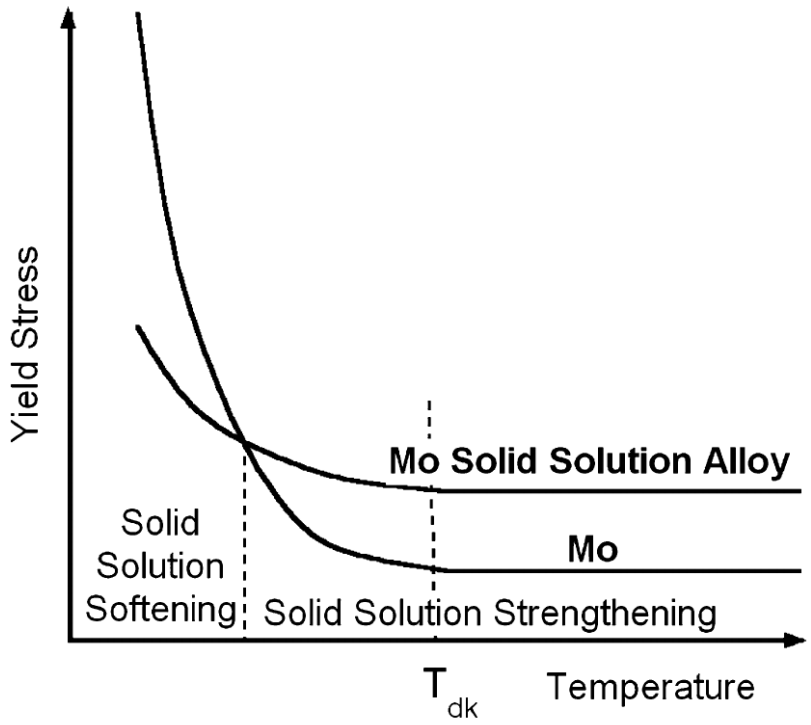

Figure 2.6: Schematic of solid solution softening [38]

quickly with the addition of Si, as shown in Figure 2.7 [38]. With larger amounts of Si, the Peierls stress becomes almost independent of temperature, and the mobilities of screw and edge dislocations are similar [38]. The transition to similar mobilities for screw and edge dislocations with increasing Si effects the strain rate sensitivity of α-Mo with relatively large amounts of Si. At higher Si content, α-Mo behaves more traditionally with strain rate insensitivity at room temperature and increasing strain rate sensitivity with increasing temperature.

Another distinct trait of yield strength in Mo is the lack of a Hall-Petch effect for grain sizes approximately 50 μm or larger [38]. While a Hall-Petch has been reported for mean grain sizes as large 500 μm in cast and wrought Mo [43], a later study on material from the same supplier only found a Hall-Petch effect for grains smaller than 100 μm [44]. In a study on the effects of Si content, no observable Hall-Petch effect was found in grain sizes as small as 50 μm for Mo with Si additions as low as 0.1 wt.%, as shown in Figure 2.8 [38]. One possible explanation is that the yield behavior

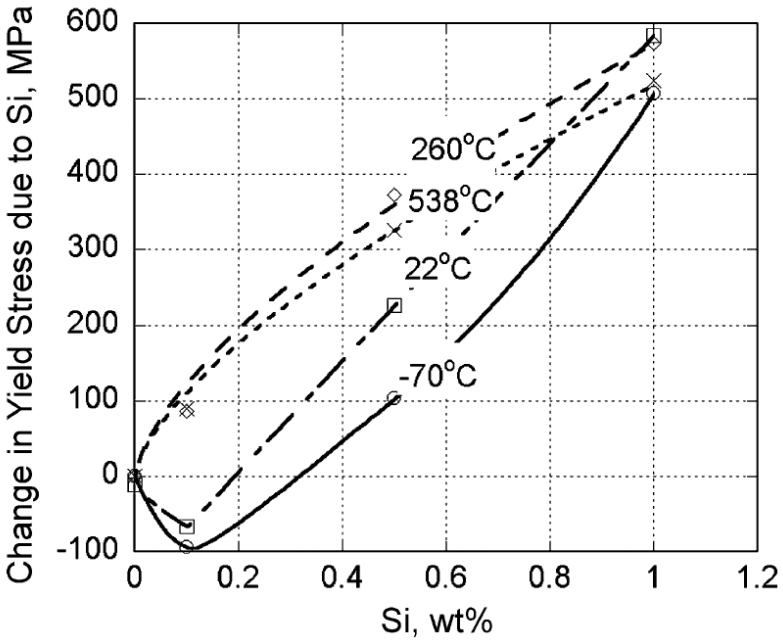

Figure 2.7: Solid solution strengthening and softening as a function of Si concentration and temperature [38]

in Mo is not dependent on dislocation pile up on the length scale of grain size, but governed by interactions of individual dislocations before pile-ups traversing an entire grain can form [38]. This explanation would allow for a transition grain size, with a Hall-Petch effect at smaller mean grain sizes and no observable Hall-Petch effect at larger grain sizes. However, a more thorough investigation is required before anything conclusive can be said about the grain size effect on yield strength in α-Mo.

In addition to increasing the yield strength, adding Si also drastically decreases the fracture toughness and ductility. It has been shown that the addition of 0.5 wt.% Si reduces the room temperature ductility of α-Mo from 25 to 3% [45, 46]. Figure 2.9 shows the fracture toughness of polycrystalline α-Mo specimens as a function of Si concentration [38]. While polycrystalline Mo without Si in solid solution fractures trangranularly at room temperature, polycrystalline α-Mo with Si in solid solution exhibits predominantly intergranular cracking at room temperature. With only small additions of Si, Mo exhibits intergranular fracture at higher temperatures, as well.

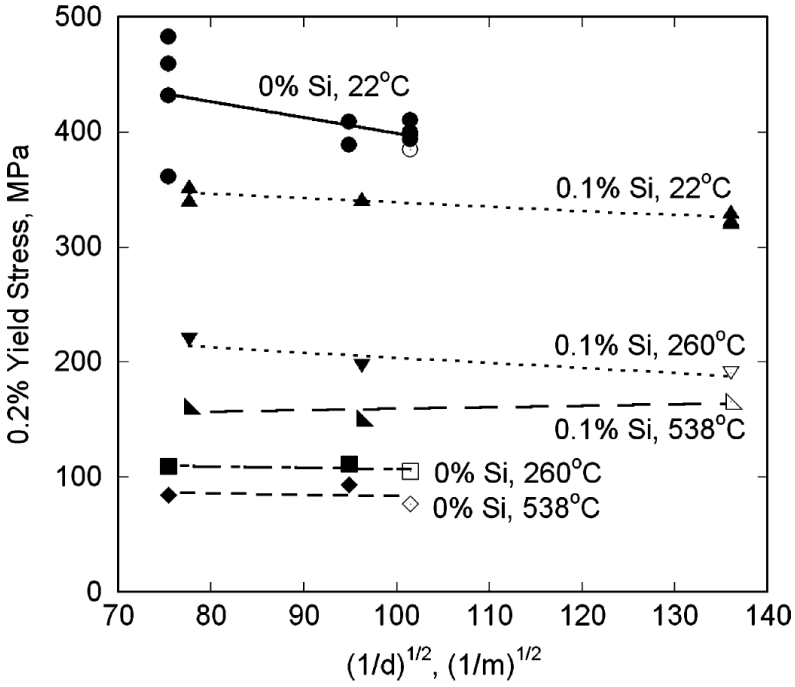

Figure 2.8: Yield strength as a function of mean grain size at various temperatures for Mo and Mo-0.1Si wt.% [38]

The transition in fracture mode of polycrystalline Mo with the addition of Si in solid solution is attributed to grain boundary embrittlement by Si segregation at grain boundaries and is the mechanism associated with decreasing fracture toughness with increasing Si content [38].

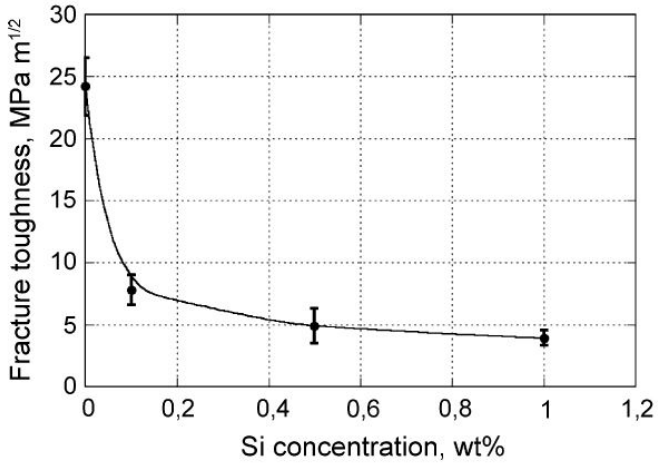

Figure 2.9: α-Mo room temperature fracture toughness as a function of Si content [38]

2.1.2 Mo_3Si (A15)

The intermetallic Mo_3Si phase is an A15 cubic phase, shown in Figure 2.10 [4]. Not much is known about the mechanical properties of this phase; however, Swadener *et al.* have investigated the room temperature properties of single crystal Mo_3Si specimens [22]. Experimental measurements of the elasticity tensor are shown in Figure 2.11 [22].

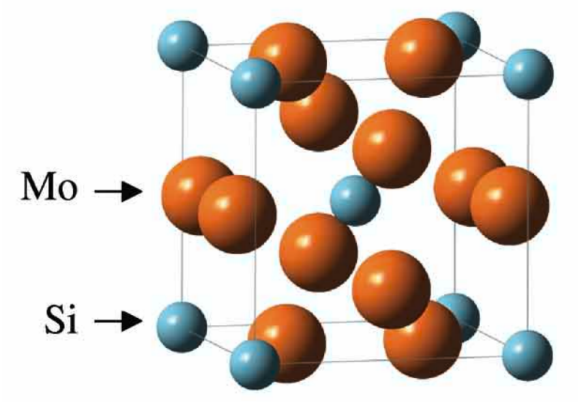

Figure 2.10: Crystal structure of Mo_3Si (A15) [4]

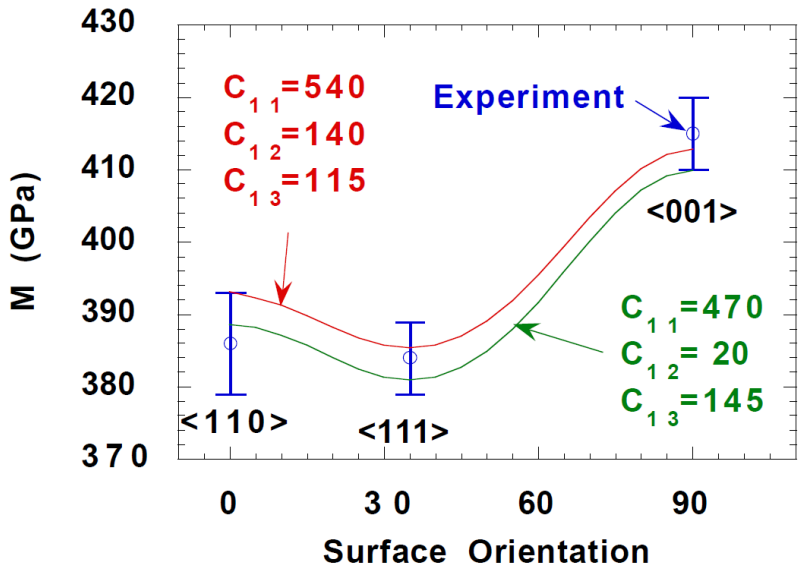

Figure 2.11: Elasticity tensor components of Mo_3Si (A15) at room temperature [22]

This phase is very strong at room temperature and shows very little plasticity

under deformation even at high temperatures. Consequently, Mo_3Si is quite brittle at room temperature, with a fracture toughness of just 3 MPa$\sqrt{\text{m}}$ [47]. Despite limited experimental data for this phase, compressions test have shown sufficient plasticity at 1400°C to determine that the yield strength is strain rate and Si content dependent [47]. These tests showed yield strengths as large as 600 MPa at high strain rates, and even at very slow strain rates, the yield strength is many times that of α-Mo. Figure 2.12 shows the yield strength of Mo_3 at 1400°C.

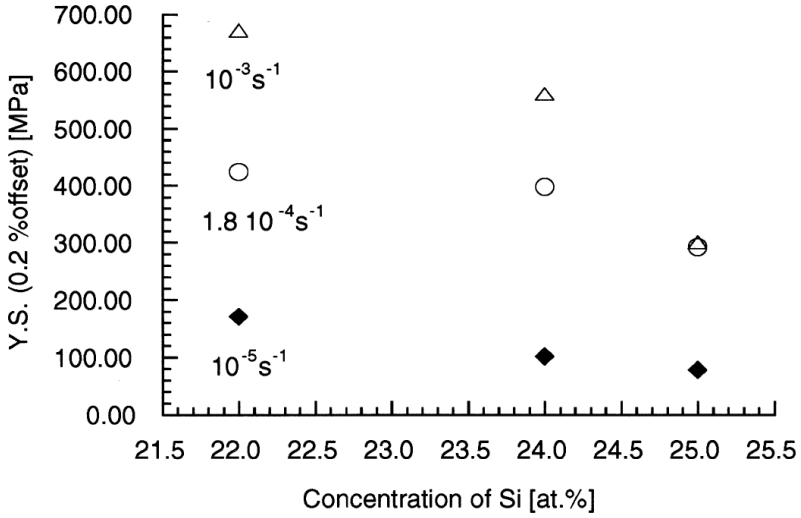

Figure 2.12: Yield strength of Mo_3Si (A15) at 1400°C. Pure polycrystalline Mo_3Si contains 24 at.% Si [47]

The coefficient of thermal expansion is provided by Choe *et al.* and shown to be similar in magnitude that of Mo [25]. This phase provides oxidation resistance by forming a nanoporous SiO_2 scale over the oxidizing surface [8, 13, 48]. Table 2.1 compares select properties of the three phases in the triplex Mo-Si-B studied in this work.

2.1.3 Mo_5SiB_2 (T2)

The intermetallic Mo_5SiB_2 (T2) phase has a body-centered tetragonal structure, shown in Figure 2.13. Like the Mo_3Si phase, this phase is strong and brittle from

room temperature up to high temperatures. High temperature mechanical properties have been explored by Ito *et al.* who determined elastic constants from room temperature up to 1100°C as shown in Figure 2.14 [23].

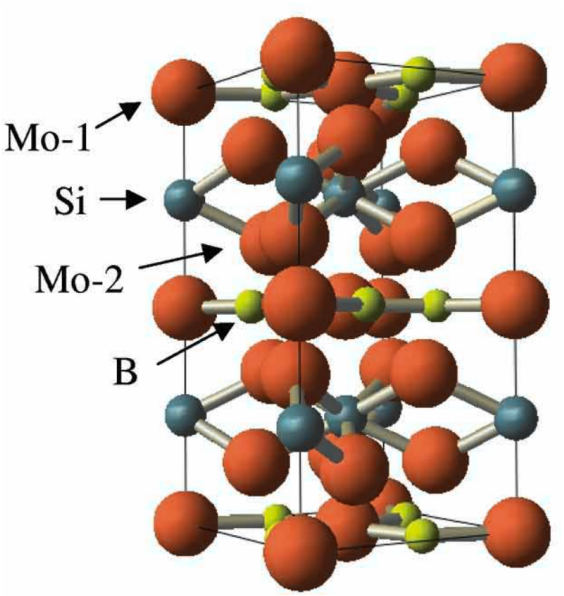

Figure 2.13: Crystal structure of Mo_5SiB_2 (T2) [4]

Figure 2.15 presents the anisotropic coefficient of thermal expansion from room temperature to 1500°C, which is determined to be similar to that of Mo and much less anisotropic than other intermetallic phases in the Mo-Si-B ternary system [23]. Other reports found an anisotropy ratio of the coefficient of thermal expansion closer to 1.1 at temperatures up to 1379°C, as shown in Figure 2.16 [49]. For the purposes of this research, the coefficient of thermal expansion is considered to be nearly isotropic, following Choe *et al.* [25].

The T2 phase is also extremely hard and brittle, with a fracture toughness of about 2 MPa$\sqrt{\text{m}}$ at room temperature [50]. The T2 phase does not demonstrate plasticity until temperatures of about 1500°C. Even at high temperatures, only a couple of slip systems demonstrate any amount of plasticity, as shown in Figure 2.17 [23].

The high strength of the T2 phase contributes to it's excellent creep resistance at temperatures as high as 1500°C [23]. Figure 2.18 presents the results of high

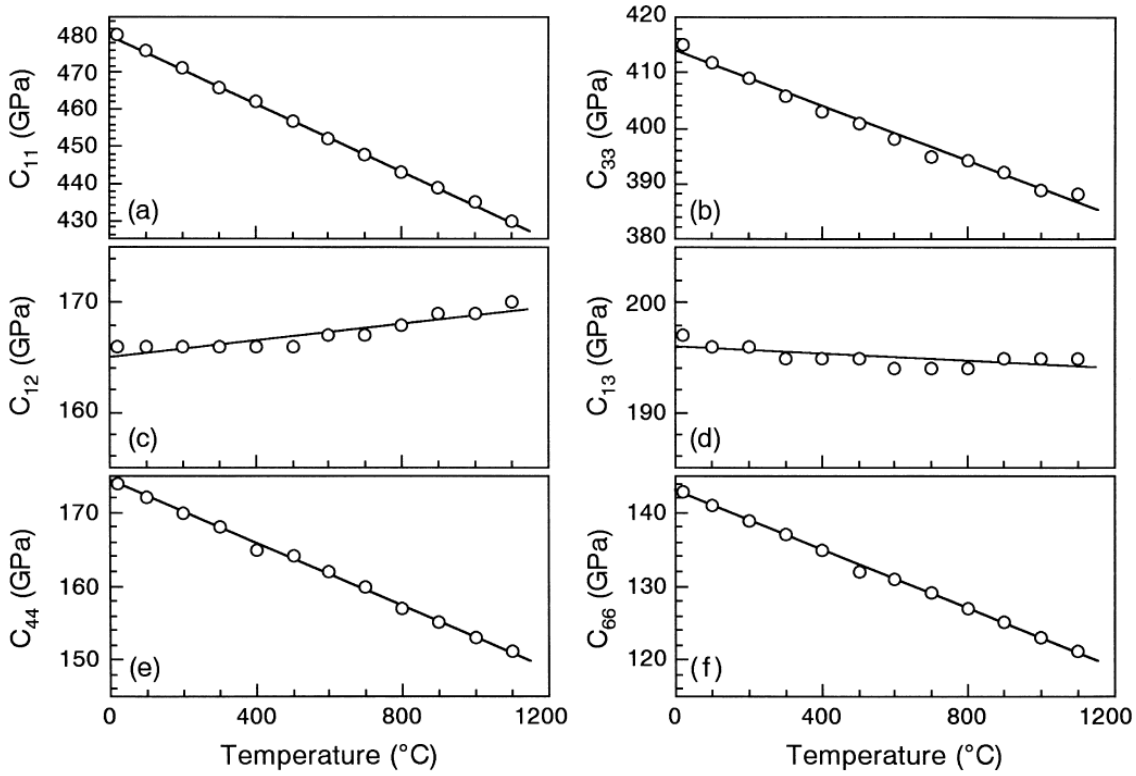

Figure 2.14: Temperature dependence of T2 single crystal elasticity tensor components [23]

temperature creep tests for the T2 phase [23].

Finally, the importance of this phase is to provide high temperature strength and oxidation resistance. The T2 phase provides oxidation resistance by forming a borosilicate scale in the early stages of oxidation. This scale then diffuses into the SiO_2 scale formed by Mo_3Si, which lowers the viscosity of the SiO_2 scale and leads to passivation of the scale. The material transitions to a steady-state oxidation when the surface is covered in borosilicate [8, 13, 48]. A schematic of the stages of oxidation in triplex Mo-Si-B is presented in the following section where oxidation is discussed in greater detail.

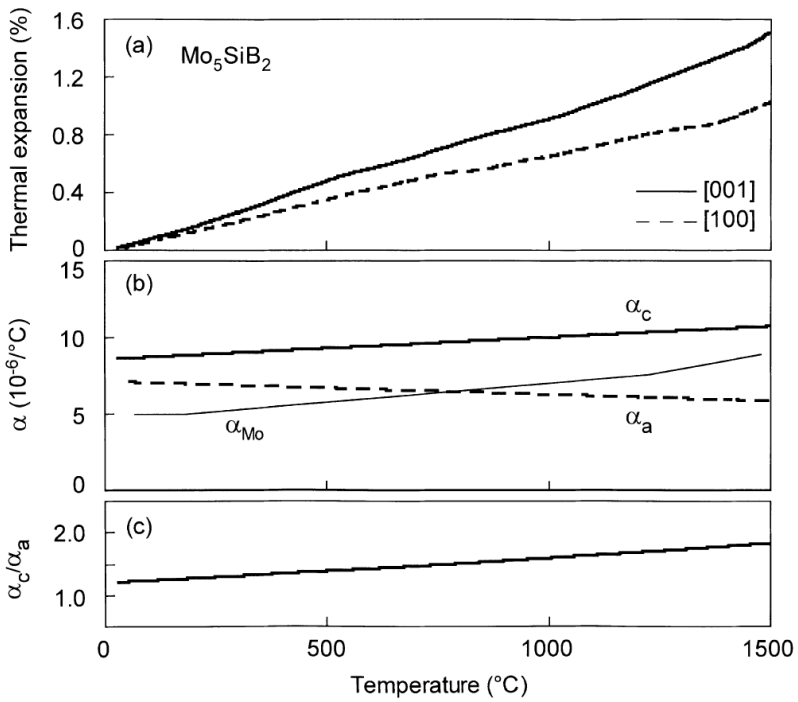

Figure 2.15: Coefficient of thermal expansion temperature dependence and anisotropy for T2 [23]

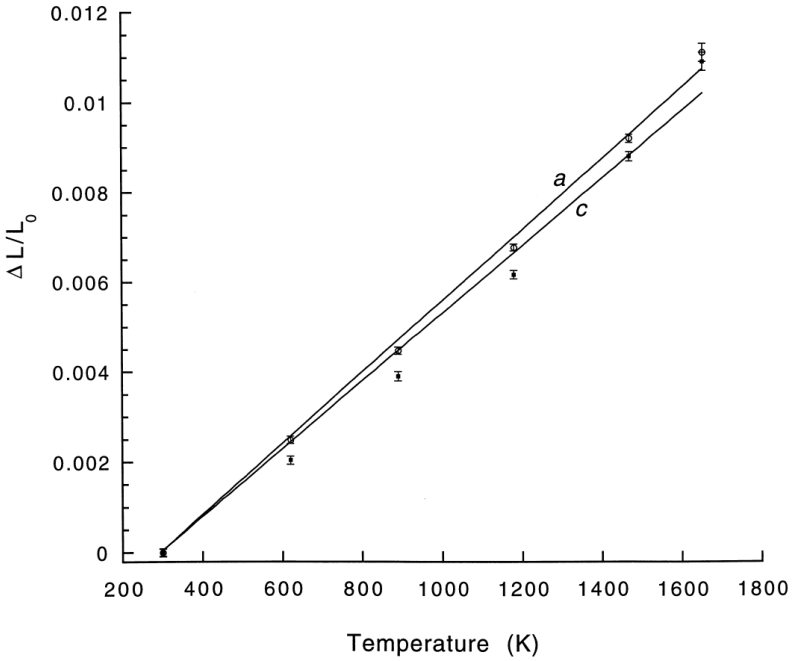

Figure 2.16: Coefficient of thermal expansion temperature dependence and anisotropy for T2 [49]

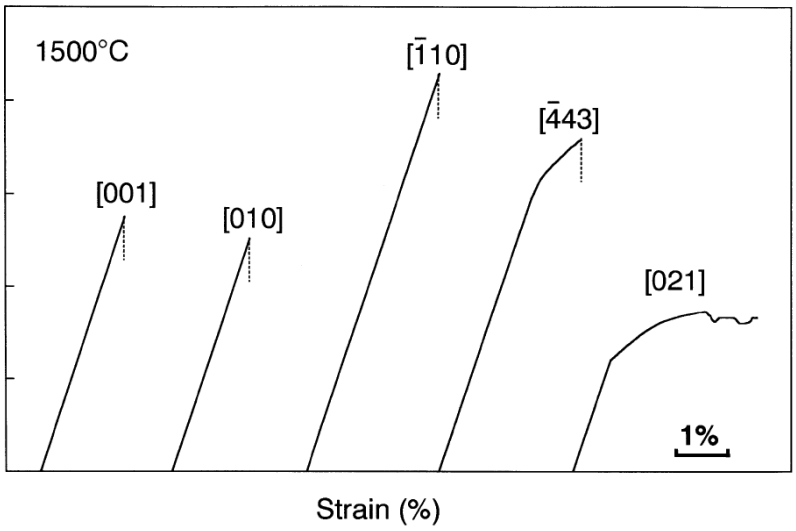

Figure 2.17: Stress-strain curves of T2 single crystals at 1500°C [23]

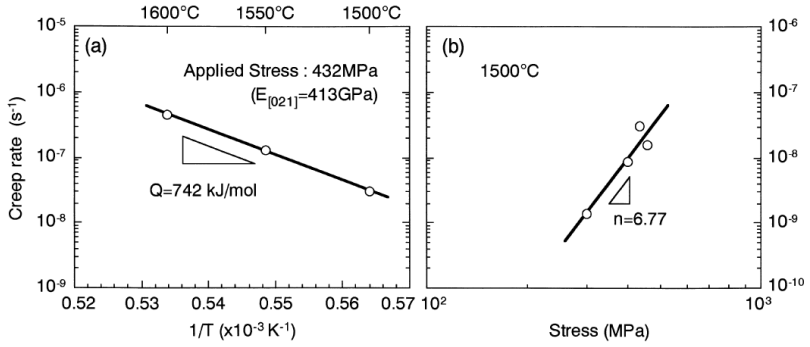

Figure 2.18: Creep results of [021] oriented T2 single crystals: (a) Temperature dependence of minimum creep rate at 432 MPa and (b) stress dependence at 1500°C [23]

2.1.4 Multiphase Mo-Si-B Alloys

The intermetallic phases are necessary to improve the high temperature oxidation resistance and creep resistance; however, these alloys are brittle even at high temperatures [23, 51]. Consequently, creating a Mo-Si-B alloy with balanced mechanical properties for use in gas turbine engines requires an optimization of the microstructure between the competing properties of ductility and fracture toughness with strength, oxidation resistance, and creep resistance. The single property optimized microstructures are shown in Figure 2.19 to highlight the mutually exclusive nature of the

mechanical properties of interest [8].

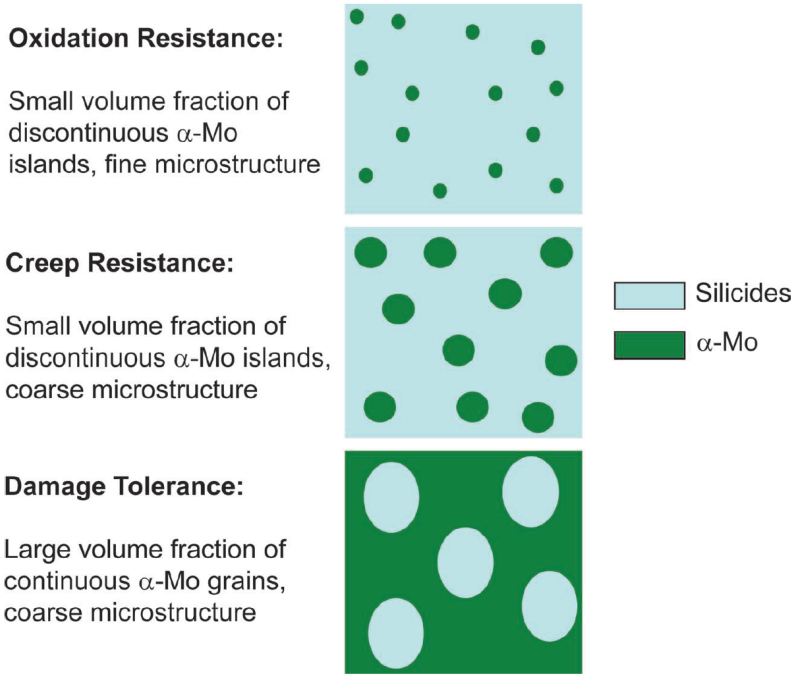

Figure 2.19: Schematic of ideal microstructures for competing mechanical properties of Mo-Si-B alloys [8]

Due to the volatility of α-Mo at relatively low temperatures for the application of Mo-Si-B alloys, the best oxidation resistance is provided by a fine microstructure of continuous intermetallics with dispersed α-Mo. Good creep resistance is provided by the same low volume fraction of α-Mo, but with a coarser microstructure. For reasonable fracture toughness, especially at room temperature, a continuous α-Mo matrix with dispersed intermetallics is required.

Since there is no other way to obtain reasonable fracture toughness and damage tolerance than including a continuous α-Mo matrix, significant work has gone into determining the best way to increase the oxidation resistance of microstructures with a relatively large volume fraction of α-Mo [36, 50, 52]. Figure 2.20 shows a schematic of the stages of oxidation in α-Mo-A15-T2 Mo-Si-B alloys [8].

Initially, each phase oxidizes independently: The α-Mo forms a MoO_3 vapor and evaporates, the A15 phase forms a nanoporous SiO_2 scale, and the T2 phase forms a

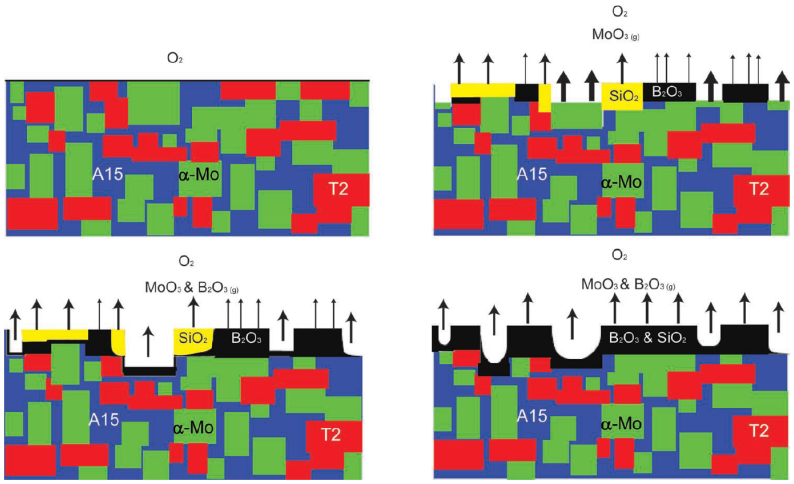

Figure 2.20: Schematic of transient oxidation stages in Mo-Si-B alloys at 1300°C [8]

borosilicate scale. With the proper balance of phase volume fractions and additives, the borosilicate scale flows to cover the α-Mo and diffuses into SiO_2, reducing its viscosity which speeds the sintering and passivation of SiO_2. Eventually, a transition to steady state oxidation is reached when the surface is covered in a protective layer of borosilicate [8]. At lower temperatures, it is possible that the protective borosilicate scale may allow oxygen diffusion to the covered α-Mo phase. In this case it is possible for MoO_3 bubbles to form and escape the borosilicate scale [13]. Figure 2.21 shows a schematic of the various oxidation kinetics observed in Mo-Si-B alloys as a function of temperature [13].

Research into the ability of a Mo-Si-B alloys with 45% volume fraction intermetallics has shown that borosilicate composition is critical in forming a scale capable of spreading across the surface before evaporating boria to become less permeable and more protective [52]. Part of this research addressed the effects of increasing intermetallic volume fraction on the properties of the α-Mo phases, which is extremely sensitive to Si content. It was found that 45% volume fraction intermetallics had minimal effect on the α-Mo plasticity when processed by reaction synthesis [52]. However, continued work is required to reduce the processing temperature of these alloys to

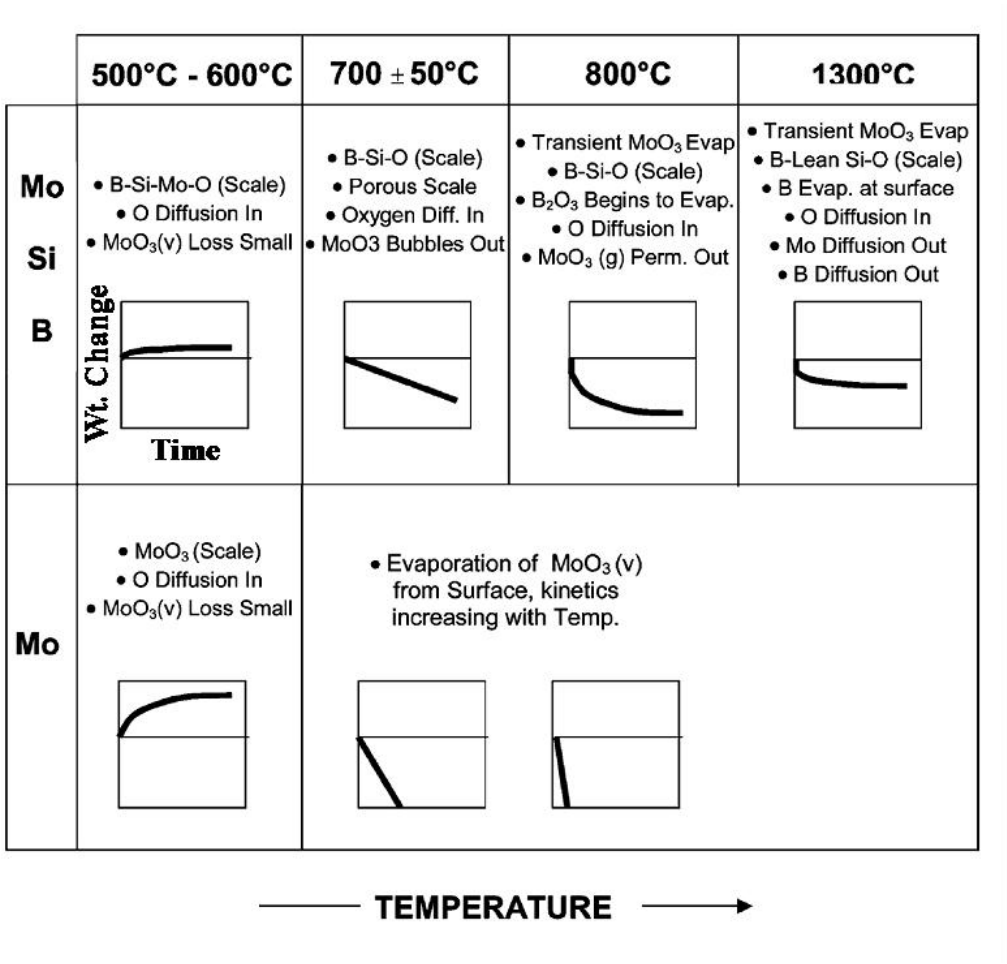

Figure 2.21: Oxidation kinetic regimes in Mo-Si-B alloys [13]

decrease the Si content in α-Mo [52].

Finally, select properties of the three phases are compared in Table 2.1 [25,49,53].

Table 2.1: Properties of interest for individual phases of ternary Mo-Si-B alloys [25, 49, 53]

Property	Units	Mo	Mo_3Si (A15)	Mo_5SiB_2 (T2)
Melting Temperature	$[^\circ C]$	2623	2025	2160
Crystal Structure	[-]	BCC	A15 BCC	D8l BCT
Thermal Conductivity	$\left[\frac{W}{mK}\right]$	138	-	-
CTE at 25°C	$\left[\frac{10^{-6}}{^\circ C}\right]$	5	3	6
CTE at 1300°C	$\left[\frac{10^{-6}}{^\circ C}\right]$	6	7	9

2.2 Synthetic Microstructure Reconstruction

2.2.1 Representative Volume Elements

When characterizing a material in order to create a simulated microstructure it is important to understand at what length scale the microstructure affects the properties of interest and how large a volume must be simulated in order to properly capture the microstructure. The need to quantitatively determine the volume size required for studying how a microstructure affects properties has lead to the concept of a representative volume element (RVE).

The concept of a RVE was originally proposed by Hill in 1963 [54]. Hill defined a RVE as the volume which is capable of representing the entire microstructure ensemble in an average sense [55]. A good introduction to the concept of a RVE can be found in the micromechanics textbook by Qu and Cherkaoui [56]. In this text, the authors consider the appropriate size of a RVE according to the length scale that gives any volume element overall properties which do not change between volume elements. The authors go on to define a RVE as a volume element that is statistically homogeneous and representative of the local continuum properties of interest in such a way that

the appropriate averaging technique results in the effective properties [56].

A RVE is often very computationally expensive and cannot capture the statistical distribution of properties such as fatigue crack formation [57]. The concept of a Statistical Volume Element (SVE) has arisen to address these problems. A SVE can be defined as the volume element which captures the locally varying heterogeneous response at the scale of individual microstructural attributes [54]. A SVE can be smaller in size than a RVE. Consequently, multiple SVEs are required to build up a statistical distribution of responses for a given microstructure [57]. It has been shown by several authors that as the size of a SVE grows, it approaches the size necessary to qualify as a RVE [58–60]. The advantage of a SVE is that the size can be much smaller than the size of a RVE, which can improve computational efficiency and allow many SVEs to be examined to build a statistical understanding of the heterogeneity of a material [57].

Both RVEs and SVEs can be re-created once the statistical distribution of all relevant microstructural features have been characterized. The microstructural features that need to be characterized vary depending on the mechanical properties of interest. However, when modeling microstructure at the scale of grains, there are several important features which cannot be ignored: grain size, shape, and orientation as well as crystal structure [54, 61–64].

2.2.2 Material Characterization

After the appropriate size for a RVE or SVE is determined and before a simulation microstructure can be created, the important microstructural features must be characterized quantitatively. This characterization should allow the physical and simulation microstructures to be compared to ensure that the simulation microstructure accurately captures the physical microstructure being modeled. The microstructural features that need to be characterized vary depending on the mechanical properties

of interest. However, when modeling microstructure at the scale of grains, there are several important important features which cannot be ignored: grain size, shape, and orientation as well as crystal structure [54, 61–64].

Ideally, a material would be characterized according to the positions of grains in space, their crystallographic orientations and shape, and the boundaries [62]. In an ideal case, these attributes would be determined in the form of statistical distributions, which could later be reproduced in a simulated material. In order to later evaluate a microstructure generator, Gross and Li define three quantitative criteria for comparison. The first criterion is the material structure, both at the atomistic structure of grains and boundaries. The second is the material topology, which can be defined by features such as grain boundaries, grain size, triple junctions, dihedral angle at the triple junctions, and misorientation. Finally, the third criterion is the statistics of all these properties gathered over a large sample of grains and microstructural features [62]. Groeber *et al.* stress the importance of not only capturing similar descriptions of a material's microstructure, but also capturing the correlation between different features, such as grain size and with the number of neighboring grains [64,65]. In practice, the microstructural attributes typically available are limited to grain size, volume fraction, orientation, and crystal structures. Additionally, these attributes are typically reported only as mean values, without a statistical distribution [62].

The three dimensional nature of microstructures makes characterization difficult [54]. In addition to the general difficulties of describing shapes in three dimensions, the tools required for three dimensional characterization are very time consuming and not widely available [63]. One such technique is to use two dimensional images to build a three dimensional model by incrementally sectioning the sample and afterward building up the three dimensional image [64]. Groeber *et al.* use such a technique, termed serial sectioning, to reconstruct the three dimensional microstructure of IN100 [64]. However, this is a time consuming and destructing technique [66].

Jiang *et al.* describe a non-destructive method for using high-resolution X-ray tomography to quantify microstructural features in three dimensions [66]. Briefly, the method used by Jiang *et al.* involves rotating a specimen on a high-precision stage while focusing X-rays through the sample onto a screen. The tomographic data can then be reconstructed to create a three dimensional representation of the sample material. Finally, the reconstructed image is used to quantify the material [66]. A diagram of the experimental setup is shown in Figure 2.22.

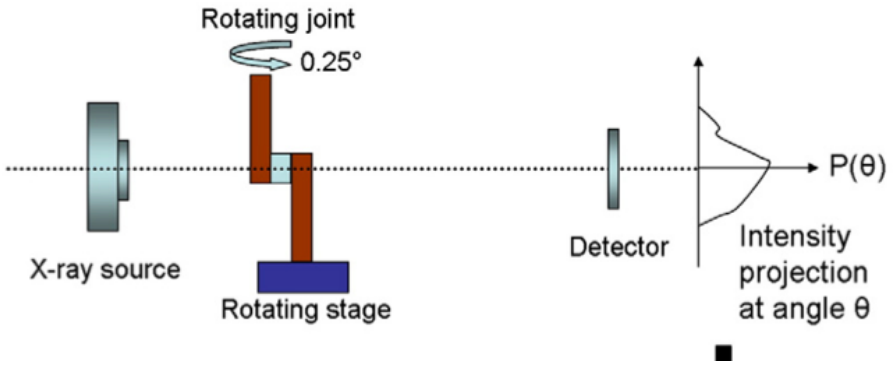

Figure 2.22: Diagram of the experimental setup used by Jiang *et al.* [66].

While the X-ray tomography method of Jiang *et al.* can produce detailed three dimensional images, the process requires great deals of time and expertise to collect the two dimensional images as well as advanced software to intrepret the images. The process is also limited to small specimens. For example, Jiang *et al.* used 745 projections taken at an angular step size of 0.25° over 180° to reconstruct the three dimensional images of a copper bar with dimensions of approximately 10 mm in length and 1 mm in thickness [66]. The reconstructed three dimensional image of Jiang *et al.* is shown in Figure 2.23 [66].

Since three dimensional images are difficult and time consuming, two dimensional stereographic approaches have been developed to approximate microstructures from

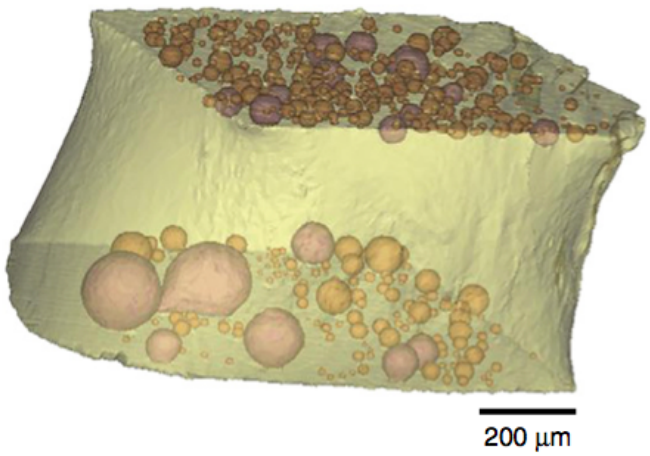

Figure 2.23: Reconstructed 3D image of solder joint from X-ray tomography work of Jiang *et al.* [66].

two dimensional data. One such approach is to use traditional two dimensional methods to image two orthogonal planes as shown in Figure 2.24 [63]. From this stereographic data, some assumptions must be made about grain shape and orientation; however, many polycrystalline materials have been shown to be approximated well with ellipsoids, which makes such an assumption quite reasonable [54, 64, 66].

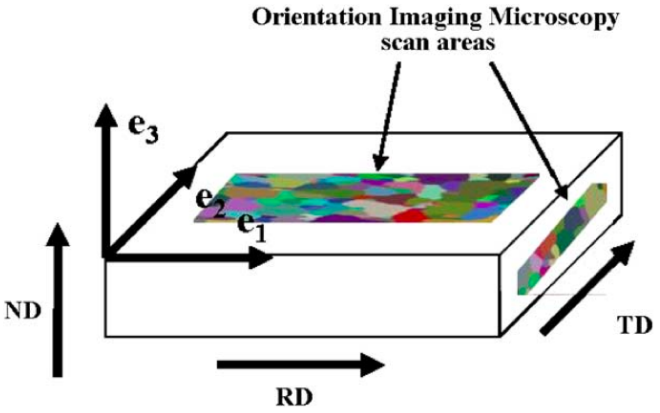

Figure 2.24: Illustration of EBSD observation areas [63].

In order to capture the required microstructural information such as grain shape, grain orientation, crystallographic orientation and misorientation, several different techniques are required. Grain shape and orientation information may be quantified

with optical or SEM images by visually fitting ellipsoids to the grain shapes [61]. Crystallographic data is obtained from electron back-scatter diffraction (EBSD). EBSD maps may also be used to define grains by mapping locations with the same orientation. Combining EBSD data with image data can help improve the clarity of grain boundaries [64]. Additional chemical mapping is also required if the material of interest has multiple phases [64].

2.2.3 Microstructure Generators

After a material's microstructure has been characterized, a simulation microstructure must be created which matches the physical microstructure for all important microstructural features and any statistical variation in those features. When optimizing a material's microstructure, the method for building the simulated microstructures must also be able to make small variations from the original physical microstructure. In making these variations, the generation method must be able to be guided or restricted to variations of microstructure which can be created with appropriate processing. In an effort to create realistic simulated microstructures, two main approaches have been taken: tessellation (typically a form of Voronoi tessellation) and ellipsoidal packing.

2.2.3.1 Voronoi Tessellation

The earliest methods for generating polycrystalline microstructures for use in computational simulations were based on the mathematical concepts of tessellation. In 1990, Horálek described three random tessellation models: the Poisson-Voronoi model, the homogeneous Johnson-Mehl model and the nonhomogeneous Johnson-Mehl model [67]. Of the three, the Poisson-Voronoi model has been used the most in more recent publications, and is the focus for the discussion of tessellation models in this paper.

The Voronoi tessellation can be defined for two and three dimensional spaces. The space is first seeded by points, which are sometimes referred to as centers of

gravity [67]. These points remain fixed in space. The next step is to define an intensity or distance function which describes the relative relationship of all points in the space with respect to the seed points. The space is then divided into regions based on the intensity function. With a simple intensity function, the regions are defined according to proximity to a seed point, where every point in space is assigned to the region of the nearest seed point. Such an intensity function results in space-filling convex polyhedra for a three dimensional space [67]. In two dimensions, the space would be divided into convex polygons as shown in Figure 2.25.

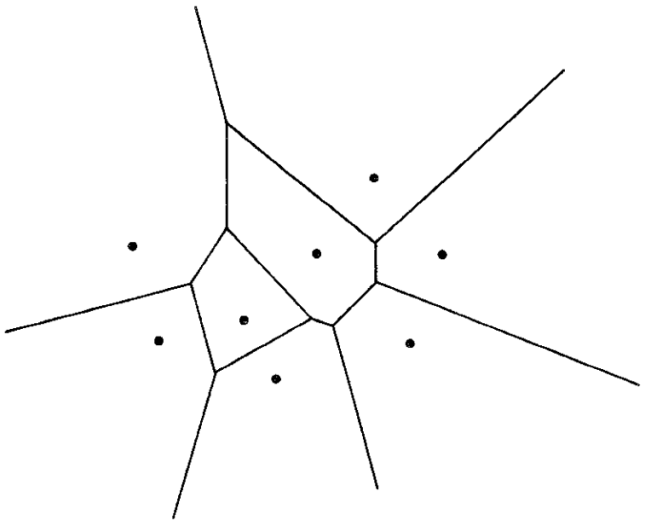

Figure 2.25: Voronoi diagram for eight points in the plane [68].

The article by Horálek focuses on comparing the equations of several tessellation schemes, but does not evaluate their applicability. In practice, it is generally recognized that a standard Voronoi tessellation scheme does not create realistic microstructures without additional control over the seed points [62,63,69]. Gross and Li explain that the topological and statistical properties of the standard Voronoi tessellation scheme are different than found in real materials [62]. Another problem with the standard Voronoi tessellation scheme is that the grain size distribution is fixed to the Poisson-Voronoi distribution, while most polycrystalline materials typically have a lognormal distribution of grain size [62, 64].

Gross and Li present a modified Voronoi tessellation approach to model in order to better capture the grain size distribution of real materials. Their approach starts with the typical information which is more routinely determined and reported: grain size, volume fraction, orientation and crystal structure [62]. For the material studied by Gross and Li, the only available information was grain size distribution; however, they note that the same algorithm may be extended to include other microstructural quantities if their distribution functions are known [62].

The algorithm of Gross and Li begins with a standard Voronoi tessellation in the designated space, where the number of seed points corresponds to the number of desired grains. After the Voronoi cells are constructed, the grain size distribution of the Voronoi cells is computed and compared to the desired distribution function, which can be taken from experiments or theory. The comparison is made using a penalty function [62]. The penalty function used by Gross and Li is similar to a root mean square error function which depends only on the grain size distribution. After computing the initial penalty function, the centers of each grain are moved at random and the process is repeated. If the penalty function is improved, the changes to a grain center are kept, otherwise, the changes are discarded. The process is repeated until the penalty function reaches a preset value [62]. After distributing the grains in space according to the grain size distribution function, the algorithm can be repeated with crystal orientation and misorientation if those distributions are known [62]. Using this method, Gross and Li re-created a two dimensional micrograph, which is shown in Figure 2.26.

Barbe *et al.* have used a similar algorithm to build FE meshes based on a Voronoi tessellation [69]. In the approach of Barbe *et al.*, the Voronoi polyhedra are discretized over a voxel map, which can be used as cubic elements. In this work, grain shape is accounted for by "deforming" the distance function to match the shapes encountered experimentally. In this manner, the grain shape anisotropy of a rolled material can

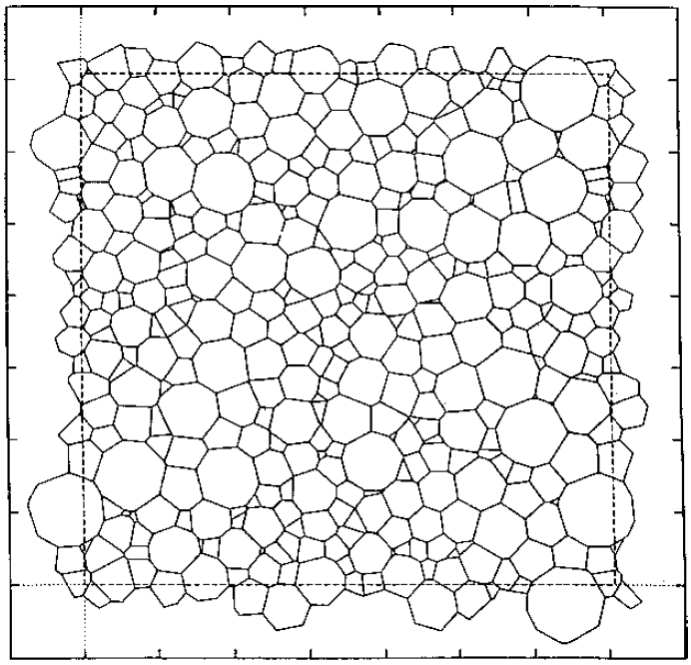

Figure 2.26: The 2D digital micrograph produced by the modified Voronoi tessellation scheme of Gross and Li [62].

be reproduced as in Figure 2.27 [69]. Barbe *et al.* used this algorithm to build three dimensional volume elements, as well. Figure 2.28 shows the FE mesh for a three dimensional volume element created with the modified Voronoi tessellation scheme of Barbe *et al.* [69].

2.2.3.2 Ellipsoidal Packing

Przybyla discusses the difficulties related to quantifying grain shape in three dimensions [54]. These difficulties arise from the general challenges associated with describing shapes in three dimensions as well from experimental difficulty in determining grain shapes in three dimensions [54, 62]. Advances have been made in experimental techniques for microstructure characterization in three dimensions; however, the capability is not widely available and remains a very time intensive task [63]. Although characterization of grain shape in three dimensions is not widely available, good estimates may be made from two dimensional stereographic techniques. In general, grain shape can be approximated using ellipsoids with varying aspect ratios between the

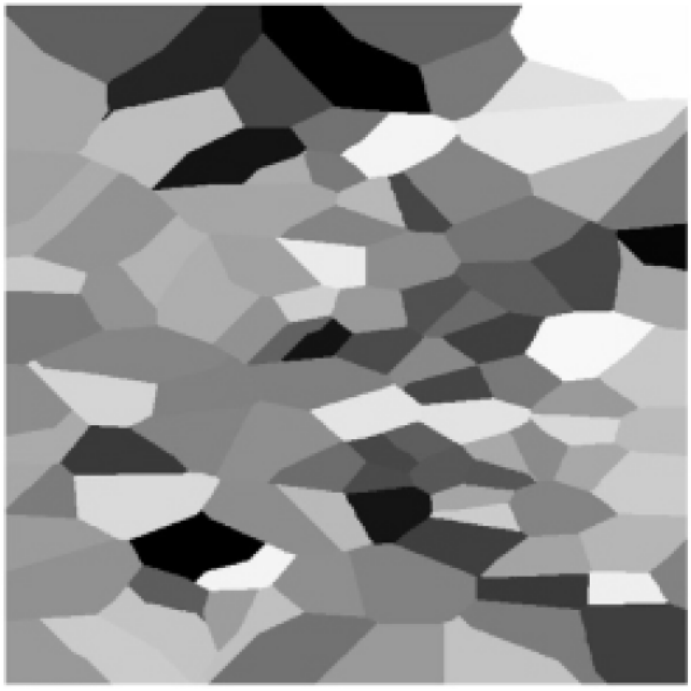

Figure 2.27: Anisotropic grains obtained by deformation of the distance function [69].

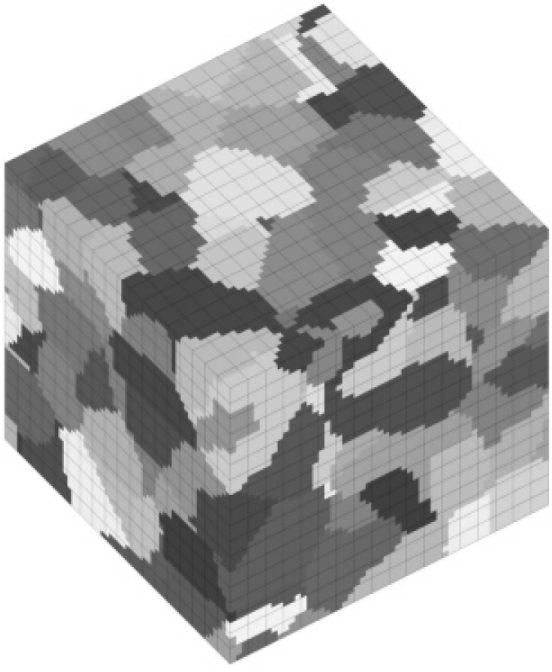

Figure 2.28: FE representation of a 3D simulated microstructure [69].

major and two minor axes [54, 63, 64].

Since grain shape can be approximated with ellipsoids in three dimensions, it makes sense to use ellipsoids as a starting point for modeling polycrystalline materials [65]. Przybyla used both a Voronoi tessellation algorithm and an ellipsoidal packing algorithm when modeling polycrystalline alloys. As part of his work, he compared the two methods, and found that the ellipsoidal packing algorithm gave greater control over grain shape distributions than the tessellation algorithm [54].

The general description of Przybyla's algorithm is as follows. First, a series of ellipsoids are generated according to the statistical distribution of grain size and shape, where shape is controlled by the ratios of the two minor axes with respect to the major axis. After the ellipsoids are generated, the ellipsoids are assigned orientations, which may be based on the statistical distribution of major and minor axes. For instance, if the algorithm is intended to simulate a rolled structure, the major axis may be constrained to lie within the rolled direction. Finally, they are placed in a volume element of pre-determined size until a "jamming limit" has been reached. After the jamming limit is reached, the remaining volume between ellipsoids is filled by simulated annealing. Figure 2.29 shows an example two dimensional cross section of ellipsoidal packing before a simulated annealing step.

This algorithm builds the polycrystalline SVE or RVE. Further modeling can take place by assigning crystal orientations to the grains in a manner that matches the desired orientation and misorientation distributions [54]. The orientation and misorientation algorithm closely resembles that of Barbe *et al.*, and requires an iterative procedure to match the orientation and misorientation distributions. This algorithm has been used by Przybyla to discretize a RVE by assigning cubic elements of a FE model to particular grains, as shown for a two dimensional cross section in Figure 2.30. The algorithm; however, is sufficiently general to apply to FE models with different element types, or to build un-discretized grains similar to the regions produced by

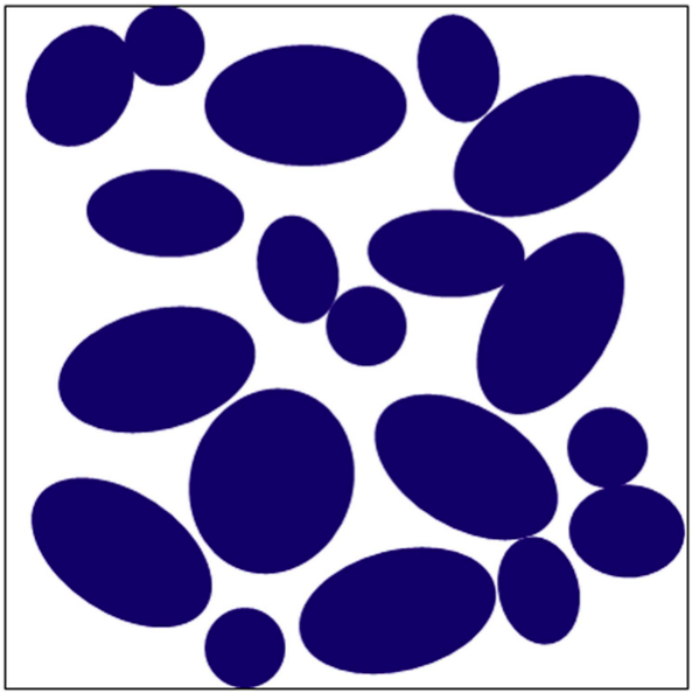

Figure 2.29: A schematic in two dimensions showing the packing of grain equivalent ellipsoids in an predefined area [54].

Voronoi tessellation, but with added control over grain shape and grain orientation.

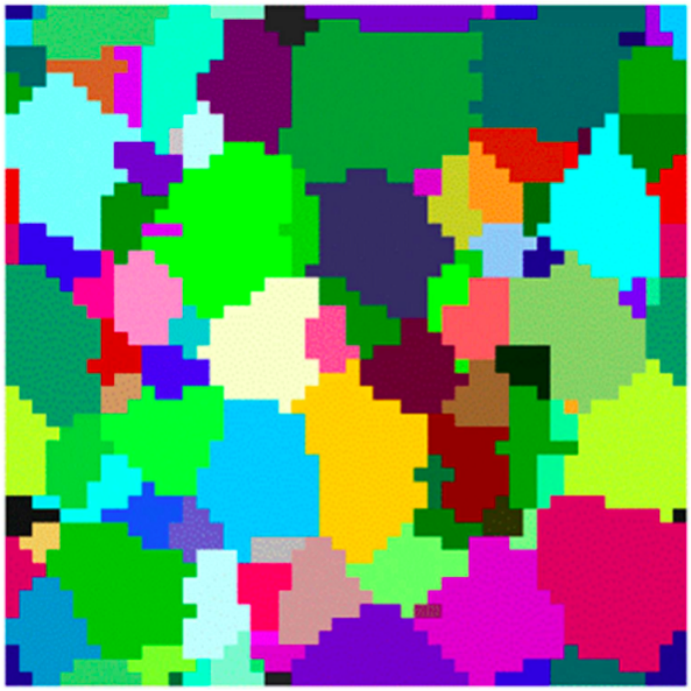

Figure 2.30: A two dimensional section of a microstructure instantiated using the ellipsoid packing algorithm of Przybyla [54].

2.2.3.3 Hybrid Methods

Others have included ellipsoidal packing as a method of refining the grain shape beyond the abilities of a Voronoi tessellation scheme; however, they still include Voronoi tessellation in the overall process. For instance, Brahme *et al.* and Groeber *et al.* each define a sort of hybrid method where grain shapes are defined by ellipsoids and packed into a volume, but the final grain definition and space filling of the RVE is performed with Voronoi tessellation [63, 64].

In the work of Brahme *et al.*, ellipsoids are packed into the predefined volume in an iterative scheme designed to create an optimal filling of the space [63]. Optimal filling is defined as "a system having minimal overlap and maximum space filling". Even after determining the optimal filling of ellipsoids, the procedure may leave regions contained in multiple ellipsoids, and some regions uncontained by an ellipsoid. Two approaches to eliminating overlap and empty space are listed by Brahme *et al.*: a cellular automaton (CA) approach and Voronoi tesselation based approach. Brahme *et al.* choose the latter for their study [63].

In the CA approach, the centroids of the ellipsoids are used as nucleation sites, and the grains are allowed to grow until the space is filled. In the Voronoi tessellation approach used by Brahme *et al.*, a sample set of seed points are chosen and the resulting Voronoi tesselation is computed; however, only the seed points which are contained in one and only one ellipsoid are kept [63]. Additional work is done to create a periodic structure from the Voronoi cells. After the Voronoi cells are created, the ellipsoidal grains are assigned to the cells, which are non-overlapping and space filling. The volume may then be discretized with any type of finite elements. Orientation assignment is performed and modified in order to match the desired orientation and misorientation distibution functions [63].

The above approach may seem overly complicated in comparison with the less involved approach of Przybyla's ellipsoidal packing algorithm; however, the results of

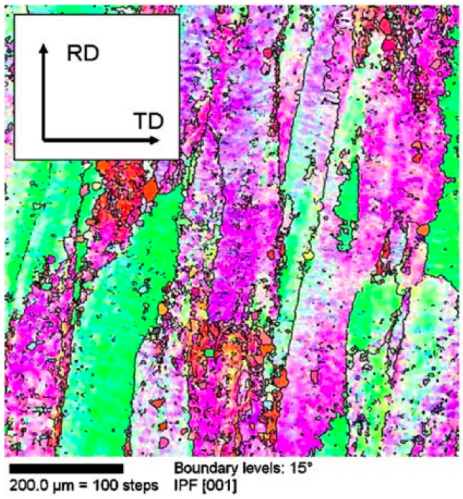

(a) Experimental microstructure in the rolling plane of AL-1050 sample studied by Brahme *et al.*

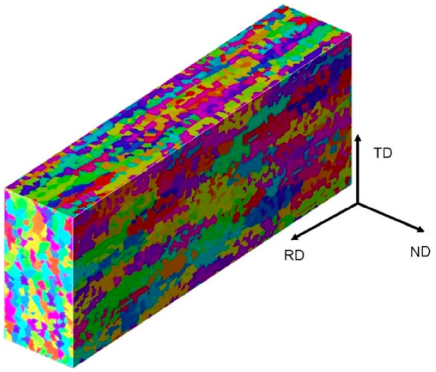

(b) Simulated microstructure created by Brahme *et al.*

Figure 2.31: Comparison of the microstructure reconstruction of Brahme *et al.* to the experimental specimen [63].

the study by Brahme *et al.* are quite good. Brahme *et al.* applied their microstructure reconstruction algorithm to a rolled aluminum alloy [63]. The microstructure characterization was performed from two dimensional stereographic observations as shown previously in Figure 2.24.

The observed microstructure of the rolled aluminum studied by Brahme *et al.* is shown in Figure 2.31a next to the simulated microstructure generated by Brahme *et al.* in Figure 2.31b [63]. A visual inspection of the rolling plane of the simulated microstructure shows that the qualitative ability of the microstructure generator to capture grain shape and orientation is good. Quantitatively, Brahme *et al.* were able to show that the grain shape minor axis aspect ratios of the simulation (5x2x1) closely approximates the observed average aspect ratios of 20x4x1 [63].

Groeber *et al.* ues a similar hybrid method to model the Ni-base superalloy IN100 [64, 65]. The first step is an "equivalent ellipsoidal grain generator" (EEGG) which creates ellipsoidal shaped grains according to the grain volume distribution, aspect ratio-grain volume correlation, and shape orientation distribution [65]. The second

step is a "constrained grain packer" which places the ellipsoidal grains created in the previous step in a predetermined volume. The EEGG and CGP algorithms are similar to those used by Brahme *et al.* and Przybyla, which have been previously described [54,63]; however, in the second step Groeber *et al.* also match the correlation between the number of neighboring grains and grain size as well as the neighbor volume to grain volume correlation [65]. The third step in the Groeber *et al.* algorithm is to employ a Voronoi tesselation to create the final grains. This step is called the "seed point generator - constrained Voronoi tessellation tool" (SPG-CVTT). The seed points are constrained by the previously performed ellipsoidal packing. The final step of this method is a "crystallographic orientation assignment" (COA) step which closely resembles that of all the other methods presented [65].

The steps of the Groeber *et al.* method are built as individual modules. This allows for microstructures to be built using a subset of the individual steps [65]. If the third step (SPG-CVTT) is omitted, the algorithm of Groeber *et al.* [65] is nearly identical to the ellipsoidal packing algorithm of Przybyla [54]. Figure 2.32 shows an example of a reconstructed microstructure for IN100 using the full Groeber *et al.* method [65].

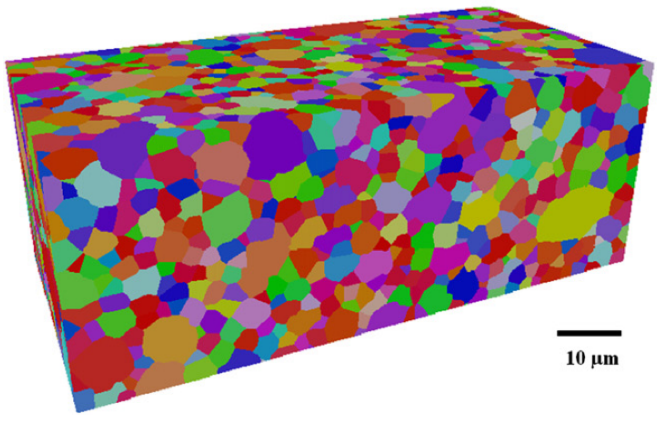

Figure 2.32: Simulated microstructure reconstructed with the method of Groeber *et al.* [65].

Groeber *et al.* found that their hybrid method improves control over the statistical

accuracy of the recreated microstructure. Specifically, their hybrid method captures: changes in the average number of neighboring grains, the log-normal distribution of grain size, and the non-uniform distributions in size and shape of grains [65]. The method used by Groeber *et al.* is probably the most thorough method reviewed in this section, because it describes a more complete material characterization and allows for more control over each aspect of the material characterization when recreating the material for simulation. In addition to the attributes accounted for by Przybyla [54] and Brahme *et al.* [63], Groeber *et al.* also capture the statistical distribution for the number of neighboring grains, the statistical distribution for the correlation between grain size and number of neighboring grains, the statistical distribution for the correlation between grain size and neighboring grain size, and the statistical distribution for the correlation between aspect ratio and grain size [65]. The hybrid method developed by Groeber *et al.* is now implemented as a free and open source tool for microstructure reconstruction known as DREAM.3D [70, 71].

2.3 Crystal-viscoplasticity

The continuum theory of crystal plasticity was developed in stages over several decades to link the micromechanics of dislocation motion along crystallographic slip planes to the deformation of single crystals and can be extended to include poly-crystals by explicitly modeling individual grains as separate single-crystals [72–83]. Crystal plasticity is a special case of Internal State Variable (ISV) constitutive theory and is a framework for including irreversible behavior and microstructure evolution in materials models as a series of internal variables [74, 84].

The fundamental concept of ISV theory is the idea that a non-equilibrium, irreversible process can be treated as a series of constrained equilibrium states [85–88]. At each constrained equilibrium state in the process, the internal state variables defining the state are considered to be fixed and non-evolving. The stages in the evolution

process are termed constrained equilibrium states because the thermodynamic driving forces associated with the fixed internal variables are may be non-zero at each non-evolving stage. Internal state variable theory addresses the non-equilibrium process of microstructure evolution through this sequence of constrained equilibrium states, where the internal variables are allowed to evolve with the thermodynamic driving forces through a non-equilibrium process between constrained equilibrium states. The concept of local constrained equilibrium states is only applicable if the rates of the thermodynamic driving forces are sufficiently slow with respect to the governing viscous or thermally activation mechanisms that the near equilibrium relaxation occurs between constrained equilibrium states, or if the driving force rates are sufficiently fast with respect to the same characteristic relaxation rates that little relaxation can occur between constrained equilibrium states [84].

Within the framework of ISV theory, crystal plasticity treats the evolution of microstructure through a series of internal state variables which describe the homogenized evolution of plastic flow along crystallographic slip systems [84]. The choice of internal state variables, their thermodynamic driving forces, and their evolution equations is non-unique [84]; however, a common approach is to treat each slip system with the classical viscoplastic variables of threshold stress, kinematic stress, and drag stress [89] which evolve according to the homogenized evolution of dislocation pile-ups or dislocation density and are driven by the resolved shear stress on each slip system [54, 90–94].

The foundational concept of crystal plasticity is the decomposition of the deformation gradient from continuum mechanics. A common decomposition of the deformation gradient is into elastic and plastic parts as

$$\mathbf{F} = \mathbf{F}^e \cdot \mathbf{F}^p \tag{2.1}$$

where $\mathbf{F}$ is the second rank deformation gradient tensor, $\mathbf{F}^e$ is the elastic portion of the deformation gradient associated with stretch and rotation of the crystal lattice,

and $\mathbf{F}^p$ is the plastic portion of the deformation gradient associated solely with the dislocation motion. As shown in Figure 2.33, this decomposition of the deformation gradient results in an intermediate configuration between the undeformed reference configuration and the current configuration after the full deformation gradient is applied [78, 95]. In Figure 2.33, the α^{th} slip system direction is denoted as $\mathbf{s}_0^\alpha$ and the slip plane normal is denoted as $\mathbf{n}_0^\alpha$ for the reference and intermediate configurations and as $\mathbf{s}^\alpha$ and $\mathbf{n}^\alpha$, respectively, in the rotated and stretched state of the current configuration.

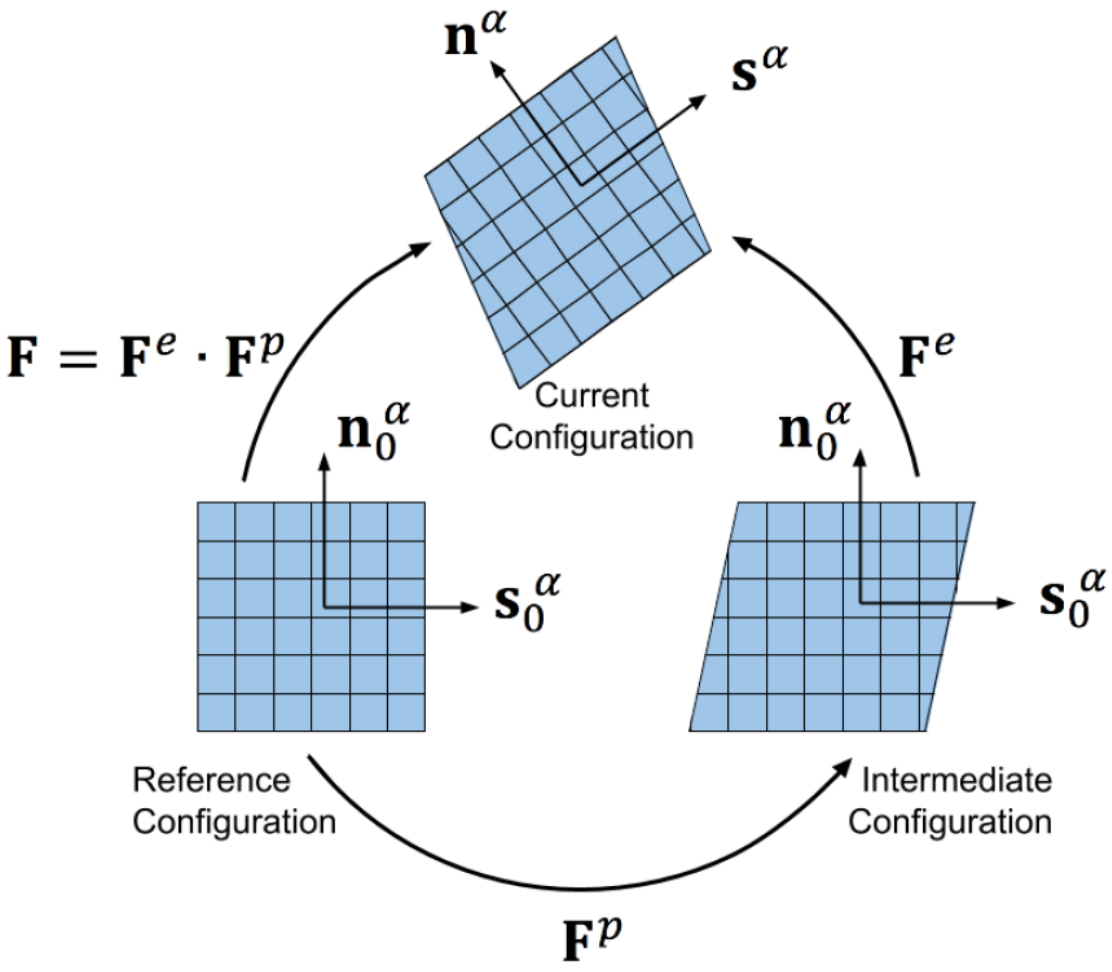

Figure 2.33: Decomposition of the deformation gradient [95]

This decomposition is purely mathematical and does not represent a physical

separation of the deformation mechanisms, which occur simultaneously in reality [73]. Instead, the decomposition of the total deformation gradient functions to separate the deformation mechanisms associated with plastic deformation from the stretch and rotation of the crystal lattice [78]. This is important for the development of crystal plasticity because it allows the intermediate configuration to be chosen as an isoclinic configuration where the material substructure orientation does not change with respect to the reference configuration. The advantage of this decomposition and choice of intermediate configuration is the separation of the thermoelastic deformation from the plastic velocity tensor, which now depends only on the plastic deformation gradient and can be calculated in the intermediate configuration with respect to the original substructure orientation.

The full velocity gradient can now be additively decomposed in the elastic and plastic parts as

$$\mathbf{L} = \dot{\mathbf{F}} \cdot (\mathbf{F})^{-1} = \mathbf{L}^e + \mathbf{L}^p \tag{2.2}$$

where $\mathbf{L}$ is the velocity gradient, $\dot{\mathbf{F}}$ is the material time derivative of the deformation gradient, $(\mathbf{F})^{-1}$ is the inverse of the deformation gradient, $\mathbf{L}^e$ is the elastic velocity gradient, and $\mathbf{L}^p$ is the plastic velocity gradient.

The final crucial development to crystal plasticity is to relate the material time derivative of the plastic deformation gradient to the shearing rates on individual slip systems as

$$\dot{\mathbf{F}}^p = \left(\sum_{\alpha=1}^{N_\alpha} \dot{\gamma}^\alpha \mathbf{s}_0^\alpha \otimes \mathbf{n}_0^\alpha \right) \cdot \mathbf{F}^p \tag{2.3}$$

where $\dot{\mathbf{F}}^p$ is the material time derivative of the plastic deformation gradient, N_α is the total number of slip systems, and $\dot{\gamma}^\alpha$ is the shearing rate on the α^{th} slip system [81]. This relationship allows the plastic velocity gradient to be calculated as a function slip system shearing rates in the intermediate configuration as

$$\mathbf{L}_0^p = \dot{\mathbf{F}}^p \cdot (\mathbf{F}^p)^{-1} = \sum_{\alpha=1}^{N_\alpha} \dot{\gamma}^\alpha \mathbf{s}_0^\alpha \otimes \mathbf{n}_0^\alpha \tag{2.4}$$

where $\mathbf{L}_0^p$ is the plastic velocity gradient in the intermediate configuration.

The current configuration elastic and plastic velocity gradients may now be calculated as

$$\mathbf{L}^e = \dot{\mathbf{F}}^e \cdot (\mathbf{F}^e)^{-1} \tag{2.5}$$

and

$$\mathbf{L}^p = \mathbf{F}^e \cdot \mathbf{L}_0^p \cdot (\mathbf{F}^e)^{-1} \tag{2.6}$$

respectively.

Finally, the elastic Green strain tensor and the second Piola-Kirchoff stress can calculated in the intermediate configuration and the Cauchy stress can be calculated in the current configuration to find the resolved shear stress on each slip system. The elastic Green strain tensor is calculated as

$$\mathbf{E}^e = \frac{1}{2}\left[(\mathbf{F}^e)^T \cdot \mathbf{F}^e - \mathbf{I}\right] \tag{2.7}$$

where $\mathbf{E}^e$ is the elastic Green strain tensor and $\mathbf{I}$ is the second rank identity tensor. The second Piola-Kirchoff stress is related to the elastic Green strain through the fourth rank elasticity tensor as

$$\mathbf{T} = \mathbb{C} : \mathbf{E}^e \tag{2.8}$$

where $\mathbf{T}$ is the second Piola-Kirchoff stress and $\mathbb{C}$ is the fourth rank elasticity tensor. Now the Cauchy stress tensor in the current configuration may be calculated from the second Piola-Kirchoff stress as

$$\boldsymbol{\sigma} = \frac{1}{det(\mathbf{F}^e)}\mathbf{F}^e \cdot \mathbf{T} \cdot (\mathbf{F}^e)^T \tag{2.9}$$

where σ is the Cauchy stress used to solve for the resolved shear stress on each slip system according to

$$\boldsymbol{\tau}^\alpha = \boldsymbol{\sigma} : (\mathbf{s}_0^\alpha \otimes \mathbf{n}_0^\alpha) \tag{2.10}$$

where $\boldsymbol{\tau}^\alpha$ is the resolved shear stress of the α^{th} slip system.

Because the resolved shear stress is the driving force for the shearing rate on each slip system, either an iterative approach or an explicit solution method is required to solve for shearing rates of the current increment. In this work, a fully implicit solution for the shearing rates on each slip system is employed based on the Newton-Raphson numerical solution method.

When this constitutive model is implemented as part of a finite element (FE) solver, the full crystal plasticity equations must be solved at each integration point in the FE model. For very large models this can become computationally expensive, so full microstructure-sensitive crystal plasticity implementations are not frequently implemented for engineering components. Instead, a microstructure-sensitive material response database may be built up from smaller crystal plasticity simulations that explicitly capture the effects of microstructure and a reduced order model fit to this database. The reduced order models can then be employed on engineering component scale simulations in order to provide microstructure-sensitive material responses without the computational cost of a fully implicit crystal plasticity constitutive law.

2.4 Fatigue

Fatigue life is a difficult property to predict due to the stochastic nature of the damage mechanisms leading to fatigue failure. This property depends on the local varying heterogeneity of the microstructure, requiring a much larger volume element to properly define an RVE. Such RVEs are typically too large to run efficient simulations. Another approach is to create a larger number of SVEs, which can be smaller and run more efficiently. If the microstructure generator is properly capturing the statistical nature of all the microstructural attributes associated with fatigue damage, one can reasonably expect that the distribution in fatigue life predicted by the SVEs represents the distribution in fatigue life of the material.

In addition to the difficulties of capturing an RVE for fatigue life predictions,

total fatigue life is governed by a series of crack lengths and damage mechanisms. Total fatigue life can be broken into a combination of fatigue crack initiation and propagation, with several crack length scales covered by each portion of fatigue life prediction [57]. Different modeling approaches are required for each portion of total fatigue life. The techniques required to predict fatigue crack initiation is the focus of the remainder of this section. Fatigue crack propagation is typically assessed with linear elastic fraction mechanics (LEFM) and assumes an existing crack or flaw to predict crack growth rates under cyclic loading. Due to the very high crack growth rates seen in triplex Mo-Si-B alloys [25, 26, 31, 35, 96–98], a reasonable approximation to total fatigue resistance may be made by neglecting this portion of total fatigue life. This assumption also saves significant modeling effort because separate models are required to assess fatigue crack initiation and fatigue crack propagation.

Fatigue crack initiation is typically assessed by tracking variables termed Fatigue Indicator Parameters (FIP). Numerous FIPs have been shown to represent different types of fatigue damage, and can be correlated to fatigue life if the damage mechanism is known [57, 99–101]. If there is more than one possible damage mechanism, it is easy to track multiple FIPs since they add very little in terms of computational cost when running a FE simulation with a UMAT. In fact, many FIPs rely directly on the results of solving the constitutive model, for instance, a common FIP is the effective cumulative plastic strain, which can be calculated quite simply from the results of solving the flow rule. For this research, two of the most common FIPs are tracked to allow for comparison of several expected damage mechanisms.

For this project, two common FIPs are used: effective cumulative plastic strain and the Fatemi-Socie parameter. The effective cumulative plastic strain is related to the formation of persistent slip bands, which has been linked to fatigue crack nucleation in single crystals [57, 102]. This parameter has been used to predict crack initiation sites for low and high cycle fatigue of polycrystalline nickel-based superalloys at the

slip band scale [103, 104]. The Fatemi-Socie parameter is introduced to account for multiaxial fatigue crack formation at the grain scale and larger scales. It has been shown to correlate well to multiaxial fatigue in both low cycle and high cycle fatigue at these scales [105]. Additional FIPs exist that may help distinguish between single slip and multislip, address crack formation at grain or phase boundaries, or include the influence of hydrostatic stress [57, 100, 101]. For this work, only the Fatemi-Socie and effective cumulative plastic strain is calculated for predicting microstructure-sensitive fatigue crack formation.

Effective cumulative plastic strain is defined as in Equation 2.11

$$P = \int_0^t \sqrt{\dot{\epsilon}_{ij}^p \dot{\epsilon}_{ij}^p} d\tau \tag{2.11}$$

where ϵ_{ij}^p is the plastic strain tensor and t is time [57]. This parameter is similar to the accumulated plastic slip used by Hochhalter [100]. The Fatemi-Socie parameter is defined in Equation 2.12

$$FS = \frac{\Delta\gamma_{max}^p}{2}\left(1 + k\frac{\sigma_{max}^n}{\sigma_y}\right) \tag{2.12}$$

where $\frac{\Delta\gamma_{max}^p}{2}$ is the maximum volume averaged cyclic plastic shear strain amplitude, σ_{max}^n is the maximum normal stress on the plane of $\frac{\Delta\gamma_{max}^p}{2}$, σ_y is the uniaxial yield strength, and k is a parameter to adjust the influence of normal stress [57, 99].

Both fatigue parameters are calculated at each integration point of a FE simulation. To account for artificial stress concentrations resulting from a voxellated FE mesh and FE mesh sensitivities, the FIP calculation is treated with a local volume averaging scheme where each integration point is averaged by the integration points within one equivalent grain radius. The distance of the local volume averaging procedure can be adjusted to reflect the short range influence of local material volume on fatigue crack formation. In this work, the local volume averaging is conducted with a Gaussian filter, where the length scale is adjusted by setting the standard deviation of

the filter. Greater detail on the local volume averaging used in this work is discussed in Chapter 7.

2.5 Modeling Damage in Quasi-Brittle Solids

Linear Elastic Fracture Mechanics (LEFM) is well established for analyzing crack growth, but requires a sufficiently large initial crack of known or assumed geometry in order to perform an analysis [106, 107]. When studying microstructure sensitive crack formation and growth, other techniques allowing for arbitrary, unknown, and multiple crack locations are required. For brittle materials or materials including brittle phases or components, LEFM is not only limited, but often the underlying assumptions of crack size with respect to the plastic zone size are invalid [106–108]. For such brittle materials, where fatigue life and fracture are dominated by crack propagation and crack coalescence instead of crack initiation, cohesive zone models (CZM) offer a method to study crack formation and propagation without assuming the crack location. CZM approaches can also allow multiple cracks to form at once [106–110]. CZM techniques have been used to model crack formation and growth in concrete, ceramics, polymers, metals, and interfaces between different materials [111–117].

CZM suffers from the same scalability issues as other continuum level finite element modeling for microstructural sensitive studies, which often require large volume elements. Allowing cracks to form at arbitrary interfaces, especially in large models with many features of interest, can result in large models which require long simulation times to complete. Often, the solution to such a problem is to reduce models from three dimensions to two dimensions, which result in faster simulation times, but sacrifice the three dimensional characteristics of real microstructures [118]. These issues are compounded by the mesh refinement sensitivity of CZM implemented in finite elements [119].

Scalability issues are also introduced when attempting to include microstructural

sensitive models with simulations of engineering scale components. In an attempt to maintain the benefits of crack initiation and propagation models while decreasing the computational cost of larger simulations, multiscale modeling techniques have been developed to help address scalability issues [120].

The following sections explore the background development of CZM, their use in crack propagation modeling, and the benefits and limitations. Following this discussion is a section on peridynamics, which is a relatively new alternative to continuum mechanics directed specifically towards addressing the problems introduced in continuum models when discontinuities such as cracks are present. Finally, some multiscale modeling techniques for overcoming the scalability issues associated with bridging length scales are discussed.

2.5.1 Brittle Fracture and Crack Formation

While LEFM predicts crack growth and fracture toughness of ductile materials, the process zone of brittle materials does not match the assumptions required for traditional fracture mechanics. Brittle and quasi-brittle materials, such as ceramics and concrete, derive their toughness from crack bridging, microcrack formation, and crack deflection instead of from the plastic deformation in front of a crack tip as in ductile materials including most metals [121, 122]. In fact, single phase ceramics behave as ideal brittle materials and crack propagation is directly linked to overcoming the surface energy of the material. In addition to modern ceramics, concrete, and geologic materials, many intermetallic metal alloys behave in a quasi-brittle manner, and their fracture behavior behaves more like concrete than traditional metals [118, 121].

Crack bridging occurs when material spans the displacement between crack faces of a macroscopic crack. Figure 2.34 shows an example of crack bridging in Al_2O_3/Al [122]. Crack bridging is expected to occur when the fracture energy of the interface between phases is low with respect to the fracture toughness of the matrix phase

[121, 123]. The interface between the matrix and secondary phase experiences Mode II loading and debonding occurs between the matrix and reinforcing second phase along the length of the crack. Frictional effects may also be involved if pull out of occurs as a competing mechanism, as if often observed in fiber reinforced composites, ceramics, and concrete [121, 124]. A schematic of the debonding of whisker fibers bridging a crack in a reinforced ceramic is shown in Figure 2.35 [124]. Crack bridging is found in composites, toughened ceramics, concrete, and qausi-brittle multi-phase intermetallics [96, 121–125].

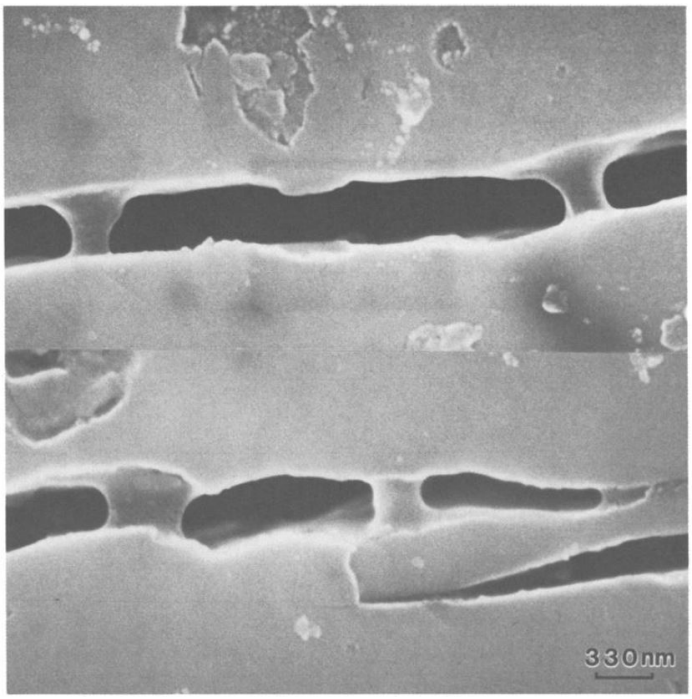

Figure 2.34: Crack bridging in Al_2O_3/Al [122]

Microcrack formation is the formation of smaller, non-critical cracks. Microcracking may act as a toughening mechanism when they form around a macroscopic crack in the process zone away from crack propagation path. Since the microcracks require work to nucleate and open, less energy is available to grow the macroscopic crack. The addition of microcracks result in an increase in compliance, provided that the microcracks remain non-critical and grow stably [121]. Microcracks may also form directly

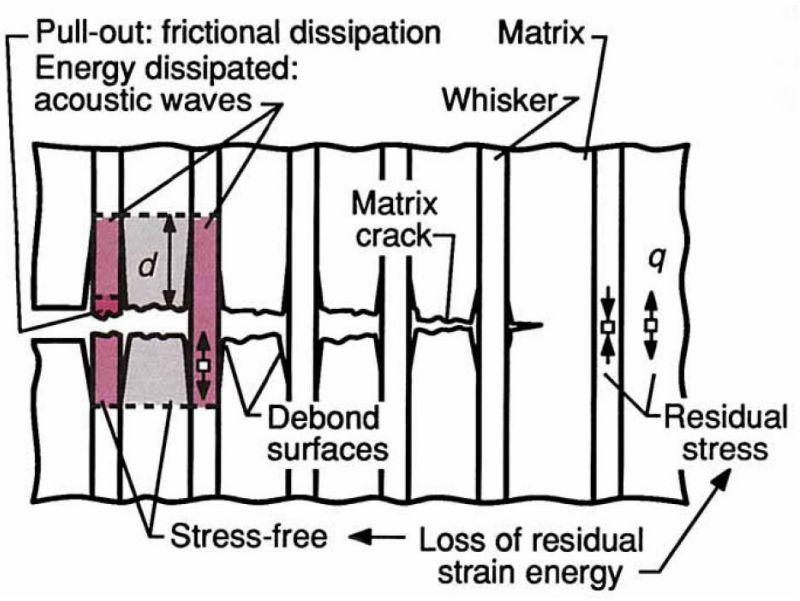

Figure 2.35: Schematic of the various contributions to toughness of reinforced ceramics [124]

ahead of the macroscopic crack tip, resulting in crack bridging. When these microcracks coalesce or the bridging material fractures or ruptures, they become part of the larger crack. A schematic of crack bridging and microcracking in the process zone of a concrete material is shown in Figure 2.36 [121]. While microcracking is a relatively weak strengthening mechanism in brittle materials such as ceramics, the toughness of unreinforced concrete is largely related to the subcritical cracking prior to large crack formation and ultimate failure [121]. Fiber-reinforced concrete demonstrates crack bridging by the fibers as the stronger toughening mechanism [125]. Brittle and quasi-brittle materials exhibiting crack bridging typically have larger toughness values than those that do not demonstrate crack bridging [121].

Similar to microcracking, crack deflection increases a material's fracture toughness by increasing the fracture surface area [121]. Crack deflection may occur when a crack reaches a hard or tough particle and must change path to either debond the particle from the surrounding material or traverse around the particle before resuming crack growth in the preferable orientation. If there is microcracking surrounding the particle

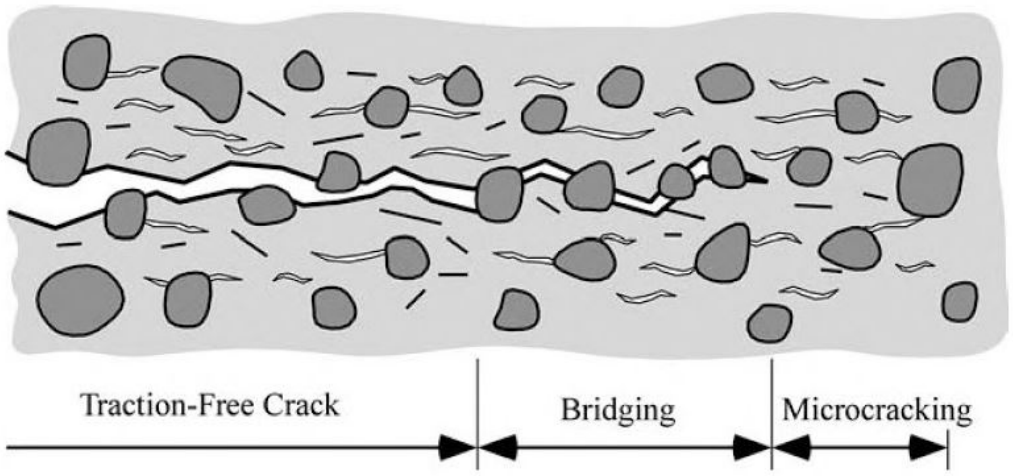

Figure 2.36: Schematic of crack growth in concrete with crack bridging and microcracking [121]

blocking a crack, the crack may bridge the particle instead of deflecting around. Crack deflection typically occurs when a brittle or quasi-brittle is reinforced with a secondary phase, but it can also occur in relatively ductile materials, although this mechanism is more often related to resistance to fatigue crack propagation in such materials. In ductile materials, a example of interfaces inducing crack deflection are an unfavorably oriented grain or hard precipitate. An everyday example of crack deflection can be found when trying to split a difficult piece of firewood around a knot or wave in the grain of the wood. No matter the material, in cases where the crack is deflected at a large angle from the preferred orientation, with the extreme of switching from Mode I to Mode II loading, crack deflection can be an efficient toughening mechanism, but is difficult to model or predict due to the mixed mode loading involved [126]. Figure 2.37 shows a schematic representation of crack branching [121].

Brittle and quasi-brittle materials may be further strengthened by the addition of ductile phases. In the case of toughened ceramics, the second phase particles provide additional energy dissipation in the more traditionally understand manner from nonlinear deformation. The ductile phase can also act as bridging elements along a crack to retard crack propagation, because the relatively tough phase is less likely

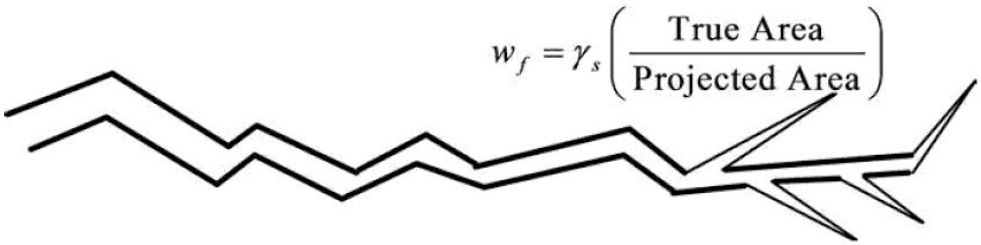

Figure 2.37: Schematic of crack meandering and branching [121]

to crack than the surrounding brittle phase and can be left intact in the propagating crack. The addition of secondary ductile phases in ceramics has given rise to a class of toughened ceramics with toughness values approaching that of lower quality steels [121, 122]. Similar approaches are taken for developing high temperature structural intermetallic alloys such as molybdenum-silicides and γ-Ti based intermetallics, which contain very brittle intermetallic phases desirable for high temperature strength and relatively ductile phases to provide room temperature ductility [35, 127–129].

Due to the different mechanisms for crack formation and propagation in brittle and quasi-brittle materials, a different technique is required for modeling the fracture mechanics of these materials. Research into the fracture of brittle materials, in particular that of concrete, has led to the development of the cohesive zone model, which are discussed in the next section.

2.5.2 Cohesive Zone Elements

Historically, Cohesive Zone Models stem from the works of Barenblatt in 1959 and Dugdale in 1960 [130–132]. It was later extended to quasi-brittle materials and cementitious composites by Hillerborg et al., as the fictitious crack model [109–111]. The foundation of the cohesive zone model is the form of the traction-separation equations defining the constitutive behavior of the model. Since the introduction of the cohesive zone concept, many traction-separation equations have been used to describe a wide range of material behaviors for metals, ceramics, polymers, composites,

and cements [109]. While cohesive zone models are separate from computational techniques, they are typically used in combination with computational methods such as the finite element method. Today, cohesive zone models are used frequently enough to be included as common element types in commercial software, such as the finite element method package Abaqus [133], and include a selection of traction-separation laws.

An example of the results of a 2-D finite element study are shown in Figure 2.38 [118]. In this example, the debonding of the relatively ductile matrix phase from the hard intermetallic phases competes with cleavage fracture of the intermetallic phase as microcrack formation mechanisms. If sufficient information is known to calibrate the constitutive laws separately for the cohesive elements at these distinct locations, microstructure studies can be conducted to help minimize or maximize different mechanisms to improve fracture toughness.

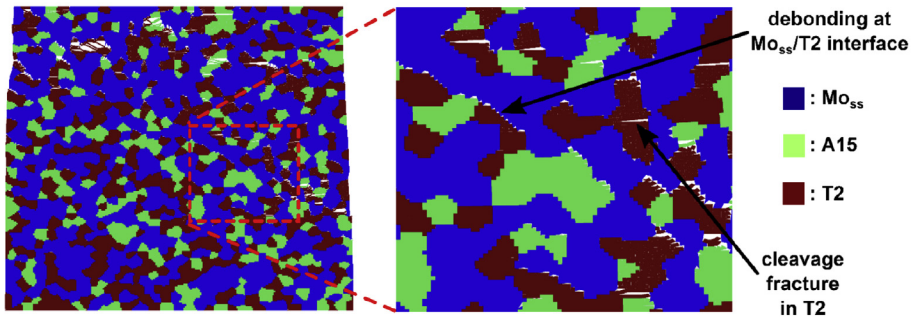

Figure 2.38: Competing damage mechanisms from a 2-D CZM Mo-Si-B simulation in Abaqus [118]

Some of the common traction-separation relationships developed for CZM are shown in Figure 2.39. The form of the traction-separation equation sorts the cohesive zone constitutive models into two classes: potential based models or non-potential based models. Non-potential based models are attractive for their relative simplicity for development and use, but do not guarantee consistent constitutive relationships for

mixed-mode loading [110]. A common form for non-potential based traction separation equations is a bilinear model, with decreasing elastic stiffness after initial damage formation [134–137]. Some potential based models have relatively simple forms and a physical basis and have been used a starting point in other works [114, 115, 138].

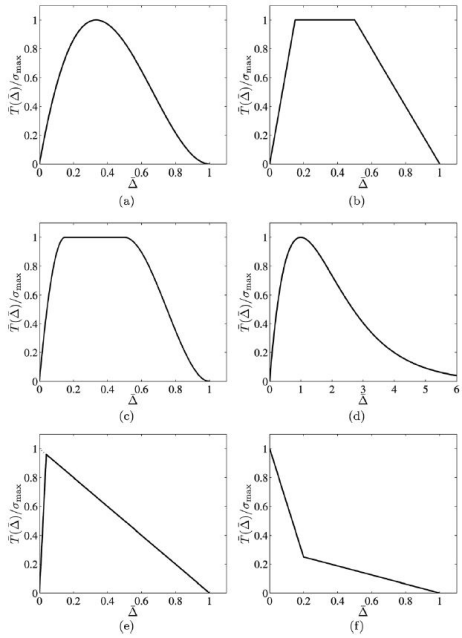

Figure 2.39: Effective traction-separation relationships: (a) cubic polynomial, (b) trapezoidal, (c) smoothed trapezoidal, (d) exponential, (e) linear softening, and (f) bilinear softening [110]

It is often important to separate the compression and tension response and include irreversible damage. This can be achieved by defining an effective stiffness in the traction separation equation as

$$t_i = k'\delta_i = (1 - D)k\delta_i \tag{2.13}$$

where the subscript i refers to the loading mode or displacement type. In two dimensions, this would take the form of shear and normal displacements.

This traction-separation equation is the form taken for the irreversible, bi-linear, softening behavior used by Camanho and Dávila and found in the FEA package Abaqus [133, 137] and originally developed for use with laminated composites and

mixed mode decohesion [139–141]. The effective stiffness is set to the initial stiffness for displacements less than the damage initiation displacement, degraded according to cumulated damage until reaching the failure displacement, and set to zero after cohesive zone failure. Insensitivity to damage for compression can be achieved by using the original stiffness during normal compressive displacements. The behavior of the effective stiffness can be shown in behavior of the isotropic damage as

$$D = \begin{cases} 0; & \delta_i^{max} \leq \delta_i^0 \\ \dfrac{\delta_i^f \left(\delta_i^{max} - \delta_i^0\right)}{\delta_i^{max}\left(\delta_i^f - \delta_i^0\right)}; & \delta_i^0 < \delta_i^{max} \leq \delta_i^f \\ 1; & \delta_i^{max} > \delta_i^f \end{cases} \tag{2.14}$$

where D is the damage of the cohesive element ranging from zero to one, δ_i^{max} is the maximum effective displacement of the loading history and is required to be positive to maintain irreversible damage, δ_i^0 is the initial effective displacement when damage starts, and δ_i^f is the effective displacement for final failure of the cohesive element. With such a definition for damage and traction-separation, unloading after damage has initiated results in a separate traction-separation path from the original loading. Subsequent displacement follows the original curve only after reaching and exceeding the maximum effective displacement from prior loading.

The initiation damage, δ_i^0, is defined as

$$\delta_i^0 = \frac{t_i^0}{k} \tag{2.15}$$

where t_i^0 is the traction for damage initiation and k is the initial stiffness of the cohesive element for that mode, usually taken to be either the Young's modulus for normal loading or shear modulus for shear loading of the associated material.

The form of the traction-separation equation is not the only important consideration when using cohesive zone models. Different fracture modes may require separate calibrations and a damage criterion must be selected to account for interactions of

mixed mode failure. In the case of the maximum nominal stress criterion as in

$$max\left\{\frac{\langle t_n\rangle}{t_n^0}, \frac{t_s}{t_n^0}, \frac{t_t}{t_t^0}\right\} = 1 \tag{2.16}$$

where $\langle\rangle$ are MacCauly brackets and equal to zero for negative values, t_n is the normal stress, and t_s and t_t are shear stresses in the two remaining basis directions, there is no mode interaction and the effective displacement in the damage law is simply the displacement corresponding to each mode. In Equation 2.16, damage can be calculated separately for each mode according to separate decohesion initiation values, and then is assigned according to the mode with the highest.

However, many mixed loading conditions, damage may form before any one component of traction reaches the damage initiation for pure single mode loading [137, 142]. For mixed mode failure, a more sophisticated damage law must be used. One typical mixed model effective displacement is based on the quadratic failure criterion [137, 142] where

$$\left(\frac{\langle\tau_n\rangle}{t_n^0}\right)^2 + \left(\frac{\tau_s}{t_s^0}\right)^2 + \left(\frac{\tau_t}{t_t^0}\right)^2 = 1 \tag{2.17}$$

This criterion has been used successfully to predict the onset of mixed mode delamination [142–144]. The initiation of damage for each mode can be defined as before, but the effective initiation displacement must be defined according to the mixed modes. First a mode mixity ratio is defined as

$$\beta = \frac{\delta_s}{\delta_n} \tag{2.18}$$

where δ_n is positive and non-zero. The mixed mode effective initiation displacement can then be defined as

$$\delta_m^0 = \begin{cases} \delta_n\delta_s\sqrt{\dfrac{1+\beta^2}{(\delta_s^0)^2 + (\beta\delta_n^0)^2}}; & \delta_n > 0 \\ \delta_s^0; & \delta_n \leq 0 \end{cases} \tag{2.19}$$

where δ_m^0 is the mixed mode initiation damage displacement and assuming that δ_s and δ_t are equal for three dimensional loading.

Accounting for mixed mode damage improves the ability of cohesive zone models to match experimentally observed cracking behavior, but problems related to mesh refinement sensitivity, reduced stiffness, and crack path propagation remain [117,134, 145–148]. When cohesive zone elements are inserted everywhere into the original mesh of a FE simulation, the cohesive surfaces become an intrinsic part of the material [117]. This allows the simulation to be carried out without an extrinsic check for crack formation at each increment of the simulation. However, the cohesive surface area can affect the simulated material behavior such as stress concentration and strain energy release, and the models require mesh sensitivity studies to determine if the simulated behavior converges [120].

An upper bound on mesh size can be defined according to the ability of the model to resolve the stress distributions at crack tips. [117]. As the mesh is refined, the computational cost rises dramatically when cohesive elements are inserted everywhere in the model. Computational cost is not the only determination of a lower bound on element size; however. Cohesive elements with finite initial stiffness reduces the observed elastic stiffness of the material, so care must be taken to minimize the influence of the cohesive element law on material behavior [117].

Finally, the shape of the mesh influences the crack path. Unordered meshes are incapable of straight crack growth as seen with macroscopic cracks and in LEFM, and highly ordered meshes may not allow crack branching or crack deflection at realistic angles with respect to loading [120,149,150]. Each of these concerns can be addressed with dynamic re-meshing or cohesive element insertion; however, dyanmic re-meshing requires an extrinsic fracture initiation criteria separate from the constitutive model [117,149,150]. While solving many common problems of fixed mesh simulations, this approach can be computationally expensive with adaptive re-meshing at crack tips and external checks at each increment of the simulation [117].

2.5.3 Peridynamics

An alternative approach to the continuum based CZM model for fracture mechanics is the relatively new theory of peridynamics developed at Sandia National Laboratory [151,152]. LEFM and CZMs are an attempt to address the difficulties introduced to continuum mechanics by cracks and discontinuities which cannot be solved with the partial differential equations forming the foundation of continuum mechanics [152]. Peridynamic theory sets out to address these issues directly by starting with an integral form for the equations of motion, which can handle the discontinuities introduced at cracks without special consideration. The original peridynamic equation of motion was proposed by Silling [151] and is given as

$$\rho(\mathbf{x})\ddot{\mathbf{u}}(\mathbf{x},t) = \int_{\mathscr{H}} \mathbf{f}(\mathbf{u}(\mathbf{x}',t) - \mathbf{u}(\mathbf{x},t), \mathbf{x}' - \mathbf{x}) dV_{\mathbf{x}'} + \mathbf{b}(\mathbf{x},t) \tag{2.20}$$

where $\mathbf{x}$ is the position vector in the reference configuration of the body, ρ is density, $\mathbf{u}$ is displacement, t is time, $\mathbf{x}'$ is a dummy of integration, $\mathbf{b}$ is a prescribed body force, and $\mathscr{H}$ is the neighborhood of influence of $\mathbf{x}$ known as the horizon and is considered a material property. The function $\mathbf{f}$ is the constitutive model describing material behavior and describes the pairwise forces between $\mathbf{x}$ and $\mathbf{x}'$ for all $\mathbf{x}'$ in $\mathscr{H}$ [152].

In the original peridynamic theory, the pairwise forces between particles are assumed to be unaffected by the surrounding particles. In an extension of the original peridynamic model, the material response is allowed to depend on all of the bonds connected to one particle. This also introduces the ability to include rate of deformation and history effects. This extension is called peridynamic states and allows peridynamic theory to be applied to a wider range of materials with more realistic material behavior than the original theory [152, 153]. Peridynamics has also been extended to include thermal cycles and material anisotropy [154, 155].

Since its proposal in 2000, a lot of work has gone into understanding the behavior and uses for peridynamic theory and peridynamic states. Early investigations

looked into aspects of linear peridynamic theory, numerical solutions, and energy balance for crack growth [151, 156, 157]. Comparison between established theories and peridynamics have also been studied, including the existence and uniqueness for the linear peridynamic balance of momentum and comparisons with Gauss's theorem and Green's functions [158–165]. The development of peridynamic states to extend the original theory included a demonstration that any elastic constitutive model can be adapted to peridynamic theory with a nonlocal approximation of the deformation gradient tensor [152, 153]. Applications of this technique have been used for strain-hardening plasticity models [166, 167]. Relating peridynamics to the continuum concept of a deformation gradient requires a corresponding nonlocal peridynamic stress tensor consistent with the nonlocal approximation of the deformation gradient [152, 157, 168]. In the limit as the horizon, $\mathscr{H}$, becomes small, classically smooth deformation approaches the constitutive model for Piola stress, demonstrating that peridynamic theory converges to classical continuum theory [152, 168].

Damage is incorporated into peridynamics as the irreversible breaking of the pairwise forces or bonds between particles [152]. Figure 2.40 shows a representation of the bond force-elongation plot including bond breakage [156]. The bond force-elongation plot can look identical to the traction-separation equations of CZM. Crack formation and propagation is the result of individual bonds breaking in organized two-dimensional surfaces. The nonlocal nature of peridynamics means that the displacement fields near cracks is bounded, even in numerical solutions [152].

While the theory of peridynamics provides a rigorous framework for dealing with discontinuities that must be treated as special cases in continuum mechanics, most peridynamic models require numerical solutions. In this regard, peridynamics suffers from some of the same numerical solution problems as CZM. Work to discretize the peridynamics equations for use with FEA was started in 2005 [157, 159]. A working demonstration of the use of peridynamics in a commercial FEA code was completed

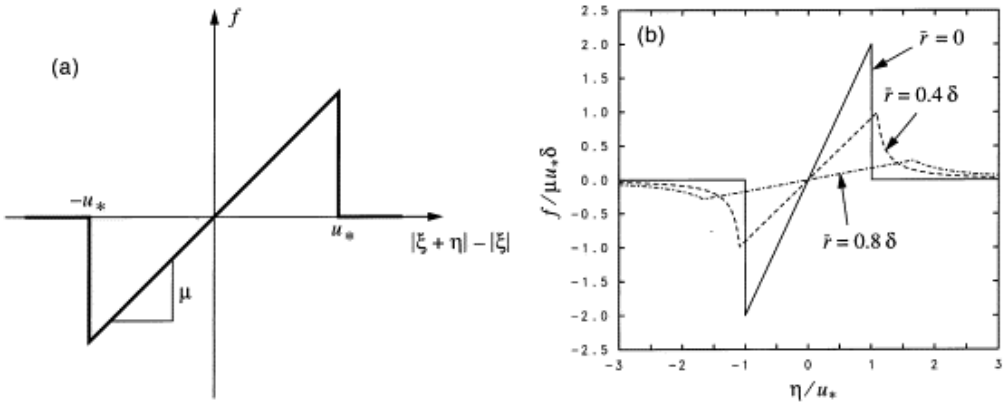

Figure 2.40: Example peridynamics material behavior including bond breakage [156]

in 2007, and also demonstrated the ability to use a mix of standard elements with peridynamic elements [169]. A one dimensional FEA example has also been completed [170]. Meshless numerical methods have also been explored at both the nano scale and macroscopic scale [171–173]. To date, peridynamics has been used to successfully model the behavior of nanofibers and nanotubes, brittle elastic membranes, electronic integrated circuit packaging, concrete, composite laminates, steel, and fiber-reinforced composites [154, 155, 160, 171–181].

While peridynamics can handle discontinuities within the foundational equations, any discretized numerical solution suffers from the same problems as numerical cohesive zone elements. Simulations depend on the refinement of the discretization, and more highly refined models require more computation time. Crack paths are limited to orientations determined by the mesh unless adaptive re-meshing is introduced. One benefit to peridynamics is the ability to include the fracture behavior as an intrinsic part of the material constitutive model without a separate constitutive behavior to describe the discontinuities.

2.5.4 Multi-scale Modeling

Both CZM and peridynamics suffer from scalability issues. High fidelity modeling at the mesoscale precludes simulations of volumes on engineering component scales. Modeling at the mesoscale becomes too computationally expensive when attempting to explicitly account for interactions at the sub-structure scale or below, such as lamellar regions, dislocation motion, and atomic interactions [182]. There are three general approaches to multi-scale modeling: concurrent modeling, hierarchical homogenization, and coupled hierarchical modeling [182–185].

Concurrent modeling is the coupled use of models at two length scales in the same domain of a model. This approach has been used to bridge length scales in dynamic fracture where Molecular Dynamics (MD) is required to analyze the physical mechanisms involved in fracture, but the boundary conditions can be better addressed with FEA at the continuum level [186]. Figure 2.41 shows an example of the coupled spatial domain between MD and continuum FEA to simulate dynamic fracture at an initial pre-crack [186]. A full MD simulation containing more than 225,000 atoms was run for verification of the concurrent method. Using the concurrent method, the MD simulation was reduced to 117,121 atoms coupled to 1024 finite elements [186]

Hierarchical homogenization involves modeling at each length scale of interest and passing information between models. This is often done sequentially, but can also be performed concurrently [184, 185]. An example where sequential multiscale modeling was used to simulate microstructure sensitive fracture of quasi-brittle materials can be found in the work of Saucedo-Mora and Marrow [120]. In that work, finite elements are use to predict the macroscale stress and strain distributions of a three point bend test specimen with a notch. The nodal solution is passed to a mesh free model of the material microstructure to predict heterogeneous stress-strain fields caused by the microstructure. The final model uses Cellular Automata (CA) to solve for the damage and fracture energy released from damaged cells. In turn, this information

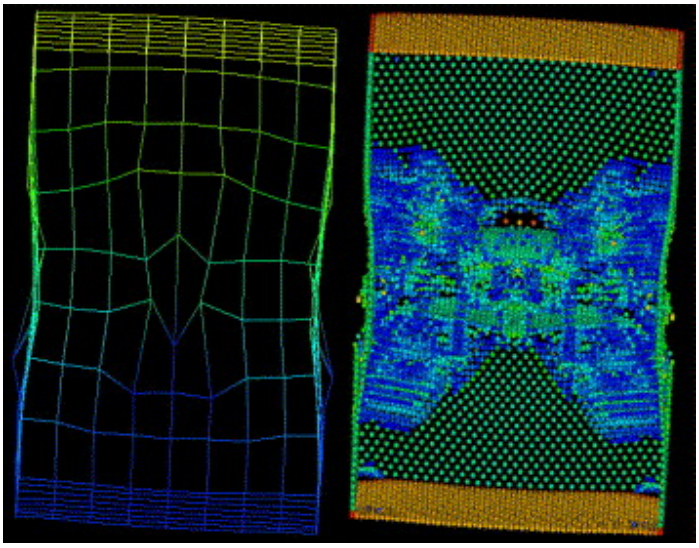

Figure 2.41: The deformed FE mesh on the left is coupled to the MD simulation on the right in the same spatial domain of the simulation [186]

is passed back up through the models to the finite element model to inform changing mechanical properties of the elements to reflect damage and microstructure evolution. Figure 2.42 shows the full specimen FE model with the local notch damage predicted from a sequential hierarchical model [120].

Coupled hierarchical modeling uses multiple length scale models concurrently in the same simulation by transitioning between length scales far from the immediate areas of interest. An example of coupled hierarchical modeling is the Finite Element-Atomistic (FEAt) method used by Gumbsch to study fracture in FCC metals [187]. In that work, the material near the crack tip is modeled with the Embedded Atom Method (EAM) and the material far from the crack tip is modeled with traditional continuum finite elements. At the transition zone from EAM to FE, atoms are coupled to FE nodes through several layers of atoms and nodes to reduce the effect of the transition zone behaving like a physical boundary [184, 187]. Figure 2.43 shows an example of the FEAt model including the transition zone between atomistic and continuum finite elements for Mode I loading of a macroscopic crack [187].

Each of these three multiscale modeling approaches can be used for bridging the

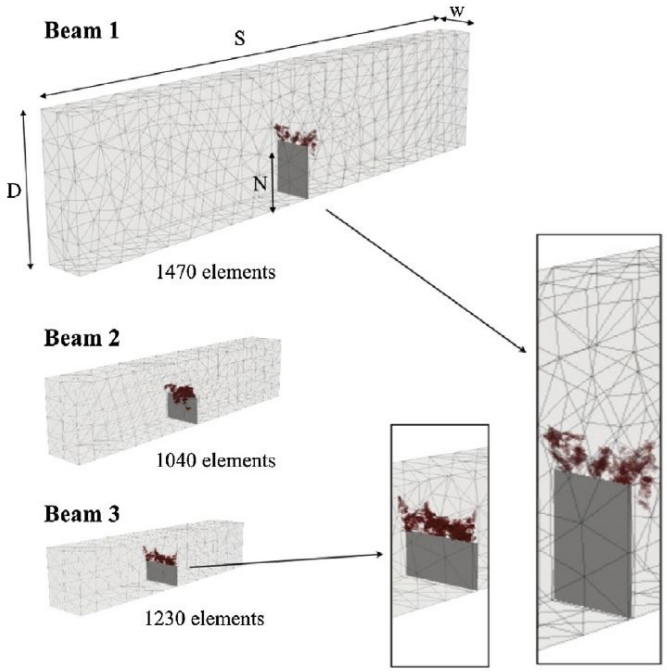

Figure 2.42: Microstructure sensitive hierarchical multiscale modeling example showing a coarse mesh FE model with damage at scales significantly smaller than the FE mesh size [120]

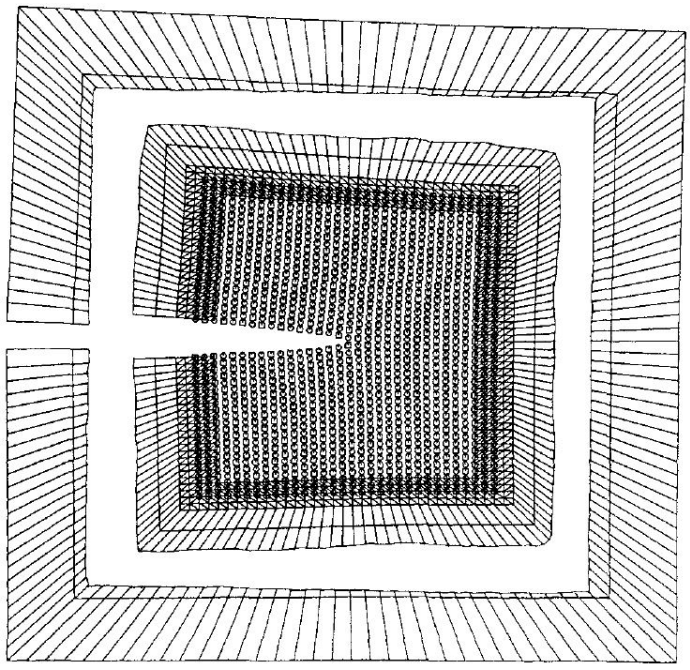

Figure 2.43: An example of the FEAt coupled hierarchical model for Mode I loading of a macroscopic crack [187]

gap between other length scales beyond those in the examples shown. All three approaches provide significant computational cost savings in comparison to fully refined, small length scale models with the same larger length scale geometry or model size. In some extreme cases, a lower length scale model of the same dimensions would require enough computation time to be essentially impossible to complete. These approaches are not without limitations, however. Concurrent modeling and coupled hierarchical modeling require a priori knowledge of the area of interest requiring the lower length scale models or highly refined meshes. For the case of brittle fracture mechanics, it is desirable to allow crack formation at multiple scales and in arbitrary locations as a function of the microstructure or sub-structure of a material. This can be addressed with hierarchical homogenization; however, to realize any significant computational time savings, some restrictions on the locations to apply lower length scale models may still be required.

No matter which approach is chosen, the bridges between models always involve some assumptions and simplifications in order to reduce the detailed information contained in the lower length scale models to fit the form of the larger length scale models. Introducing the bridges between models can add unintended and unrealistic behavior, so the choice of bridge must be made carefully. Understanding the uncertainty in model form and calibration and how this uncertainty is passed between multiscale models is a field of study of its own. adding one more area of expertise required to properly use and understand multiscale modeling beyond the separate fields of modeling involved in the multiscale model itself.

CHAPTER III

MATERIAL

3.1 Triplex Mo-Si-B

The material chosen for the focus of this research is a triplex Mo-Si-B alloy with a continuous α-Mo matrix containing the intermetallic Mo_3Si and T2 phases. A promising example of a triplex Mo-Si-B microstructure created with powder metallurgy and containing an α-Mo matrix can be found from the work of Middlemas [36], and is reproduced in Figure 3.1.

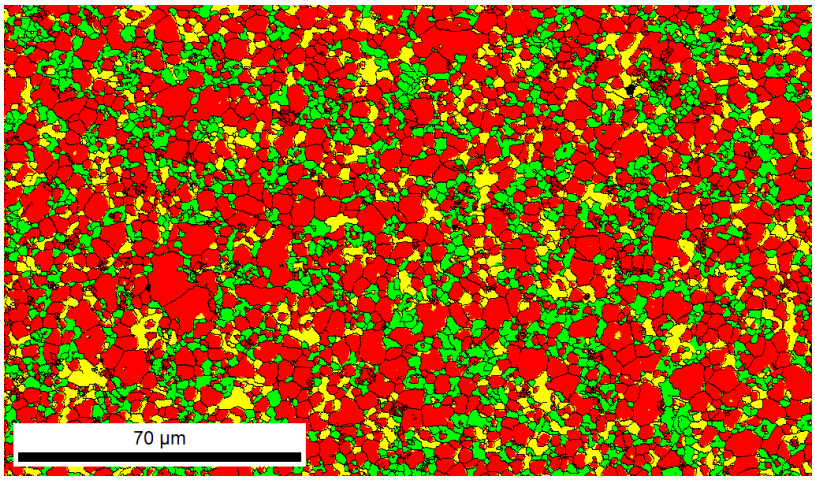

Figure 3.1: EBSD map of a triplex Mo-Si-B alloy prepared with powder metallurgy. Red - α-Mo. Yellow - Mo_3Si. Green - Mo_5SiB_2 (T2) [36]

The representative triplex Mo-Si-B material is the subject of a parametric study designed to help optimize the microstructure's mechanical properties. The baseline microstructure for the representative material comes from two sources: microstructures characterized in literature and a promising microstructure provided by the sponsor of this work. Generically, the microstructures contain fine, equiaxed grains with

the intermetallic phases dispersed in a continuous α-Mo matrix. Following the modeling work of Patra *et al.*, the literature characterization is based on the material of Jain and Kumar and contains grains with diameters near 20 μm and a α-Mo volume fraction of approximately 0.51. [29, 118]. The details of the full range of microstructures simulated in the parametric study is presented in Chapter 7.

Since the intermetallic phases demonstrate very little plasticity, even at temperatures of up to 1500°C [22, 23, 51], the intermetallic phases are treated as purely elastic and only the α-Mo phase is treated with the full CVP constitutive model. The intermetallic phases are treated with a temperature dependent, anisotropic elasticity tensor. This approach limits the amount of experimentation required to calibrate the constitutive model so that only single phase compression specimens of α-Mo are required.

3.2 α-Mo

In order to calibrate the constitutive law for the α-Mo phase as a function of temperature and Si content, as-cast arc melted buttons with varying Si content are prepared from high purity elemental powders by Pratt & Whitney. No additional heat treatment is performed on this material, so the microstructure is unrefined and contains regions of textured, elongated grains. These buttons are then machined into rectangular prisms and loaded in compression. Further details on the compression experiments are provided in Chapter 5. An example button is shown in Figure 3.2.

OIM was performed at Pratt & Whitney to characterize the arc melted α-Mo material. Figure 3.3 shows an EBSD map of a sample of α-Mo with 0.40 wt.% Si (Mo-0.40Si), including an overlay of the approximate specimen size. The arc melted α-Mo specimen microstructures vary with Si content. Figure 3.4 shows the EBSD map of the α-Mo with no Si (Mo-0.00Si). Due to the heterogeneous, anisotropic microstructure and the variety of microstructures in material with differing Si content, extra care

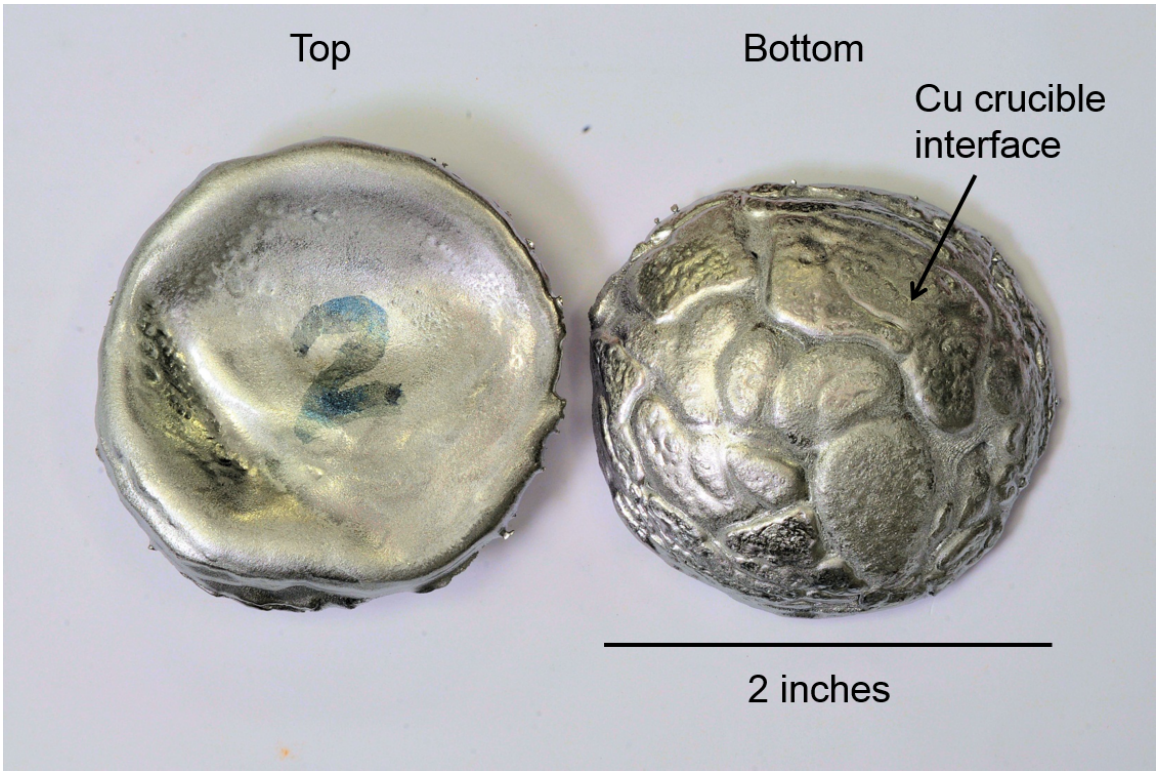

Figure 3.2: Arc melted Mo-1.16Si (wt%) hemispherical button

must be taken to properly characterize and model the arc melted α-Mo material in order to obtain a suitable calibration of the constitutive model from the measured macroscopic compression deformation. Note that the grain sizes are much larger than the grain sizes of the representative baseline triplex microstructure shown in Figure 3.1. A more complete description of the arc melted α-Mo material is discussed in the material characterization portion of this chapter.

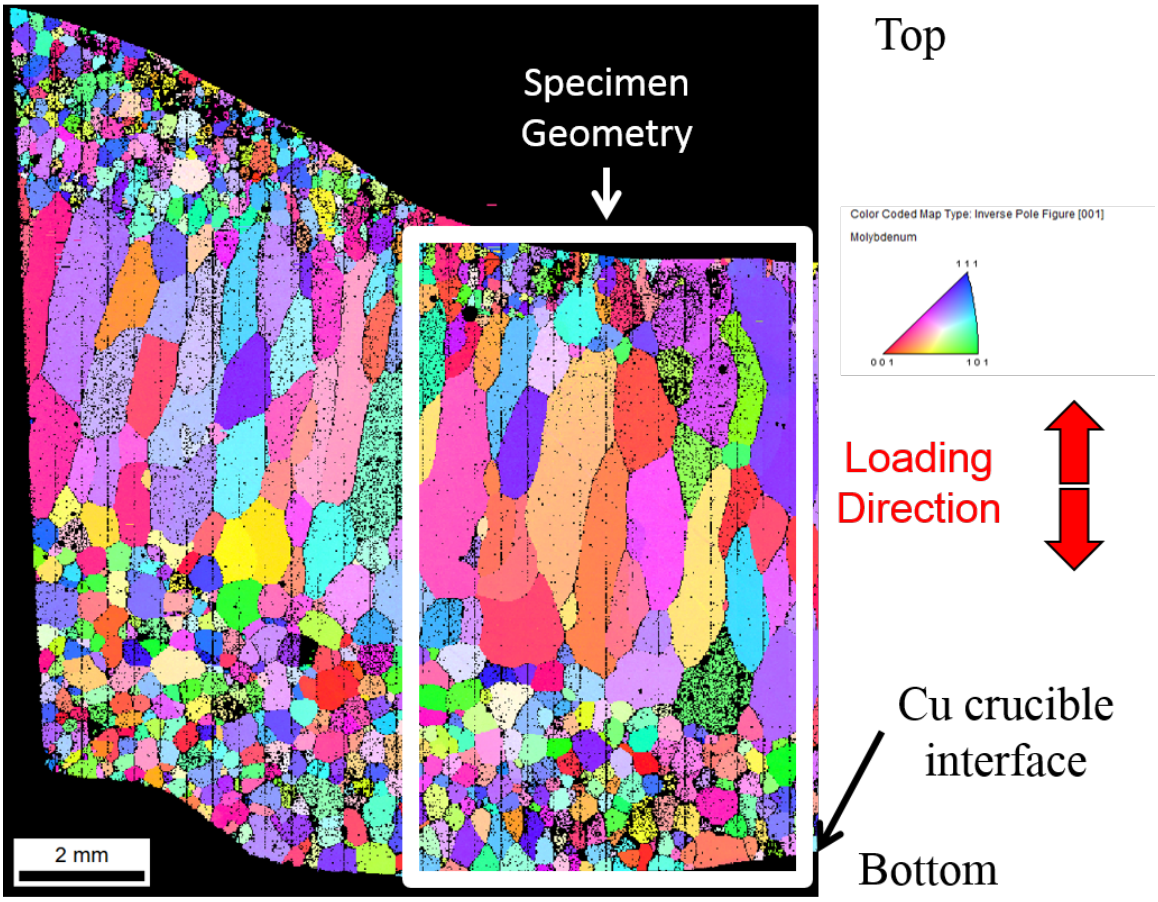

Figure 3.3: EBSD map of arc melted α-Mo material: Mo-0.40Si (wt%)

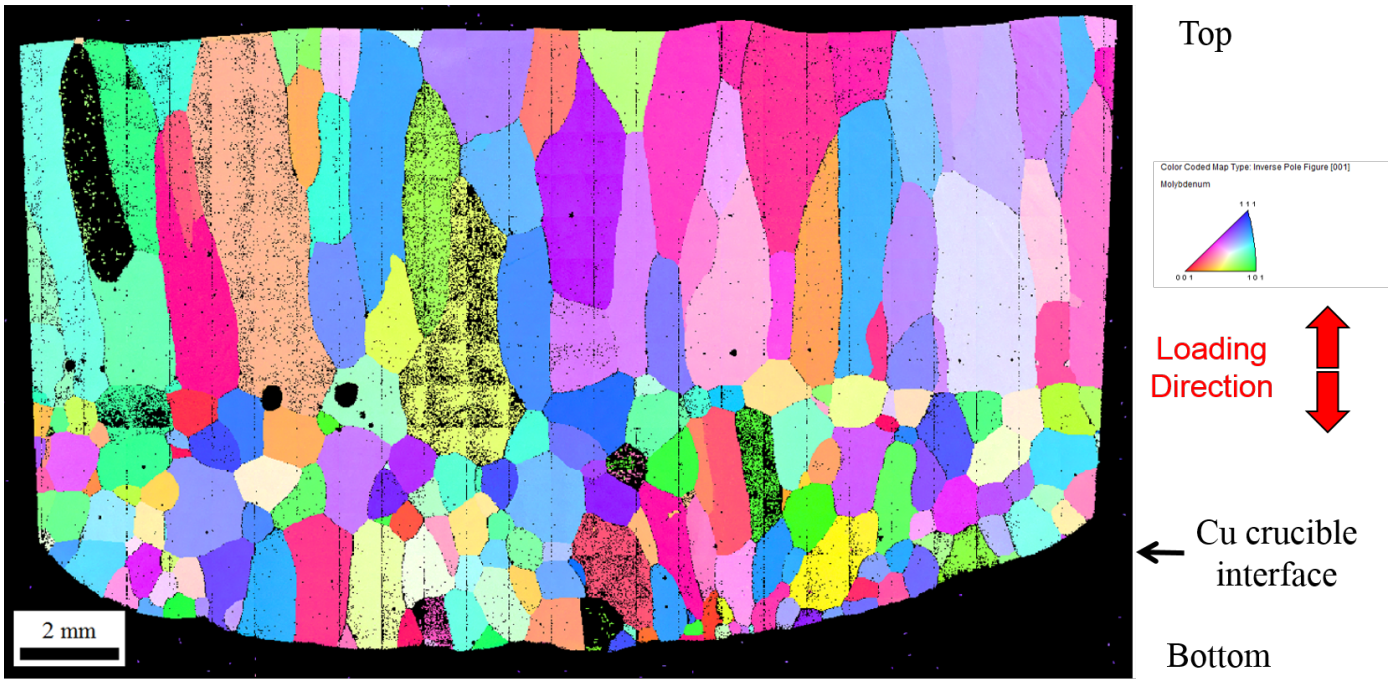

Figure 3.4: EBSD map of arc melted α-Mo material: Mo-0.00Si (wt%)

3.3 Material Characterization

The material must be characterized before the microstructure generator can be used to create synthetic microstructures. The triplex Mo-Si-B alloys that are modeled in this work come from literature where they have been partially or completely characterized. The compression specimens are characterized through Orientation Image Microscopy (OIM) because OIM is capable of capturing all of the microstructural features that the chosen microstructure generator is capable of reproducing.

While OIM provides good detail in orientation maps that also show grain shape and distributions, the data is only two dimensional. Since it is time consuming and expensive to capture three dimensional data [54], some assumptions must be made in order to convert this two dimensional data into three dimensional synthetic microstructures. Namely, it is assumed that the material is symmetric about any chosen plane perpendicular to the loading direction and can be represented as prolate ellipsoids. The relationship between two dimensional ellipses and three dimensional ellipsoids size and shape distributions has been solved for prolate ellipsoids [188]. However, due to the large grain sizes seen in the arc melted α-Mo material, there are an insufficient number of grains in each specimen to provide meaningful results from such a calculation. Instead the two dimensional results are taken as a reasonable estimate for the three dimensional microstructure.

3.3.1 Mo-0.40Si (wt.%)

Figure 3.3 shows three distinct regions of microstructure in the Mo-0.40Si material. The lower region near the water-cooled crucible interface, here referred to as the equiaxed region, contains relatively small, relatively equiaxed grains with a random texture. The middle region, referred to as the columnar region, contains large columnar grains with a fiber texture. The uppermost region is characterized as well, however, most of the test specimens are cut from material closer matching the right

hand side of Figure 3.3 where this uppermost region is small or non-existent. Consequently, the upper region is neglected from the synthetic reconstruction of the arc melted α-Mo specimens. The effects of this assumption are discussed in greater details in Chapter 5. These regions are characterized separately for separate input in the two region microstructure generator that is described in Chapter 4. This microstructure generator is created specifically for modeling the distinct microstructure regions of the arc melted α-Mo material.

Figure 3.5 shows the overall texture of the Mo-0.40Si material shown in Figure 3.3, including a weak fiber texture. Figure 3.6 highlights the grains contributing to the fiber texture and shows that almost all of the large columnar grains contribute to the fiber texture. Figure 3.7 shows the random texture obtained from the equiaxed region.

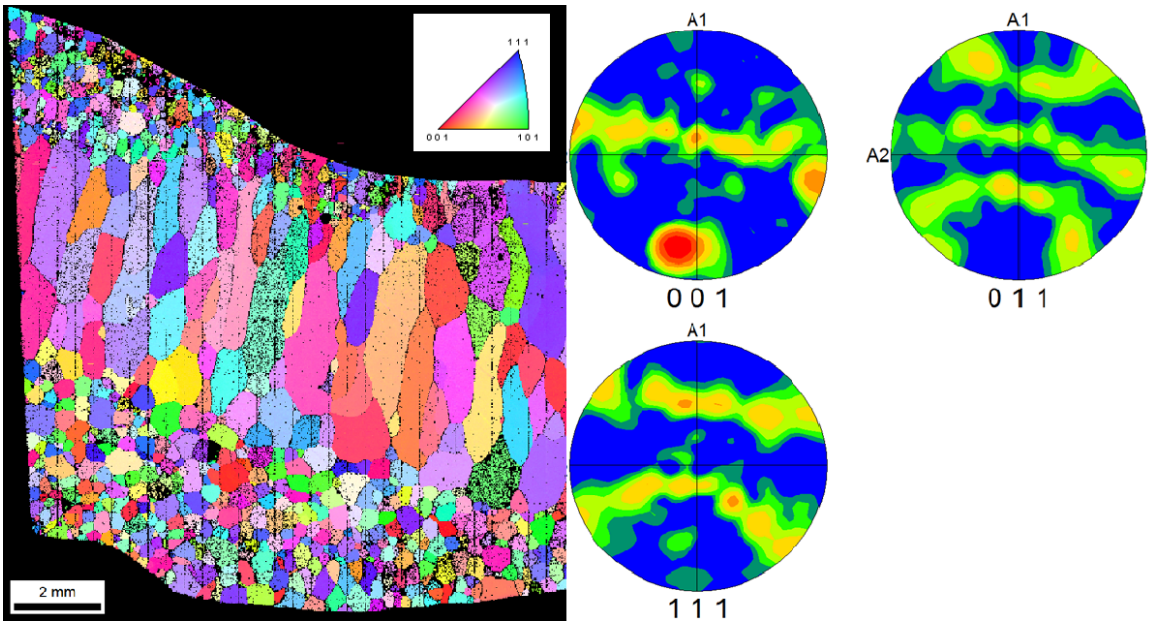

Figure 3.5: Pole figures of arc melted α-Mo material: Mo-0.40Si (wt%)

Once the OIM data is separated into the equiaxed region and the columnar region, each region's grain size and aspect ratio distributions can be characterized separately. Two method of separating the OIM data are possible: hand selecting a polygon shape to crop the data set and partitioning the data set by grain size. Since the boundary

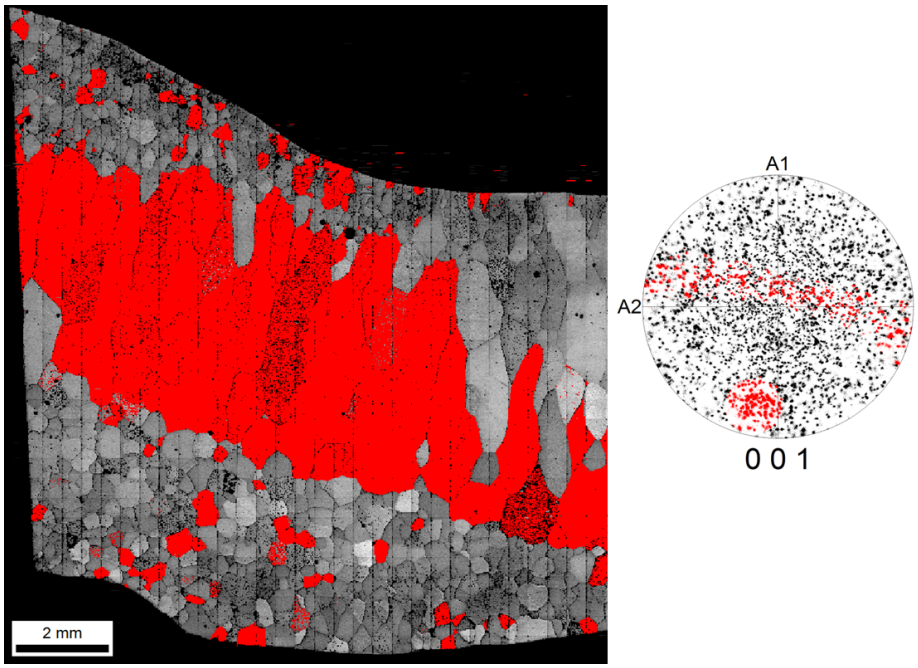

Figure 3.6: Columnar grains contributing to weak fiber texture of the entire sample: Mo-0.40Si (wt%)

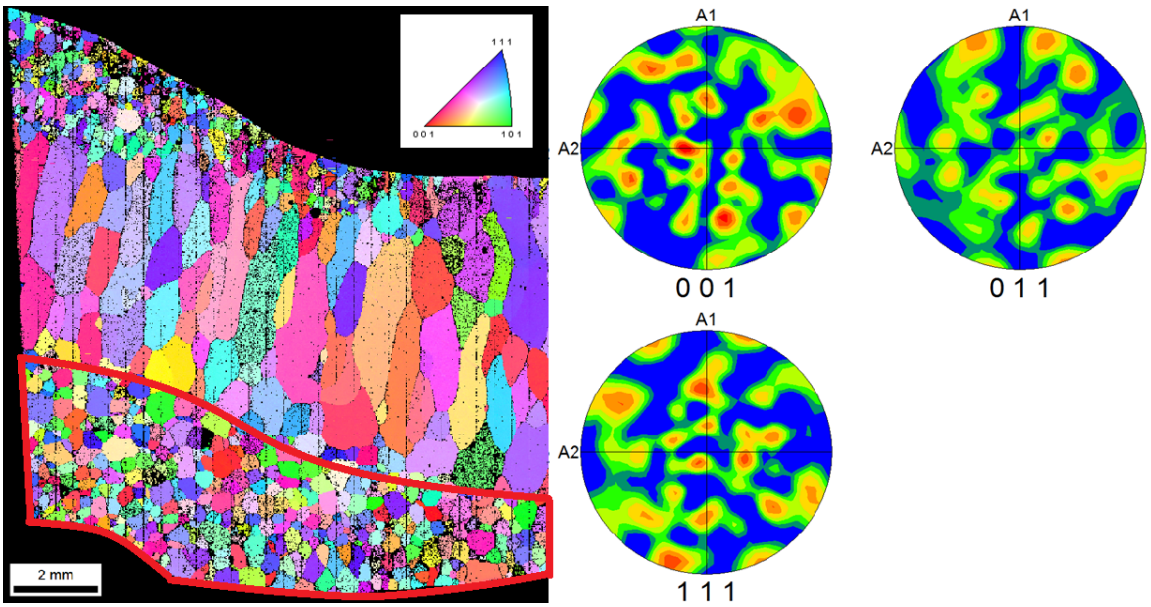

Figure 3.7: Pole figures of relatively small, equiaxed grains outlined in red: Mo-0.40Si (wt%)

of the two regions is not well defined by a straight edge and the grain sizes are very distinct, the second method is preferred. However, for the Mo-0.40Si material, a polygon shape crop of the data is required to separate the smaller columnar shaped

grains that are similarly sized to some of the larger grains in the lower region. After cropping, a partition by grain size is required to remove partially cropped grains from the data set.

The equiaxed region crop is shown separated from overall OIM data in Figures 3.8 and 3.9. Figure 3.8 shows the cropped data after filtering out grains smaller than 25 μm in diameter. In this image, small portions of grains that are cropped at the upper edge of the equiaxed region are still contained in the data set, incorrectly lowering the calculated mean grain diameter and affecting the grain shape orientation distribution. However, this partition also eliminated a number of small grains with complete orientation data located in the middle of the cropped data set.

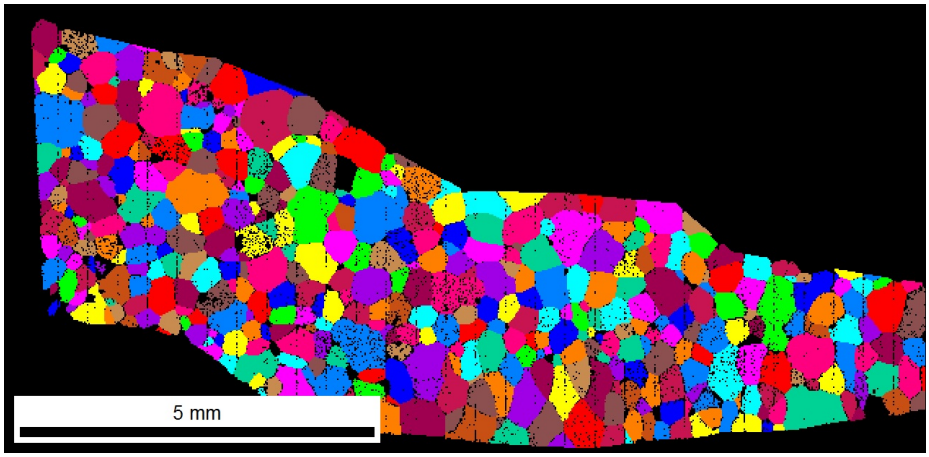

Figure 3.8: Region one crop and 25 μm equivalent grain diameter lower limit partition: Mo-0.40Si (wt%). Colors are assigned to unique grains

Figure 3.9 shows the same cropped data set after filtering out grains smaller than 100 μm in equivalent diameter. Some cropped grains are still contained in the data set, but a larger number of small grains have been partitioned out from the center of the data set.

The grain diameter distributions for both partitions are shown Figure 3.10. Neither partition contains enough grains for a smooth grain diameter distribution. Consequently, the grain diameter mean and standard deviation must be treated as rough approximations. Because the compression specimens themselves have even fewer grains

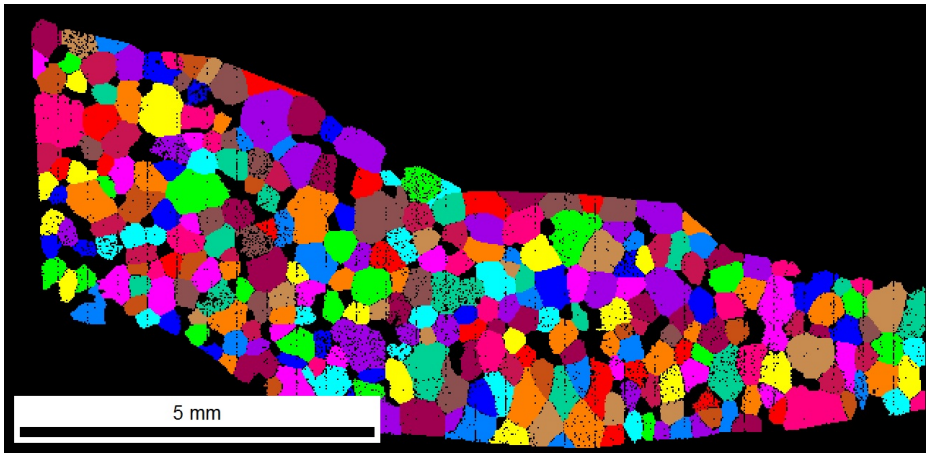

Figure 3.9: Region one crop and 100 μm equivalent grain diameter lower limit partition: Mo-0.40Si (wt%). Colors are assigned to unique grains

in each region, this has a significant effect on the creation of synthetic volume elements and the calibration of the constitutive model. The arc melted α-Mo specimens are not large enough to be treated as representative or even statistical volumes. Instead, an accurate calibration would require characterizing each test specimen in 3D and recreating each test specimen in a unique synthetic volume element. However, such a material characterization study represents a significant time investment and the return on such an investment would be small with respect to the inaccuracies of the arc melted α-Mo test data. The details of the difficulty this presents for synthetic volume generation and constitutive model calibration and the approach taken to make the best use of the limited information available are discussed in Chapters 4 and 5, respectively.

Despite the limited data set and approximations made in partitioning the data, both grain size partitions result in similar grain size and aspect ratio, presented in Table 3.1.

Region two of the Mo-0.40Si material is similarly partitioned and analyzed for grain diameter and aspect ratio. Figures 3.11 and 3.12 show the columnar region crop from the overall OIM data. Figure 3.11 shows the crop after filtering out grains of grain diameter less than 250 μm. As with the equiaxed region crop, some partial

Table 3.1: Mo-0.40Si (wt%) equiaxed region grain diameter and aspect ratio by partition size

Parameter	>25 μm partition	>100 μm partition
Grain Dia. Mean [μm]	321	381
Grain Dia. Std. Dev.	139	115
Aspect Ratio Mean	0.49	0.50
Aspect Ratio Std. Dev.	0.11	0.10

grains from both edges of the crop are contained in this data set and some small grains from the middle of the data set are excluded based on the equivalent grain diameter filter.

Figure 3.11 shows the same cropped data set after filtering out grains smaller than 450 μm in equivalent diameter. Again, some cropped grains are still contained in the data set, however, most of the small grains removed from the center of the data set are already removed by the 250 μm grain diameter filter.

Region two of the Mo-0.40Si material contains even fewer grains than the equiaxed region, and calculated equivalent grain diameter and aspect ratio do not even approximate a distribution. Figure 3.13 presents the measured equivalent grain sizes in the columnar region.

The equivalent grain size and aspect ratios for the columnar region in the Mo-0.40Si material are presented in Table 3.2.

Table 3.2: Mo-0.40Si (wt%) columnar region grain diameter and aspect ratio by partition size

Parameter	>250 [μm] partition	>450 [μm] partition
Grain Dia. Mean [μm]	890	995
Grain Dia. Std. Dev.	454	437
Aspect Ratio Mean	0.37	0.36
Aspect Ratio Std. Dev.	0.14	0.14

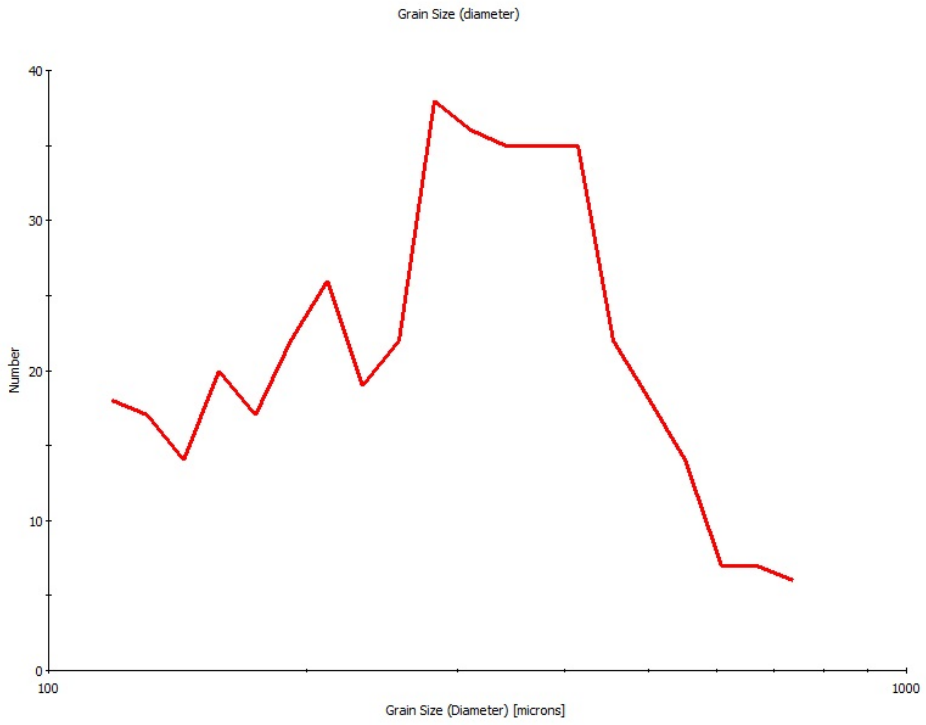

(a) Partition with grains >25 μm

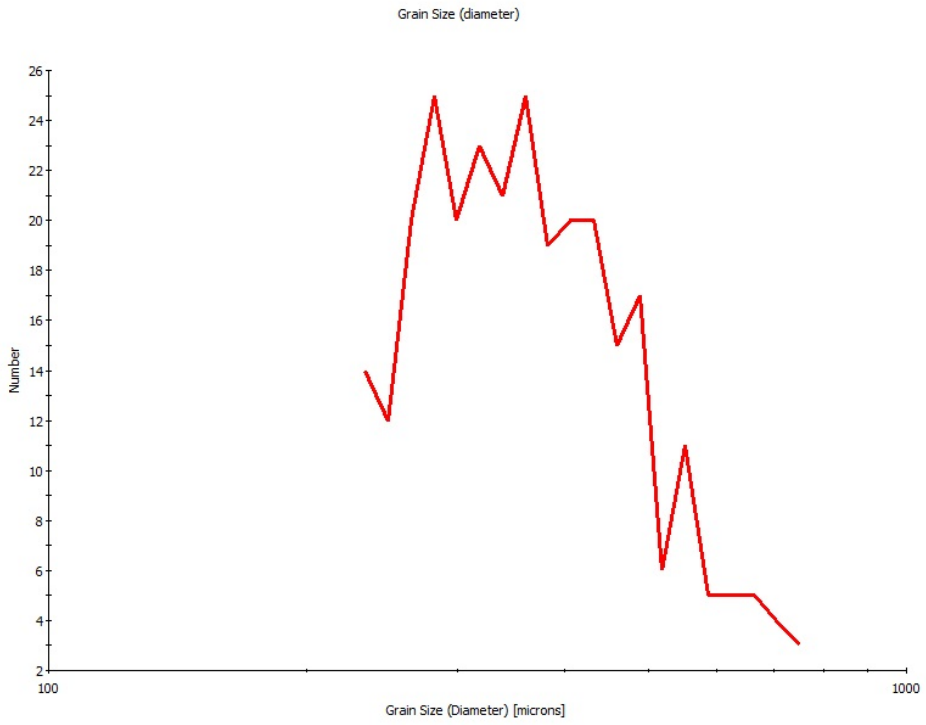

(b) Partition with grains >100 μm

Figure 3.10: Mo-0.40Si equiaxed region equivalent grain size diameter distribution

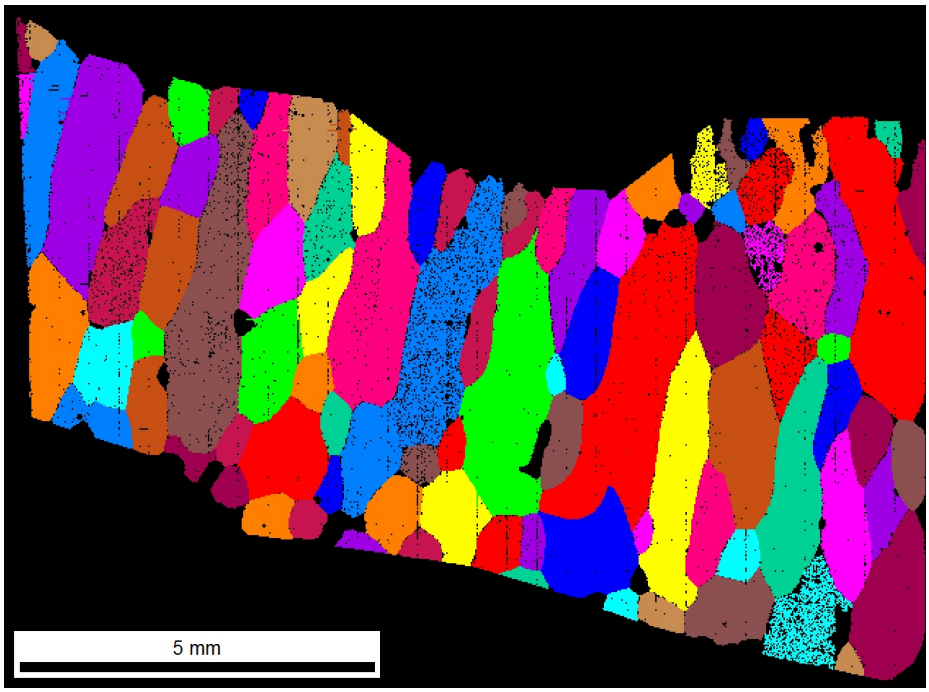

Figure 3.11: Region two crop and 250 μm equivalent grain diameter lower limit partition: Mo-0.40Si (wt%). Colors are assigned to unique grains

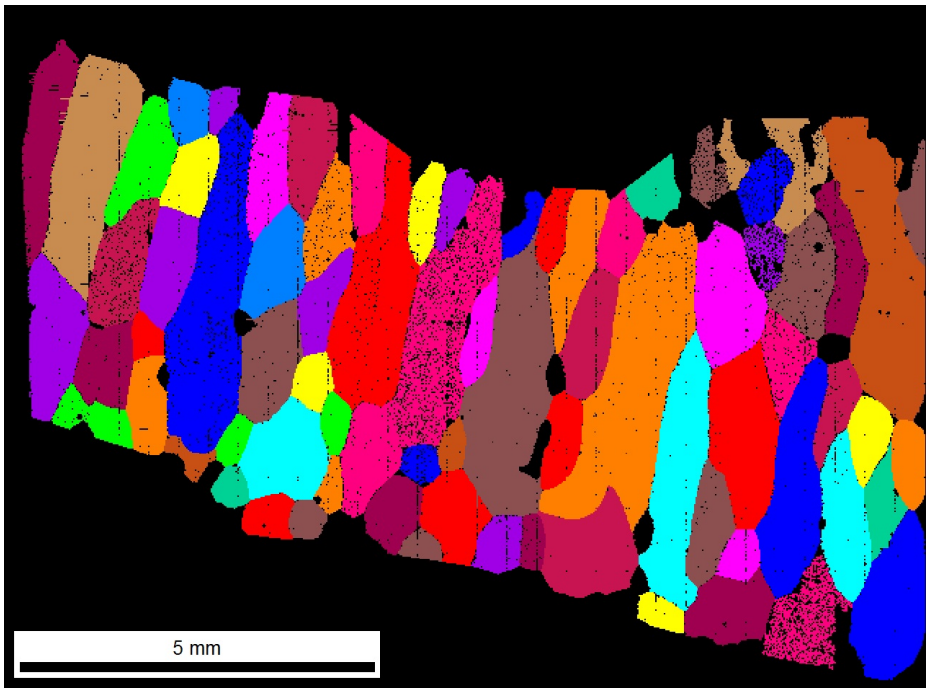

Figure 3.12: Region two crop and 450 μm equivalent grain diameter lower limit partition: Mo-0.40Si (wt%). Colors are assigned to unique grains

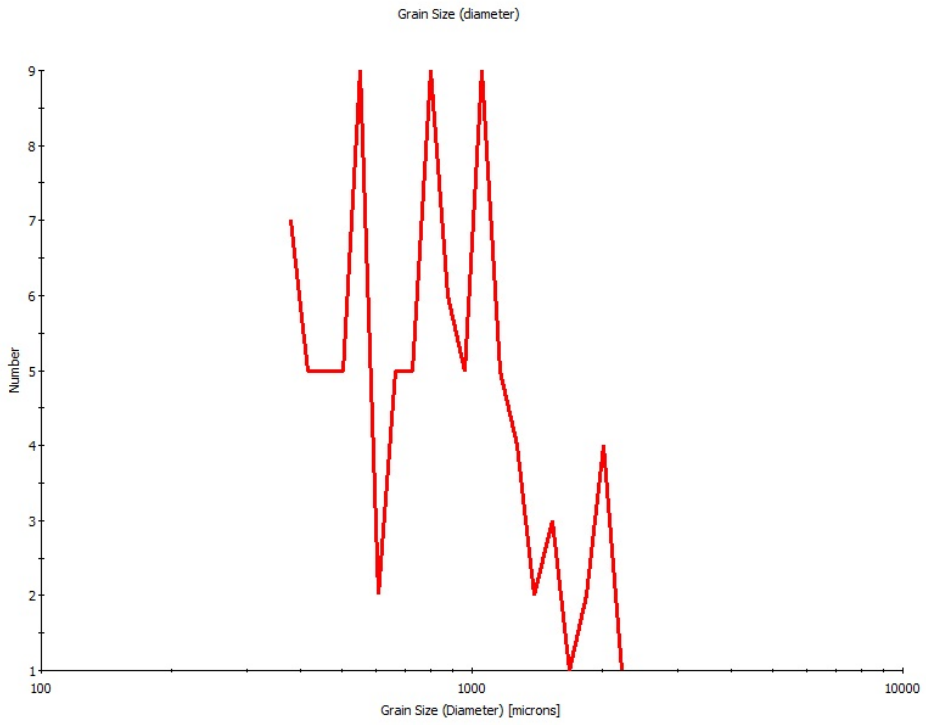

(a) Partition with grains >250 μm

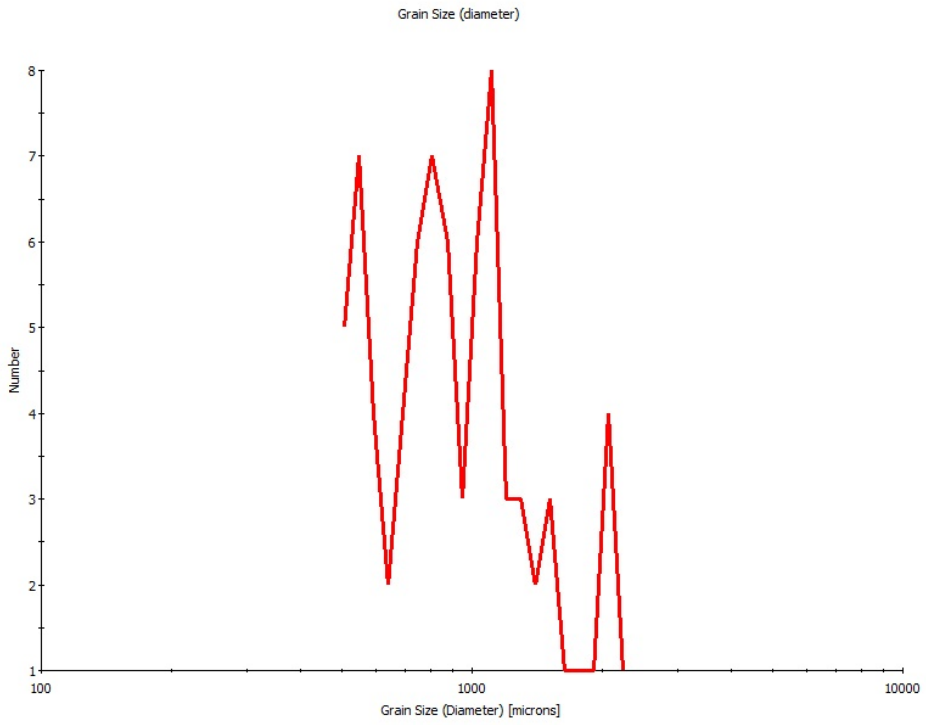

(b) Partition with grains >450 μm

Figure 3.13: Mo-0.40Si columnar region equivalent grain size diameter distribution

3.3.2 Mo-0.00Si (wt.%)

Shown previously in Figure 3.4, the arc melted pure Molybdenum material (Mo-0.00Si), contains a similar two region microstructure as the Mo-0.40Si material. However, the Mo-0.00Si grains are much larger and exhibit slightly different aspect ratios. In this material, the equiaxed region again refers to the lower region with relatively small, randomly textured, equiaxed grains and the columnar region refers to the larger, columnar grains with a fiber texture. There is no upper region with smaller grains in the Mo-0.00Si material, so no assumption is required when creating synthetic volume elements with only two regions; however, the larger grains amplify the problems with volume element size and the variability in mechanical response due to microstructure inhomogeneity.

The equiaxed region crop data and partitions with separate minimum equivalent grain diameters are shown separated from the overall image data in Figures 3.14 and 3.15. Figure 3.14 shows the cropped data after filtering out grains smaller than 25 μm in equivalent diameter. Unlike the Mo-0.40Si data, the Mo-0.00Si data is easier to partition to remove the cropped grains without removing a significant number of grains in the middle of the cropped data set.

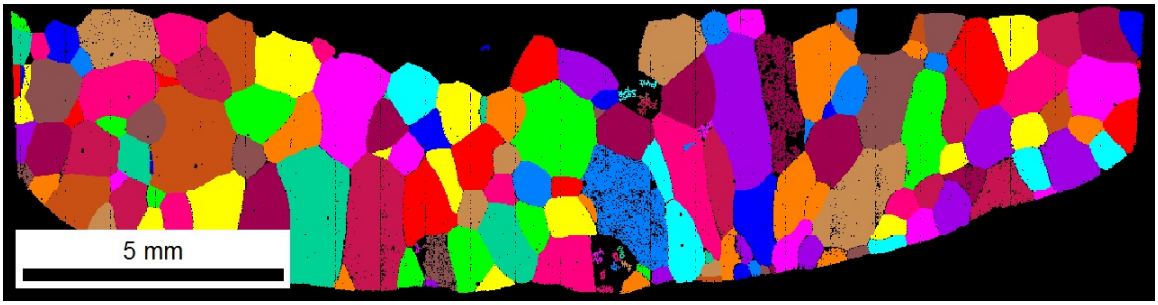

Figure 3.14: Region one crop and 25 μm equivalent grain diameter lower limit partition: Mo-0.00Si (wt%). Colors are assigned to unique grains

Figure 3.15 shows the equiaxed region crop after filtering out grains less than 100 μm in equivalent diameter. Only the smallest of grains which are much smaller than the mean equivalent grain diameter are removed with the large minimum grain size

filter.

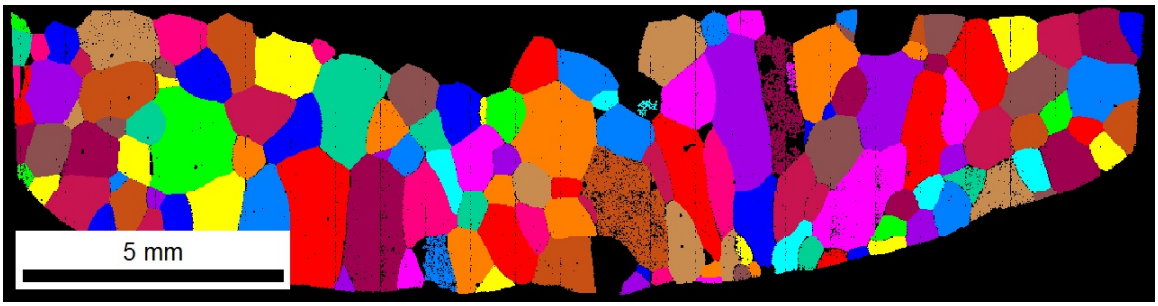

Figure 3.15: Region one crop and 100 μm equivalent grain diameter lower limit partition: Mo-0.00Si (wt%). Colors are assigned to unique grains

The equivalent grain diameter and aspect ratio distributions suffer from the same small dataset as did the Mo-0.40Si material. The equivalent grain diameter and aspect ratios for the Mo-0.00Si equiaxed region data sets are presented in Table 3.3.

Table 3.3: Mo-0.00Si (wt%) equiaxed region grain diameter and aspect ratio by partition size

Parameter	>25 [μm] partition	>100 [μm] partition
Grain Dia. Mean [μm]	682	777
Grain Dia. Std. Dev.	429	397
Aspect Ratio Mean	0.47	0.48
Aspect Ratio Std. Dev.	0.14	0.13

The columnar region crop and data partitions are shown in Figures 3.16 and 3.17. This data set contains a number of grains with poor quality orientation data. In order to include as many grains as possible, the data in the cropped region is run through a cleaning algorithm to fill in missing data or poor quality data, where poor quality data is assigned the orientation of nearby higher quality data. This processing allowed the inclusion of five large columnar grains, and a handful of smaller grains near the cropped edge. Figure 3.16 shows a comparison of the partitioned data before and after the image processing with a minimum equivalent grain diameter filter of 100 μm.

Figure 3.16a shows the crop after processing and partitioning the OIM data by a minimum equivalent grain diameter of 100 μm. The processed data set is used in the equivalent grain diameter and aspect ratio analysis presented in Table 3.4.

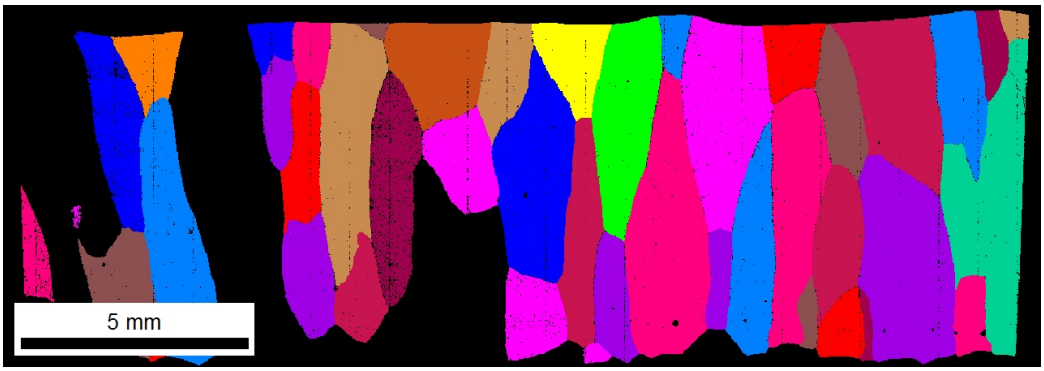

(a) Partition with grains >100 μm

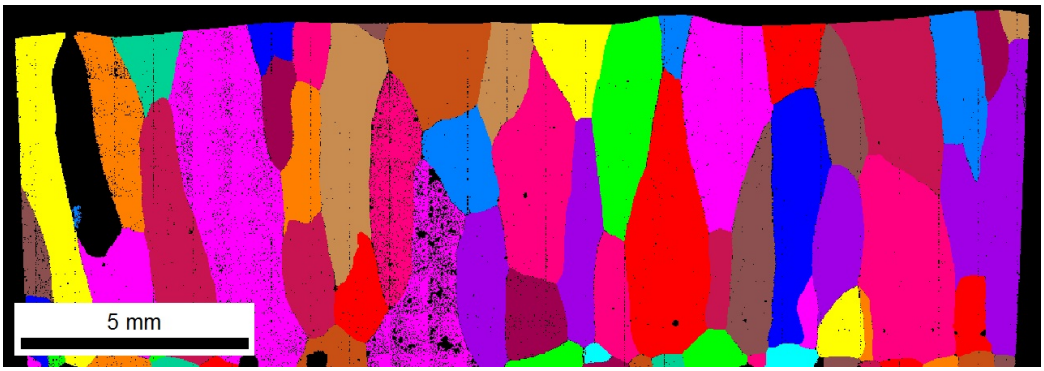

(b) Processed partition with grains >100 μm

Figure 3.16: Mo-0.00Si columnar region cropped and partitioned OIM data

Figure 3.17 shows the processed data set after partitioning with a minimum equivalent grain diameter of 450 μm.

The columnar region data for Mo-0.00Si (wt.%) suffers the most from a lack of grains. The equivalent grain diameter and aspect ratios for the Mo-0.00Si columnar region cropped, processed, and filtered data sets are presented in Table 3.4

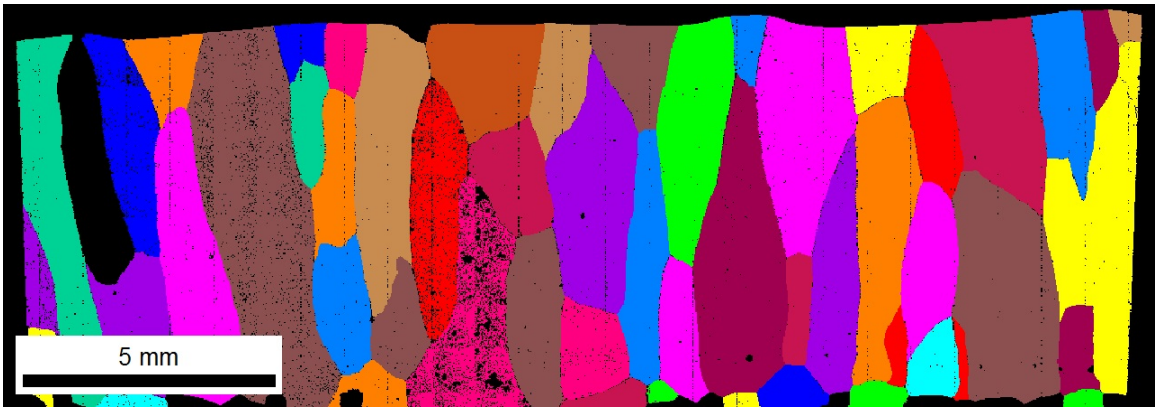

Figure 3.17: Region two cropped and processed OIM data with a 450 μm equivalent grain diameter lower limit partition: Mo-0.00Si (wt%). Colors are assigned to unique grains

Table 3.4: Mo-0.00Si (wt%) columnar region grain diameter and aspect ratio by partition size after processing OIM data

Parameter	>100 [μm] partition	>450 [μm] partition
Grain Dia. Mean [μm]	1433	1724
Grain Dia. Std. Dev.	914	820
Aspect Ratio Mean	0.34	0.33
Aspect Ratio Std. Dev.	0.13	0.13

3.3.3 Mo-0.29Si, Mo-0.58Si, and Mo-1.16Si

The arc melted α-Mo material with 0.29 wt.% Si has a similar microstructure to the Mo-0.40Si material. A large enough EBSD data set was difficult to obtain due to the large grains. Instead, the Mo-0.29Si material is assumed to have the same microstructure as the Mo-0.40Si material.

The arc melted α-Mo material with Si content greater than 0.40 wt.% contains a more homogeneous microstructure where the grains are relatively equiaxed and randomly textured. The entire microstructure resembles the equiaxed region microstructure of the Mo-0.40Si material shown in Figure 3.3. Unfortunately, OIM data on a large enough field of view to provide enough grains for analysis proved difficult

to obtain for the specimens with larger Si contents. Without OIM data to analyze, the Mo-0.58Si and Mo-1.16Si specimens are assumed to have a single region defined by the characteristics of the Mo-0.40Si equiaxed region data. This assumption clearly introduces uncertainty to the calibration of the larger Si content constitutive model; however, the uncertainty shown in the arc melted α-Mo data itself is shown to contain enough uncertainty that this assumption can be considered to be reasonable within the scope of the overall calibration. The steps taken to address these difficulties are discussed in great detail in Chapter 5.

3.3.4 Chemical Characterization

In addition to characterizing the microstructural attributes, it is important to verify the chemical composition of the α-Mo specimens. Although the final composition is controlled by the composition of the elemental materials, local variation in Si content can still occur. A small study of the chemical composition of the Mo-0.29Si, Mo-0.58Si, and Mo-1.16Si was conducted by Energy-dispersive X-ray spectroscopy (EDX) at Pratt & Whitney.

Figure 3.18 shows the EDX analysis of several regions for the Mo-0.29Si material. The equiaxed region shows oxygen impurities in the final material. In addition to local impurities, the columnar region and the uppermost region show the local spatial variation of Si content, varying from 0.42 wt.% to 1.34 wt.% Si. Since this material has an overall composition of Mo-0.29Si, these locally high concentrations of Si must result in local low concentrations in other portions of the material. The scale of this spatial variation of Si content shown in this figure is roughly two orders of magnitude smaller than the specimen dimensions, so it is quite likely that the final compression specimens have an overall composition matching the desired α-Mo Si content. However, a more thorough composition study at longer length scales would be required to confirm.

Figure 3.19 presents the results of the EDX analysis on the Mo-0.58Si material.

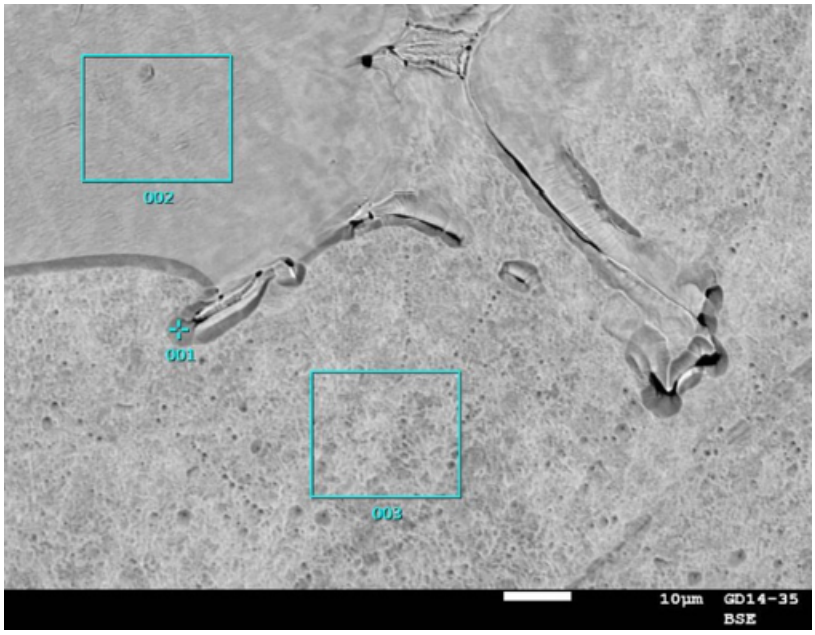

(a) Regions of EDX analysis

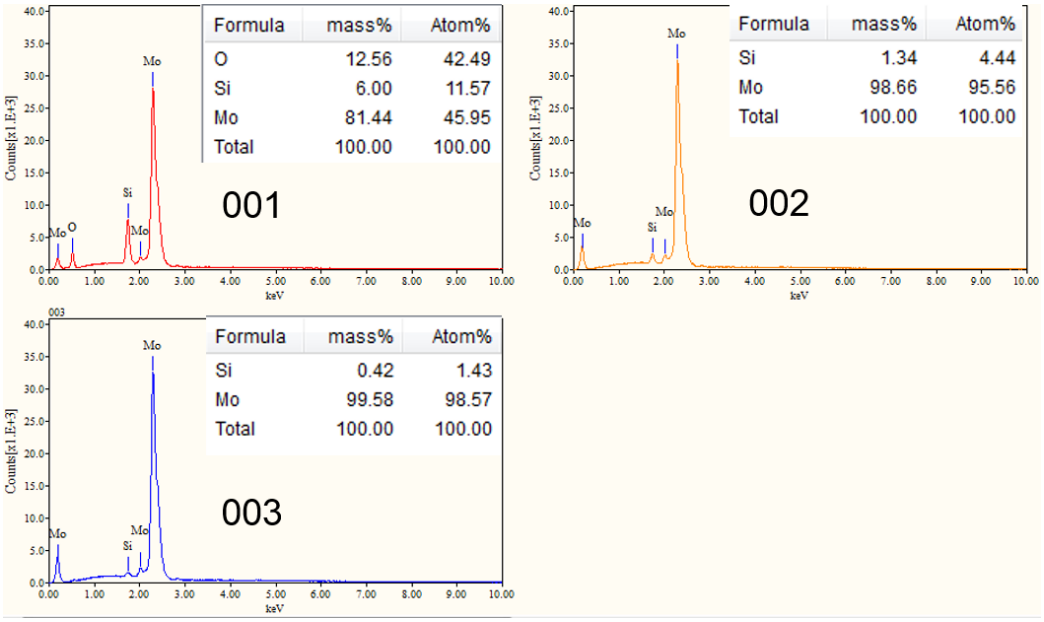

(b) EDX spectra and semiquantitative composisitions of selected areas

Figure 3.18: Mo-0.29Si EDX

This analysis shows another silicate in the equiaxed region. Region 002 shows a Si content of 0.44 wt.% Si, lower than the overall composition of 0.58 wt.% Si for this sample. The region investigated is an order of magnitude smaller than the grain size of this material, and suggests that the Si content may vary grain by grain.

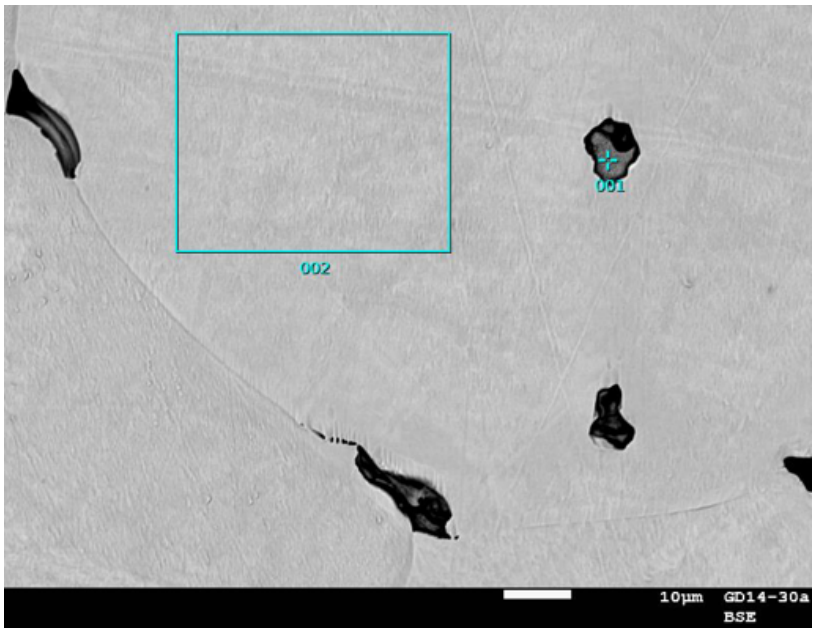

(a) Regions of EDX analysis

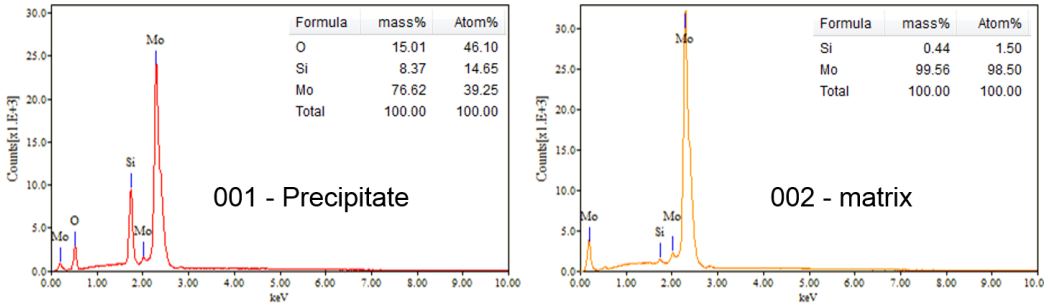

(b) EDX spectra and semiquantitative composisitions of selected areas

Figure 3.19: Mo-0.58Si EDX

Figure 3.20 shows the EDX analysis of the Mo-1.16Si material. Region o001 is a similar silicate resulting from oxygen impurities. Region 002 shows a very similar high content of Si as the overall material, at 1.34 wt.% Si. Region 003 shows a much smaller 0.42 wt.% Si composition only 30 μm away from the high concentration of Si.

Modeling precipitates, impurities, and spatial variation of composition is important to mechanical properties predictions. However, the silicate impurities are on too small a scale to capture explicitly in the calibration of α-Mo or the parametric study of triplex Mo-Si-B alloys of this work. Starting from the tools presented in this work, a more detailed study of a specific sub-set of microstructures could include explicit

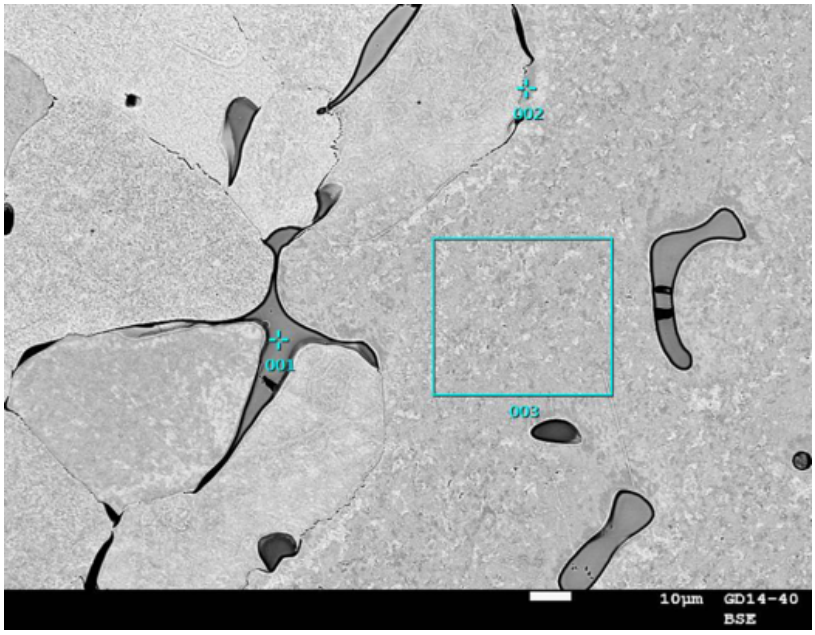

(a) Regions of EDX analysis

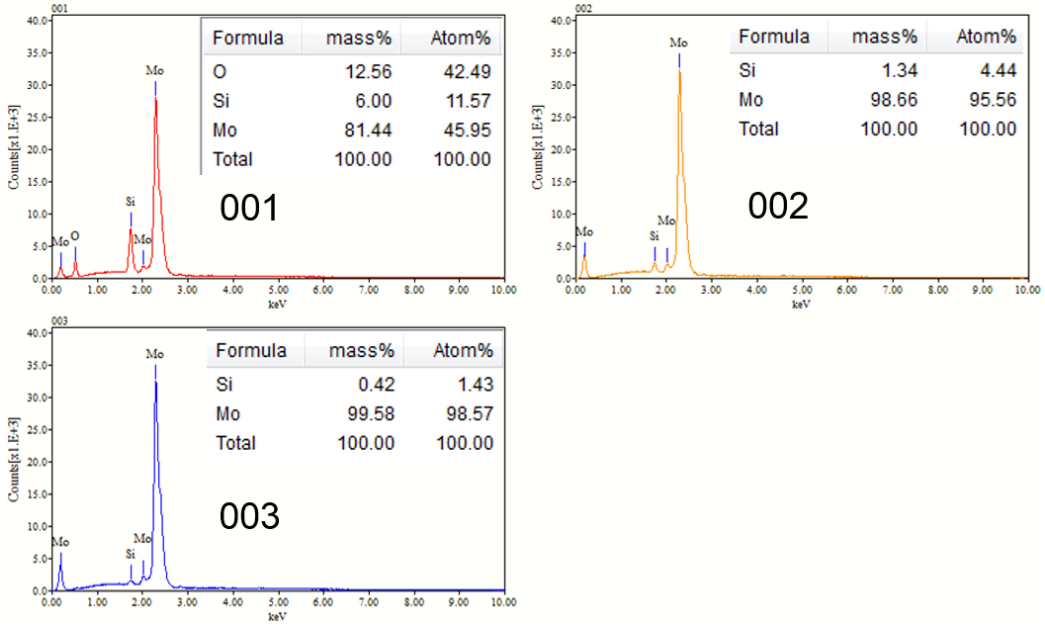

(b) EDX spectra and semiquantitative composisitions of selected areas

Figure 3.20: Mo-1.16Si EDX

models of the impurities provided that a suitable characterization is conducted to guide the computational analysis. Similarly, the tools built in this work are suitable for modeling spatial variation of Si content; however, such a study is left to future work.

3.3.5 Representative Triplex Mo-Si-B

Although a large range of triplex microstructures are simulated in the parametric study, a brief characterization of a promising representative triplex Mo-Si-B material is performed to help guide the ranges of microstructures simulated. The representative material provided by Pratt & Whitney is formed from powder metallurgy, HIPed, and forged. Example material with different processing can be found in literature, but frequently lacks important information such as Si content or grain size distribution. Of particular interest when characterizing the representative example material is the phase volume fraction, grain size distribution, grain aspect ratio, grain shape orientation, and any crystallographic texture that may be present. Additionally, it is important to know the Si content of the α-Mo phase and to understand if there are any precipitates or inclusions that may be important to mechanical properties.

The microstructure generator is capable of re-creating all of these features in synthetic microstructures. While precipitates and inclusions are not modeled explicitly in this early work, once the framework for modeling Mo-Si-B has been established, expanding the microstructure generator and constitutive model to include these features may be accomplished relatively quickly and easily.

Although mean grain size and phase volume fraction can be determined from optical microscopy of etched samples, this approach cannot provide detailed distributions of grain size or distributions of grain shape and orientation. With the exception of precipitates and Si content of the α-Mo phase, all of the features of interest and their distributions can be captured best by electron backscatter diffraction (EBSD). For phase chemistry and precipitates energy dispersive spectroscopy (EDS) is required. Because Si content of the α-Mo phase is varied across the entire possible range in the parametric study, detailed EDS is not pursued.

Both optical microscopy and EBSD are performed on the representative triplex Mo-Si-B microstructure provided by Pratt & Whitney and containing the α-Mo,

A15, and T2 phases. The optical images are performed on sample material etched with Murakami's etchant. Because this etchant does not reveal grain boundaries, the optical images are mostly useful as a visual check that the parametric study parameters cover the representative microstructures of interest, both in literature and for material provided by the sponsor of this work. The phase volume fractions are one of the parameters that is varied across a wide range, so volume fraction estimates are not made from these optical images. The optical images are slightly over etched, preferentially eroding the intermetallic phases.

Figure 3.21 shows a representative optical image taken after etching with Murakami's etchant to reveal the separate phases. This image shows locally varying spatial distributions of the α-Mo phase (white) and different size distributions between phases.

Figures 3.22 and 3.23 show the spatial heterogeneity in greater detail in two different portions of the microstructure.

Figures 3.24 and 3.25 show regions of relatively uniform spatial distribution of the phases.

Figure 3.26 gives a sense of the grain size difference between the smaller intermetallic grains and the larger α-Mo grains; however, Murakami's etchant does not reveal the grain boundaries so mean grain size estimates cannot be taken from these images.

Capturing locally varying spatial heterogeneity in phase volume fraction is an important consideration when modeling this triplex material. Capturing such a spatial variation in phase volume fraction can be accomplished with a relatively small algorithm change in the microstructure generator. However, the purpose of this early work is to help choose an optimized microstructure to study in greater depth from a wide variety of microstructures, so this level of detailed modeling is left to future work. The microstructure simulations in this work do not contain any spatial variation in

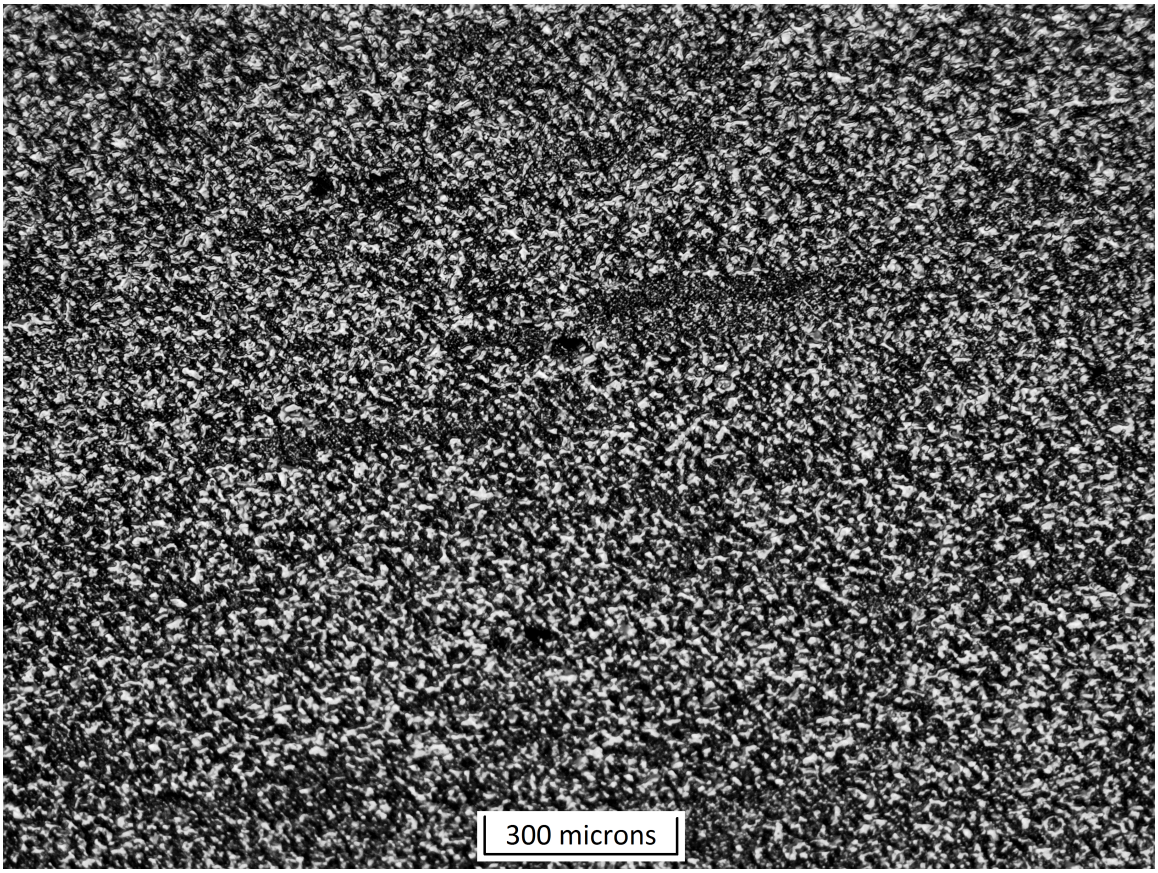

Figure 3.21: Optical microscopy at 50X of a representative triplex Mo-Si-B microstructure etched with Murakami's etchant. White: α-Mo. Gray: A15. Dark Gray: T2.

phase volume fraction or clustering of the intermetallic phases.

Although not characterized as part of this work, it is also possible to find spatial variation in the Si content of the α-Mo phase. Even small changes in Si content can drastically effect the properties of this phase. Therefore, variation in Si content of the α-Mo phase is an important part of the parametric study performed in this work. However, due to the breadth of this study, the α-Mo phase is treated with a uniform Si content throughout the volume elements created and the effects of spatial variation in Si content must be left to a more detailed study of a subset of promising microstructures in future work.

The EBSD imaging of triplex Mo-Si-B proved to be very difficult. A procedure

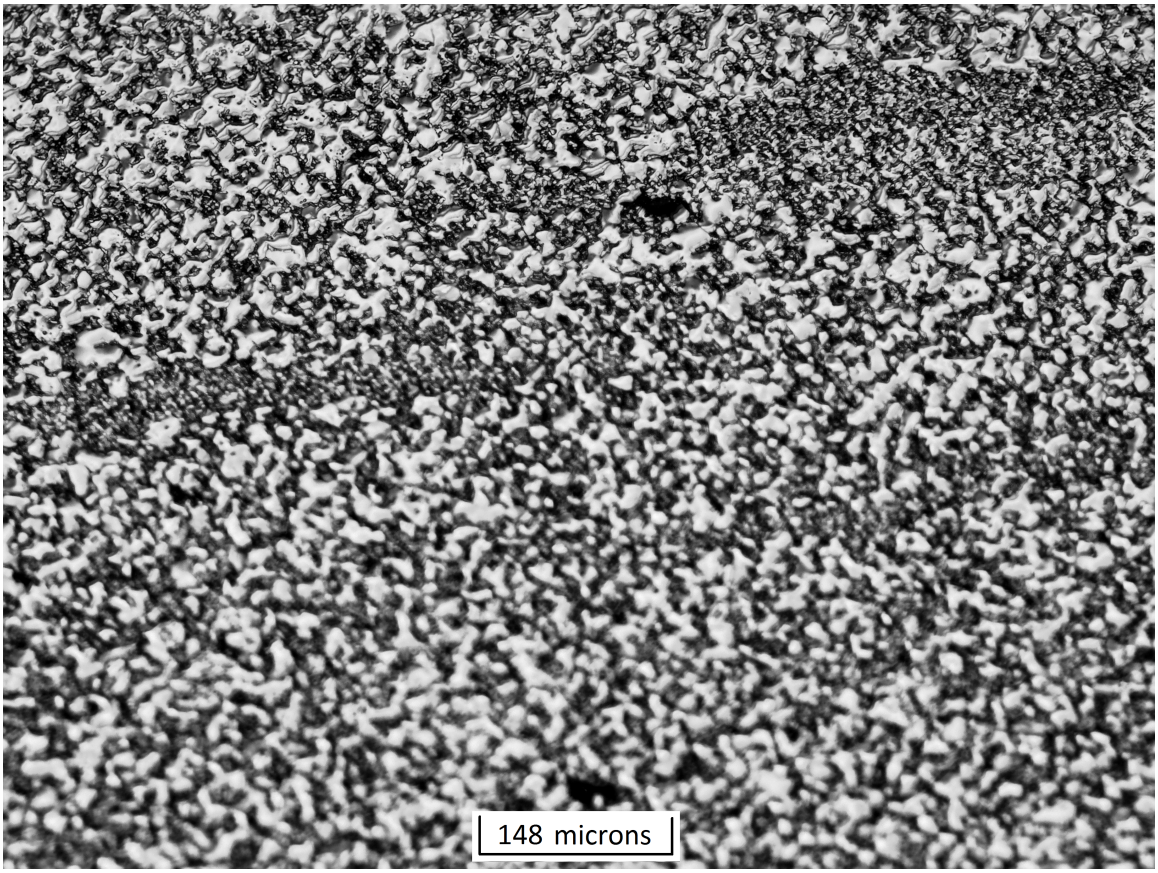

Figure 3.22: Optical microscopy at 100X of a representative triplex Mo-Si-B microstructure etched with Murakami's etchant. White: α-Mo. Gray: A15. Dark Gray: T2.

for material prep of α-Mo is developed that allowed very good images to be taken of polycrystalline α-Mo; however, this same procedure did not work well for the triplex material. Figure 3.27a shows an image quality map for the best quality EBSD scan of the triplex material indexing off of the BCC α-Mo phase. This image shows clear grain boundaries; however, the intermetallic phases could not be indexed well in post-processing and the only grains with acceptable confident index are the large grains corresponding to α-Mo. Figure 3.27b shows the same image quality map after partitioning by data with an acceptable confidence index. The problem can be best seen in plots of the orientation and kernel average mis-orientation images in Figure 3.28. Here, large mis-orientations within individual grains can be seen. This can

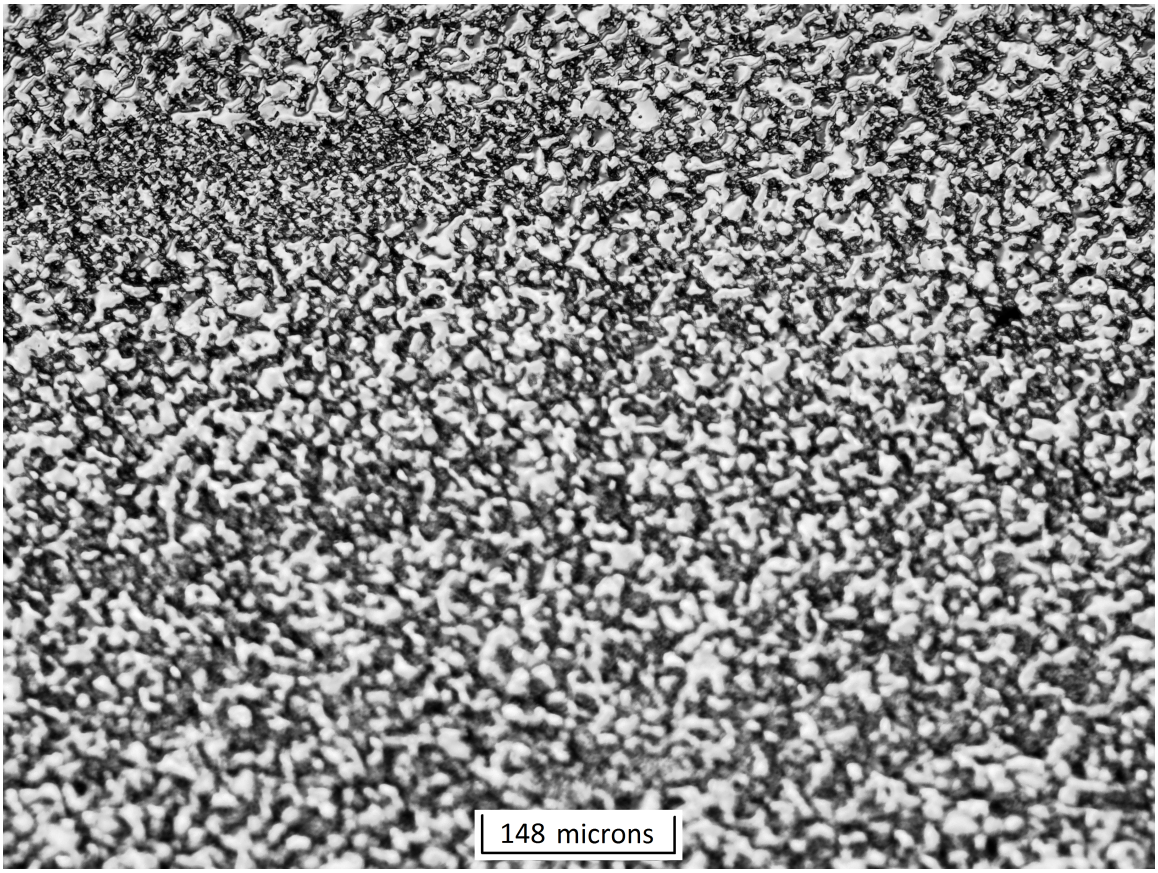

Figure 3.23: Optical microscopy at 100X of a representative triplex Mo-Si-B microstructure etched with Murakami's etchant. White: α-Mo. Gray: A15. Dark Gray: T2.

arise when the material is heavily deformed during processing, such as the forging step used to create this material. Unfortunately, such high levels of deformation make the task of OIM very difficult, and a complete characterization of the representative material is not possible.

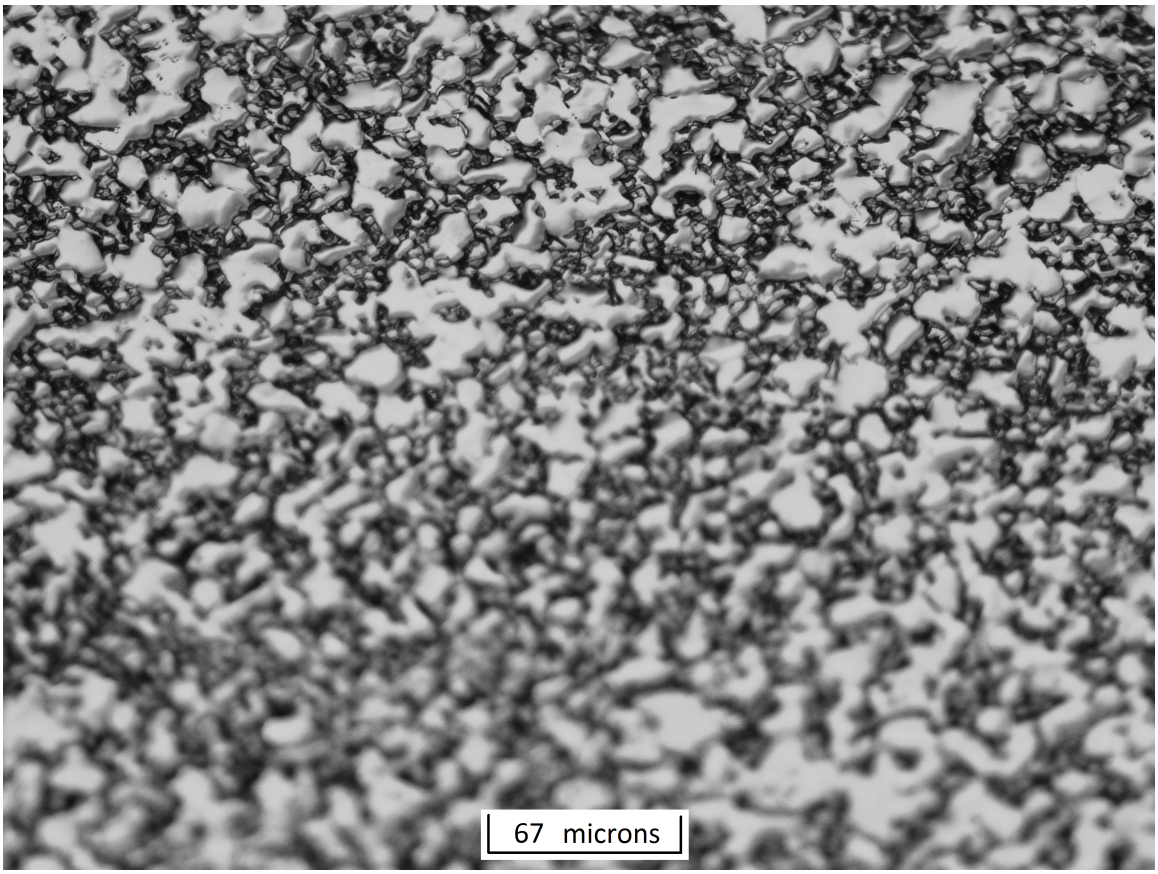

Figure 3.24: Optical microscopy at 200X of a representative triplex Mo-Si-B microstructure etched with Murakami's etchant. White: α-Mo. Gray: A15. Dark Gray: T2.

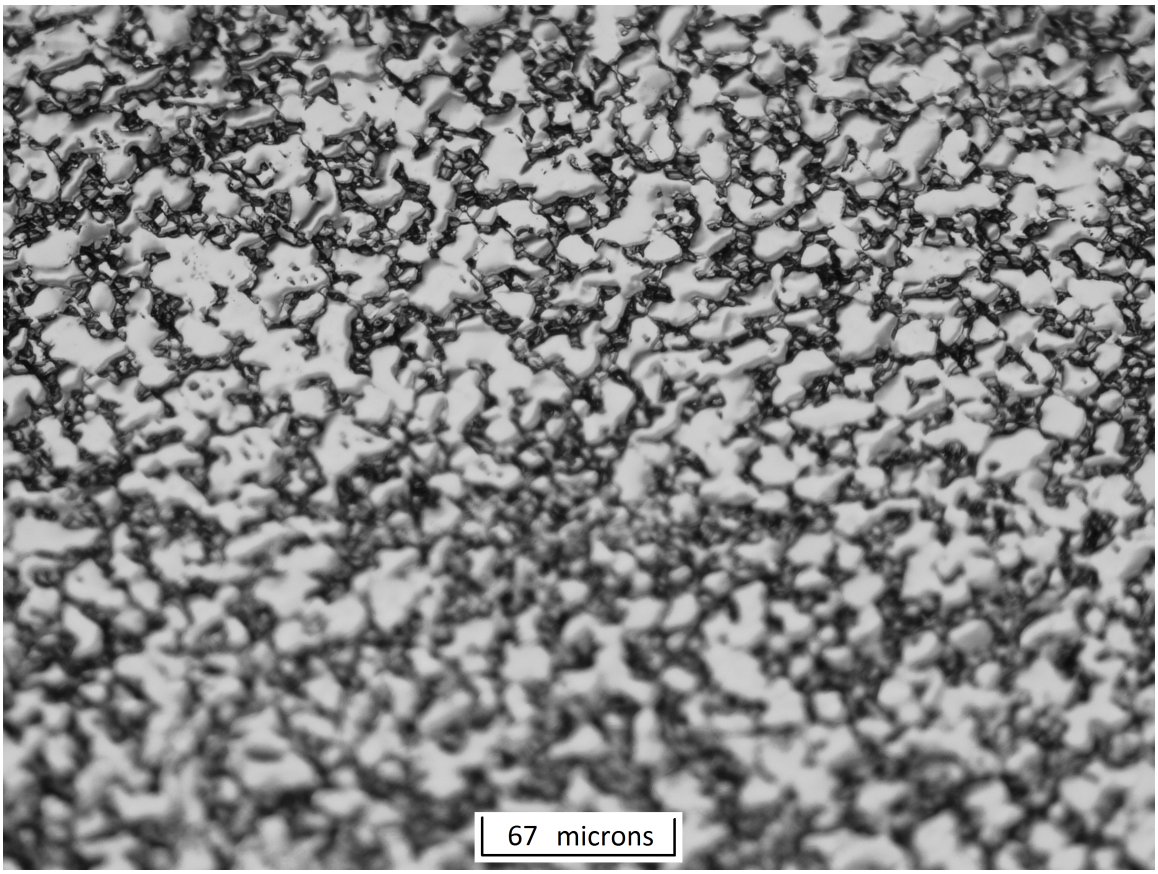

Figure 3.25: Optical microscopy at 200X of a representative triplex Mo-Si-B microstructure etched with Murakami's etchant. White: α-Mo. Gray: A15. Dark Gray: T2.

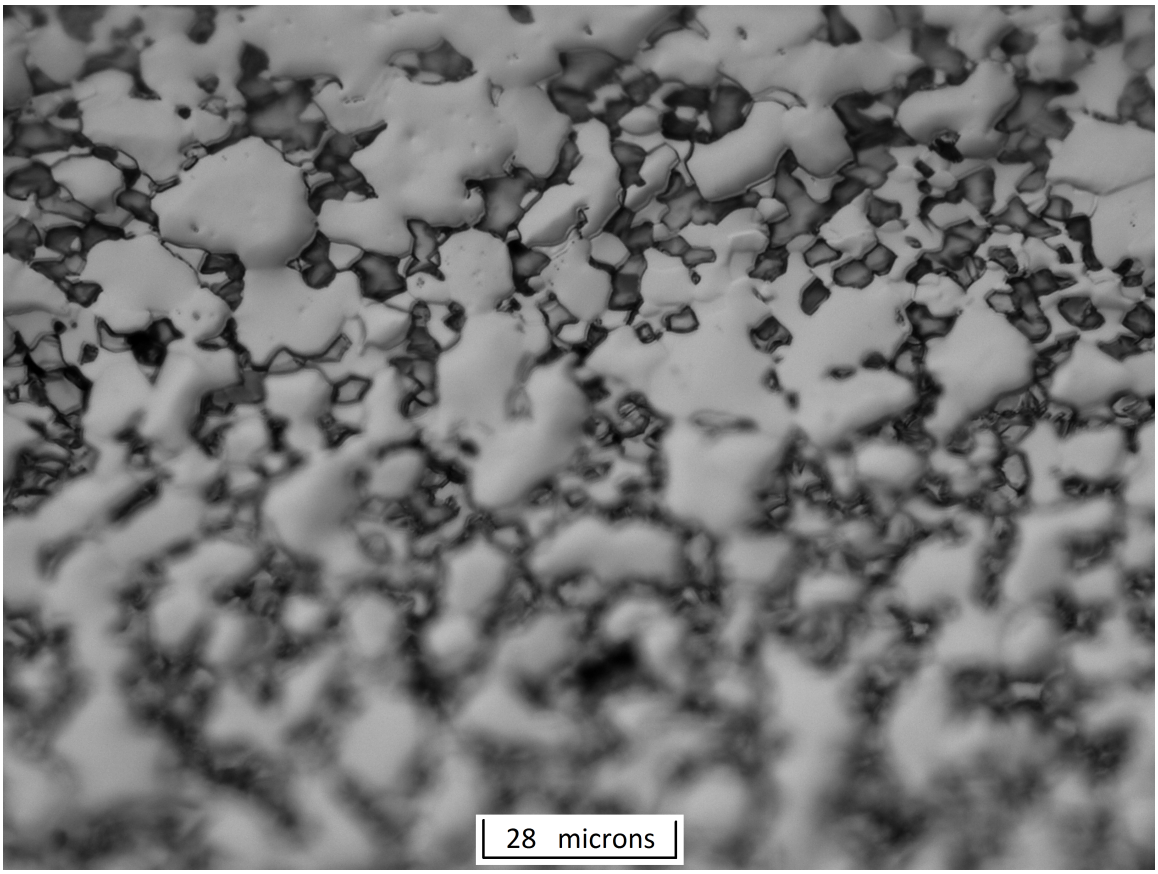

Figure 3.26: Optical microscopy at 500X of a representative triplex Mo-Si-B microstructure etched with Murakami's etchant. White: α-Mo. Gray: A15. Dark Gray: T2.

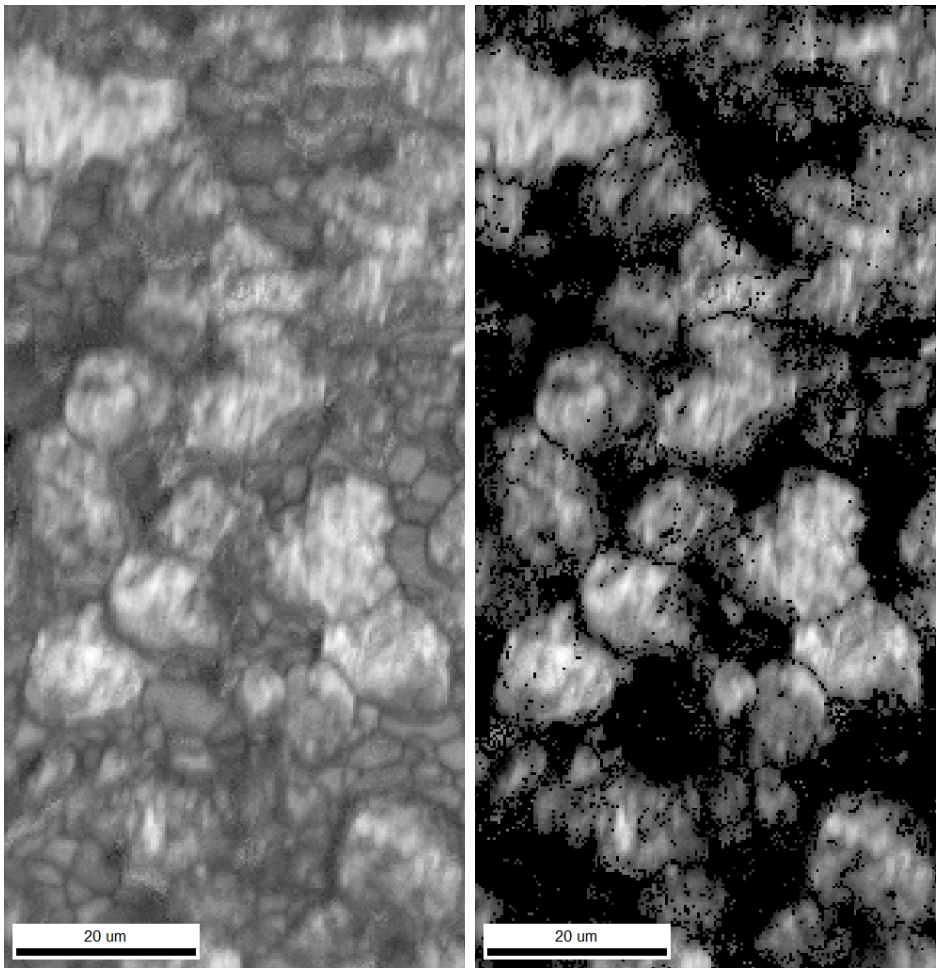

(a) EBSD image quality map of a representative triplex Mo-Si-B microstructure

(b) EBSD image quality map of a representative triplex Mo-Si-B microstructure partitioned by acceptable confidence index

Figure 3.27: EBSD image quality maps of a representative triplex Mo-Si-B microstructure

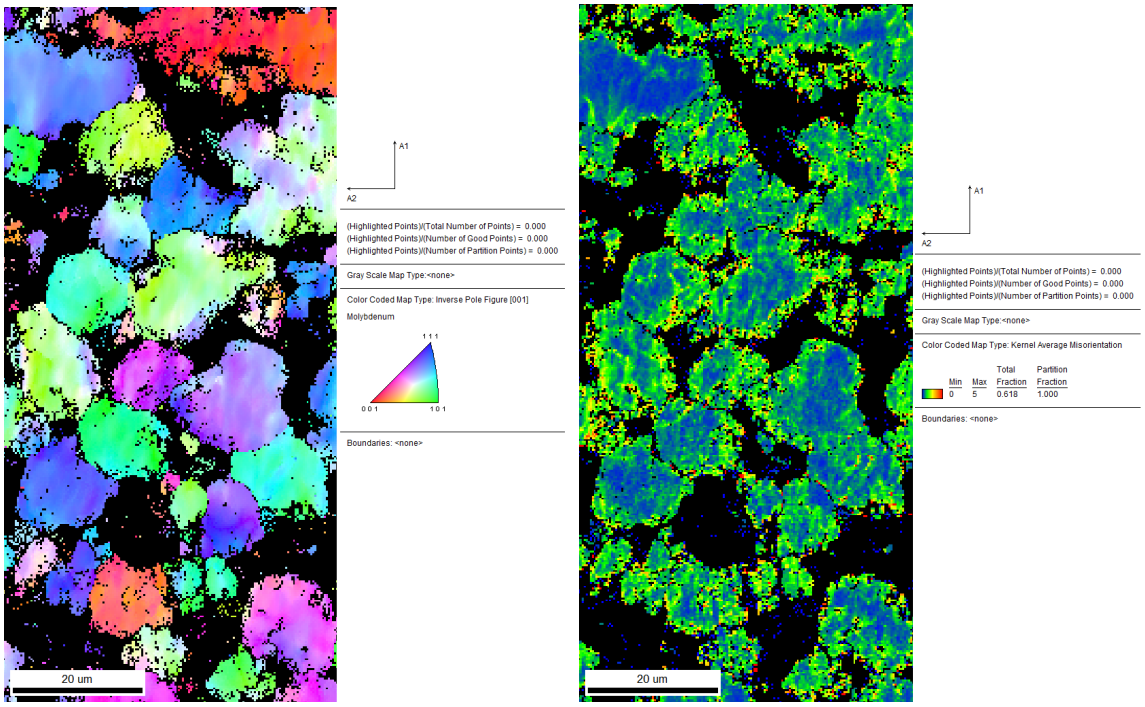

(a) EBSD IPF map of a representative triplex Mo-Si-B microstructure partitioned by acceptable confidence index

(b) EBSD kernel average mis-orientation map of a representative triplex Mo-Si-B microstructure partitioned by acceptable confidence index

Figure 3.28: EBSD orientation and kernel average mis-orientation maps of a representative triplex Mo-Si-B microstructure

3.4 Summary

The characterization of polycrystalline α-Mo material for texture, grain size distribution, and grain aspect ratio distribution is performed to supply input for creation of synthetic volume elements used to calibrate the α-Mo crystal-viscoplastic constitutive law. The microstructure of the α-Mo material changes with Si content, with the lower Si content materials showing two distinct regions with separate textures, grain sizes, grain shapes, and grain shape orientation. The chemical characterization of the α-Mo material also exhibits spatial variation of Si content, which is not addressed directly in the calibration of the α-Mo constitutive law, but can be modeled in future work using the tools presented in the following chapters.

Finally, a representative triplex Mo-Si-B material created by powder metallurgy and HIPed and forged is characterized to guide a parametric study of triplex Mo-Si-B alloys. This material is shown to be too highly deformed for analysis by OIM; however, optical microscopy shows phase volume fraction and grain sizes similar to that of material reported in literature. Optical microscopy also shows spatial variations in phase distribution; however, the parametric study assumes a random distribution of phases and a thorough characterization using n-point spatial statistics is left to future work. Similar to the spatial distribution of α-Mo Si content, the tools developed and exercised in later chapters are suitable for modeling spatial distributions of phase, following suitable characterization of those features in the material of interest.

3.5 Significance

The difficult nature of the α-Mo material characterization presents challenges for the generation of accurate synthetic volume elements and the calibration of the α-Mo constitutive law. The arc melted α-Mo material specimens motivate the need for a custom microstructure generator in order to perform the best calibration of the constitutive possible with the experiments of this work. The large differences in the

arc melted α-Mo material microstructure and triplex Mo-Si-B microstructures also require the use of literature data for a complete α-Mo constitutive law calibration.

Variations in the spatial distribution of phases and the spatial distribution of α-Mo Si content are important material features for more targeted future modeling work of an optimized triplex Mo-Si-B microstructure. Although these variations are not directly addressed in this work, they motivate the need to build in future capability to the modeling tools developed and exercised in this work.

CHAPTER IV

MICROSTRUCTURE GENERATOR

4.1 Introduction

This chapter focuses on the first tool in the microstructure-sensitive mechanical property modeling workflow, shown in Figure 4.1, and describes the synthetic microstructures generated for calibration of the α-Mo constitutive law and for the triplex Mo-Si-B parametric study.

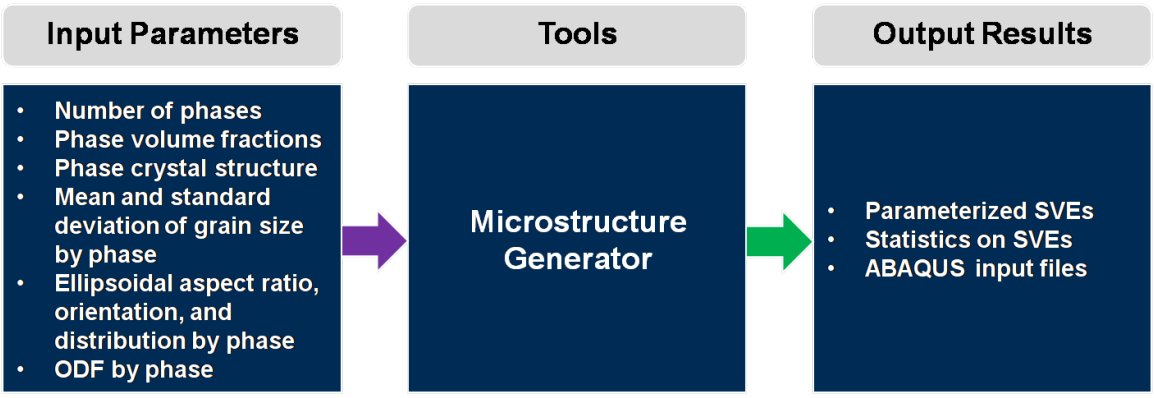

Figure 4.1: Microstructure-sensitive mechanical property modeling workflow: Microstructure generator

4.2 Microstructure Generator Input

The microstructure generator developed for this work is based on an ellipsoidal packing algorithm developed by Przybyla [54] and related to the work of Groeber *et al* [65], which Przybyla showed to give greater control over grain shape distributions in comparison to Voronoi tessellation based algorithms [54]. This is especially important for the arc-melted α-Mo specimen material, which exhibits two unique regions of microstructure as discussed in Chapter 3. This microstructure generator is chosen for its ability to capture the unique traits for separate phases as well as the phase volume

fractions for each phase. For each phase, the microstructure generator is capable of capturing the following:

1. Crystal structure
2. Mean and standard deviation of grain size
3. Grain shape distribution
4. Grain shape orientation distributions
5. Orientation distribution

The crystal structure is captured by passing the phase to the constitutive model, which captures the elastic anisotropy and slip systems associated with the crystal structure of that phase. Grain size statistics are defined as a mean and standard deviation for a uniform distribution, which the microstructure generator then converts to a log normal distribution. Grain shape is captured by approximating grains with ellipsoids defined by major and minor aspect ratios which vary according to a beta distribution. Orientation distributions are captured through the free and open source, third party, Matlab toolbox MTEX, which can be found at `https://mtex-toolbox.github.io/` [189].

The microstructure generator is also capable of capturing the misorientation distribution for single phase, single region microstructures; however, the two region microstructure generator required for creating synthetic microstructures of the α-Mo compression specimens complicates these calculations and cannot currently account for misorientation distribution.

Although microstructure reconstruction algorithms can have significant effects on the variation in the 2^{nd} order spatial statistics of synthetic volume elements, and therefore the variation in predicted mechanical properties, evaluating the effects of

the algorithm used to perform microstructure reconstruction is outside the scope of this work.

4.2.1 α-Mo Material

As described previoulsy, the microstructure in the compression test specimens used to calibrate the α-Mo CVP model is single phase, polycrystalline α-Mo, where α-Mo refers to a solid solution of Si in Mo. Material with five separate Si contents are tested and simulated, each with a unique material characterization requiring a unique microstructure to be generated. Three of these materials, Mo-0.00Si, Mo-0.29Si, and Mo-0.40Si where Si is in weight percent, require a two region microstructure. The two higher Si content materials, Mo-0.58Si and Mo-1.16Si, require a single region microstructure.

The synthetic microstructures created for the arc-melted α-Mo Mo-0.00Si and Mo-0.40Si (wt.%) materials are shown in Figures 4.3 and 4.4, respectively. Without a separate Mo-0.29Si material characterization, the Mo-0.40Si synthetic microstructure is used for the Mo-0.29Si material. The simulated microstructures are loaded along the vertical axis and maintain a fixed number of 27 elements per edge. The number of elements per edge is chosen to balance the ability to match the microstructural features, mesh refinement, and simulation run time.

Twenty-seven elements per edge is determined to be a reasonable balance between mesh refinement and computational cost during a preliminary convergence study of both mesh refinement and number of total grains for the Mo-0.40Si material. However, the final parametric study is carried out on SVEs with 33 elements per edge which offered an advantage in fitting the grain diameter distributions of three phase microstructures. Figure 4.2 shows the results of a the convergence study with a Mo-0.40Si calibration and material SVE at room temperature. Table 4.1 gives a complete description of the variation in each SVE for the convergence simulations. The study

shows convergence of yield strength for all four SVEs and convergence of the plastic hardening for SVEs with 828 grains or more. Due to the uncertainty in the experimental data for plastic hardening, a smaller SVE with a relatively coarse mesh is chosen to reduce the computational cost of the calibration simulations.

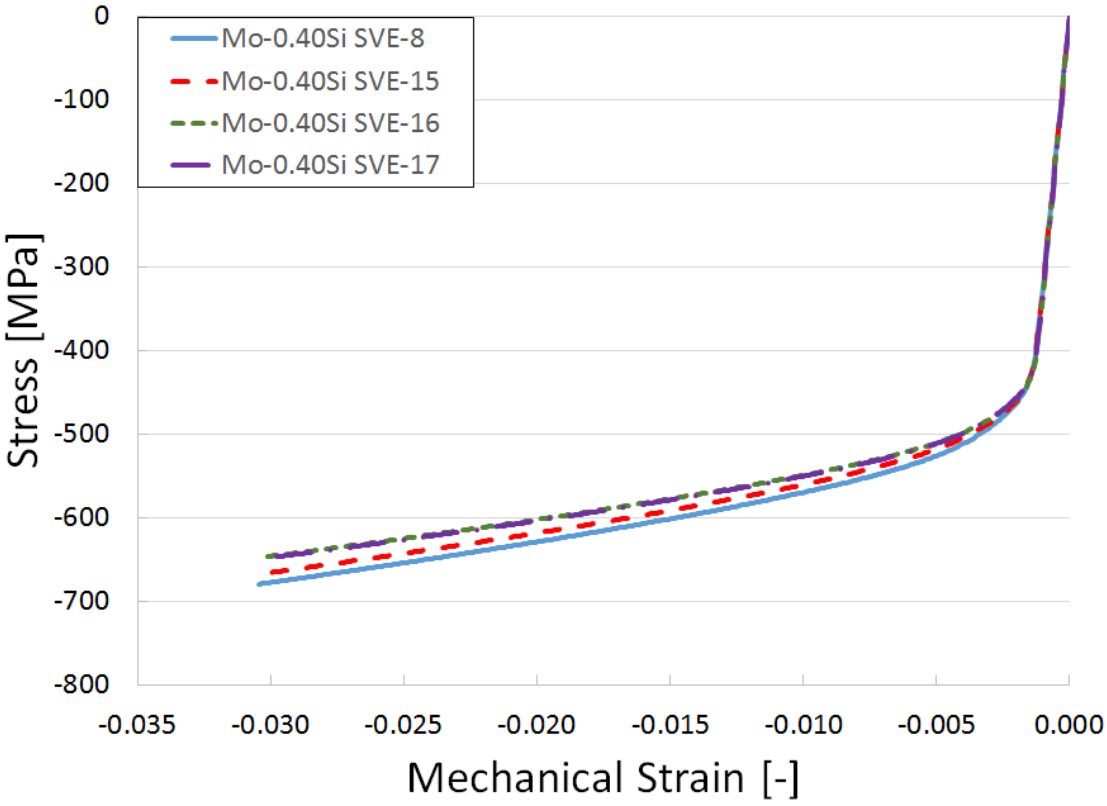

Figure 4.2: α-Mo convergence study

Table 4.1: α-Mo convergence study SVE descriptions

SVE instantiation	8	15	16	17
SVE Edge Length [μm]	5.000	5.000	7.115	7.115
Elements per edge	26	33	37	47
Element edge length [μm/elem]	0.192	0.152	0.192	0.151
No. of Grains	322	474	828	1134

The Mo-0.00Si SVE has an edge length of 9 mm and 302 total grains. The edge

length is chosen to balance:

1. the log normal equivalent grain diameter distribution estimated from the processed equiaxed region >100 μm partition and columnar region >450 μm partition mean and standard deviation equivalent grain diameter

2. the mesh refinement of the relatively small grains in the equiaxed region

Due to the large difference in grain sizes between the equiaxed and columnar regions, it is difficult to match the equivalent grain diameter distributions of both regions without a highly refined mesh that is too computationally expensive for practical use. Consequently, the grains of the equiaxed region average approximately 10 elements per grain, while the grains in thie columnar region average closer to 200 elements per grain. The minimum number of elements per grain in this SVE is 7, and the maximum number of grains per element is 1469. This large difference in the number of elements per grain highlights the difficulty of recreating these two region microstructures.

An unstructured mesh generator with a more highly refined mesh for the equiaxed region, and a coarser mesh for the columnar region would improve the ability to match each regions microstructure definition with sufficient mesh refinement for the changing length scales. Such a mesh generator is beyond the scope of this work. The previously mentioned convergence suggests that 300 grains per SVE results in convergence of the stress-strain response; however, the poor mesh refinement of the equiaxed region is still undesirable. In Chapter 5, the convergence study and α-Mo calibration data are presented. Given the level of accuracy expected from the arc-melted α-Mo compression data, the SVEs presented here are likely to be sufficient for a calibration of the plastic hardening law within the limits of the data.

The Mo-0.40Si SVE has an edge length of 5 mm and 610 total grains and makes the same trade-offs between mesh refinement and SVE size. The material characterization for each region is taken from the equiaxed region >100 μm and the columnar region

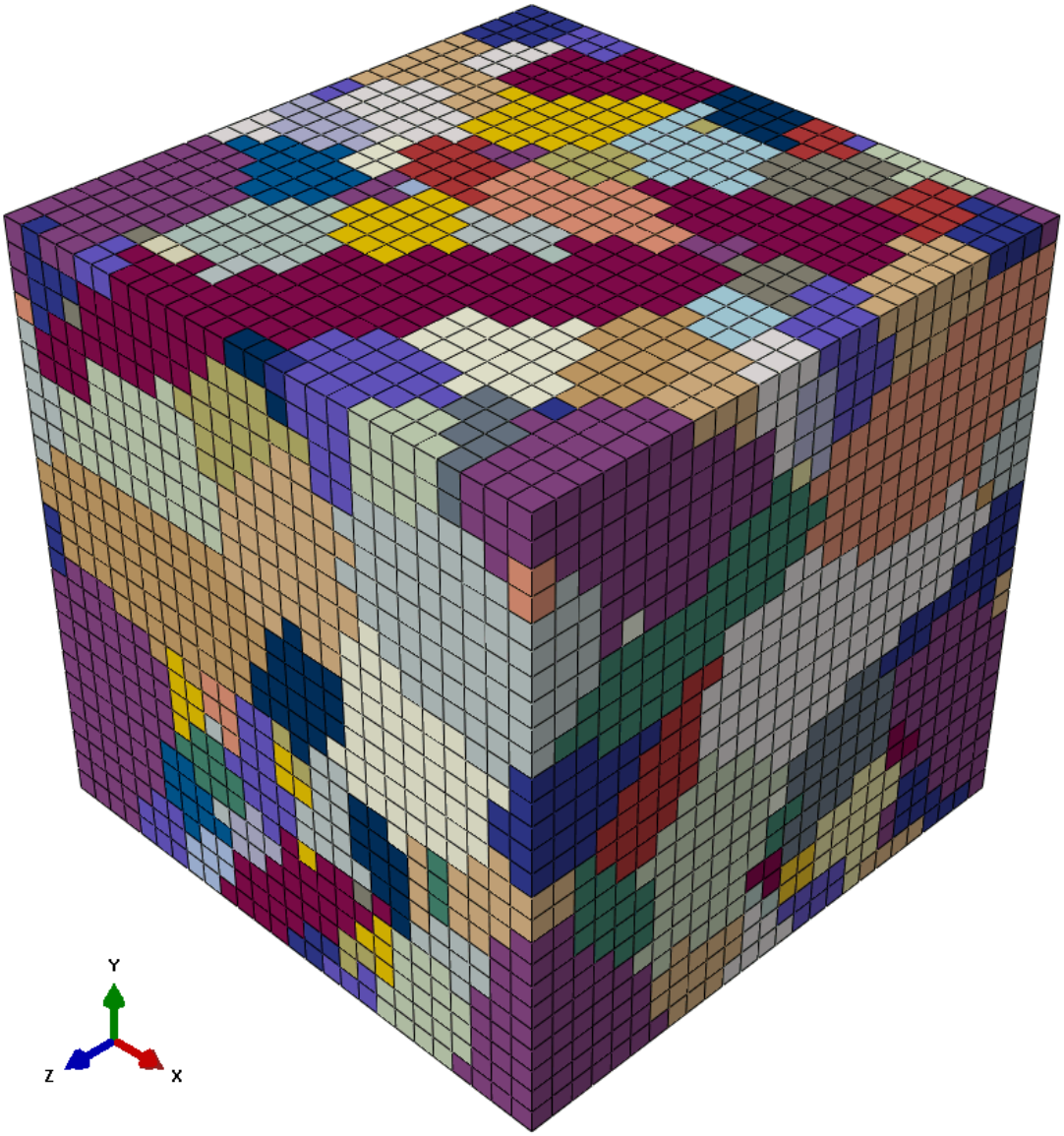

Figure 4.3: Two region synthetic Mo-0.00Si microstructure with an edge length of 9 mm and 302 total grains. Colors are assigned to unique grains.

>450 μm partitions, respectively. While determining an appropriate edge length for the two region microstructures, an effort is made to keep the edge length on the same scale as the test specimens.

The Mo-0.00Si and Mo-0.40Si synthetic microstructures show the ability of the microstructure generator to create two distinct regions from separate microstructure definitions. The lower region can be instantiated according to the equiaxed region

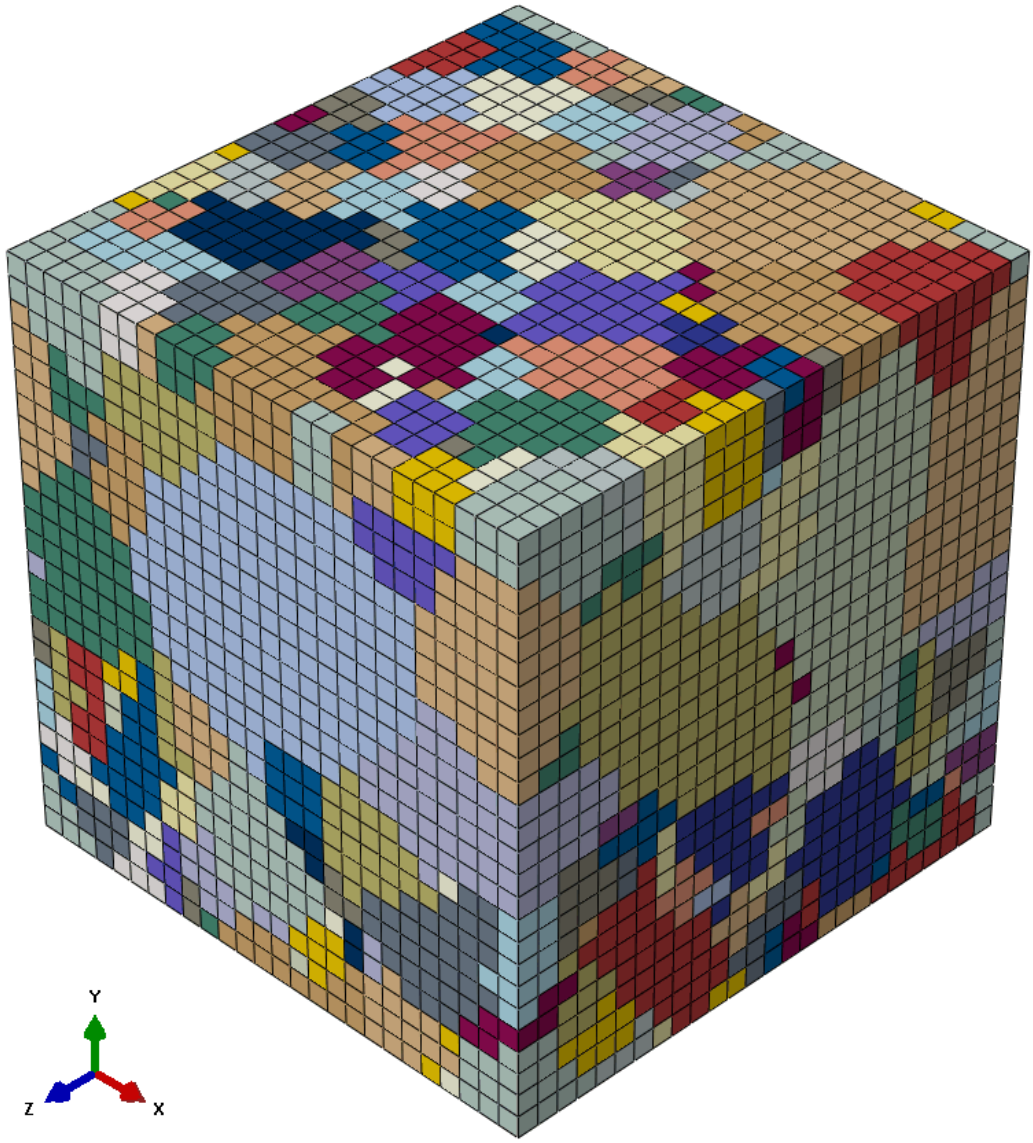

Figure 4.4: Two region synthetic Mo-0.29Si and Mo-0.40Si microstructure with an edge length of 5 mm and 610 total grains. Colors are assigned to unique grains.

microstructure found in the Mo-0.00Si and Mo-0.40Si arc-melted α-Mo material, while the upper region is instantiated according to the columnar region microstructures.

The microstructure generator approaches the individual ellipsoidal packing of each of the two regions in turn after dividing the entire volume along a chosen plane defined by one of the global axes of the volume. In the arc-melted α-Mo simulations, the volumes are loaded along the global Y axis and the volume element is divided along

a plane with a unit normal parallel to the global Y axis. This plane can be placed at any distance along the chosen axis, provided that the dividing plane lies within the volume element boundaries. For the arc-melted α-Mo simulations of the Mo-0.00Si and Mo-0.40Si, this plane is placed such that the equiaxed region fills 1/3 of the total volume and columnar region comprises the final 2/3 of the volume. Figure 4.5 shows the Mo-0.00Si microstructure with the division plane highlighted in red. In this figure, many grains can be seen crossing the division plane, allowing a more natural division of the microstructure than a hard limit for each region.

After the volume has been subdivided by region, the equiaxed region is filled with ellipsoids generated to fit the material definition of the equiaxed region until the equiaxed region jamming limit is reached. The ellipsoids are placed in order from largest to smallest. When placing ellipsoids, the dividing plane is not treated as a hard limit on ellipsoid placement. Instead, ellipsoid centers are restricted to the equiaxed region, which allows a more natural overlap between the two regions. Additionally, the microstructure generator uses a periodic boundary condition, which means ellipsoids that extend beyond the edge of the volume element continue from the positive face to the negative face of the volume element and vice versa.

This boundary condition is intended to approximate the boundary conditions of a small volume of material residing in a much larger volume. While this is an appropriate modeling assumption for the Sturm *et al.* α-Mo SVEs and the parametric study SVEs that are presented later in this section, it is not as accurate for the arc-melted α-Mo SVEs, which are on the same size as the physical test specimens. However, for the simplicity and consistency when creating many simulations, the arc-melted α-Mo SVEs follow the same boundary conditions as the majority of the simulations. It is assumed that any inaccuracies of the applied boundary conditions for the arc-melted α-Mo simulations fall within the inaccuracies of the arc-melted α-Mo calibration data, and the SVEs are acceptable for the calibration of the plastic

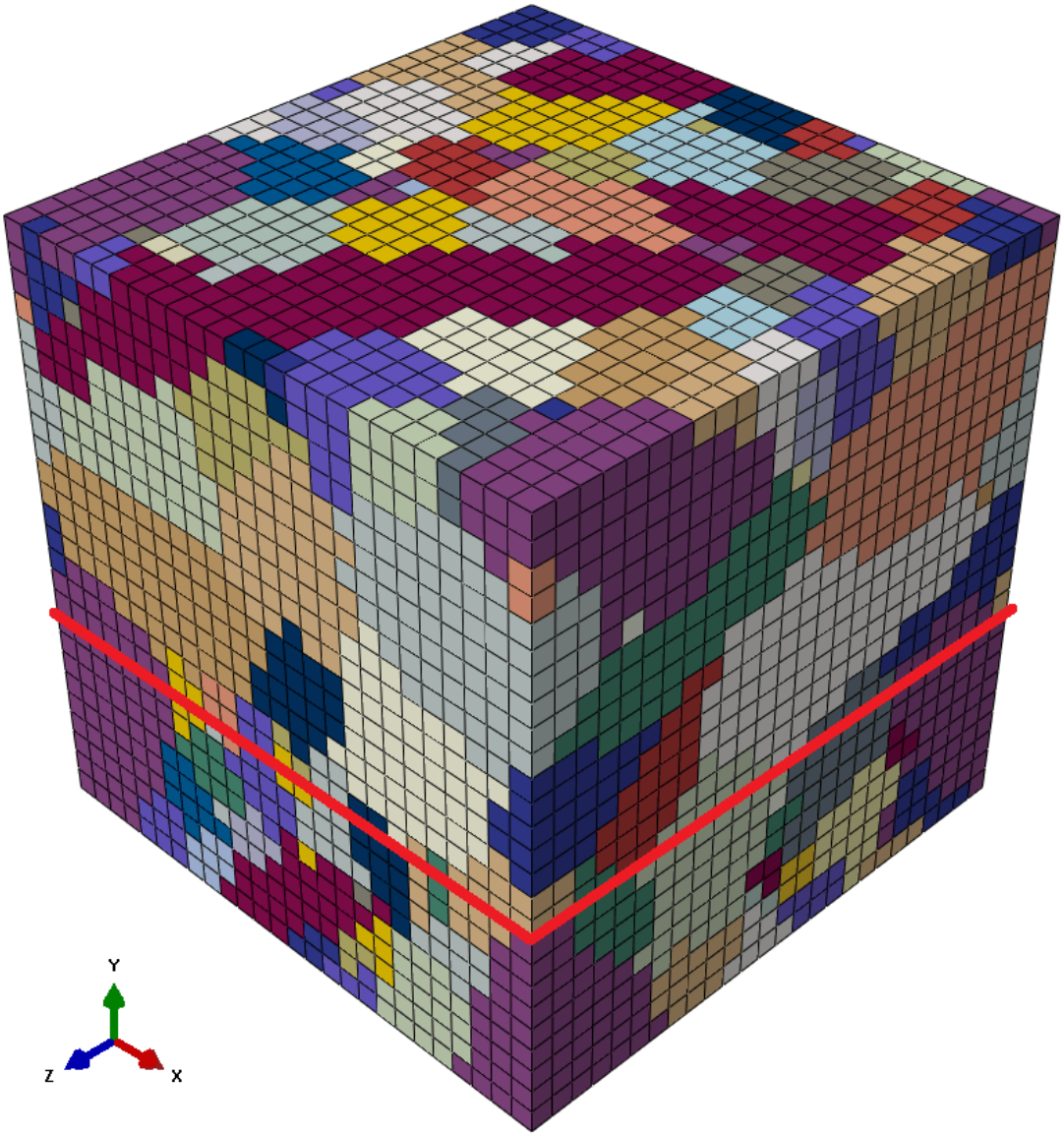

Figure 4.5: Two region synthetic Mo-0.00Si microstructure with division between regions highlighted in red. Colors are assigned to unique grains.

hardening law.

Following the initial placement of ellipsoids in the equiaxed region, the columnar region is populated with ellipsoids generated according to its separate material definition until the columnar region jamming limit is reached. The jamming limit can be set independently for each region for better control of the final microstructure.

After all of the initial ellipsoids have been placed in the total volume, a simulated annealing procedure is carried out over both regions simultaneously to fill the remaining volume. In this step, each ellipsoid grows by one voxellated step outward in order of ellipsoid placement until the volume is filled. At the end of this step, the ellipsoids have formed the final grains of the simulated volume. Each grain is then assigned a crystal orientation from a distribution of crystal orientations matching the desired final texture of the region in which the grain resides. For the two region microstructures, the equiaxed region is randomly textured and the columnar region has a fiber texture. For the single region microstructures, the entire volume is randomly textured.

The final step is to analyze the material characteristics of the final microstructure. Plots of equivalent grain diameter distribution, grain aspect ratio distribution, and texture are created and compared to the target characteristics for each region and the entire volume. If the targeted microstructural characteristics are not met, the algorithm control parameters are adjusted manually until a satisfactory visual fit is established. Given the limited 2D dataset and assumptions involved in re-creating a 3D microstructure from a limited 2D data set, a more rigorous fitting method is not pursued.

Figure 4.6 shows the grain size distribution for both regions of the Mo-0.00Si microstructure. In Figure 4.6a, the smallest grain sizes in the equiaxed region are difficult to match due to the coarse mesh refinement for the relatively small grains. Figure 4.6b reflects the small number of grains in this region due to the large grains and small volume. The combination of a small volume and relatively fine mesh make the largest grains difficult to match for the columnar region.

Figure 4.7 shows the same equivalent grain diameter comparison for both regions of the Mo-0.29Si and Mo-0.40Si synthetic microstructure. The difficulties matching the smallest grains of the equiaxed region and the largest grains of the columnar region are

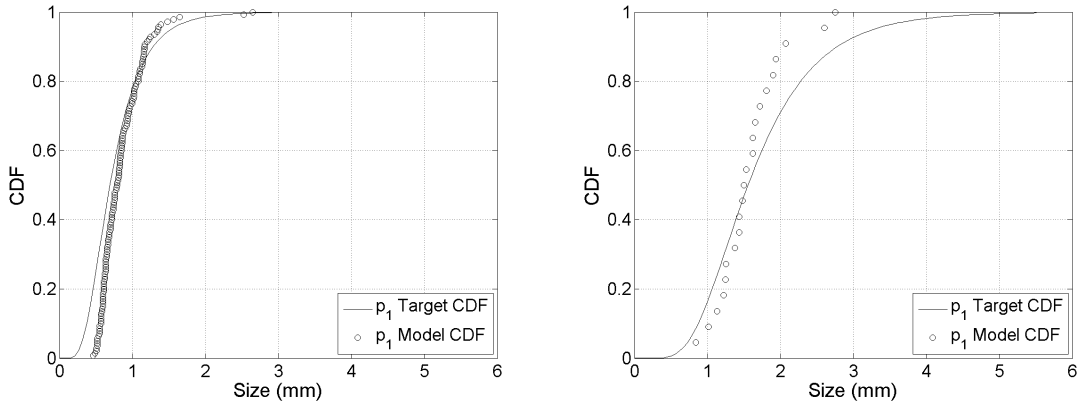

(a) Region one **(b)** Region two

Figure 4.6: Mo-0.00Si synthetic microstructure equivalent grain diameter distribution by region

again shown for a two region microstructure with large differences in microstructure characterization.

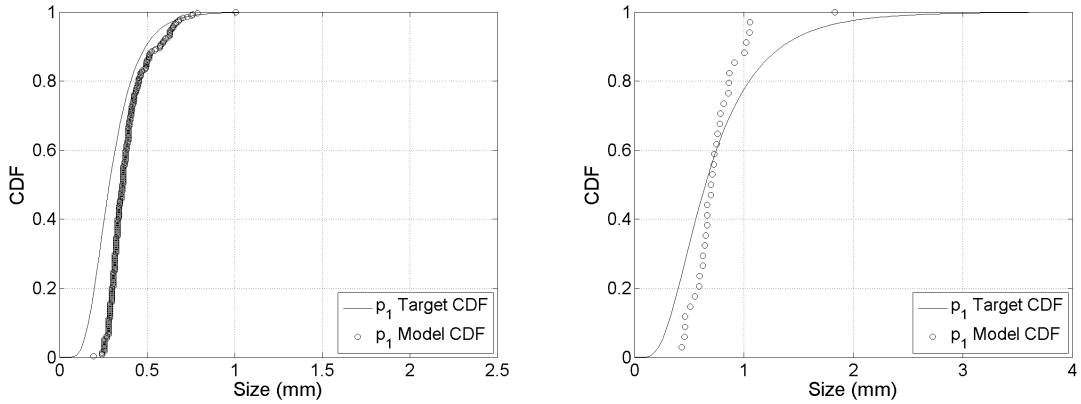

(a) Region one **(b)** Region two

Figure 4.7: Mo-0.29Si and Mo-0.40Si synthetic microstructure equivalent grain diameter distribution by region

Figures 4.8 and 4.9 compare the target and model textures of the Mo-0.00Si synthetic microstructure for the equiaxed region and the columnar region, respectively. Region one targets a random texture, while the columnar region targets an (001) fiber texture. Note that the equiaxed region texture plots of Figure 4.8 are plotted at different scales due to the differences between the limited number of grains in the

model compared with the well-populated data used to re-create the theoretical target texture. Figure 4.9 shows a remarkably good reproduction of the fiber texture in the columnar region of the model, especially considering the small number of grains making up this region. The Mo-0.29Si and Mo-0.40Si synthetic microstructure has the same targeted textures for each region. Since this SVE has a greater number of elements, the model texture is a closer match to the targeted texture than that of the Mo-0.00Si SVE, so it is not reproduced here.

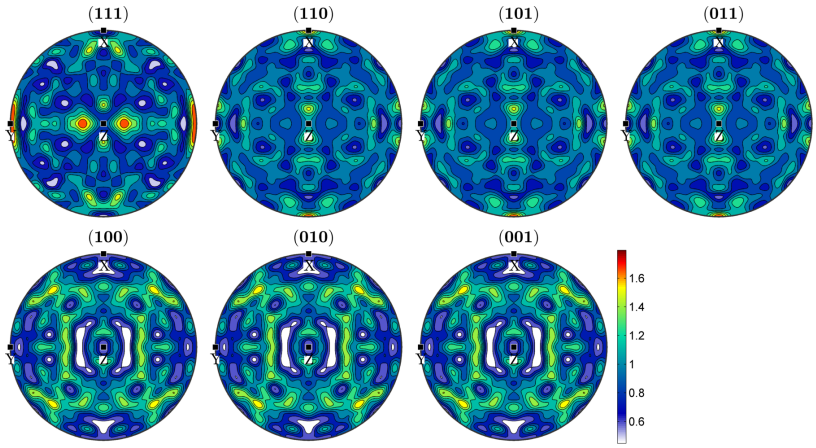

(a) Target texture

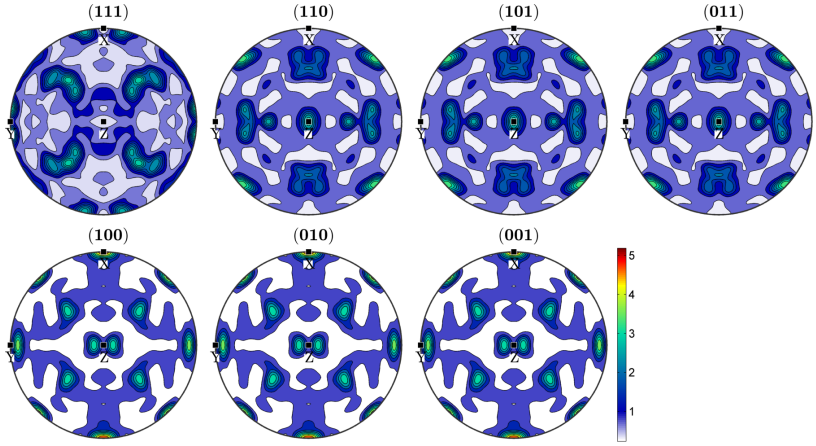

(b) Model Texture

Figure 4.8: Mo-0.00Si synthetic microstructure equiaxed region texture comparison

The final comparison between the targeted microstructure and the model microstructure is a comparison of the grain aspect ratios by region. Figure 4.10 shows

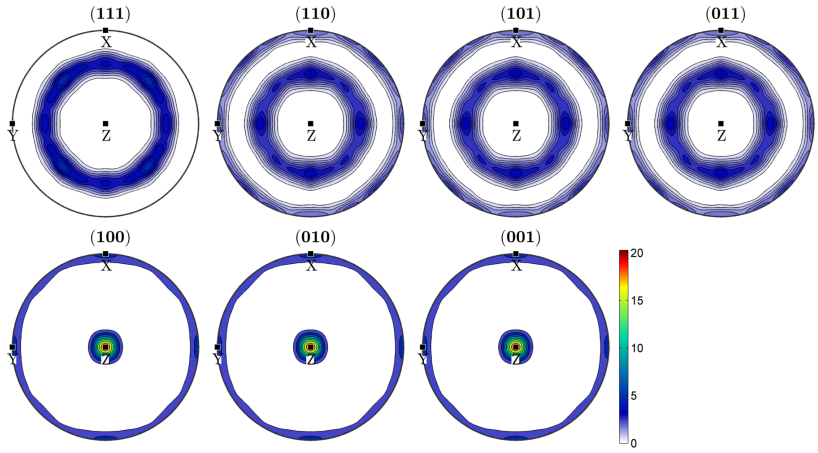

(a) Target texture

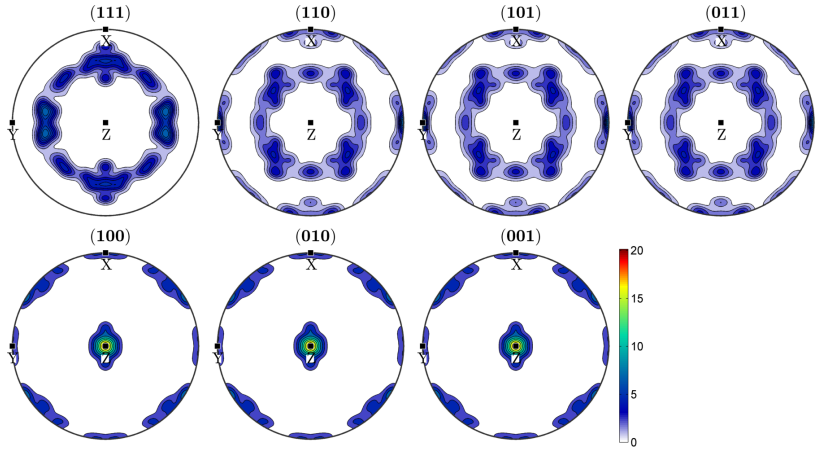

(b) Model Texture

Figure 4.9: Mo-0.00Si synthetic microstructure columnar region texture comparison

the Mo-0.00Si equiaxed and columnar region comparisons of target and model grain shape aspect ratio. The targeted aspect ratios are shown in red as the generated ellipsoid aspect ratios prior to voxellation and the simulated annealing step. The final grain aspect ratios are estimated from the voxellated mesh with the results shown as open blue circles. On this plot, the minor axes are normalized by the major axis with the semi-major axis plotted along the horizontal axis and the semi-minor axis plotted on the vertical axis. Points plotted on the rising diagonal represent prolate ellipsoids with the top right corner representing a sphere.

An incomplete beta distribution has been shown to match material characterizations of aspect ratio distribution for more complete data sets in other material systems [54]. However, a normal distribution is chosen for the columnar region in order to achieve the columnar grains seen in this region, with the parameters of the distribution taken from the limited data characterizing the arc-melted α-Mo material of this work. The equiaxed region of the two region microstructures and the single region microstructures also use a normal distribution to match the limited data from the material characterization of the arc-melted α-Mo microstructures in this work.

In both regions, the simulated annealing step tends to draw the final grain aspect ratios towards prolate ellipsoids trending more towards spheres than the original ellipsoid aspect ratios. The characterized aspect ratios of the equiaxed region are not quite equiaxed, and this is reflected in the number of grains which are better represented by prolate ellipsoids. However, the columnar region still shows a much more elongated set of grains with final aspect ratios closer to the origin than the upper right corner on the normalized aspect ratio plot. The Mo-0.29Si and Mo-0.40Si synthetic volume shows a similar distribution of aspect ratios, with the only the difference in the total number of grains plotted.

The synthetic microstructure representing the arc-melted α-Mo material generated for Mo-0.58Si and Mo-1.16Si are shown in Figure 4.11. This single region microstructure does not require any special treatment to subdivide into separate regions and has an edge length of 2.7 mm containing 200 grains. The minimum number of elements per grain is 8, while the maximum is 799 with the majority of grains containing approximately 20 elements. The packing algorithm proceeds as before, but without the additional steps to subdivide and separately pack the volume.

Figure 4.12 shows the equivalent grain diameter comparison for the single region Mo-0.58Si and Mo-1.16Si synthetic microstructure. In this single region microstructure, the difficulty matching the tails of the log normal equivalent grain diameter

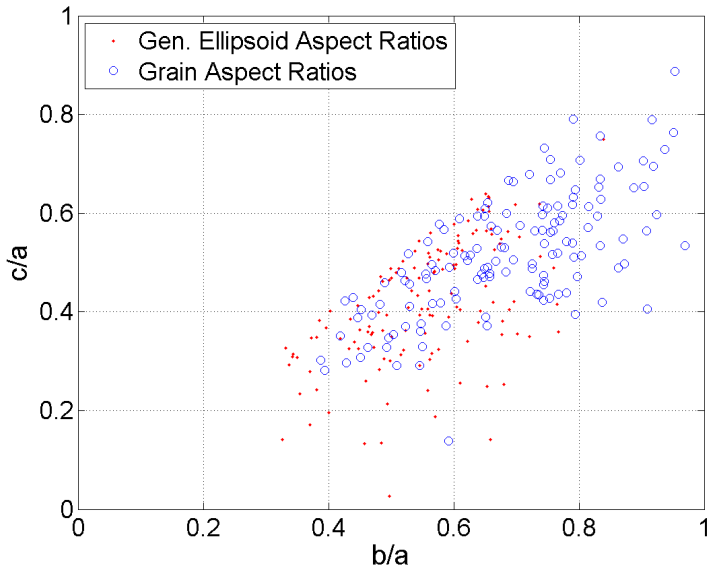

(a) Region one

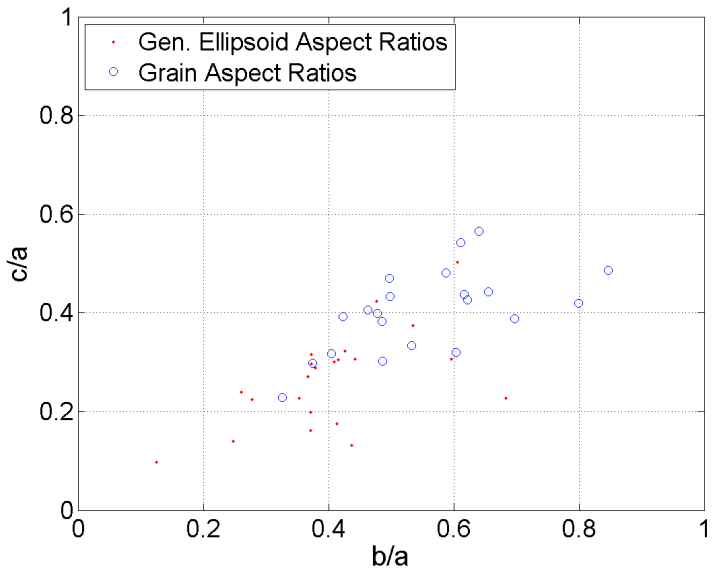

(b) Region two

Figure 4.10: Mo-0.00Si synthetic microstructure grain aspect ratio comparison by region

distribution comes from the combination of the mesh refinement and total volume size. The mesh size is a bit too coarse to match the smallest grains, but a balance must be struck in mesh size in order to come close to matching the larger grain sizes without increasing the volume dimensions. If the mesh refinement is held constant, a

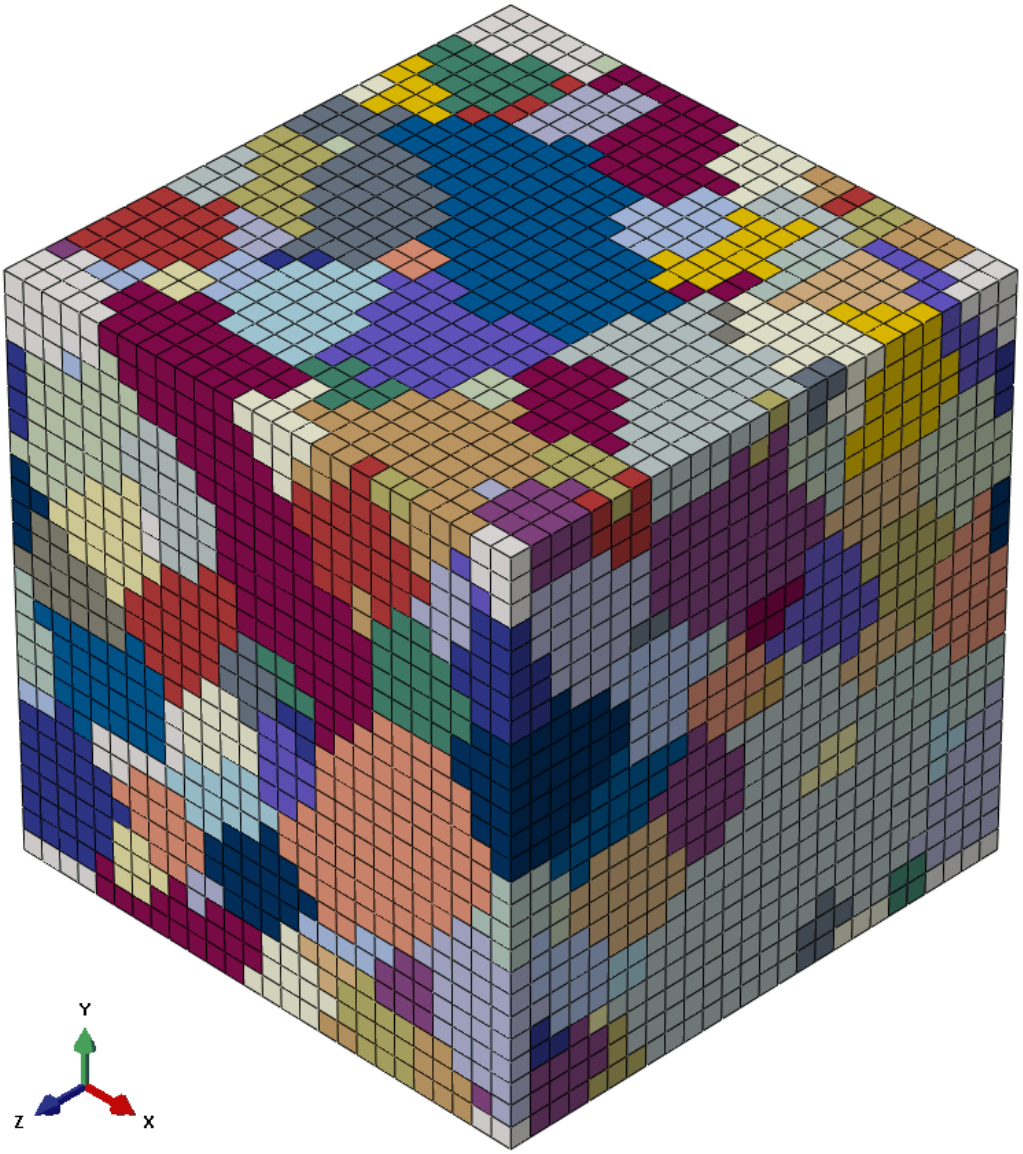

Figure 4.11: Single region synthetic Mo-0.58Si and Mo-1.16Si microstructure with an edge length of 2.7 mm and 200 total grains. Colors are assigned to unique grains.

better job matching the larger grain sizes can be achieved by increasing the volume dimensions and decreasing the jamming limit so that the additional volume remains open for the largest grains to fill during the simulated annealing step. It is also possible that some algorithm changes could be made to better control the order of grain growth during the simulated annealing step in order to better fit the target grain size distribution. However, in this work, the incomplete material characterization and

small number of grains in the physical test specimens make such an algorithm change a greater effort than is worth the small return in grain size distribution accuracy.

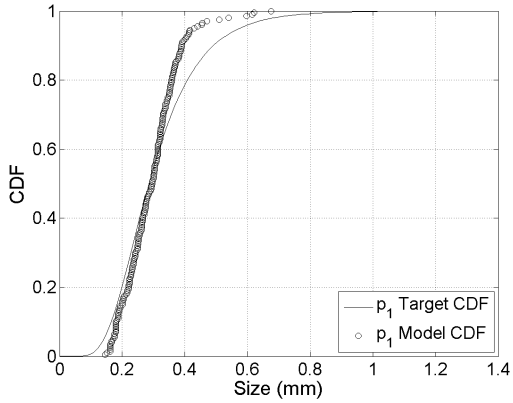

Figure 4.12: Mo-0.58Si and Mo-1.16Si synthetic microstructure equivalent grain diameter distribution

Figure 4.13 shows a comparison of the target and model texture for the single region Mo-0.58Si and Mo-1.16Si synthetic microstructure. Here, the target texture of the entire volume is a random texture, which is matched well despite the lower number of total grains in this SVE.

Finally, Figure 4.14 presents the targeted and model grain aspect ratio distribution. The target aspect ratios are taken from the material characterization of the equiaxed region in the Mo-0.40Si material, and the final grain aspect ratios exhibit the same trends as the equiaxed region grain aspect ratios in both the Mo-0.00Si and Mo-0.40Si SVEs.

Ideally, both the arc-melted α-Mo material tested and the synthetic volume elements simulated would be large enough that the mechanical properties of volume averaged elastic modulus and yield strength would be invariant with the specimen and volume element simulation, respectively. However, due to the small number of grains and the large heterogeneity of the arc-melted α-Mo material used in this work, there is no guarantee that the response of the physical specimens is insensitive to the specific specimen tested. Instead, the synthetic volume element size corresponds

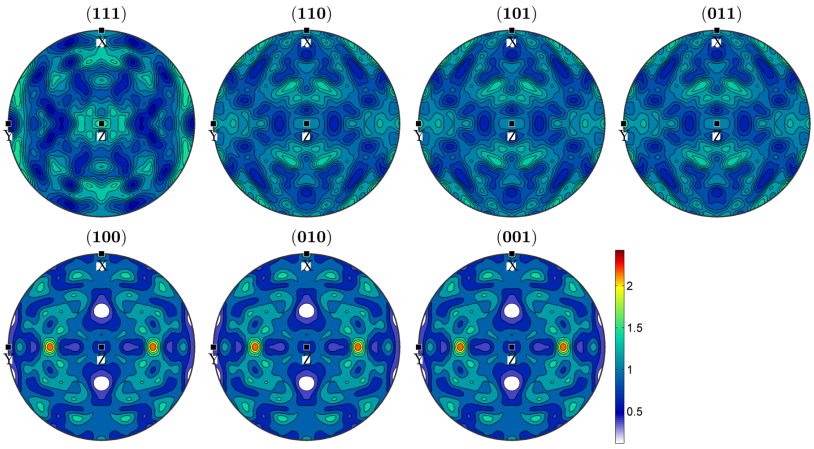

(a) Target texture

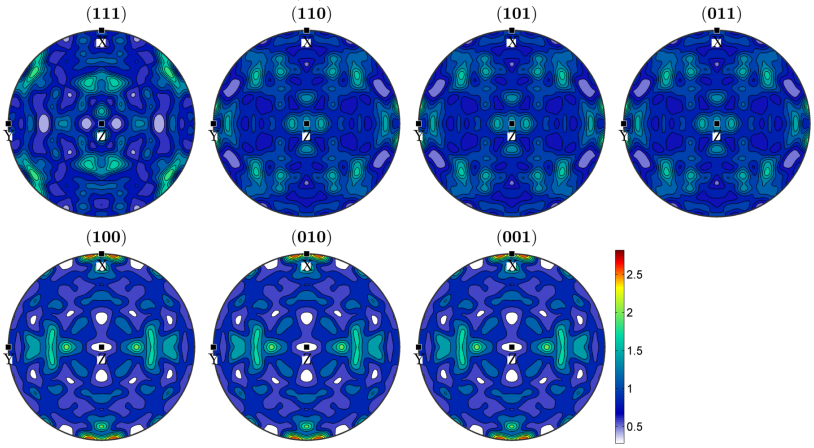

(b) Model Texture

Figure 4.13: Mo-0.58Si and Mo-1.16Si synthetic microstructure texture comparison

directly to the specimen dimensions.

While this may not guarantee a converged stress-strain response of the arc-melted α-Mo synthetic volume elements, it allows the constitutive model to be calibrated for plastic hardening within the accuracy allowed by the experimental specimens and sufficient for a first order study over a broad range of microstructures. The variability in yield strength from the arc-melted α-Mo material of this work does not allow an acceptable calibration of the corresponding constitutive model parameters. Instead, separate volume elements are created matching Sturm *et al.* α-Mo material [38] specifically for calibrating the yield strength of α-Mo as a function of Si content and

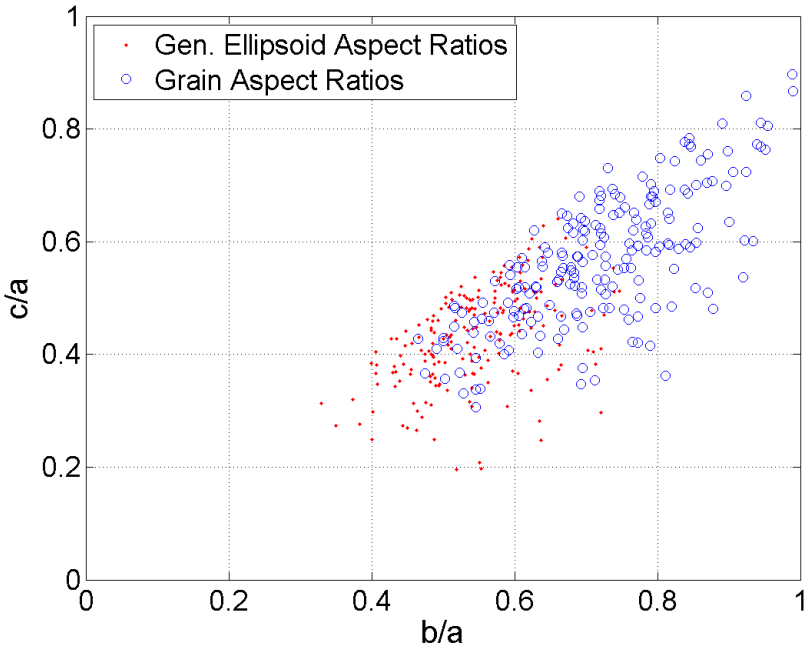

Figure 4.14: Mo-0.58Si and Mo-1.16Si synthetic microstructure grain aspect ratio comparison

temperature.

Four volume elements are created with equiaxed, randomly textured grains according to the characteristics of the Sturm *et al.* α-Mo with four different Si contents: 0.0, 0.1, 0.5, and 1.0 weight percent Si [38]. In this data set, only the mean grain size varies with Si content and is 97, 54, 35, and 82 μm, respectively [38]. Figures 4.15 through 4.18 show the synthetic microstructures for the Sturm *et al.* Mo-0.00Si, Mo-0.10Si, Mo-0.50Si, and Mo-1.00Si material, in that order. These volume elements have a slightly finer mesh at 33 elements per edge. Each volume element has a random texture and equiaxed grains.

The increased mesh density and single equivalent grain diameter distribution give these volume elements relatively well resolved grains. In the Mo-0.00Si Sturm *et al.* volume element, there is a minimum of 54 elements per grain and a maximum of 294, with most grains containing around 100 elements. The other volume elements

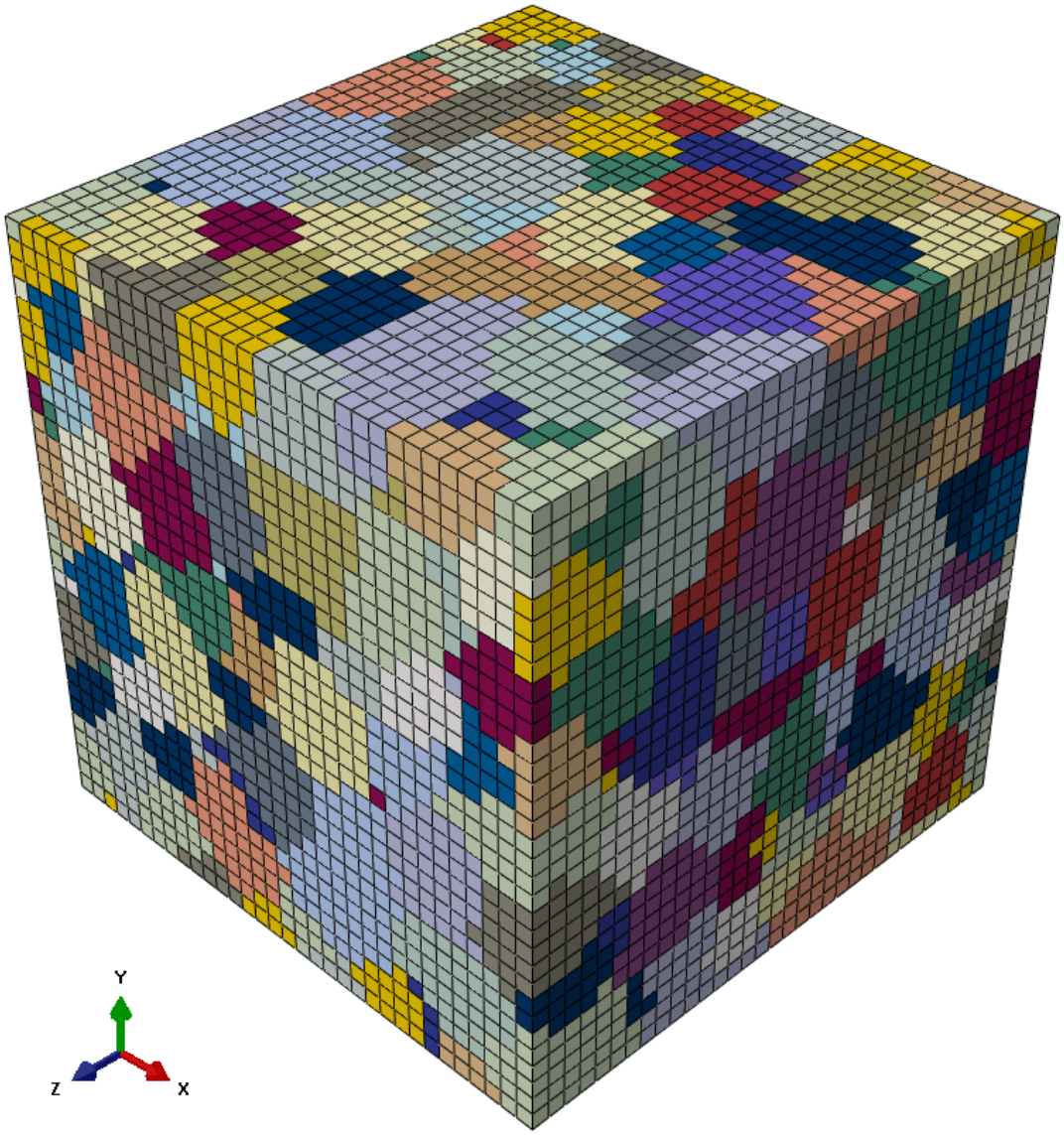

Figure 4.15: Single region synthetic Sturm *et al.* Mo-0.00Si microstructure with an edge length of 0.9 mm and 290 total grains. Colors are assigned to unique grains.

have similar minimum and maximum elements per grain. The equivalent grain diameter distributions of each volume element are presented in Figure 4.19. There is no information on the actual grain size distribution of the Sturm *et al.* material, so a log normal distribution is created from the mean grain diameter and an assumed standard deviation approximately ten times smaller than the mean diameter.

Figure 4.20 shows a comparison of the target and model texture for the Sturm

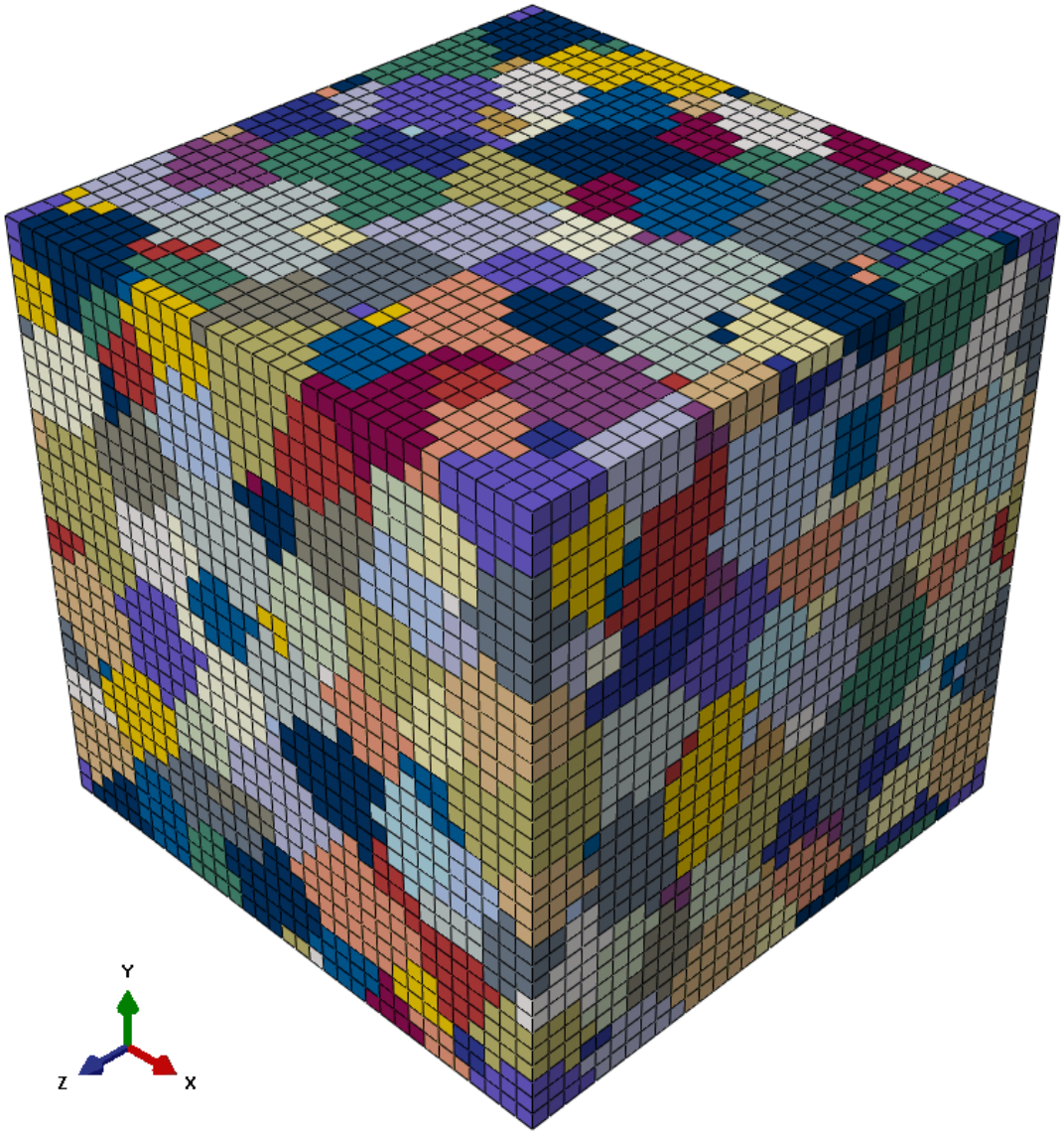

Figure 4.16: Single region synthetic Sturm *et al.* Mo-0.10Si microstructure with an edge length of 0.56 mm and 374 total grains. Colors are assigned to unique grains.

et al. Mo-0.00Si SVE, which has the fewest grains and would therefore be the most likely of the four SVEs to miss the target texture.

The original ellipsoid aspect ratios and approximated grain aspect ratios of all four SVEs are presented in Figure 4.21. The targeted microstructure contained an equiaxed microstructure. The final aspect ratios are similar to the equiaxed region of the Mo-0.00Si and Mo-0.40Si arc-melted α-Mo SVEs previously presented. As

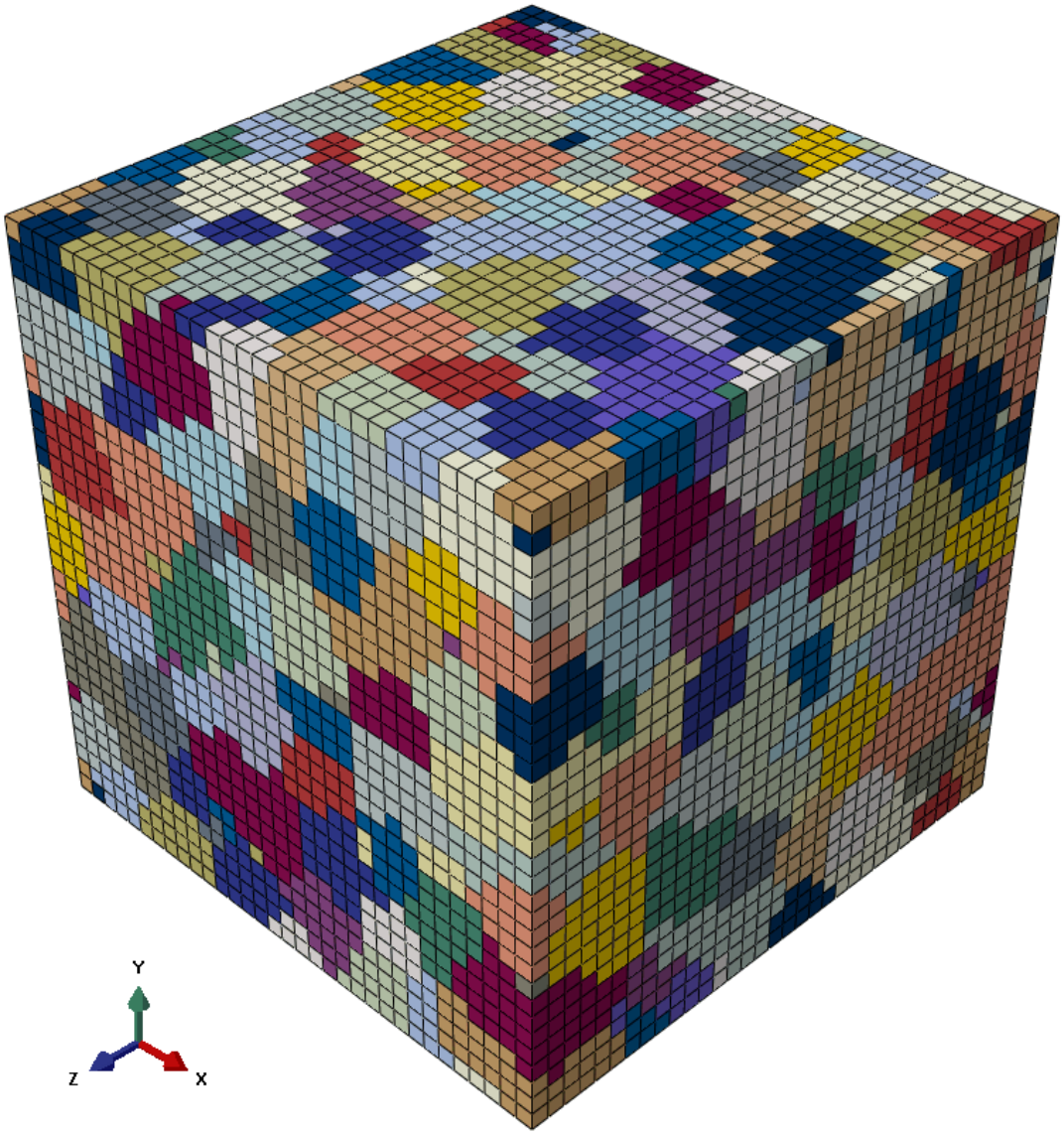

Figure 4.17: Single region synthetic Sturm *et al.* Mo-0.50Si microstructure with an edge length of 0.4 mm and 424 total grains. Colors are assigned to unique grains.

before, the actual grain aspect ratio distribution of the material is unknown, so the difference between the original ellipsoids and the final grains shape does not indicate a poor synthetic reconstruction. Instead, these figures are presented to show that the final SVE contains a relatively equiaxed microstructure and that a more complete characterization could be fit if the data are known.

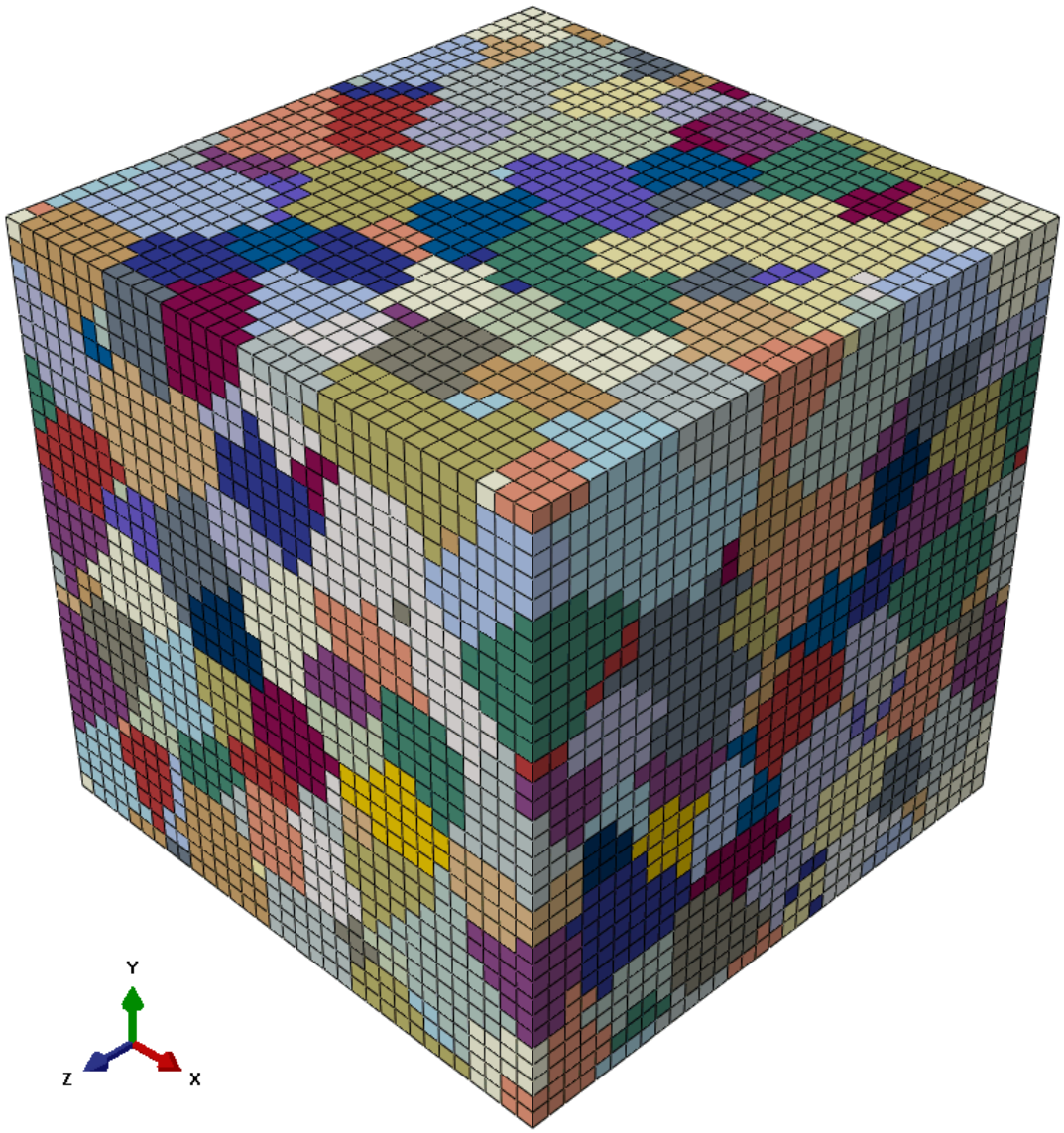

Figure 4.18: Single region synthetic Sturm *et al.* Mo-0.00Si microstructure with an edge length of 0.8 mm and 312 total grains. Colors are assigned to unique grains.

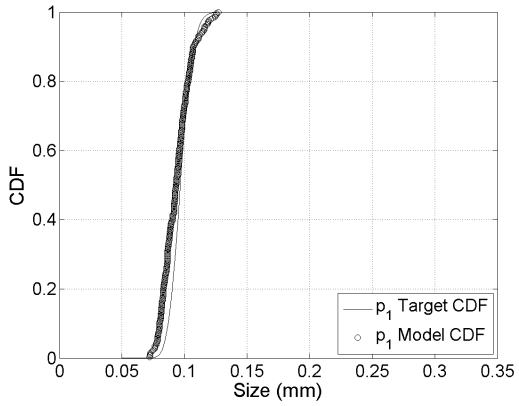

(a) Sturm *et al.* Mo-0.00Si SVE

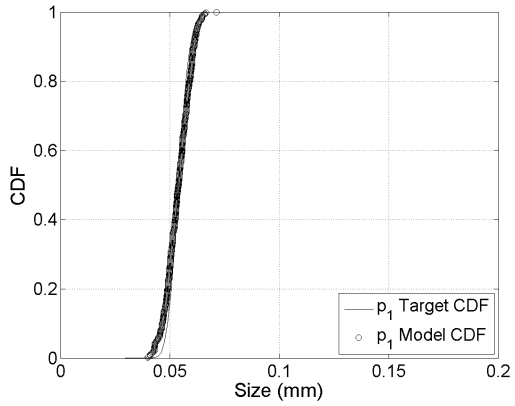

(b) Sturm *et al.* Mo-0.10Si SVE

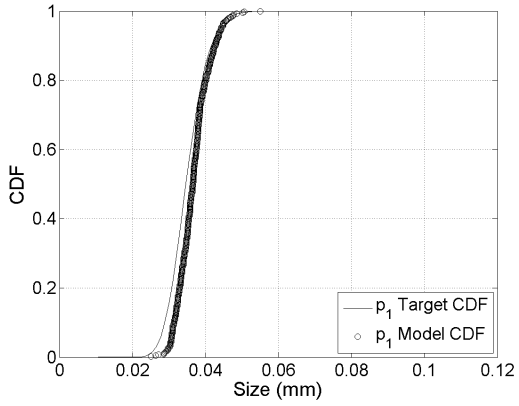

(c) Sturm *et al.* Mo-0.50Si SVE

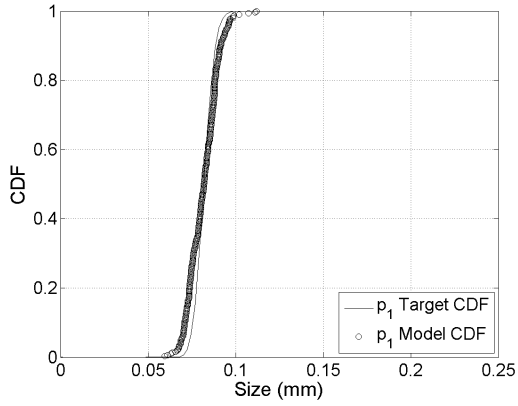

(d) Sturm *et al.* Mo-1.00Si SVE

Figure 4.19: Sturm *et al.* α-Mo SVE equivalent grain diameter distributions

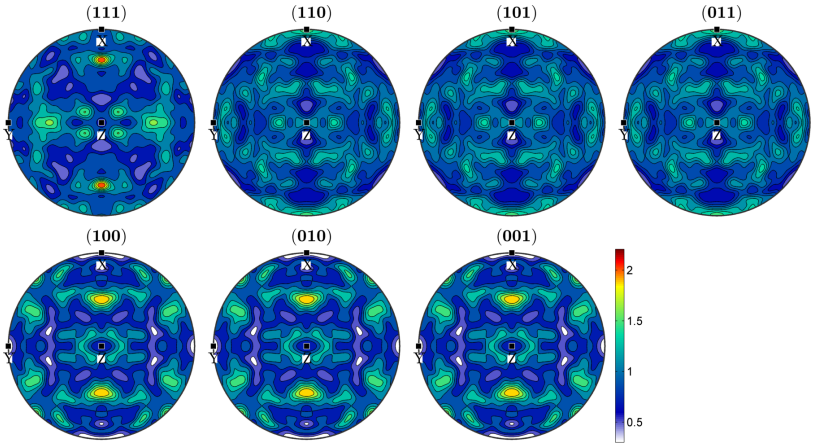

(a) Target texture

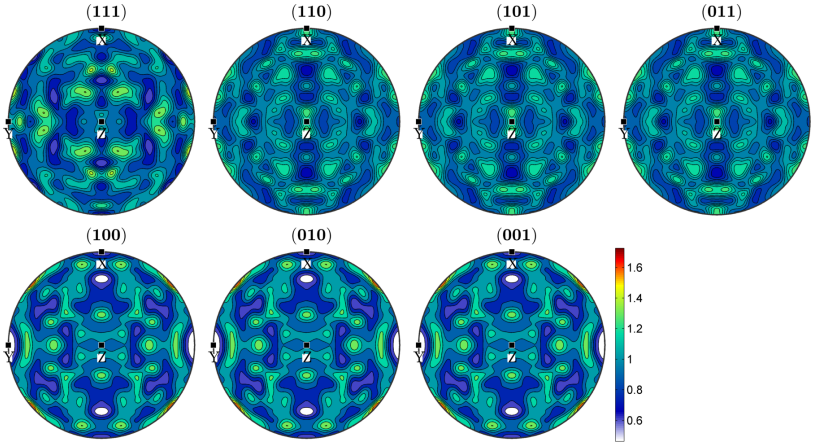

(b) Model Texture

Figure 4.20: Sturm *et al.* Mo-0.00Si synthetic microstructure texture comparison

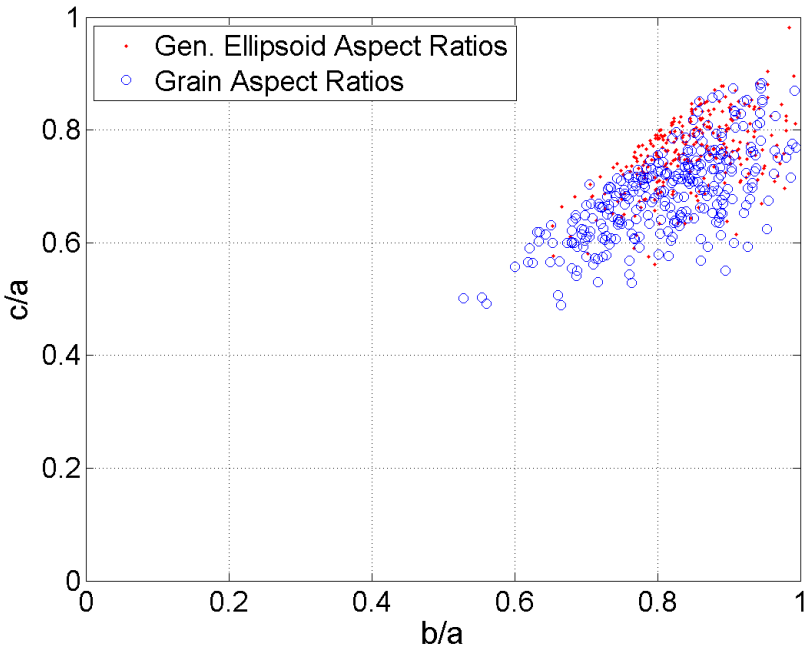

(a) Sturm *et al.* Mo-0.00Si SVE

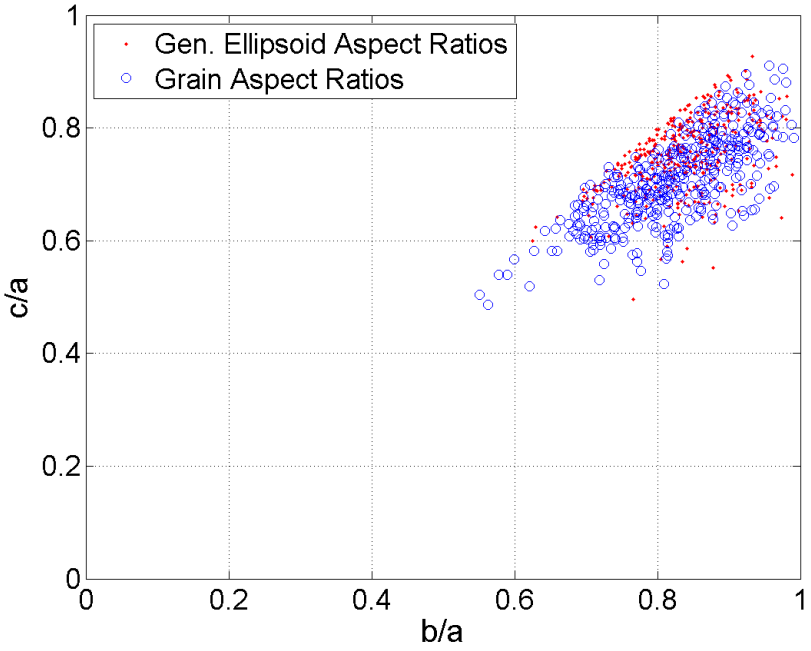

(b) Sturm *et al.* Mo-0.10Si SVE

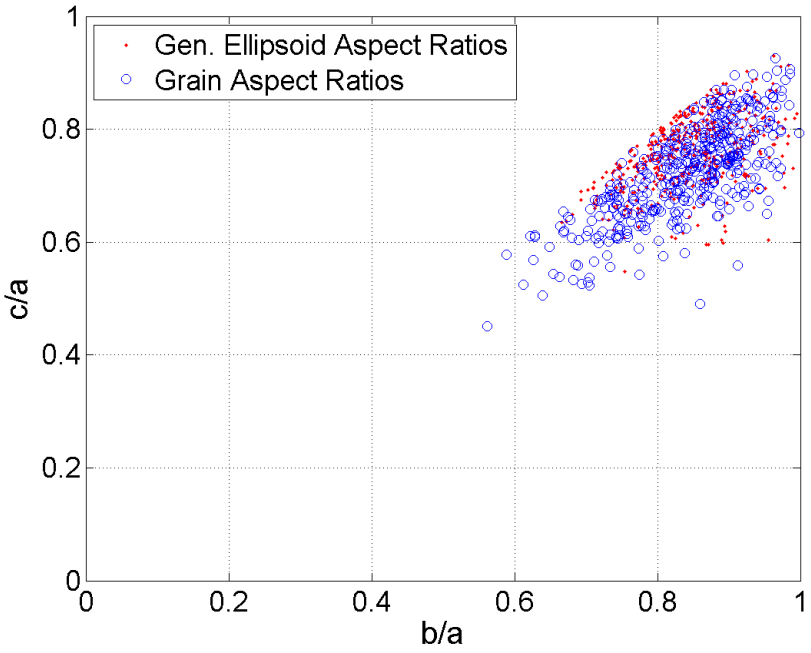

(c) Sturm *et al.* Mo-0.50Si SVE

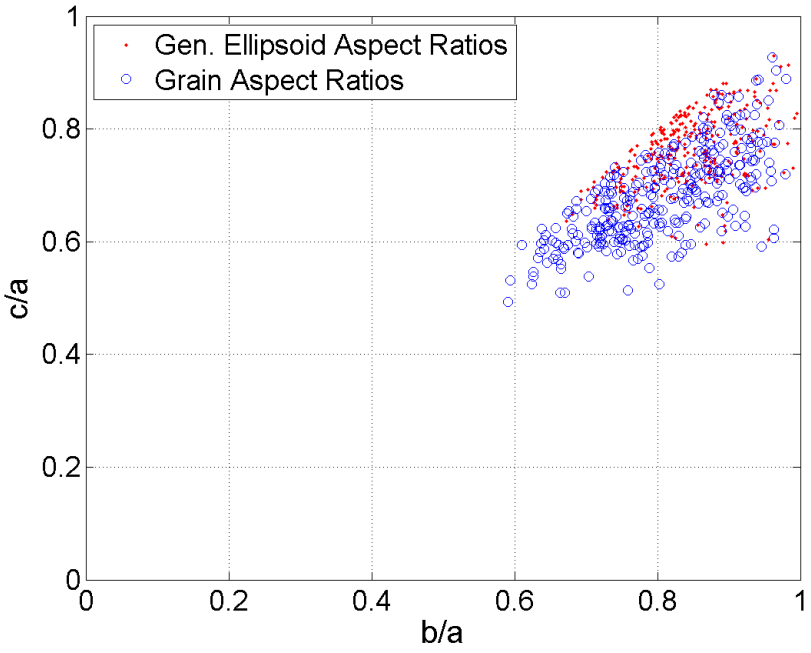

(d) Sturm *et al.* Mo-1.00Si SVE

Figure 4.21: Sturm *et al.* α-Mo SVE equivalent grain aspect ratio distributions

4.2.2 Triplex Mo-Si-B Material

The triplex Mo-Si-B material synthetic microstructure instantiations are randomly textured, three phase, single region volume elements with random spatial distribution of phases created with the same microstructure generator used to instantiate the arc-melted α-Mo volume elements. The parametric study varies two parameters: volume fraction of each phase and Si content of the α-Mo phase. The variation in Si content is achieved through the calibration of the constitutive model, but the volume fraction of each phase is captured explicitly in the volume element instantiations. For the triplex Mo-Si-B material in the parametric study, the volume fraction of α-Mo is varied from 0.45% to 80% and the remaining volume fraction is divided between the intermetallics at a constant ratio of 1:2 A15 to T2 phase. The volume element definitions for the parametric study are presented in Table 4.2. The first six volume element definitions explore variations in α-Mo volume fraction and the final two explore order of magnitude grain size changes at a fixed α-Mo volume fraction.

Following the reconstruction method previously presented for the arc-melted α-Mo SVEs, a normal distribution is used to create a distribution of grain aspect ratios. The resulting distribution of grain aspect ratios resembles those created from an incomplete beta distribution; however, the resulting aspect ratios are clustered around aspect ratios closer to spherical for a predominantly equiaxed microstructure. Table 4.2 presents the target equivalent grain parameters and aspect ratios for each phase.

When placing grains from multiple phases into a volume, the microstructure generator starts with the phase with the smallest mean equivalent grain diameter and proceeds with packing a single phase until the adjusted phase volume fraction is met before moving to the phase with the next largest mean grain diameter. The phase volume fraction is adjusted to account for changes in final phase volume fraction that occur during the final simulated annealing step. For the triplex microstructures of the parametric study, the intermetallic phases are placed first. The intermetallic phases

Table 4.2: Parametric study microstructure parameters

Parameter	**SVE1**	**SVE2**	**SVE3**	**SVE4**	**SVE5**	**SVE6**	**SVE7**	**SVE8**
Edge length $[mm]$	0.090	0.090	0.090	0.090	0.090	0.090	0.900	0.009
Number of elements per edge	33	33	33	33	33	33	33	33
Vv α-Mo	0.45	0.54	0.63	0.71	0.76	0.80	0.63	0.63
Vv A15	0.37	0.31	0.25	0.19	0.16	0.13	0.25	0.25
Vv T2	0.18	0.15	0.12	0.10	0.08	0.07	0.12	0.12
α-Mo mean dia. $[\mu m]$	10	10	10	10	10	10	100	1
α-Mo std. dev. dia. $[\mu m]$	2	2	2	2	2	2	20	0.02
A15 mean dia. $[\mu m]$	8	8	8	8	8	8	80	0.80
A15 std. dev. dia. $[\mu m]$	1	1	1	1	1	1	10	0.01
T2 mean dia. $[\mu m]$	8	8	8	8	8	8	80	0.80
T2 std. dev. dia. $[\mu m]$	1	1	1	1	1	1	10	0.01
α-Mo mean aspect ratio [-]	0.80	0.80	0.80	0.80	0.80	0.80	0.80	0.80
α-Mo std. dev. aspect ratio [-]	0.08	0.08	0.08	0.08	0.08	0.08	0.08	0.08
A15 mean aspect ratio [-]	0.80	0.80	0.80	0.80	0.80	0.80	0.80	0.80
A15 std. dev. aspect ratio [-]	0.08	0.08	0.08	0.08	0.08	0.08	0.08	0.08
T2 mean aspect ratio [-]	0.80	0.80	0.80	0.80	0.80	0.80	0.80	0.80
T2 std. dev. aspect ratio [-]	0.08	0.08	0.08	0.08	0.08	0.08	0.08	0.08

had the same equivalent grain diameter distribution parameters which are slightly smaller than the α-Mo mean equivalent grain diameter. As before, the mean and standard deviation are converted to a log normal distribution prior to generating the ellipsoids to be packed into the volume.

A second parametric study is conducted to explore the effects of mean grain diameter on the predicted properties at a set volume fraction and Si content. These SVEs are created from the same microstructural features, with the only variation found in the grain sizes. The mean and standard deviation of the equivalent grain diameters for the grain size parametric study are increased and decreased by one order of magnitude.

Before the parametric study volume elements can be created, an appropriate volume element size and mesh density must be chosen. For this work, the volume elements are required to be large enough to provide representative volume elements (RVE) for the mechanical properties of elastic modulus and yield strength. Volume elements sufficiently large enough to be considered representative for modelling microstructure sensitive fatigue crack formation and damage initiation are computationally intractable. Instead representative volume elements (RVE) for yield strength are considered statistical volume elements (SVE) for fatigue crack formation and damage initiation.

The SVE dimension variation can equally well be presented as a variation in the number of grains within the volume element. Just as all FE simulations are sensitive to the number of elements making up the model, microstructure sensitive FE simulations are sensitive to the number of grains within the model. With too few grains, individual grains may dominate the mechanical response. Consequently, a minimum bound on the number of grains and mesh density is set by the requirement that the volume averaged mechanical properties of elastic modulus and yield strength converge within the limits of the accuracy of the material calibration. An upper bound to the SVE

size and mesh refinement is determined by the time required to run a simulation and balanced against the convergence of the volume averaged properties of elastic modulus and yield strength. Convergence of these properties for the six instantiations at each volume fraction α-Mo is presented in Chapter 7 with the results of the parametric study.

Once the ellipsoidal packing algorithm parameters are determined that allow an acceptable match to the desired material characteristics for a particular volume element instantiation, six separate instantiations are created for each material definition in the parametric study. Example instantiations at each volume fraction of α-Mo are presented in Figures 4.22-4.27. The triplex Mo-Si-B SVEs are 0.09 mm on each edge with 33 elements per edge and range from 45% to 80% volume fraction α-Mo. The minimum and maximums number of elements per grain varies from instantiation to instantiation, but is near 20 and 400, respectively.

The number of grains per SVE also varies from instantiation. For the smallest volume fraction α-Mo, each instantiation had approximately 380 total grains, with around 110 grains of α-Mo, 80 grains of A15, and 190 grains of T2. For the largest volume fraction of α-Mo, each instantiation has approximately 300 total grains, with around 190 grain of α-Mo, 40 grains of A15, and 70 grains of T2.

While each instantiation matches the statistical description of the grain size, grain shape, grain shape orientation, and texture, individual instantiations exhibit locally varying microstructural features that may effect the mechanical properties. Specific features such as misorientation have been shown to be important for predicting fatigue response [57] and may be anticipated to effect damage initiation as well. The purpose of these multiple instantiations is to provide an idea for how much the mechanical properties are effected by the locally varying inhomogeneity of the microstructure.

Although some variation in the uncontrolled material characteristics is expected, it is possible that using a single instantiation algorithm may result in a relatively

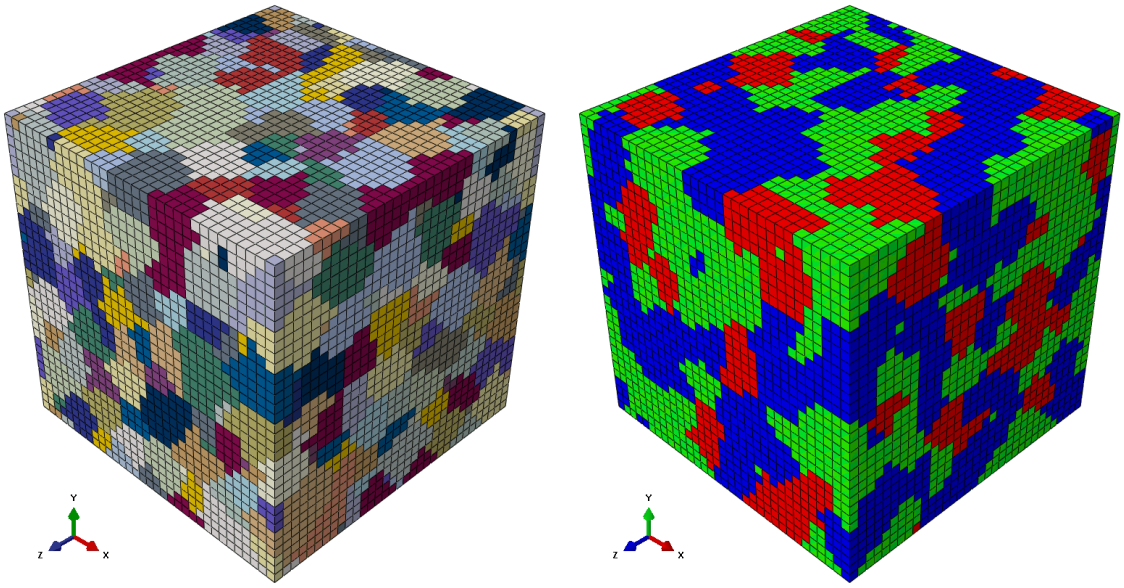

(a) Colors assigned by unique grains

(b) Colors assigned by phase. Blue: α-Mo. Green: A15. Red: T2.

Figure 4.22: Triplex Mo-Si-B synthetic microstructure with 45% volume fraction α-Mo.

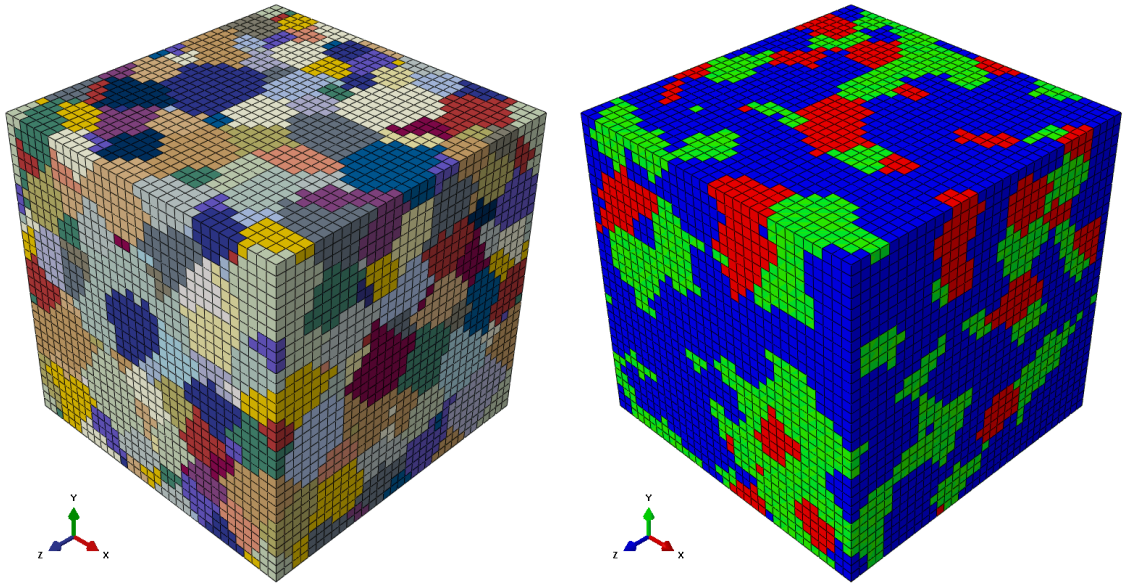

(a) Colors assigned by unique grains

(b) Colors assigned by phase. Blue: α-Mo. Green: A15. Red: T2.

Figure 4.23: Triplex Mo-Si-B synthetic microstructure with 54% volume fraction α-Mo.

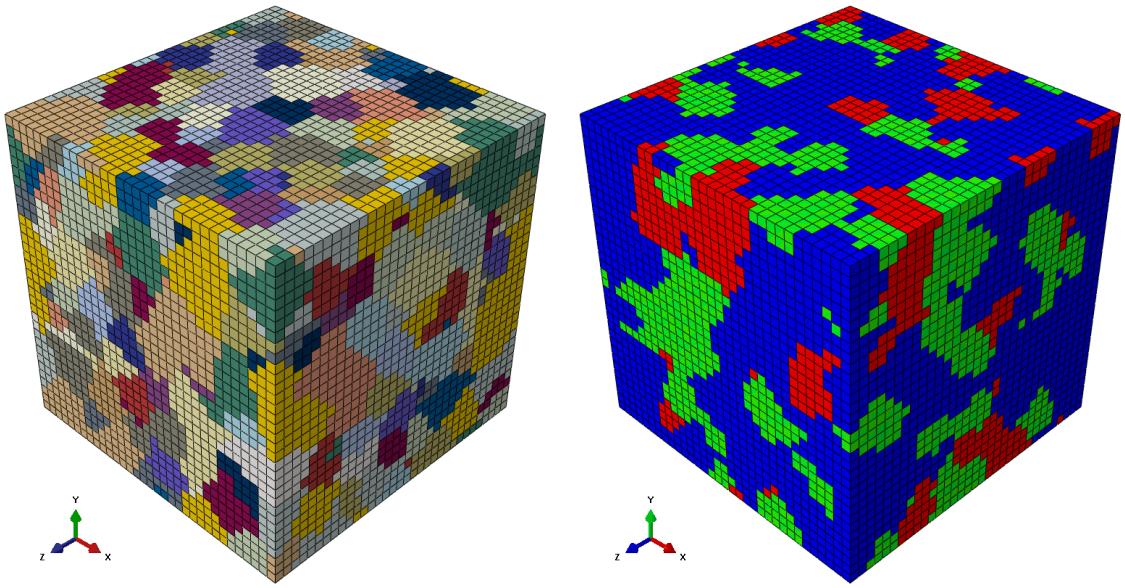

(a) Colors assigned by unique grains

(b) Colors assigned by phase. Blue: α-Mo. Green: A15. Red: T2.

Figure 4.24: Triplex Mo-Si-B synthetic microstructure with 63% volume fraction α-Mo.

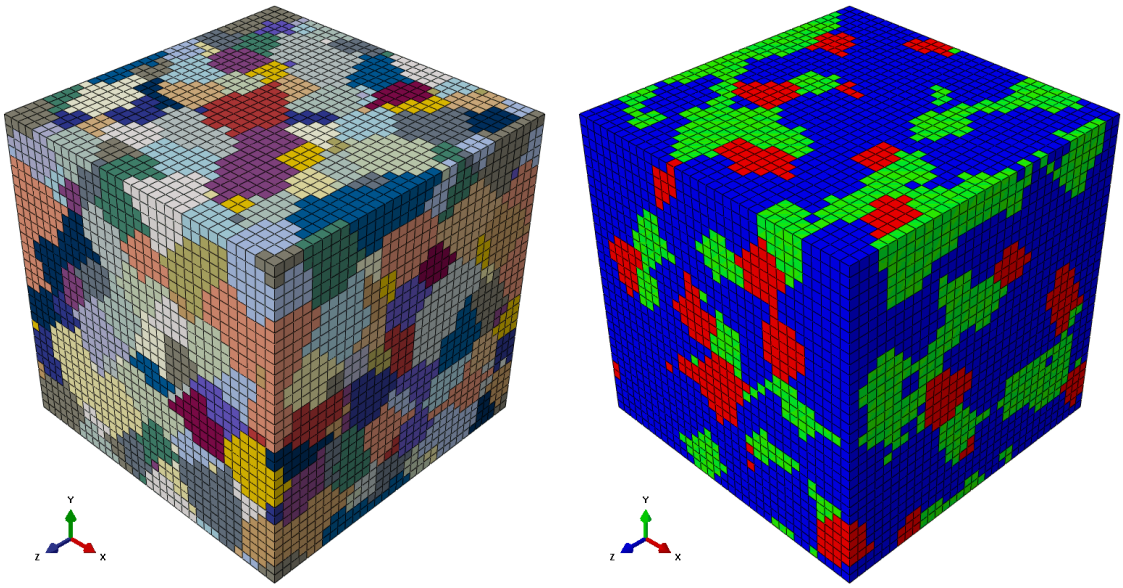

(a) Colors assigned by unique grains

(b) Colors assigned by phase. Blue: α-Mo. Green: A15. Red: T2.

Figure 4.25: Triplex Mo-Si-B synthetic microstructure with 71% volume fraction α-Mo.

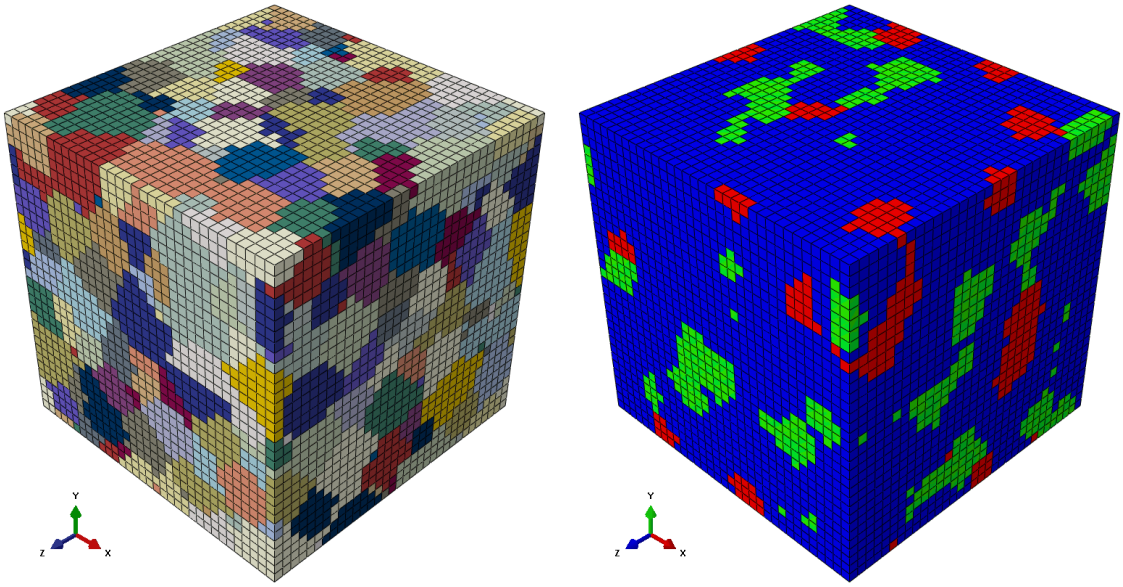

(a) Colors assigned by unique grains

(b) Colors assigned by phase. Blue: α-Mo. Green: A15. Red: T2.

Figure 4.26: Triplex Mo-Si-B synthetic microstructure with 76% volume fraction α-Mo.

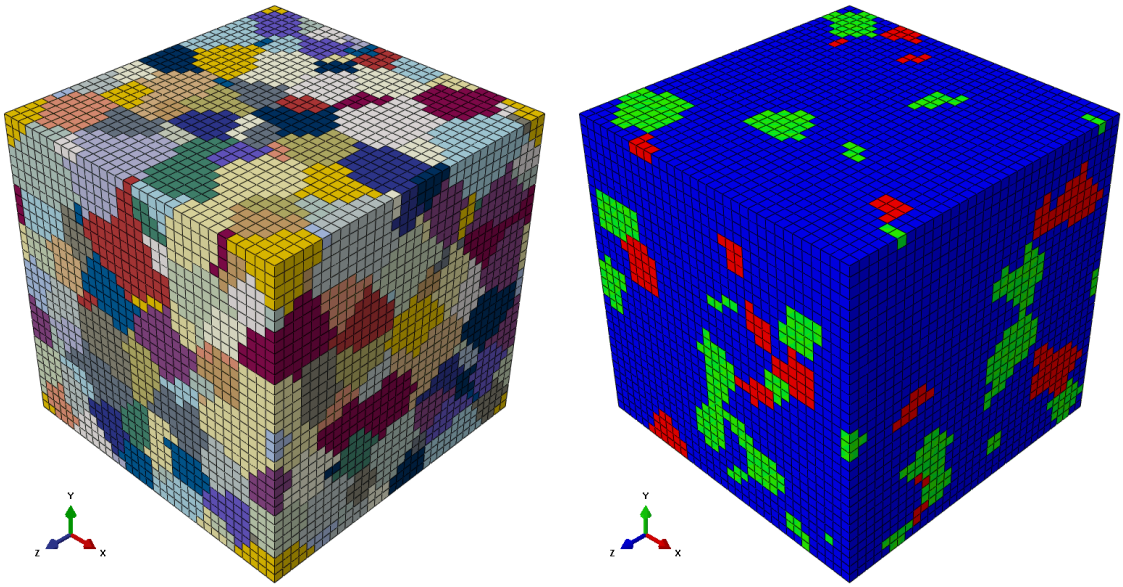

(a) Colors assigned by unique grains

(b) Colors assigned by phase. Blue: α-Mo. Green: A15. Red: T2.

Figure 4.27: Triplex Mo-Si-B synthetic microstructure with 80% volume fraction α-Mo.

narrow variation in these uncontrolled characteristics. For instance, in this work the ellipsoids are packed in order from largest to smallest for a single phase at a time; however, packing in the reverse order or by alternating phases may result in different second order spatial statistics. Re-creating microstructures in 3D is a complicated problem and research is ongoing into more sophisticated reconstruction techniques beyond ellipsoidal packing and Voronoi tesselation to better capture the 2^{nd} order spatial statistics [190–194]. These methods may allow for greater variation in the uncontrolled characteristics than the microstructure reconstructions in this work and result in even greater variation in predicted mechanical properties than is shown in Chapter 7.

A complete SVE study for fatigue requires several hundred instantiations, at a minimum, for each material definition under investigation. Given the broad scope of the material definitions in this work, such a detailed fatigue study must be left to future work of a targeted subset of microstructures. Instead, the general trends in fatigue response to large variations in microstructure are characterized with the understanding that a more complete fatigue study is required once a target microstructure is chosen.

It is recommended that such a study be coupled with a more complete calibration of the constitutive model, which requires additional experimentation and material characterization beyond that presented in this work. A complete set of recommended work required to conduct such a study is presented in Chapter 8.

4.3 Summary

A custom microstructure generator is created from an ellipsoidal packing algorithm [54] to address the microstructure inhomogeneity of the α-Mo material used in the experiments of this work. The microstructure generator explicitly accounts for grain size distribution, grain shape and grain shape orientation distributions, phase crystal

structure, and texture for up to three phases in two distinct regions of microstructure. A small convergence study balanced volume element size and mesh density against computational cost to ensure that the α-Mo and triplex Mo-Si-B SVE instantiations converged for elastic modulus and uniaxial yield strength. Volume elements are created corresponding to the material characterization of α-Mo material processed in two different ways and resulting in distinct microstructures in order to provide the most robust calibration of the α-Mo constitutive law.

Triplex Mo-Si-B volume elements are created for a range of α-Mo volume fractions with a random texture, grain size distribution, and grain shape and grain shape orientation distribution. Two additional volume elements with mean grain diameters an order of magnitude larger and smaller than the rest of the volume elements are created at 63% α-Mo volume fraction to study grain size effects on mechanical properties. The triplex Mo-Si-B volume elements required a finer mesh in order to properly capture the equivalent grain diameter distribution of three separate phases. Multiple instantiations at each α-Mo volume fraction are created to understand the effects of instantiation differences on predicted fatigue resistance and susceptibility to microcracking as well as verify converged elastic modulus and yield strength for the triplex Mo-Si-B simulations.

4.4 Significance

This chapter presented a custom microstructure generator created from an existing ellipsoidal packing algorithm with the addition of seamlessly meshing inhomogeneous microstructures containing distinct spatial boundaries. The development of such a microstructure generator is driven by the highly inhomogeneous microstructures of the arc-melted α-Mo material for the experiments of this work. The small number of grains and two region microstructure present in the experimental specimens has a significant impact on the measured stress-strain response and an accurate calibration

cannot be conducted without synthetic volume elements capturing these microstructural features.

CHAPTER V

CONSTITUTIVE MODELS

5.1 Introduction

This chapter focuses on the second tool in the microstructure-sensitive mechanical property modeling workflow, shown in Figure 5.1, and describes the calibration of the crystal viscoplastic flow rule for the α-Mo phase.

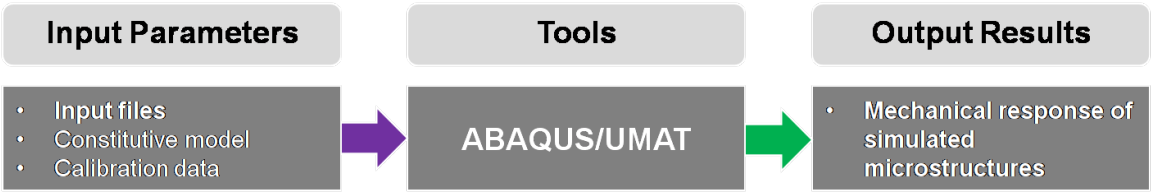

Figure 5.1: Microstructure-sensitive mechanical property modeling workflow: constitutive models

5.2 Crystal-Viscoplasticity

One general crystal viscoplastic model is used for each phase of the triplex Mo-Si-B with different calibration parameter sets representing each phase. The model includes the fully anisotropic elasticity tensors, the crystal slip systems, the flow rule, and evolution equations. The hard, brittle, intermetallic phases are treated as purely elastic, while the relatively ductile α-Mo phase is treated with a full crystal-viscoplasticity (CVP) flow rule over the 12 $\{100\}\langle 111\rangle$ and 12 $\{112\}\langle 111\rangle$ BCC slip systems. The option to build upon this work by including the possibility of plasticity in the intermetallic phases is maintained by using the full CVP flow rule for these phases, but assigning the calibration parameters in such a way that plasticity is inactive.

The flow rule for this work is based on the general flow rule represented as

$$\dot{\gamma}^{\alpha} = \dot{\gamma}_0 \left\langle \frac{|\tau^{\alpha} - \chi^{\alpha}| - \kappa^{\alpha}}{D^{\alpha}} \right\rangle^{\frac{1}{m}} sgn\left(\tau^{\alpha} - \chi^{\alpha}\right) \tag{5.1}$$

where α is a slip system index, $\dot{\gamma}^{\alpha}$ is the inelastic shear strain rate on the α^{th} slip system, $\dot{\gamma}$ is the reference inelastic shearing rate, τ^{α} is the resolved shear stress on the α^{th} slip system, and χ^{α}, κ^{α}, and D^{α} are the current values of back stress, threshold stress, and drag stress on the α^{th} slip system, respectively. The $\langle\rangle$ brackets are MacCauly brackets and $sgn\left(\right)$ returns positive or negative unity, depending on the sign of the term in parentheses. The variable m in the exponent is the strain rate sensitivity exponent. Both $\dot{\gamma_0}$ and m are material parameters that are typically treated as constants, but can vary with microstructure and temperature in theory.

Generally speaking, back stress, threshold stress, and drag stress may all evolve over the course of loading. Depending on the material under consideration, many different types of equations have been used for the evolution of back stress, threshold stress, and drag stress. For back stress and drag stress, the most common evolution equations follow the direct hardening, dynamic recovery form of the Armstrong-Frederick equations [195].

For the α-Mo phase, the drag stress is treated as a non-evolving constant dependent on temperature and Si content and back stress evolves as

$$\dot{\chi^{\alpha}} = B\dot{\gamma^{\alpha}} - C\chi^{\alpha}\left|\dot{\gamma^{\alpha}}\right| \tag{5.2}$$

where B and C are functions of temperature and Si content. The reference inelastic shearing rate $\dot{\gamma_0}$ is also a function of temperature and Si content and the strain rate sensitivity exponent m is a function of Si content. The threshold stress κ^{α} could also be an evolving function of temperature, Si content, and grain size; however, this parameter is not used due to the limited information available for calibrating the model.

Instead the drag stress parameter is used to calibrate the yield strength as a function of temperature and Si content, the strain rate sensitivity exponent is used to account for differences in yield strength as a function of strain rate, and back stress evolution is used to calibrate the plastic hardening after yield. Since no single crystal information is available for the α-Mo phase to individually calibrate each slip system, all 24 slip systems previously mentioned are treated equally; however, the model implementation retains the option of treating up to three separate types of slip systems with unique calibrations and can be extended to treat each system individually.

Because the stress-strain information available on this material is limited to monotonic uniaxial compression and tension tests, no calibration can be made for the cyclic response. Instead, it is assumed that the material is cyclically stable and the stabilized hysteresis curve is obtained from the monotonic calibration. This amounts to assuming that there is no cyclic hardening or softening of the material when modeling fatigue.

The constitutive equation is implemented as a User Material subroutine (UMAT) for the general purpose finite element code ABAQUS [196]. The specific Fortran code used in this work is a derivative of one for γ-TiAl alloys [197] and has been modified for Mo-Si-B alloys by adding the appropriate slip systems, evolution equations, the evolution equation derivatives, and temperature dependence for the elastic and thermal properties.

5.3 Elastic and Thermal Properties

The fully anisotropic elasticity tensors and coefficient of thermal expansion for each phase are obtained from literature data [21–23]. The elasticity tensor components for Mo are shown in Figure 5.2. The elasticity tensor is known from room temperature to 700°C [21]. In order to use the constitutive model at higher temperatures, this

data is fit with a linear regression and extrapolated to 1400°C. Although the majority of the parametric study is for Mo with Si in solid solution, it has been shown that the addition of Si has very little effect of the elastic modulus [38]. Consequently, the assumption that the elastic and thermal properties of α-Mo are constant with respect to Si content is reasonable.

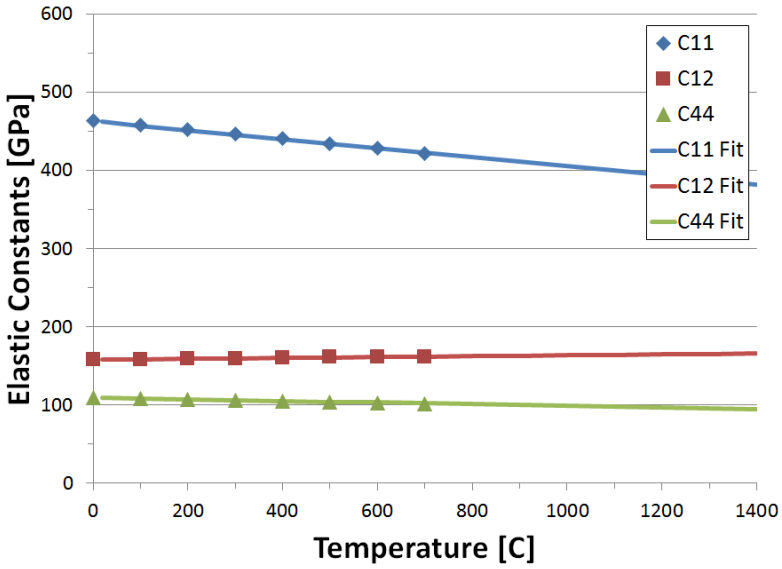

Figure 5.2: α-Mo anisotropic elasticity tensor components as a function of temperature. Data points from reference [21]. Lines represent the linear regression and extrapolation.

The elasticity tensor components for the T2 phase are shown as a function of temperature up to 1100°C in Figure 5.3 [23]. The elasticity tensor is similarly fit with a linear regression and extrapolated to higher temperatures for this phase.

The elasticity tensor components for the A15 phase are shown at room temperature in Figure 5.4 [22]. The elasticity tensor components for this phase are only known at room temperature. Instead of an extrapolation based on a linear regression, the slope of the linear regression for the elasticity tensor components of the BCC Mo data is used to extrapolate the cubic A15 elasticity tensor components to higher temperatures.

One of the benefits of the intermetallics in this Mo-Si-B material is that their

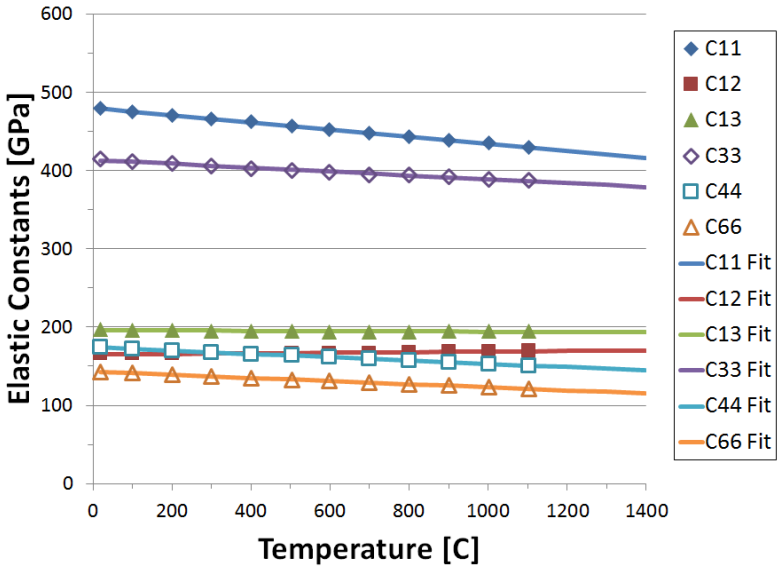

Figure 5.3: T2 anisotropic elasticity tensor components as a function of temperature. Data points from reference [23]. Lines represent the linear regression and extrapolation.

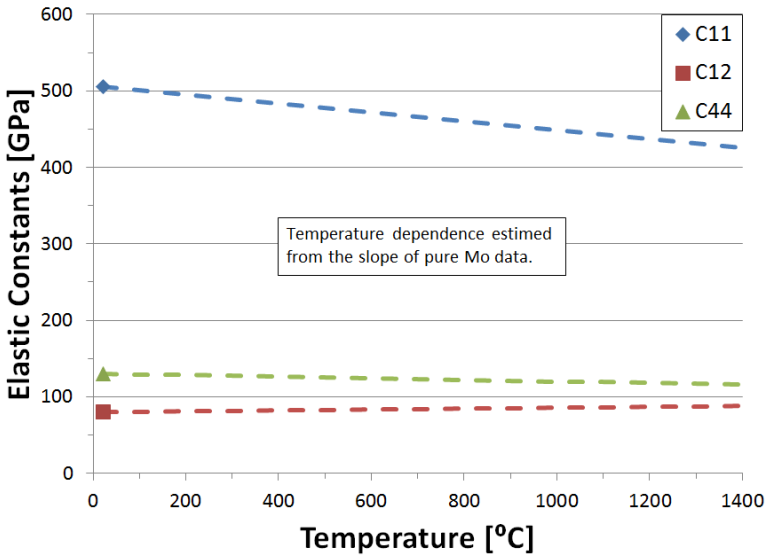

Figure 5.4: A15 anisotropic elasticity tensor components at room temperature and their estimated functions of temperature. Data points from reference [22]. Lines represent the linear regression and extrapolation.

coefficients of thermal expansion are close to the coefficient of thermal expansion of α-Mo, which minimizes stresses caused by thermal strain mismatch. The coefficients of thermal expansion are found in literature, and reproduced in Figure 5.5 [25].

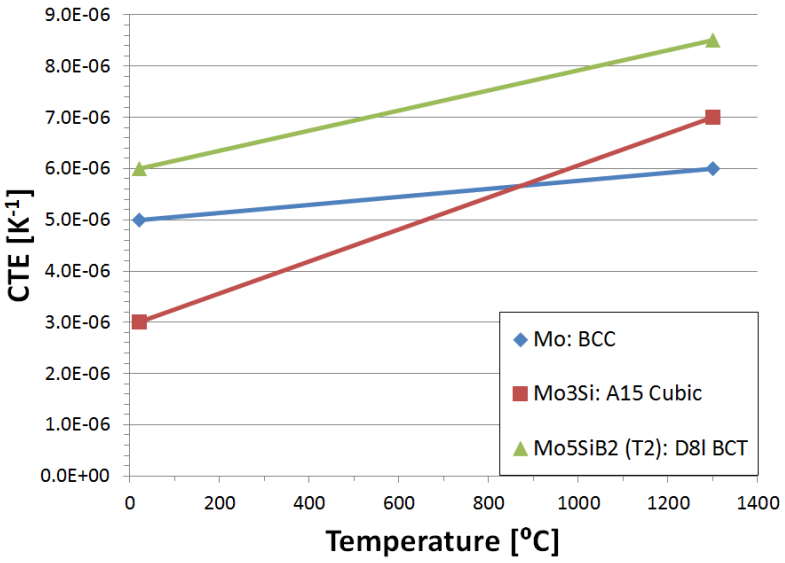

Figure 5.5: Coefficient of thermal expansion as a function of temperature and phase. Data points from reference [25]. Lines represent the linear regression used to calculate CTE at different temperatures in this work.

5.4 Viscoplastic Property Calibration: α-Mo

Compression test specimens cut from the arc-melted α-Mo buttons were conducted by Pittsburgh Materials Technology to calibrate the constitutive model at multiple temperatures and strain rates for each Si content ranging from pure Mo to Mo with 1.16 wt.% Si in solid solution. Tests were conducted at two strain rates approximately two orders of magnitude apart, $1.66 \times 10^{-4}\left[\frac{\mathbf{1}}{\mathbf{s}}\right]$ and $2.77 \times 10^{-2}\left[\frac{\mathbf{1}}{\mathbf{s}}\right]$, at room temperature, 600°C, 1100°C, and 1400°C. Molybdenum oxidizes readily above 600°C [8], so all tests above room temperature were conducted in a vacuum. The full test schedule is shown in Table 5.1. There was insufficient material for duplicate test specimens, so a single test was conducted for each point in the test schedule.

The test specimens were cut as rectangular prisms with dimensions that varied between specimens but was nominally 0.20 in width and 0.30 inches tall. The full measurements for each specimen were recorded before and after testing. Specimens were compressed between two platens and the axial force and cross-head displacement were measured throughout the test. It was not possible to directly measure the

Table 5.1: Compression experiments on α-Mo for each x.xx wt.% Si: 0.00, 0.29, 0.40, 0.58, 1.16.

Strain Rate $[\frac{1}{s}]$	**Temperature** [°C]			
	25	600	1100	1400
2.77×10^{-2}	Mo-x.xxSi	Mo-x.xxSi	Mo-x.xxSi	Mo-x.xxSi
1.66×10^{-4}	Mo-x.xxSi	Mo-x.xxSi	Mo-x.xxSi	Mo-x.xxSi

strain of the gage section due to the difficulty of performing strain measurements at high temperatures in a vacuum. The high strength of the Mo-1.16Si (wt.%) samples broke a test fixture and required a special high strength fixture, especially at room temperature. Consequently, the compression tests were not conducted to specimen failure, but were stopped after yield was obtained. These testing difficulties combined with the very coarse grained, heterogeneous microstructure, made re-constructing reliable engineering stress-strain curves very difficult.

Two methods for separating the machine compliance from the specimen gage section deformation are attempted. First, the machine compliance is calculated from the difference between the measured displacement and the difference between the initial and final gage length of the specimen. However, this method yielded inconsistent results for machine compliance. The second method involved estimating the specimen modulus from the synthetic volume elements and the anisotropic, temperature dependent elasticity tensors presented earlier in Figure 5.2 [21]. The estimated elastic modulus was subtracted from the elastic portion of the load-displacement data to determine the machine compliance. Once the machine compliance was known, it was subtracted from the total load-displacement data to obtain the engineering stress-strain curve. The resulting engineering stress-strain curves are shown in Figures 5.6-5.10.

The yield strength plots are compared to results by Sturm *et al.* [38] in Figures 5.11 and 5.12. These plots show that the arc-melted material captures the expected

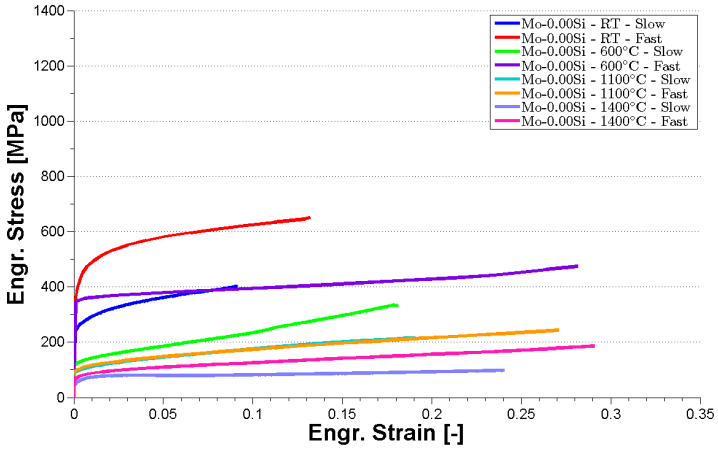

Figure 5.6: Engineering stress-strain curve for Mo-0.00Si experiments.

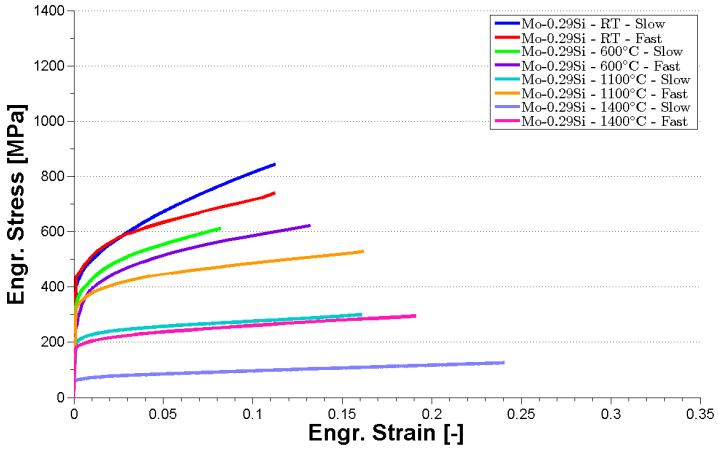

Figure 5.7: Engineering stress-strain curve for Mo-0.29Si experiments.

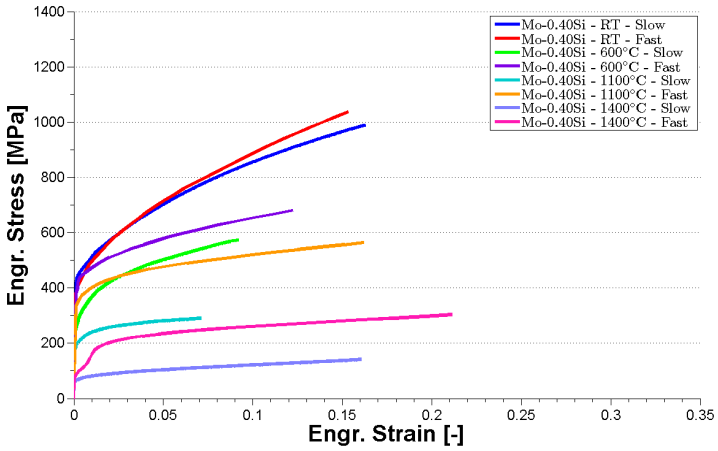

Figure 5.8: Engineering stress-strain curve for Mo-0.40Si experiments.

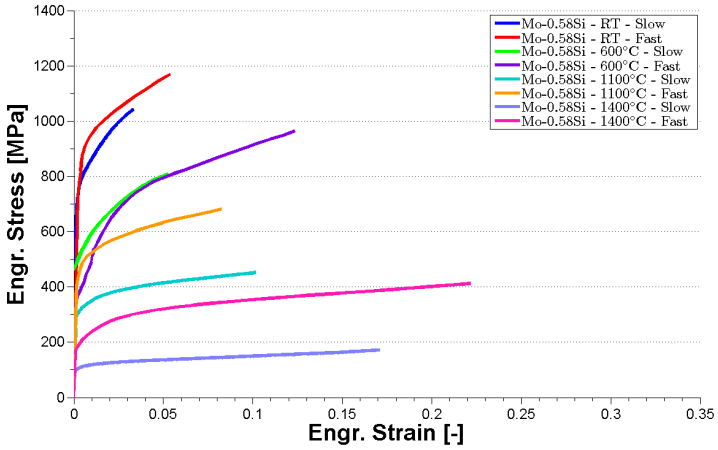

Figure 5.9: Engineering stress-strain curve for Mo-0.58Si experiments.

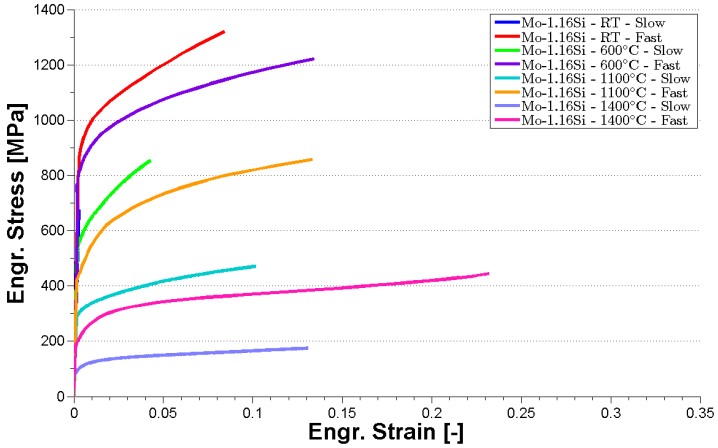

Figure 5.10: Engineering stress-strain curve for Mo-1.16Si experiments.

general trends of increasing strength with strain rate and decreasing strength with temperature. However, some of the α-Mo calibration data from this work shows increasing strength with temperature, as in the Mo-0.29Si data at 600 and 1100°C and the fast strain rate in Figure 5.12. It is hypothesized that this is a result of the highly heterogeneous and sparsely populated microstructure of the experimental specimens. Although the volume elements captured the characteristics of the two region microstructures with the intention of addressing these problems in the calibration, the sparse number of total grains in the test specimens would require direct modeling of

the microstructure in individual test specimens to capture the effects of microstructure on yield strength. Consequently, the yield strength is ultimately calculated from the Sturm *et al.* data of a material with finer, equiaxed grains and random texture. Separate volume elements matching the Sturm *et al.* material are created to perform this calibration. The resulting yield strength calibration is presented in Figure 5.13.

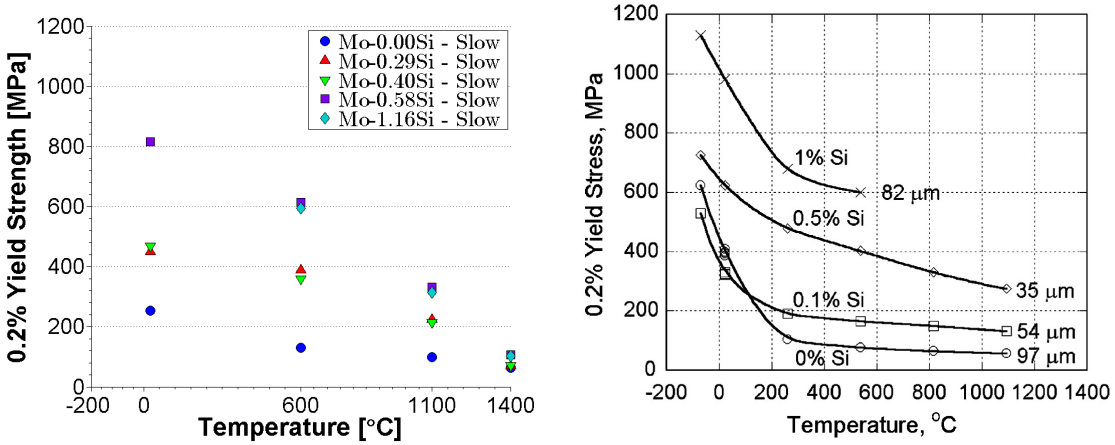

(a) Experimental results from arc-melted α-Mo material with a strain rate of $1.66 \times 10^{-4}\left[\frac{1}{s}\right]$

(b) Experimental results at a strain rate of $2.20 \times 10^{-3}\left[\frac{1}{s}\right]$ [38]

Figure 5.11: Calibration material yield strength as a function of temperature at the slow strain rate in comparison to Sturm *et al.* data [38]

The strain rate sensitivity and plastic hardening is calibrated from the experiments of this work. To calibrate strain rate sensitivity, the inelastic strain rate and stress is plotted from the yield point. At each temperature and Si content, a power law can be fit to the data and the exponent of this fit is the strain rate sensitivity exponent. Figures 5.14-5.18 present the strain rate sensitivity exponent calibration plots for a 0.2% offset yield strength. Because of the variability in the yield strength data, some of the yield strengths from the fast strain rate tests are actually lower than low strain rate tests. Consequently the exponent of the power law is negative, which is an unrealistic result contradictory to the mechanisms driving strain rate sensitivity. Expected values for a strain rate sensitive material are around 5-8, while a strain rate insensitive material response results in a strain rate sensitivity exponent of 20 or

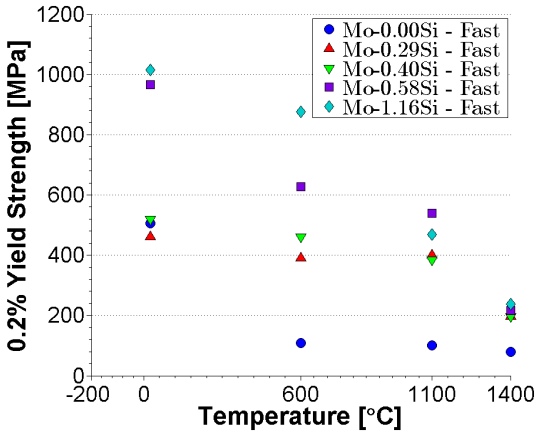

(a) Experimental results from calibration material with a strain rate of $2.77 \times 10^{-2}\left[\frac{1}{s}\right]$

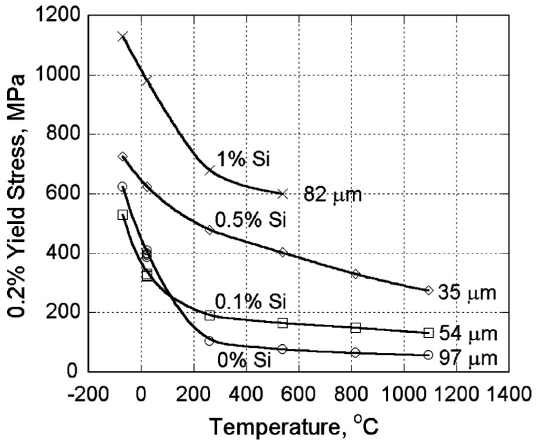

(b) Literature experimental results at a strain rate of $2.20 \times 10^{-3}\left[\frac{1}{s}\right]$

Figure 5.12: Calibration material yield strength as a function of temperature at the fast strain rate in comparison to Sturm *et al.* data [38]

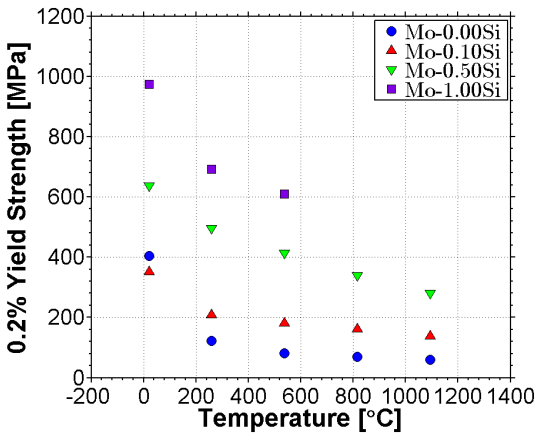

(a) Yield strength calibration to Sturm *et al.* data results.

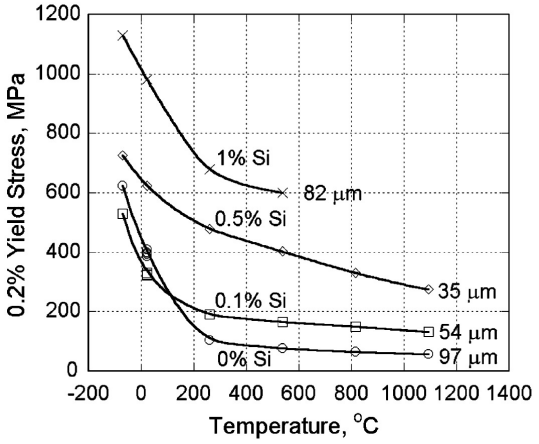

(b) Sturm *et al.* experimental results at a strain rate of $2.20 \times 10^{-3}\left[\frac{1}{s}\right]$

Figure 5.13: Yield strength calibration results as a function of temperature in comparison to the Sturm *et al.* data used to make the calibration [38]

higher, with some studies reporting values as large as 70 [93].

To address the inconsistencies of the experimental data, the strain rate sensitivity exponent is separated into two calibrations: one for the pure Mo material (Mo-0.00Si) and another for the Mo with Si in solid solution. This is a natural result of the experimental data from this work, and corresponds to the changing dislocation mobilities

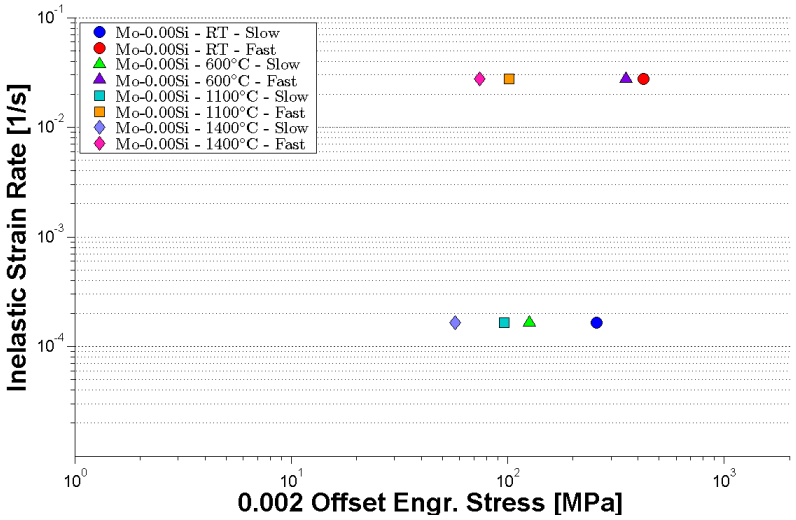

Figure 5.14: Strain rate sensitivity calibration plot of inelastic strain rate vs. 0.2% offset yield stress as a function of temperature for Mo-0.00Si

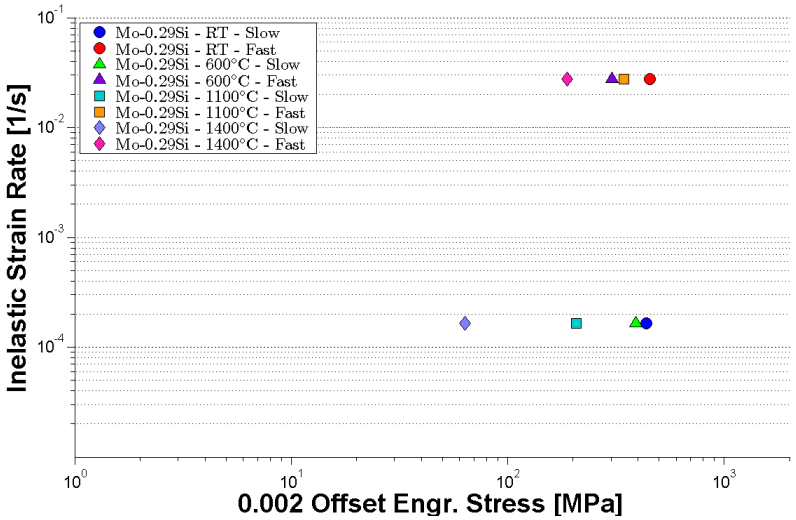

Figure 5.15: Strain rate sensitivity calibration plot of inelastic strain rate vs. 0.2% offset yield stress as a function of temperature for Mo-0.29Si

of Mo with any addition of Si in solid solution discussed in Chapter 2. The inconsistency in experimental yield strength as a function of strain rate meant that a reliable calibration of strain rate sensitivity could not be made from any single offset yield strength calculation. Instead, a power law is fit to 0.02%, 0.2%, and 2% offset strength calculation and the calibration is chosen from a mix of the average results and engineering judgment with respect to the expected trends. An example of the

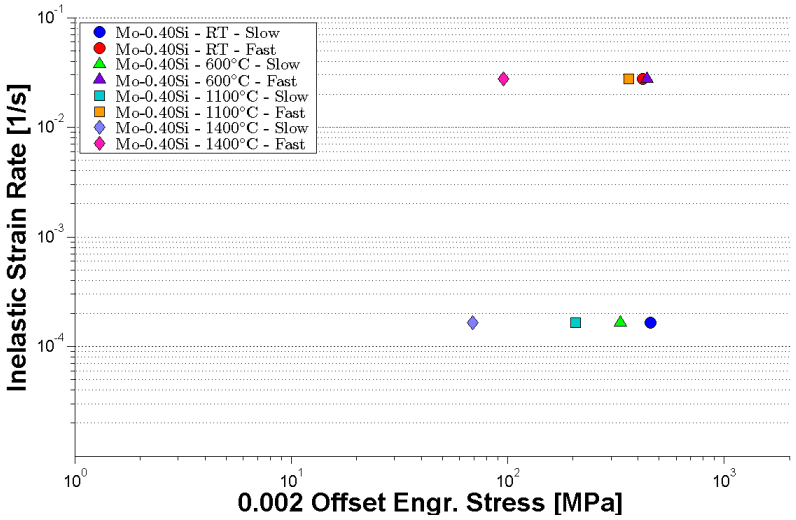

Figure 5.16: Strain rate sensitivity calibration plot of inelastic strain rate vs. 0.2% offset yield stress as a function of temperature for Mo-0.40Si

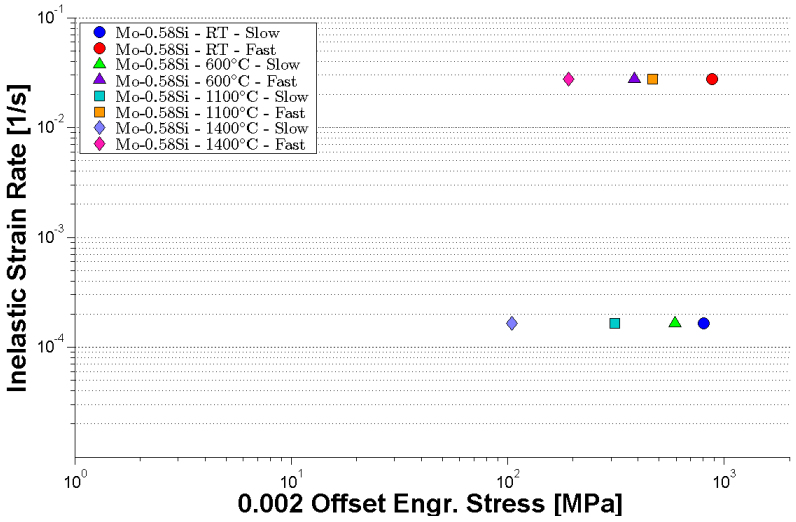

Figure 5.17: Strain rate sensitivity calibration plot of inelastic strain vs. 0.2% offset yield stress as a function of temperature for Mo-0.58Si

power law fit is shown in Figure 5.19 for Mo-0.40Si with a 0.2% offset yield strength, which is one of the best examples from the experiments in this work of the expected trends in strain rate sensitivity as a function of temperature. The final calibration of the strain rate sensitivity exponent as a function of Si content and temperature is presented in Table 5.4.

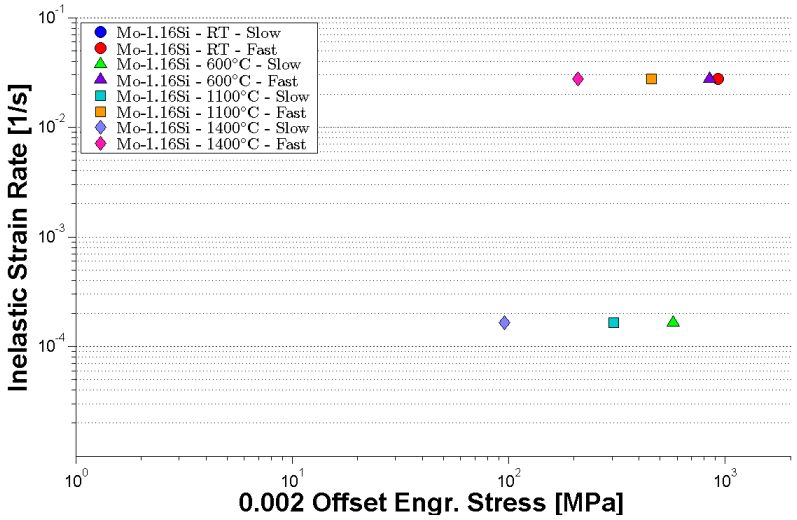

Figure 5.18: Strain rate sensitivity calibration plot of inelastic strain rate vs. 0.2% offset yield stress as a function of temperature for Mo-1.16Si

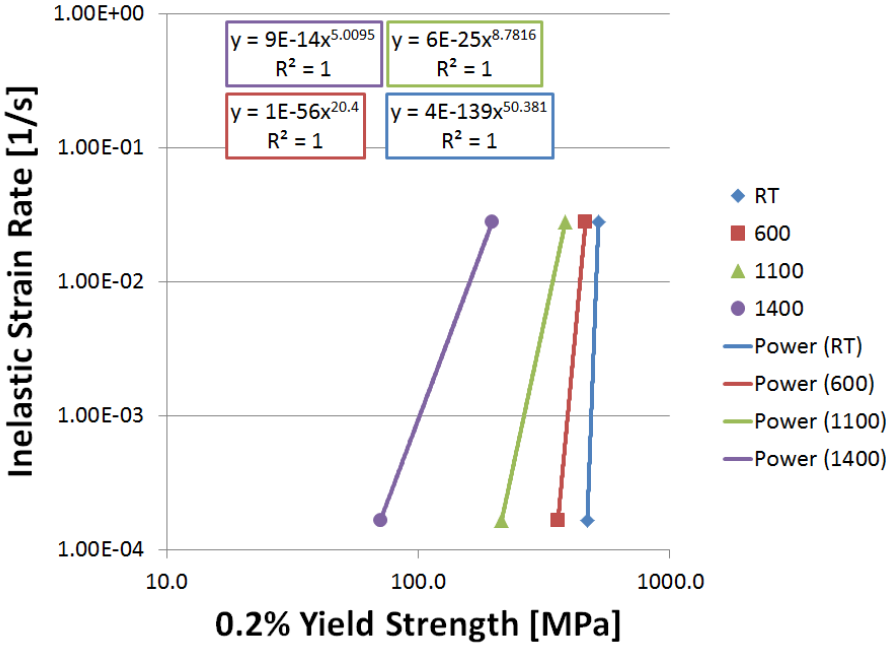

Figure 5.19: Strain rate sensitivity calibration plot of inelastic strain rate vs. stress as a function of temperature for Mo-0.40Si including power law fits to data

After calibrating the strain rate sensitivity exponent, the yield strength is calibrated through the initial drag stress, D_0. With the limited information available, yield strength is assumed to be a function of the initial drag stress alone and each slip

system is treated identically. Consequently, a maximum of three simulations are required to complete the calibration of initial drag stress. A first estimate of initial drag stress can be made from prior work using a similar constitutive model on materials with similar yield strengths or from a sensitivity study on the influence of parameters on the predicted material response of the constitutive model. The second estimate of initial drag stress can be made from the aforementioned sensitivity study, or by assuming a linear scaling between the initial drag stress and yield strength. Finally, the initial drag stress can be calculated from linearly interpolation as a function of the first and second simulation predictions of yield strength as

$$D_0^f = \left(D_0^2 - D_0^1\right) \frac{(\sigma_Y - \sigma_Y^1)}{(\sigma_Y^2 - \sigma_Y^1)} + D_0^1 \tag{5.3}$$

where D_0^f is the final initial drag stress calibration, σ_Y is the experimentally determined yield strength, D_0^1 and D_0^2 are the first and second estimates of initial yield strength, and σ_Y^1 and σ_Y^2 are the simulation predictions of yield strength corresponding to the first and second estimates of initial yield strength, respectively. Better calibrations could be made as a function of slip system or slip system type or family if single crystal stress-strain data is available.

After calibrating the initial drag stress, the evolution parameters for back stress are calibrated. To make a complete calibration with drag stress evolution, back stress evolution, and threshold stress evolution, a full set of fatigue experiments are required and must include the cyclic hardening or softening of the resultant cyclic stress-strain behavior in addition to the stabilized cyclic response. With limited information available it is assumed that the material is cyclically stable and that isotropic hardening is negligible so cyclic behavior can be determined from the monotonic stress-strain behavior. Therefore, back stress evolution is assumed to be the only set of parameters affecting the plastic hardening, and can be calibrated almost directly. Linear interpolation no longer works, but only a small number of simulations are required for a reasonable fit if a sensitivity study has been conducted on the variation in plastic

hardening with a variation in the back stress parameters. A quantitative fit may require additional iteration or a more sophisticated approach using a fitting function or surrogate models.

Ideally, the plastic hardening could be calibrated quantitatively from a series of points along the stress-strain curve at one strain rate, for instance at the 0.2% and 2% offset strengths, and the calibration would be validated by matching the curves of the second strain rate. The separate direct hardening and dynamic recovery terms can be calibrated iteratively by requiring a calibration both to early hardening behavior and the later linear hardening behavior. The direct hardening term determines the initial slope of early plastic hardening, while the dynamic recovery term determines how quickly the plastic hardening saturates, ultimately limiting additional plasticity to perfectly plastic behavior. However, due to the separate calibration of the yield strength and the large variation in apparent strain rate sensitivity, the calibration is conducted by fixing the dynamic recovery coefficient, C, at 10.0 for all Si contents and temperatures and varying the direct hardening parameter, B, until a reasonable fit of hardening slope could be made for the slow strain rates at strains up to 3%. Because the calibration is only performed up to 3% strain, the engineering stress-strain plot is sufficiently accurate for this calibration. The final calibration plots for plastic hardening are presented in Figures 5.20-5.24.

After the final calibration, the resulting plastic hardening is simulated with the Sturm *et al.* volume elements and compared to the experimental results from Sturm *et al.* as shown in Figure 5.25. Given the extreme differences in microstructure and the number of assumptions involved in calibrating the flow rule, the resulting similarity in the plastic hardening calibration and the plastic hardening seen in the Sturm *et al.* experimental results is reasonable.

The material parameters are presented in Tables 5.2-5.4. Linear interpolation is required to mesh the calibration parameters for each set of calibration simulations

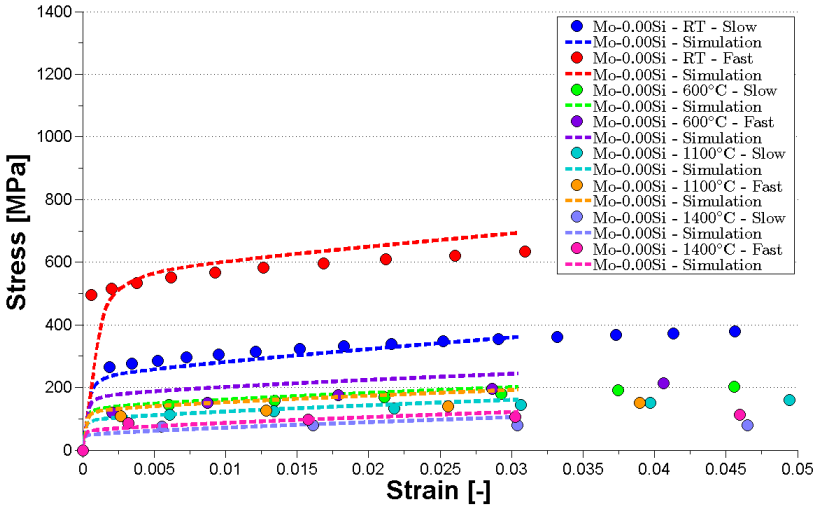

Figure 5.20: Plastic hardening calibration plot for Mo-0.00Si

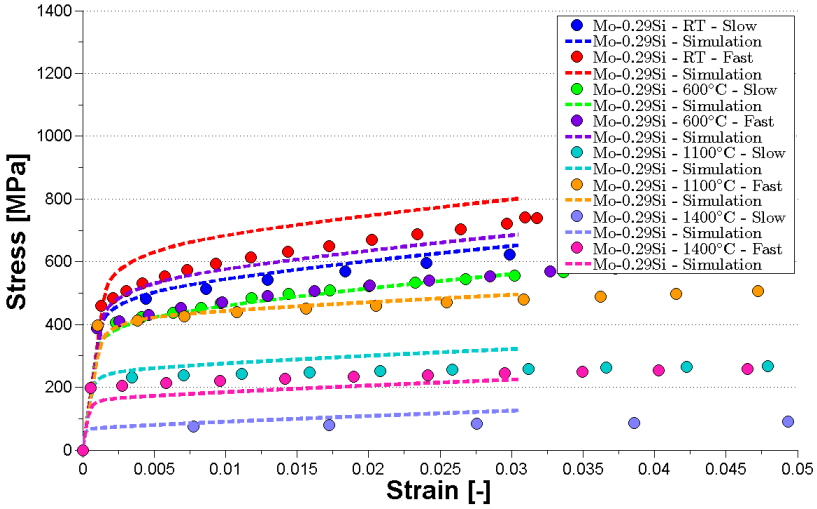

Figure 5.21: Plastic hardening calibration plot for Mo-0.29Si

which correspond to the experiments of this work and those of Sturm *et al.*. Linear interpolation is first carried out by temperature, and then by Si content, except for the initial drag stress, D_0, at 1400°C where it is found that a power law made a better fit than a linear regression as a function of temperature at fixed Si content.

The values in bold are calibrated to the specific Si content and temperature, while the rest are values that are interpolated from nearby calibration points. The values

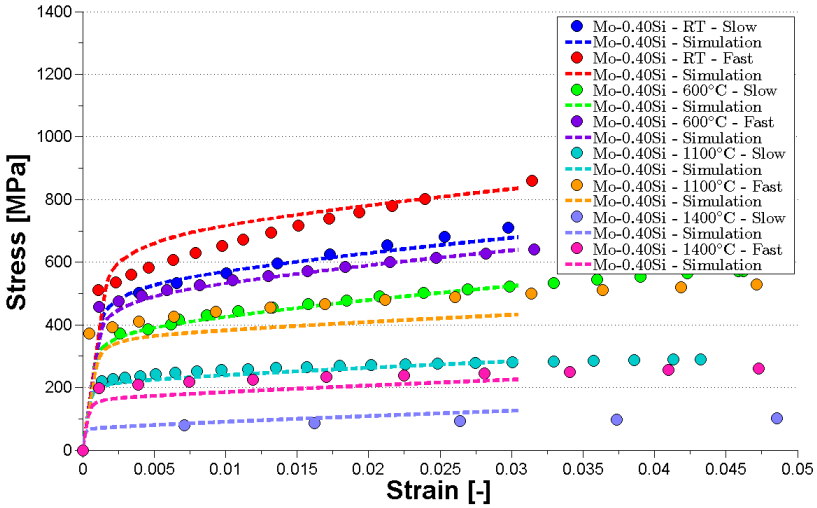

Figure 5.22: Plastic hardening calibration plot for Mo-0.40Si

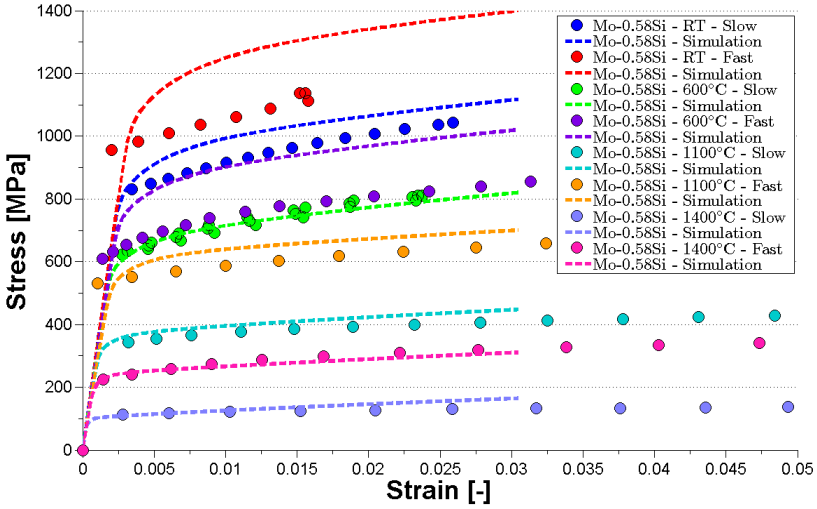

Figure 5.23: Plastic hardening calibration plot for Mo-0.58Si

in italics are calculated for use in the final triplex Mo-Si-B microstructure simulations. Missing values are never calculated, either because they are not included in the calibration simulations or because they are not needed for the target material calibrations. For linear interpolation with a Si content below Mo-0.29Si material, the calibration is extrapolated from the Mo-0.29Si and Mo-0.40Si instead of interpolating between Mo-0.00Si and Mo-0.29Si. As discussed in Chapter 2, this is necessary because the material response of pure Mo is significantly different from the response

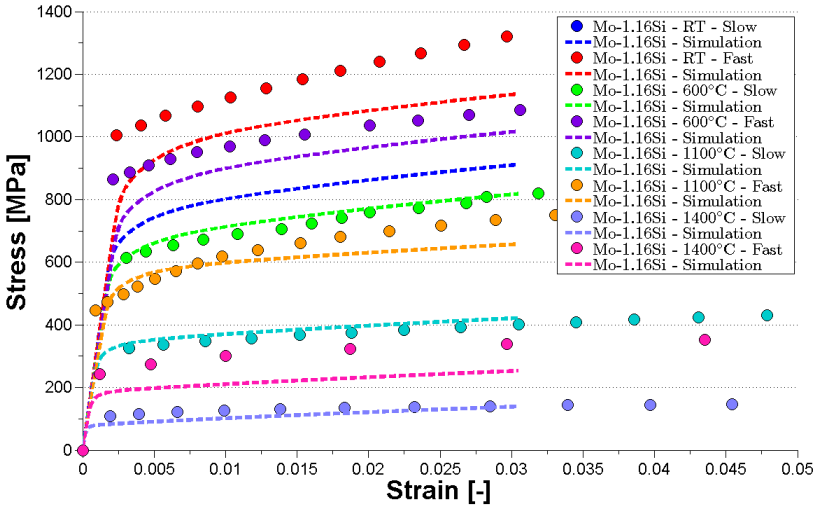

Figure 5.24: Plastic hardening calibration plot for Mo-1.16Si

of Mo with any small amount of Si in solid solution.

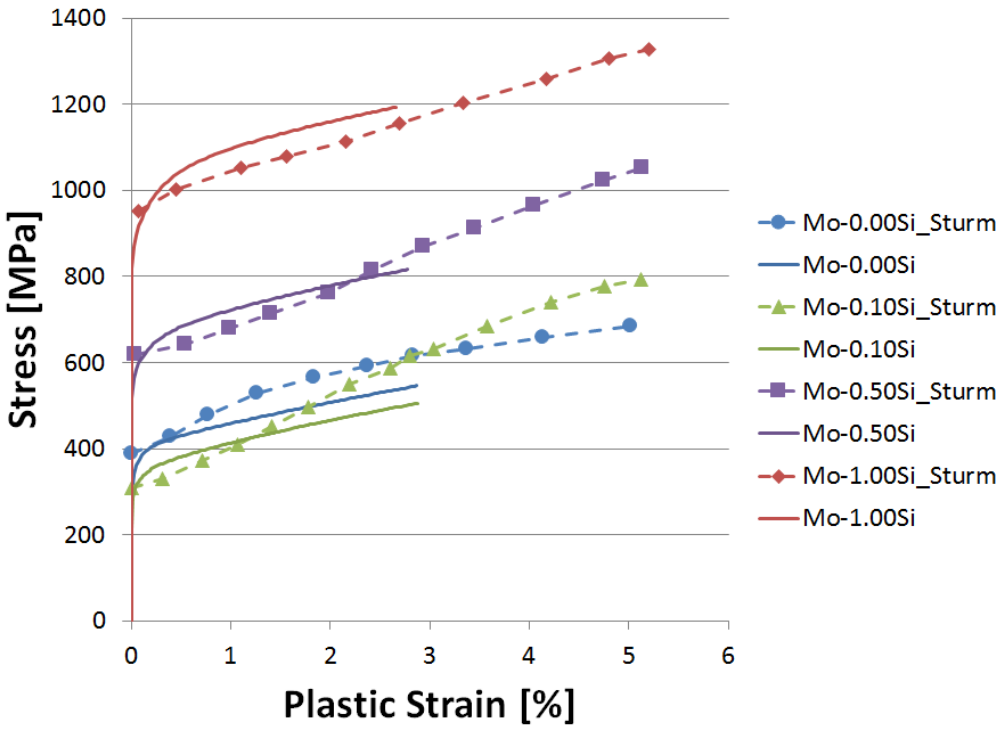

Figure 5.25: Plastic hardening calibration comparison to Sturm *et al.* data at room temperature and a strain rate of 2.20×10^{-3} $\left[\frac{1}{s}\right]$ using simulation volume elements matching the Sturm *et al.* material. Simulation results are plotted with solid lines. Digitized Sturm *et al.* results are plotted with broken lines and digitization data points. [38]

Table 5.2: Initial drag stress, D_0, for α-Mo

Initial drag stress, D_0 [MPa]										
Temperature [°C]	**Si content [wt.%]**									
	0.00	0.10	0.25	0.29	0.40	0.50	0.58	0.75	1.00	1.16
22	**157.6**	**135.0**				**260.5**			**411.0**	
25	*156.2*	134.3	*181.3*			*259.7*		*334.6*	*409.4*	
260	**43.0**	**76.4**				**198.5**			**283.4**	
538	**28.6**	**65.1**				**163.5**			**247.9**	
600	27.6	63.7				156.5				
816	**23.9**	**58.9**				**132.1**				
1093	**20.5**	**51.4**				**109.2**				
1100										
1400	*17.8*	50.7	*70.3*			*102.9*		*159.3*	*215.7*	

Table 5.3: Back stress direct hardening, B, for α-Mo

Back stress direct hardening, B [MPa], with fixed back stress dynamic recovery, $C = 10.0$ [-]										
Temperature [°C]	**Si content [wt.%]**									
	0.00	0.10	0.25	0.29	0.40	0.50	0.58	0.75	1.00	1.16
22	5014.3	5000.0				4436.9			3986.5	
25	***5000.0***	5000.0	*4788.8*	**5000.0**	**5000.0**	*4436.9*	**3986.5**	*4211.7*	*3986.5*	**3986.5**
260	3879.7	5000.0				4436.9			3986.5	
538	2554.5	5000.0				4436.9			3986.5	
600	**2258.9**	5000.0		**5000.0**	**5000.0**	4436.9	**3986.5**		3986.5	**3986.5**
816	2258.9	3815.8				3496.0			3240.2	
1093	2258.9	2297.3				2289.4			2283.1	
1100	**2258.9**	2258.9		**2258.9**	**2258.9**	2258.9	**2258.9**		2258.9	**2258.9**
1400	***2258.9***	2258.9	*2258.9*	**2258.9**	**2258.9**	*2258.9*	**2258.9**	*2258.9*	*2258.9*	**2258.9**

Table 5.4: Strain rate sensitivity exponent, m, for α-Mo

Strain rate sensitivity exponent, m [-], with a fixed reference shearing rate, $\dot{\gamma} = 0.001$ $[\frac{1}{s}]$										
Temperature [°C]	**Si content [wt.%]**									
	0.00	0.10	0.25	0.29	0.40	0.50	0.58	0.75	1.00	1.16
22	5.9	20.0				20.0			20.0	
25	***6.0***	20.0	*20.0*	**20.0**	**20.0**	*20.0*	**20.0**	*20.0*	*20.0*	**20.0**
260	11.7	20.0				20.0			20.0	
538	18.5	20.0				20.0			20.0	
600	***20.0***	20.0		**20.0**	**20.0**	20.0	**20.0**		20.0	**20.0**
816	20.0	15.7				15.7			15.7	
1093	20.0	10.1				10.1			10.1	
1100	**20.0**	10.0		**10.0**	**10.0**	10.0	**10.0**		10.0	**10.0**
1400	***20.0***	6.0	*6.0*	**6.0**	**6.0**	*6.0*	**6.0**	*6.0*	*6.0*	**6.0**

5.5 Constitutive Model Validation

There is extremely limited availability of stress-strain behavior of two and three phase Mo-Si-B materials. What little data exists was performed without a reliable strain measurement, likely due to the difficulty of performing accurate measurements at high temperatures in a vacuum or inert atmosphere. Although there are no good data sets for the stress-strain response of triplex Mo-Si-B materials useful for validating the full constitutive model, a reasonable comparison of yield strength data for triplex Mo-Si-B material can be made to the triplex Mo-Si-B simulations. Tables 5.5 and 5.6 present a comparison of the triplex Mo-Si-B simulations with the yield strength and available characterization of the most complete triplex Mo-Si-B materials from literature [28, 30, 36]. A full description and the full results of the parametric study cover predicted variations in yield strength in Chapter 7.

A relatively recent study on the fabrication, strength, and oxidation of Mo-Si-B alloys includes high temperature tensile tests of a triplex Mo-Si-B alloy including the α-Mo, A15, and T2 phases [36]. This study included a very complete characterization of a single microstructure and analysis of the fracture surfaces of tensile specimens. However, the tensile tests are performed without a strain measurement and are uncorrected for the test frame compliance, so a direct stress-strain comparison is not useful. Tensile tests are conducted at 100°C increments from 900°C to 1300°C at a single strain rate for two separate microstructures. The 0.2% offset yield strengths from the highest temperature tests are presented in Table 5.5 [36].

An exact match of the experimental microstructures are not included in the parametric study; however, several simulations are close enough to show that the triplex Mo-Si-B simulations fall in a similar range of strength values. The experimental material has higher yield strengths than both the Mo-0.50Si and Mo-0.75Si α-Mo calibrations for SVEs including 45% and 54% α-Mo volume fraction. This is expected due to the lower experimental test temperature and 0.2% offset yield strength

reported; however, a more direct set of simulations would be required to more accurately compare to the experimental material. The reported Si content of the α-Mo phase is not measured directly, so a range of simulations with varying α-Mo Si content would still be required for comparison purposes.

A more direct comparison can be made to a slightly older study on a similar triplex Mo-Si-B alloy from the work of Jéhanno *et al.* [28, 30]. In this study, the ductility of triplex Mo-Si-B alloys is determined experimentally at 1300°C and 1400°C for an alloy with the same three phases: α-Mo, A15, and T2. Although the stress-strain curves are reported to be true stress and true strain and the reported elastic modulus is quite close to the expected values, no mention is made of the method for measuring strain directly or removing machine compliance. In any case, the material demonstrated as much as 396% strain before failure at 1400°C with a strain rate of $10^{-4}\ \frac{1}{s}$, so the published figure has inadequate resolution for a stress-strain comparison at strains of 3%, which is the limit for calibration of plastic hardening in the α-Mo phase. Additionally, the relative volume fractions of the A15 and T2 phase and the Si content of the α-Mo phase are not characterized, only the volume fraction of α-Mo is characterized.

A reasonable comparison with the probable closest matching material characteristics from this work is presented in Table 5.6, where an estimation of the α-Mo Si content is taken from Patra *et al.* [118] which also used the yield strength results of this triplex Mo-Si-B alloy. The simulations of this work bounding the α-Mo volume fraction and Si content of the expected values for the Jéhanno *et al.* material suggest that the Si content estimate is reasonable and that the resulting triplex Mo-Si-B mechanical behavior is in reasonable agreement given the unknowns in material characterization. The differences in modulus as a function of temperature are likely a result of the unknown volume fractions of intermetallics, but could also result from the unknown texture of the Jéhanno *et al.* material.

The most direct comparison is found for the Jéhanno *et al.* material tested at 1400°C at a strain rate of $1.0\text{x}10^{-3}$. The maximum stress is reported as 107 MPa; however, the plotted data suggests a 0.02% offset closer to 85 MPa. The closest material microstructure, calibration, and test conditions for the triplex Mo-Si-B simulations has a yield strength of 75.2 MPa. These columns are shown in bold in Table 5.6. The remaining differences in yield strength are small with respect to the parametric study variation and could be explained by the differences in the material or test conditions between the experiments and simulations. Targeted simulations would be required to verify these differences and would still require a range of microstructures and material calibrations due to the incomplete material characterization.

There is additional data available for two phase Mo-Si-B alloys containing the α-Mo and T2 phases [24, 31]; however, more recent work studying a Mo-Si-B alloy of very similar composition resulted in the triplex material presented in the right-most column of Table 5.5. Due to the differences in phases, these studies are not presented in comparison to the triplex Mo-Si-B alloys simulations of this work.

Table 5.5: Comparison of Middlemas material yield strength to simulated triplex Mo-Si-B predicted yield strength [36]
*0.2% offset yield strength reported
**A later study reported the Si content of this material closer to 1.3 wt.% Si [19].

Parameter	Simulation				Middlemas [36]		
0.02% offset σ_Y [MPa]	313.5	446.1	287.1	414.9	419*	577*	477*
α-Mo vol. frac. [%]	45.0	45.0	54.0	54.0	47.8	47.8	67.2
A15 vol. frac. [%]	0.37	0.37	0.31	0.31	33.4	33.4	9.2
T2 vol. frac. [%]	0.18	0.18	0.15	0.15	18.8	18.8	27.3
α-Mo Si content [wt.%]	0.50	0.75	0.50	0.75	0.61**	0.61**	0.61**
Temperature [°C]	1400	1400	1400	1400	1300	1200	1200
Strain rate [$\frac{1}{s}$]	2.2x10^{-3}	2.2x10^{-3}	2.2x10^{-3}	2.2x10^{-3}	1.0x10^{-4}	1.0x10^{-4}	1.0x10^{-4}

Table 5.6: Comparison of Jéhanno *et al.* material yield strength to simulated triplex Mo-Si-B predicted yield strength, continued [28, 30]
*Yield strength not reported and stress-strain plot has insufficient strain resolution for accurate 0.02% offset calculation
**As estimated by Patra *et al.* [118]

Parameter	Simulation				Jéhanno [28, 30]			
Elastic Modulus [GPa]	297.6	297.6	**290.8**	290.8	264	264	**259**	259
0.02% offset σ_Y [MPa]	90.1	185.9	**75.2**	165.1	300*	64*	**85***	27*
max σ [MPa]	-	-	**-**	-	315	102	**107**	45
α-Mo vol. frac. [%]	45.0	45.0	**54.0**	54.0	50	50	**50**	50
A15 vol. frac. [%]	0.37	0.37	**0.31**	0.31	?	?	**?**	?
T2 vol. frac. [%]	0.18	0.18	**0.15**	0.15	?	?	**?**	?
α-Mo Si content [wt.%]	0.00	0.10	**0.00**	0.10	0.01**	0.01**	**0.01****	0.01**
Temperature [°C]	1400	1400	**1400**	1400	1300	1300	**1400**	1400
Strain rate [$\frac{1}{s}$]	2.2x10^{-3}	2.2x10^{-3}	**2.2x10^{-3}**	2.2x10^{-3}	1.0x10^{-3}	1.0x10^{-4}	**1.0x10^{-3}**	1.0x10^{-4}

5.6 Summary

This chapter presents the crystal-viscoplastic (CVP) constitutive law and evolution equations. The α-Mo phase is calibrated through a mix of experiments performed for this work and polycrystalline *alpha*-Mo data from Sturm *et al.* [38]. Due to the limited stress-strain data for the intermetallics, and the limited plasticity exhibited by these phases, they are treated as elastic only in the constitutive law. However, the option to calibrate the full constitutive model for the intermetallic phases is retained by applying the full CVP equations to these phases, where plastic deformation is eliminated through the application of insurmountably large initial threshold stresses.

The elastic properties of the α-Mo and T2 phases are taken from literature and capture the full elasticity tensor as a function of temperature [21–23]. The A15 phase elasticity tensor components are taken from the work of Ito *et al.* [23] at room temperature and extrapolated to higher temperatures according to the temperature dependent slope of the α-Mo phase, which share a similar cubic crystal structure. The coefficient of thermal expansion for each phase is available at room temperature and 1300°C for each phase [25] and linearly interpolated at intermediate temperatures and linearly extrapolated to 14°C.

A direct stress-strain response validation of the triplex Mo-Si-B constitutive model is not possible because the available triplex Mo-Si-B data contains an incomplete material characterization required for accurate synthetic volume element reconstruction and α-Mo CVP parameter determination. However, comparisons of yield strength suggest that the fully triplex Mo-Si-B simulations result in yield strengths comparable to experimental results for similar triplex alloys.

5.7 Significance

The experimental results presented in this chapter serve as only the third study demonstrating solid-solution softening effect of Si in α-Mo. The experimental results

also provide further experimental evidence is presented for the changing deformation mechanisms between pure Mo and α-Mo with any amount of Si content through the abrupt changes in strain-rate sensitivity behavior when Si is added to α-Mo.

The experimental results are captured in a crystal-viscoplastic constitutive law to model the α-Mo phase in triplex Mo-Si-B alloys. The crystal-viscoplastic constitutive law, implemented and calibrated for polycrystalline α-Mo, is the first CVP constitutive law calibrated for this material system. The constitutive law accounts for the effects of α-Mo Si content, strain rate sensitivity as a function of α-Mo Si content, and the effects of temperature. These effects are critical for evaluating the suitability of triplex Mo-Si-B alloys for use in a variety of applications and for optimizing the microstructure of triplex Mo-Si-B alloys for specific applications as the material system is developed.

CHAPTER VI

DAMAGE INDICATOR PARAMETER

6.1 Introduction

This chapter develops one of the post-processing tools for the final step in the microstructure-sensitive modeling workflow, shown in Figure 6.1.

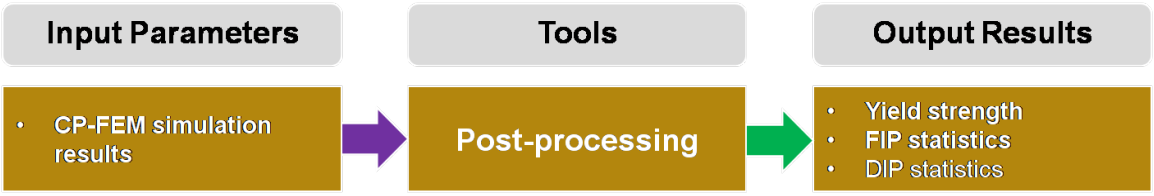

Figure 6.1: Microstructure-sensitive mechanical property modeling workflow: post-processing

Before attempting to make a first order optimization of the volume fraction and Si content of a triplex Mo-Si-B alloy, a computationally efficient damage indicator parameter (DIP) must be developed for predicting the relative ductility or damage tolerance. The challenges of modeling fracture toughness in brittle and quasi-brittle materials is discussed in Chapter 2 Section 2.5. While cohesive zone elements offer a method for initiating and growing multiple cracks at arbitrary locations, a large volume with sufficient microstructural detail for predicting fatigue properties for microstructure optimization makes a three dimensional cohesive zone element model computationally intractable. Consequently a DIP is sought that can emulate damage nucleation from the damage law of cohesive zone models up to the formation of large scale cracking, but without the computational cost of cohesive zone elements. This DIP is developed alongside and validated against two dimensional plane strain simulations using a simple isotropic constitutive model which are suited to conducting cohesive simulations in a reasonable time frame.

6.2 Modeling Approach

6.2.1 Microstructure instantiation

The 2D, three-phase microstructures are instantiated using a weighted Voronoi tessellation approach. The algorithm uses input values for mean grain diameter and volume fraction for each phase and employs a log-normal size distribution to fill the volume in order of decreasing grain diameter. The A15 and T2 phases are seeded initially, with α-Mo phase seeded afterwards to develop a continuous phase in the microstructure. Further details on the 2D microstructure instantiation are described in previous work [118].

In this work, the simulations are instantiated with 200 elements along each edge of an ordered, voxellated mesh of square continuum elements and contained at least 299 grains per phase with a minimum of 1442 total grains. After the α-Mo volume fraction is chosen, the intermetallic phases filled the remaining volume with a volume fraction ratio of approximately 1:2 A15 to T2 phase. Figure 6.2 shows a representative microstructure instantiation.

Grains are initially equiaxed with log-normal distributions of grain diameter. The mean grain size is specified as 3.3, 2.6, and 2.0 microns in diameter for the α-Mo, A15, and T2 phases, respectively. The grain diameter distributions for each phase are shown in Figure 6.3.

6.2.2 Mechanical Properties

The constitutive models and parameters for the three phases are taken from the prior work of Patra *et al.* [118]. Each phase of the triplex microstructure is modeled as isotropic. The elastic modulus and Poissons ratio for each phase are given in Table 6.1 [198].

The α-Mo phase yield strength and its dependence on Si content are calibrated

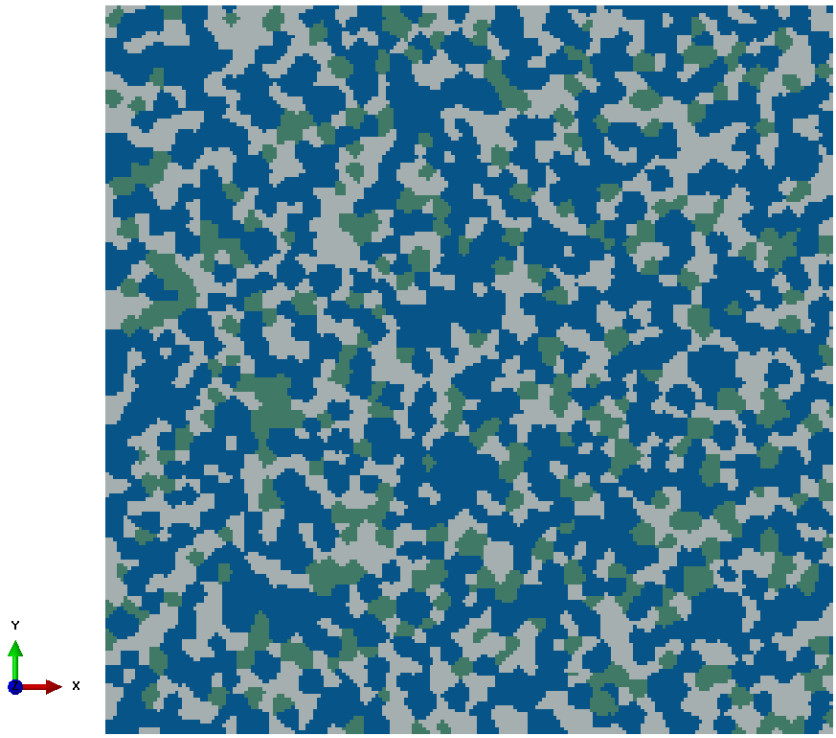

Figure 6.2: Representative microstructure instantiation with 52% α-Mo volume fraction. Blue: α-Mo. Gray: A15. Green: T2.

Table 6.1: Isotropic elastic parameters. Temperature ranging from 1273 to 1473 Kelvin [118].

Parameter	Value
$E_{\alpha\text{-}Mo}$, $\nu_{\alpha\text{-}Mo}$	$311.9 - 4.34\text{x}10^{-2}T$ GPa, 0.320
E_{A15}, ν_{A15}	$305.9 - 4.34\text{x}10^{-2}T$ GPa, 0.329
E_{T2}, ν_{T2}	$399.8 - 5.69\text{x}10^{-2}T$ GPa, 0.298

from triplex Mo-Si-B experimental data using a Voigt approximation for the composite yield strength as a function of the three phases

$$\sigma_{Y-MSB} = v_{\alpha\text{-}Mo}\sigma_{\alpha\text{-}Mo} + v_{A15}\sigma_{A15} + v_{T2}\sigma_{T2} \tag{6.1}$$

where v_i and σ_i are the phase volume fraction and stress of the i^{th} phase. If it is assumed that the intermetallic A15 and T2 phases deform elastically and that each phase has a uniform strain at the yield point, the contributions from the intermetallic

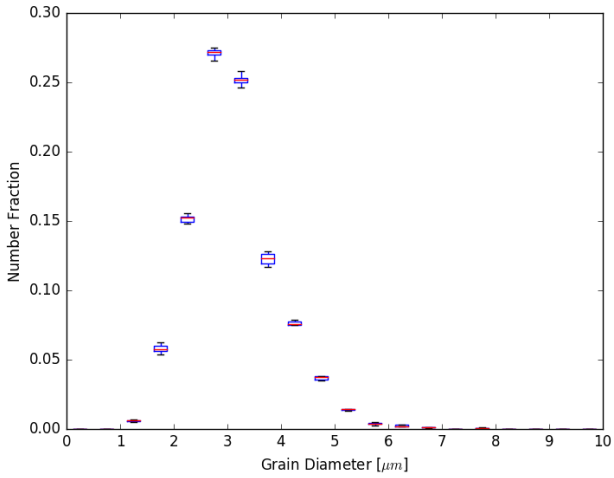

(a) α-Mo

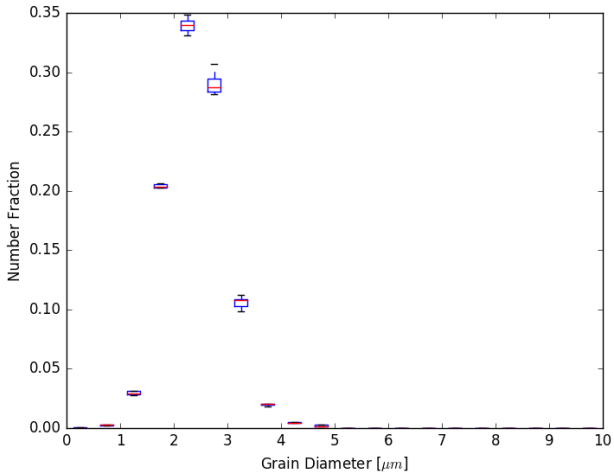

(b) A15

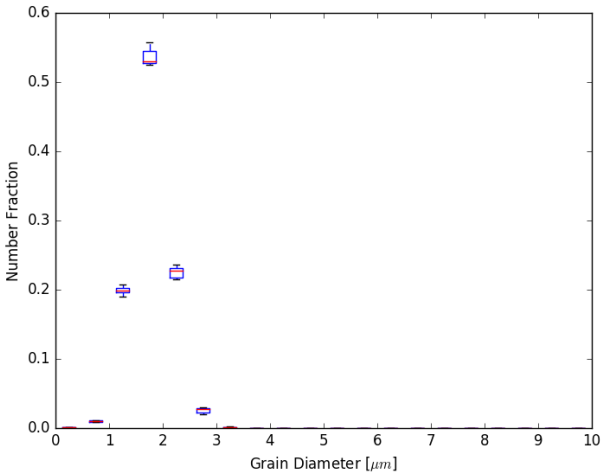

(c) T2

Figure 6.3: Representative grain diameter distributions from ten instantiations

phases can be estimated as

$$\sigma_i = E_i \epsilon_Y \tag{6.2}$$

where ϵ_Y is set in the vicinity of the initial yield point $\epsilon_Y = 0.002$ and E_i is the elastic modulus of the i^{th} phase.

For this, estimates of the yield strength of several alloys and the volume fractions for each individual phase of those alloy are required. The yield strength of each phase is also a function of Si content because of Si solute strengthening. The yield strength data is extracted from experimental data taken from literature [27, 36, 199]. Finally, the strain hardening response of the α-Mo phase is estimated by performing FE simulations of single phase, polycrystalline α-Mo and comparing those results with previous experimental data [29].

The α-Mo phase is treated as elastic-plastic and the intermetallic phases are treated as purely elastic. The flow stress, σ_f, for the elastic-plastic α-Mo phase is modeled as the initial yield strength, σ_Y, with a contribution from strain hardening as

$$\sigma_f = \sigma_Y + H\left(\bar{\epsilon}^{in}\right)^n \tag{6.3}$$

where $\bar{\epsilon}^{in}$ is the equivalent inelastic strain, H is the hardening coefficient, and n is the hardening exponent. For the α-Mo phase, solid solution strengthening is assumed to affect the initial yield strength only and to vary linearly as a function of the Si atomic concentration as

$$\sigma_Y = k_1(k_2 + k_3 c_{Si}) \tag{6.4}$$

where k_1 is a temperature dependent material parameter, k_2 and k_3 are parameters independent of the absolute temperature, and c_{Si} is the Si solute concentration in the α-Mo phase in atomic percent in the range of $9.8x10^{-3}$ to $4.1x10^{-2}$ at.% Si. The solid solution strengthening and plastic hardening parameters are given in Table 6.2 [118].

For the simulations in this work used to develop and validate the damage indicator

parameter (DIP) for susceptibility to microcracking, the Si content of the α-Mo phase is fixed at $c_{Si} = 0.04136$ at.% and the temperature is fixed at 1373 K.

Table 6.2: Material properties for the Mo-Si-B system. Temperature ranging from 1273 to 1473 Kelvin [118].

Parameter	Value
k_1	$-110.5 + 0.172T - 6.571\text{x}10^{-5}T^2$ MPa
k_2	64.36
k_3	6294 $(\text{at.}\%)^{-1}$
H	$105704 - 144.7T + 4.952\text{x}10^{-2}T^2$ MPa
n	$-19.16 + 3.123\text{x}10^{-2}T - 1.222\text{x}10^{-5}T^2$

6.2.3 Cohesive Zone Model

Many cohesive zone models have been employed by different researchers since the cohesive zone concept was introduced by Barenblatt in 1959 [130]. These different cohesive zone models have different target applications ranging from cracking in brittle materials, to particle-matrix decohesion, and crack growth in elastic-plastic materials [109]. The traction-separation model used previously to study Mo-Si-B [118] is an irreversible, bilinear traction-separation that allows for different responses to normal and shear loading [118, 133, 137]. The model form is

$$t_i = k'\delta_i = (1 - D)\, k\delta_i \tag{6.5}$$

where t_i is the traction on the i^{th} direction, k' is the effective stiffness of a cohesive element, δ_i is the relative displacement or separation between the faces of the cohesive element, D is the isotropic damage variable, and k is the original, undamaged stiffness

of the cohesive element. Figure 6.4 shows the effective traction-separation plot for this model.

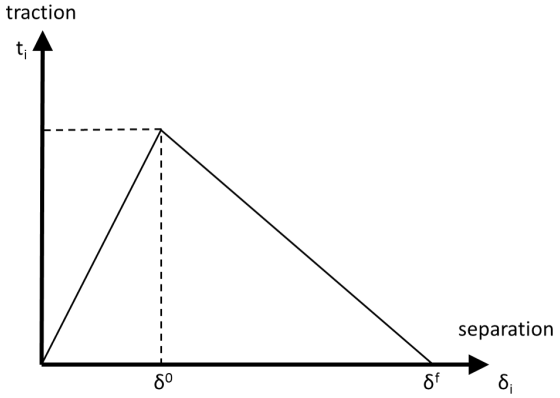

Figure 6.4: Bilinear traction-separation CZM

The relevant damage law for this bilinear traction-separation cohesive zone model is

$$D = \begin{cases} 0; & \delta_i^{max} \leq \delta_i^0 \\ \dfrac{\delta_i^f \left(\delta_i^{max} - \delta_i^0\right)}{\delta_i^{max}\left(\delta_i^f - \delta_i^0\right)}; & \delta_i^0 < \delta_i^{max} \leq \delta_i^f \\ 1; & \delta_i^{max} > \delta_i^f \end{cases} \tag{6.6}$$

where D is the damage of the cohesive element ranging from zero to one, δ_i^{max} is the maximum effective displacement of the loading history and is required to be positive to maintain irreversible damage, δ_i^0 is the initial effective displacement when damage starts, and δ_i^f is the effective displacement for final failure of the cohesive element.

Damage initiation is defined by a maximum nominal stress criterion given in three dimensions by

$$max\left\{\frac{\langle t_n \rangle}{t_n^0}, \frac{|t_s|}{t_s^0}, \frac{|t_t|}{t_t^0}\right\} = 1 \tag{6.7}$$

where the angled brackets, $\langle\rangle$, are Macaulay brackets, t_n is the normal traction, t_s and t_t are the shear tractions in the 3D case, and the superscript 0 refers to the traction required to initiate damage. With this damage initiation criterion, the subscript i in Equation 6.6 refers to the direction of displacement. In the 2D plane strain case, this

corresponds to the normal direction and one shear direction. The damage criterion relates the damage initiation displacement to the appropriate traction as

$$\delta_i^0 = \frac{t_i^0}{k} \tag{6.8}$$

where the k is the cohesive zone element stiffness. Damage is then assigned according to the maximum value from the separate normal and shear damage calculations.

The important displacement values for calculating damage from Equation 6.6 can be calculated from the material parameters in Table 6.3 [118]. The damage initiation displacement for the interfaces of interest is calculated as in Equation 6.8, where $t_i^0 = T_{max}$ and T_{max} is the interface strength. The failure displacement, δ_i^f, is defined with respect to the maximum relative displacement, Δ_{max} and the damage initiation displacement as

$$\delta_i^f = \delta_i^0 + \Delta_{max} \tag{6.9}$$

In the cohesive zone simulations, cohesive elements are placed at the grain boundaries between the α-Mo phase and the intermetallics as well as in the intermetallic phases. The damage initiation stress for cleavage of the intermetallic phases can be calculated from the fracture toughness and properties of the intermetallic phases according to

$$T_{max|j} = \frac{2}{\Delta_{max}} \frac{K_j^2 \left(1 - \nu_j^2\right)}{E_j} \tag{6.10}$$

where Δ_{max} is the maximum separation for total failure of the cohesive element, K_j is the fracture toughness of the j^{th} intermetallic phase, and E_j is Young's modulus of the j^{th} intermetallic phase [118].

The cohesive zone model parameters are estimated from a combination of literature estimates [29, 109, 121, 200] and model calibration for a range of temperatures between 1273 K and 1473 K [118]. The cohesive element properties are selected for cohesive zone interfaces between the α-Mo and the A15 phase and between the α-Mo and the T2 phase, as well as for the intraphase domains of the A15 and T2 phases.

For all cohesive zone elements, the stiffness of the cohesive zone element is assigned according to the modulus of the intermetallic phase making up the grain boundary or intraphase domain, shown previously in Table 6.1, modified by a large multiplying factor of 1000 to reduce the spurious effects of a finite stiffness cohesive element on the elastic modulus of the simulation.

The fracture toughness, K_{T2} and K_{A15} of the intermetallic phases are taken from literature [10, 200], where the room temperature A15 phase fracture toughness is assumed to scale with temperature at the same rate as the T2 phase fracture toughness [118]. The maximum separation Δ_{max} follows similar values used for quasi-brittle materials in literature [109, 134]. The same Δ_{max} is used for the cohesive zones at each interface and intraphase domain [118]. The interface strengths between the α-Mo phase and the intermetallics, $T_{max|\alpha\text{-}Mo/A15}$ and $T_{max|\alpha\text{-}Mo/T2}$, are estimated from simulations which varied these parameters to fit the peak tensile stress of two and three phase Mo-Si-B alloys found in literature [29]. With no clear evidence of the relative contribution of these interfaces to fracture toughness, the interfaces are assumed to have the same strength [118]. In future work, the interface strengths and fracture toughness values can be made functions of both temperature and Si content to account for important changes in material behavior with increasing Si content.

Table 6.3: Material properties for the damage law. Temperature in Kelvin [118].

$T_{max\|\alpha\text{-}Mo/A15}$	450 MPa
$T_{max\|\alpha\text{-}Mo/T2}$	450 MPa
K_{T2}	$4.75 - 6.8\text{x}10^{-3}T + 7.0\text{x}10^{-6}T^2$ MPa$\sqrt{\text{m}}$
K_{A15}	$\frac{3.0}{3.356}K_{T2}$ MPa$\sqrt{\text{m}}$
Δ_{max}	0.2 μm

In the cohesive element simulations, this damage is used to modify the stiffness of the element throughout the simulation. As damage evolves and the stiffness degrades,

stress re-distribution can occur as elements fail. The damage is irreversible, but the effects on stiffness are restricted to tensile loading by restricting damage evolution to positive displacements and using the original stiffness during compressive loading.

6.3 Damage Indicator Parameter

The chosen damage law for the development of a DIP is the same bilinear traction-separation damage law,Equation 2.14, used in the cohesive element simulations for the bilinear traction-separation model shown in Figure 6.4. The purpose is to eliminate the need for cohesive zone elements, so the damage must be calculated from the local stress-strain field during post-processing instead of through a cohesive element traction-separation relationship. When placing cohesive elements in a simulation they have no initial displacement between the nodes of the bounding continuum elements. Instead they are assigned an arbitrary initial length of unity.

As a result, the traction-separation equations may be considered equivalently in terms of strain. The damage initiation displacement, δ_i^0, and interface failure displacement, δ_i^f, can be treated as a damage initiation strain and failure strain, respectively. Recognizing this, the damage initiation displacement, δ_i^0, can be defined as before in Equation 6.8, with the cohesive element stiffness k replaced with the relevant material property: Young's modulus for normal displacement and the shear modulus for shear displacement. The failure strain is then defined directly as in Equation 6.9. The maximum effective displacement, δ_i^{max}, may also be calculated as a strain. Instead of directly using the displacement of the nodes of a cohesive element, the normal and shear tractions at the interface between two elements must be computed from the local strain tensor.

The damage calculation is carried out on the elements on either side of a location where cohesive zone elements would normally be placed, shown schematically in Figure 6.5. In the non-cohesive element simulations, there are no defined properties for

the boundary between different phases as there would be if a cohesive element were present. Instead, the damage is calculated separately for each element making up the boundary using the properties and local strain tensor of that element. In the case of an intraphase domain, the properties of each element would be the same. The largest calculated damage between two elements making up an interface is then assigned to that interface as

$$D_j = max\left\{D_1, D_2\right\} \tag{6.11}$$

where D_j is the damage of the j^{th} interface, D_1 is the damage calculated for the first element making up the interface, and D_2 is the damage calculated for the second element making up the interface.

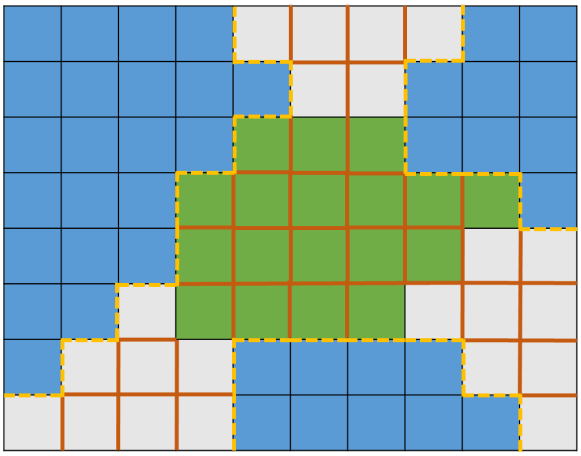

Figure 6.5: CZM placement schematic. Blue: α-Mo. Gray: A15. Green: T2. Orange dashed lines represent the α-Mo/A15 and α-Mo/T2 phase boundary cohesive element locations. Red solid lines represent the A15/A15 and T2/T2 intraphase domain cohesive element locations.

For this study, the locations of interest are between the matrix α-Mo phase and each of the intermetallic A15 and T2 phases, e.g. the α-Mo/A15 and α-Mo/T2 grain boundaries, as well as within the intermetallic grains. However, predicting the location of cracking in the intermetallic grains is a difficult task without cohesive elements. For this exercise, intermetallic cracking is neglected in order to simplify the post-processing DIP development. In addition to simplifying the DIP development,

this can be justified by the preferred intergranular cracking observed in both two and three phase Mo-Si-B alloys [31, 98, 201, 202] and is discussed in Chapter 2.

For comparing damage between simulations and microstructures, the total damage present in the SVE is calculated from the damage of individual interfaces. Since the damage is only calculated at the α-Mo/intermetallic grain boundaries, an interface average damage parameter may be calculated over the interfaces of interest as

$$DIP_{avg} = \frac{\sum_{j=1}^{N_{Mo/Inter}} D_j}{N_{Mo/Inter}} \tag{6.12}$$

where DIP_{avg} is a measure of the mean damage over all *alpha*-Mo/intermetallic interfaces within the SVE, $N_{Mo/Inter}$ is the total number of interfaces of interest where the damage calculation has been performed, and D_j is the damage calculated on the j^{th} interface of interest. This DIP_{avg} represents the mean damage, D_j, over all of the interfaces which are allowed to initiate damage and is calculated over the entire volume of a single SVE instantiation. A larger DIP_{avg} indicates a greater susceptibility to microcrack initiation at the interfaces considered. A mean value metric is chosen as a comparison metric over localization metrics, such as the extreme values of local damage D_j, to capture the dependence of fracture on widespread cracking and crack percolation and coalescence. Between two different microstructure simulations, the simulation with a larger DIP_{avg} at a set macroscopic strain would be more likely to develop wide spread cohesive element failure in a cohesive simulation.

A volume averaged metric is chosen to compare relative amounts of predicted susceptibility to microcracking over the extreme values or extreme value distributions which are often used with fatigue indicator parameters (FIP) [54, 57], due to the large number of instantiations required to properly evaluate extreme value statistics. In optimizing triplex Mo-Si-B alloys, a large variation in microstructures must be considered and simulating several hundred instantiations at each point in a large parametric study is prohibitively expensive computationally. It is anticipated that

further development of this reduced order method would evaluate the locally calculated DIP with a similar approach used to evaluate the extreme value probabilities of FIPs, but including the effects of spatial distribution and a percolation threshold for crack coalescence and damage propagation.

In order to understand at what point the stress-strain field differs significantly between simulations with and without cohesive zone elements, a study is performed on 2D microstructural models that are identical except for the inclusion or exclusion of cohesive zone elements.

6.4 Results

6.4.1 Validation against cohesive element simulations

Simulations are run under plane strain conditions for 10 instantiations with fixed microstructure characteristics with cohesive zone finite elements inserted between the matrix α-Mo phase and the intermetallic A15 and T2 phases, e.g. α-Mo/A15 and α-Mo/T2, as well as within the intermetallic A15 and T2 grains. For an exact comparison without the effects of microstructure, the cohesive elements are removed from each instantiation to create identical FE models without cohesive zone elements. A schematic of the simulation loading and boundary conditions is shown in Figure 6.6. The models are loaded to 3% uniaxial strain with a strain rate of 10^{-4} s^{-1} by a prescribed displacement of the positive y edge. Roller boundary conditions are applied along the negative y edge elements, with the center node along this edge fixed in space to eliminate rigid body motion.

A representative macroscopic stress-strain plot is shown for a cohesive element simulation in Figure 6.7a. After yielding, there is a marked drop off in supported load for each simulation, occurring between approximately one and two percent strain, with the majority of simulations occurring near one percent strain. This drop off corresponds to a large number of cohesive elements failing and is shown to be the point

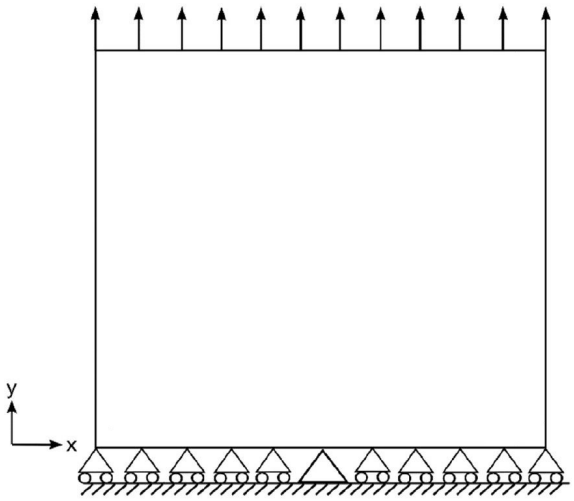

Figure 6.6: Schematic of volume element loading and boundary conditions [118]

at which the stress-strain fields of the non-cohesive element simulations begin to differ significantly from the cohesive element simulations. The corresponding stress-strain curve for the non-cohesive simulation is shown in Figure 6.7b.

Ten instantiations are created for each of four different volume fractions of α-Mo: 52.5, 63, 71, and 76. The ratio of intermetallic phase volume fractions is kept constant at 2:1 A15 to T2. The effects of Si content are not considered in this study, so the constitutive calibration of the α-Mo phase remained constant at $c_{Si} = 0.04136$ at.% and $T = 1373$ K. The mean results from ten instantiations and error bars for two standard deviations are plotted in Figure 6.8 for modulus and Figure 6.9 for 0.02% offset yield strength. The lower modulus and yield strength of the cohesive element simulations are associated with the finite stiffness of the cohesive zone elements at element interfaces, which should be rigid to provide an accurate comparison, and the decreasing cohesive element stiffness with increasing cohesive element damage.

The first step in determining if a reduced order indicator of damage initiation can be developed for use in simulations without cohesive zone elements is to compare the stress and strain fields of the simulations. For this first order estimate of the differences introduced in the strain field by removing the cohesive elements, the

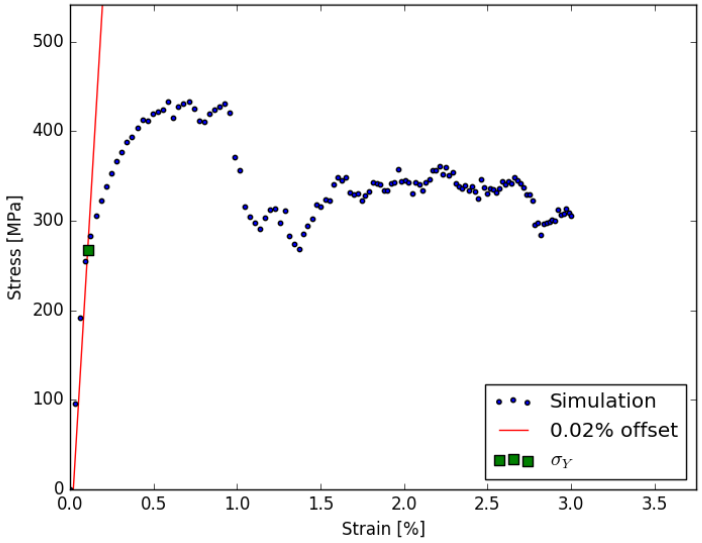

(a) Cohesive simulation

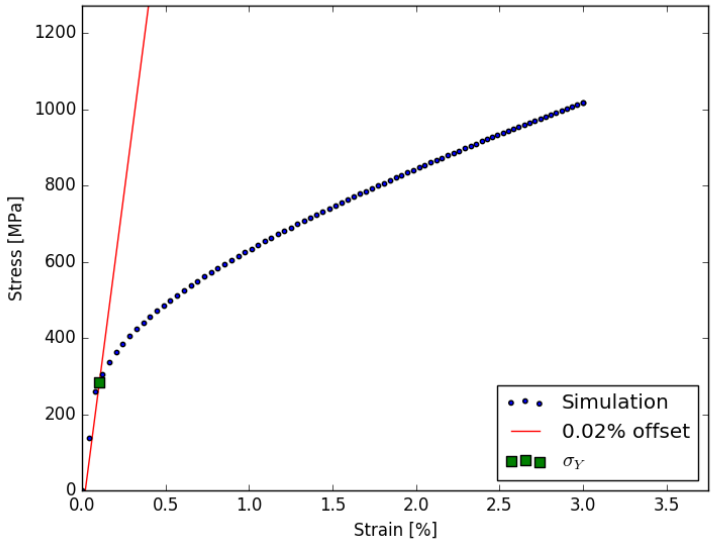

(b) Non-cohesive simulation

Figure 6.7: Representative stress-strain responses

maximum in-plane principal strains is used to create a visual aid. First, we show a comparison of the maximum principal strain fields near the macroscopic yield point of a representative instantiation with and without cohesive elements in Figure 6.10. At the macroscopic yield point near 0.3% strain, the simulations show very similar stress and strain fields, both in magnitude and in distribution.

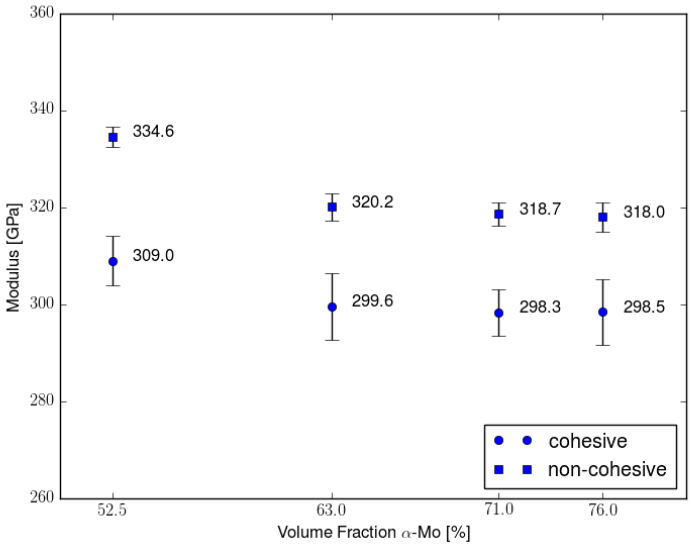

Figure 6.8: Mean instantiation modulus

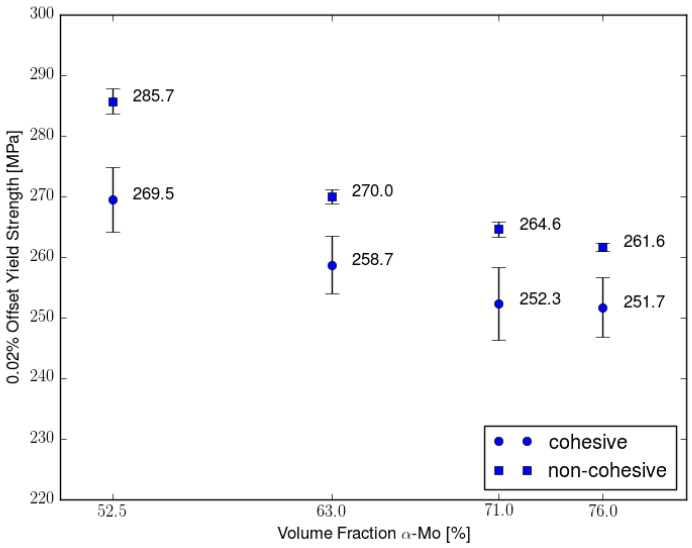

Figure 6.9: Mean instantiation yield strength

Figure 6.11 shows the same comparisons of maximum principal strain fields at approximately 1% macroscopic strain for the same instantiation. Differences in the stress and strain fields begin to show, but are still similar, at 1% macroscopic strain.

At 3% macroscopic strain, show in Figure 6.12, larger differences in the maximum principal strain fields can be seen. By 3% macroscopic strain, large numbers of

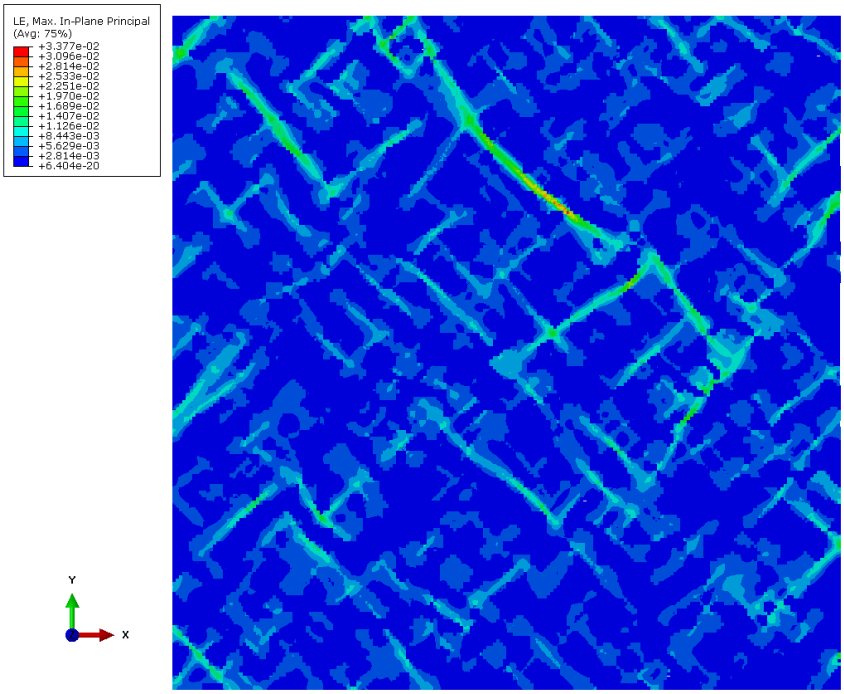

(a) Cohesive simulation

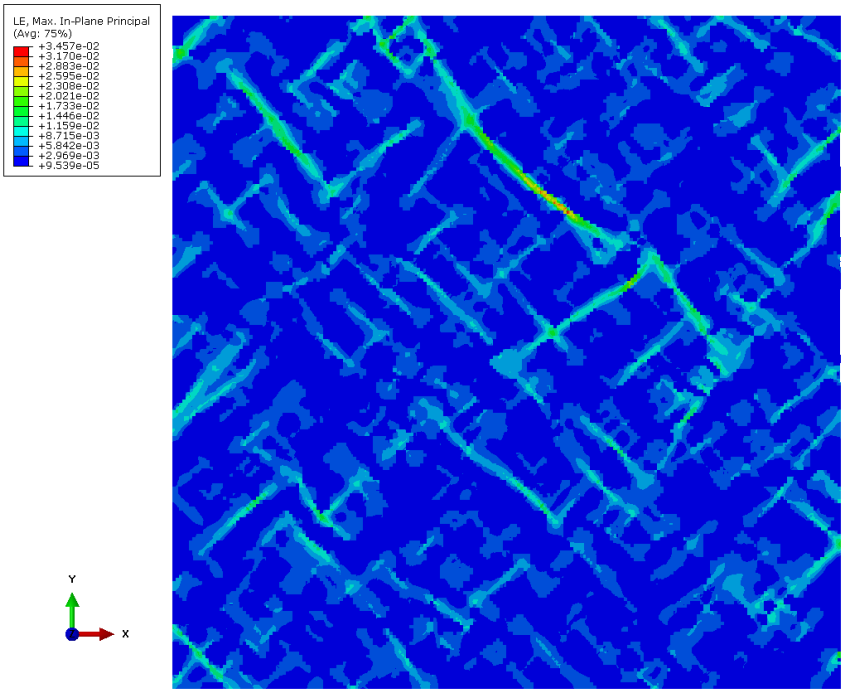

(b) Non-cohesive simulation

Figure 6.10: Representative maximum principal strain fields at 0.3% strain

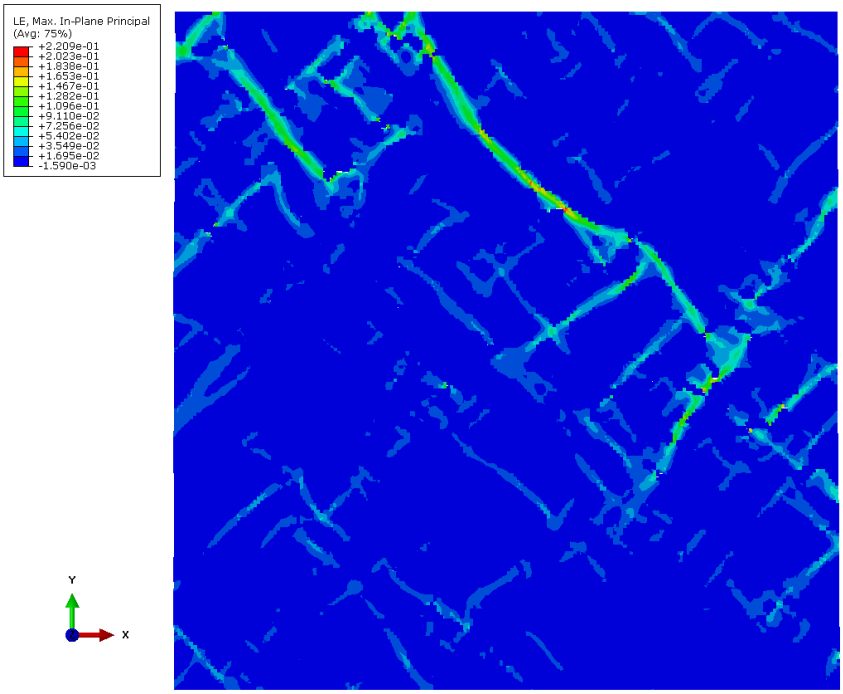

(a) Cohesive simulation

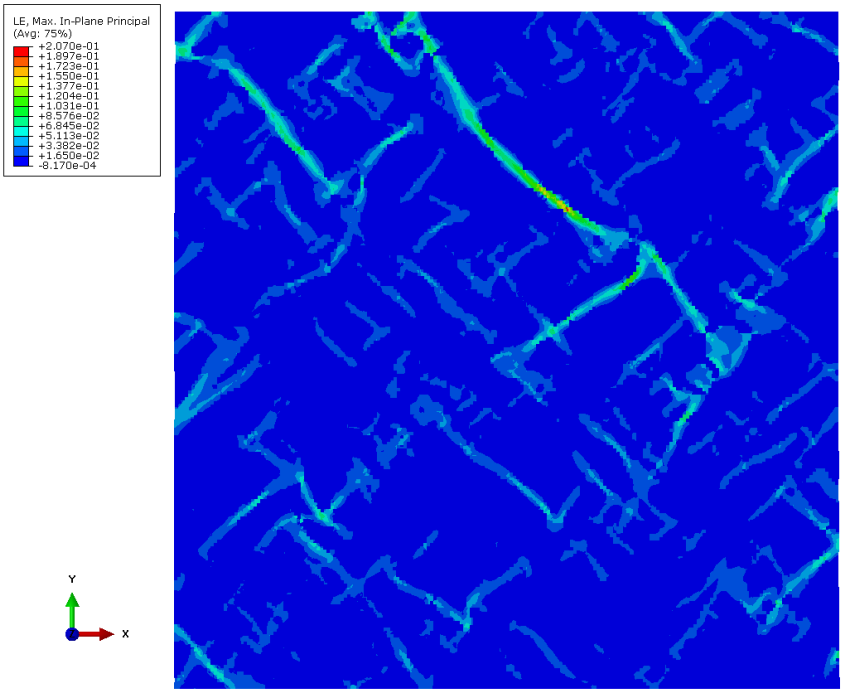

(b) Non-cohesive simulation

Figure 6.11: Representative maximum principal strain fields at 1.0% strain

cohesive elements have failed, leading to stress re-distribution that is not reflected in the non-cohesive simulation.

The point when many cohesive elements begin to fail must be captured by the non-cohesive simulation to develop a useful reduced order DIP_{avg} for comparing susceptibility to brittle microcracking between microstructures. From these stress-strain fields, it is seen that the simulations have similar strain fields up to approximately 1% macroscopic strain, when the cohesive elements begin to fail on a large scale.

The second step in determining if a reduced order indicator of damage initiation can be developed for use in simulations without cohesive zone elements is to compare the local damage calculations, D_j, between simulations with and without cohesive zone elements. The local damage is calculated from the continuum elements forming the grain boundaries where cohesive elements are located in the cohesive simulations, i.e. between the α-Mo/A15 and α-Mo/T2 grains. For now, the damage introduced within the intermetallic grains is ignored due to the difficulty of predicting the location for cohesive element failure within a grain.

In order to create a visual aid of the local damage calculations, D_j from Equation 6.11, local interface damage is associated with one of the two continuum elements forming the local grain boundary interface at every location cohesive elements are present in the cohesive simulation. Figure 6.13 shows a representative calculation of the local damage, D_j using this element-by-element visual aid at approximately 1% macroscopic strain. Dark blue locations correspond to locations where the local damage is not calculated, e.g. grain interiors and grain boundaries between the same phase. Dark red locations correspond to interfaces predicted to fail and separate if a cohesive element are present.

Having verified that the local damage field is sufficiently similar between the two types of simulation, the interface average DIP_{avg} is calculated for each type of simulation and over all instantiations. Figure 6.14 compares the results of the cohesive

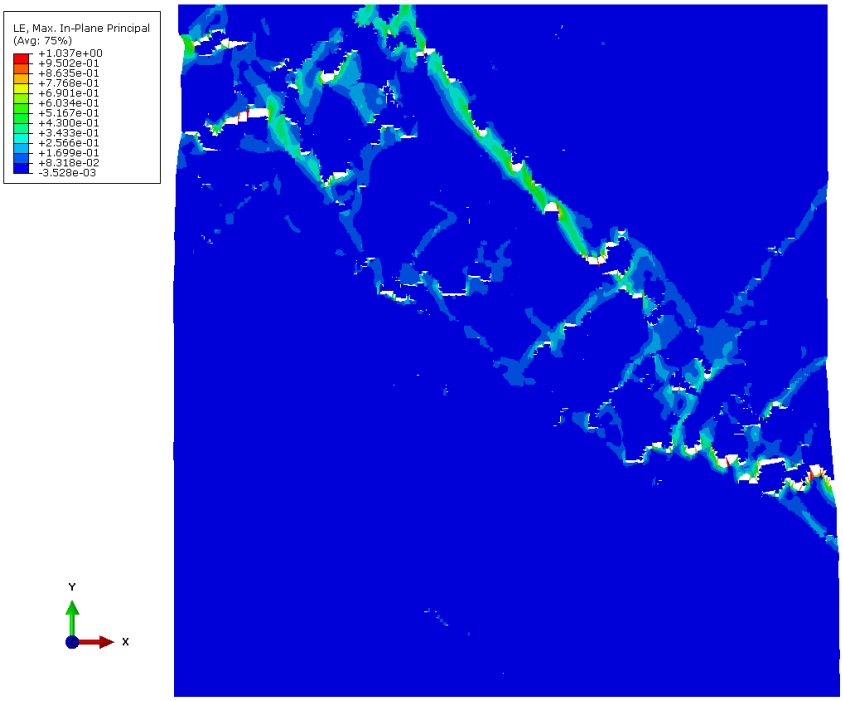

(a) Cohesive simulation

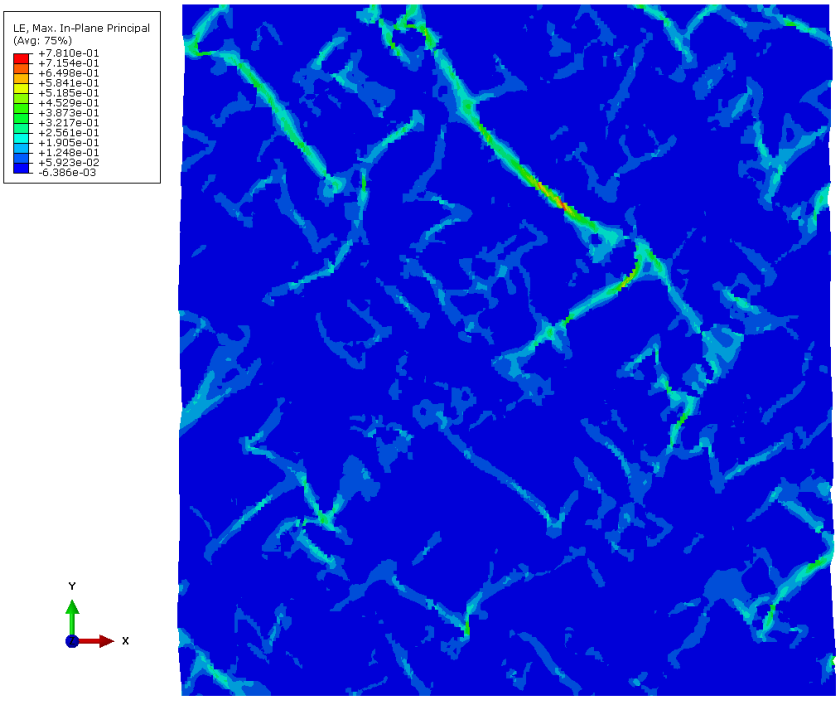

(b) Non-cohesive simulation

Figure 6.12: Representative maximum principal strain fields at 3.0% strain

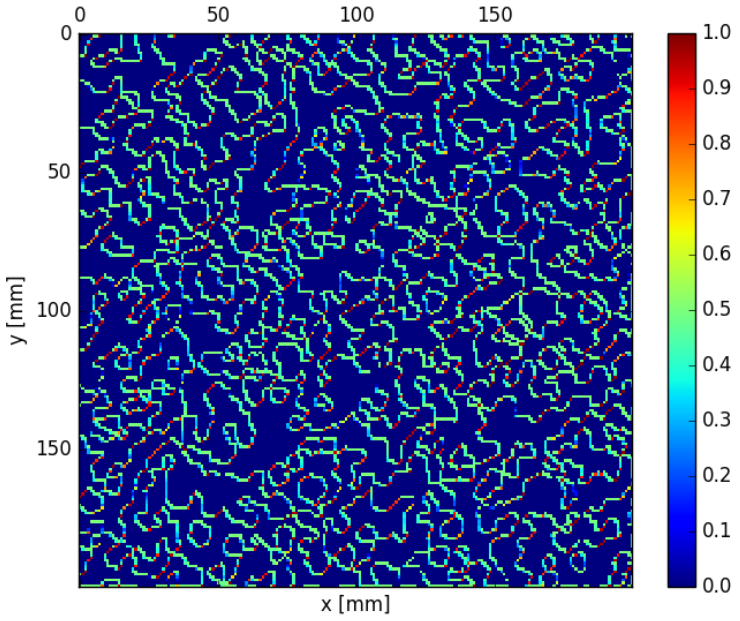

Figure 6.13: Representative cohesive simulation showing local damage, D_j, calculation on an element-by-element basis

and non-cohesive simulations as a function of volume fraction α-Mo. As before, each data point represents the average of ten instantiations of the same microstructure, and the error bars correspond to two standard deviations. The results of the DIP_{avg} calculation are shown at 1% and 3% macroscopic strain to show the deviation in the DIP_{avg} of the non-cohesive simulations from the DIP_{avg} of the cohesive simulations as a large number of cohesive elements fail in the cohesive simulations.

From Figure 6.14, the DIP_{avg} shows the correct trends at 1% macroscopic strain. At this strain, the DIP_{avg} decreases with increasing volume fraction of α-Mo. The DIP_{avg} is inversely correlated with the strain at the maximum tensile stress of the cohesive simulations and indicator of ductility. Thus, the DIP_{avg} correctly indicates increasing ductility with increasing volume fractions of α-Mo.

As cohesive elements fail in the cohesive simulations, they leave behind cracks with free surfaces, which are traction free. The stress is redistributed around the cracks in the cohesive simulations but not in the non-cohesive simulations, causing

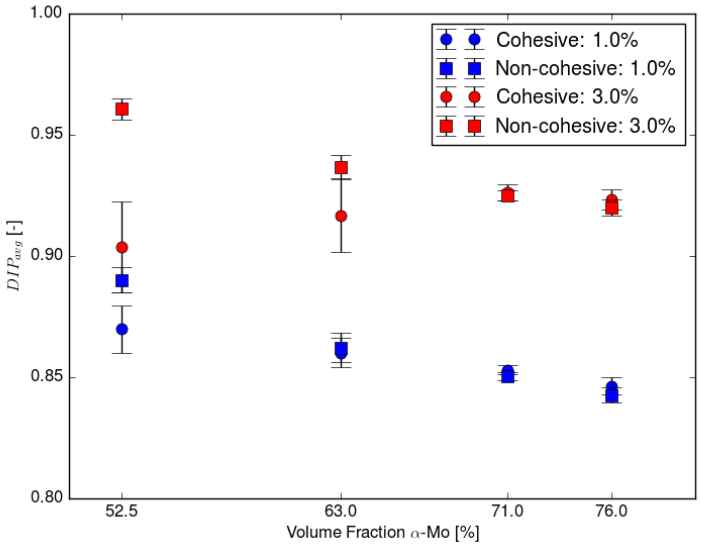

Figure 6.14: Average instantiation DIP_{avg} calculated at 1% and 3% macroscopic strain

differences in the stress and strain fields of the cohesive and non-cohesive simulations. Additionally, since the local damage, D_j, is calculated from the traction at the interface elements where cohesive elements are failing, the traction free surfaces in the cohesive simulations reduce the calculated local damage with respect to that of the non-cohesive simulations at the same macroscopic strain. In Figure 6.14, the failure of a large number of cohesive elements and the resulting free surfaces are the reason for the large differences between the calculated DIP_{avg} of the cohesive and non-cohesive simulations at low volume fractions of α-Mo, especially at a macroscopic strain of 3.0%.

Figure 6.14 also shows the limitations of the DIP_{avg} as cohesive elements fail on a large scale. At 3% macroscopic strain, a large number of cohesive elements have failed in the lower α-Mo volume fraction simulations indicating widespread damage formation; however, the DIP_{avg} is smaller than that of the larger α-Mo volume fraction simulations where few cohesive elements have failed as indicated by the good

agreement of the DIP_{avg} between the cohesive and non-cohesive simulations. Because the DIP_{avg} can only capture damage initiation and the percolation threshold of crack formation and not the widespread crack formation, propagation, and coalescence, care must be taken to ensure the DIP_{avg} is calculated and compared at a macroscopic strain small enough that a cohesive element simulation would not show widespread crack formation. Despite the differences between the DIP_{avg} calculation between cohesive and non-cohesive simulations at large macroscopic strains, at any particular volume fraction α-Mo the non-cohesive simulation DIP_{avg} correctly ranks the relative susceptibility to microcracking of each microstructure.

Although the volume average approach with DIP_{avg} is shown to yield good results for ranking relative susceptibility to microcracking, it is anticipated that a more thorough development of the DIP may extend the usefulness of this approach. If the DIP is evaluated according to extreme value statistics and includes the effects of spatial distribution of microcrack formation, it may be possible to capture the percolation threshold of crack initiation and propagation at which the non-cohesive simulations deviate from the cohesive simulations. Such a development would enable the DIP to build more detailed structure-property linkages by identifying specific microstructure characteristics driving the threshold at which microcracks begin to coalesce and limit the load bearing capacity of the material.

6.4.2 Using the DIP_{avg}

The damage indicator parameter developed for 2D microstructures is suitable for predicting relative amounts of damage initiation between differing microstructures prior to the formation of cracks on the order of grain size. When evaluated at a set strain, this parameter can be related to the relative susceptibility to microcracking of quasi-brittle alloys where local damage initiation controls failure. In the 2D simulations, excluding cohesive elements reduced the computation time by factor of 2 to 4

depending on the volume fraction of α-Mo present, where simulation with larger volume fractions of α-Mo tended to complete faster and show smaller improvements in computation time due to fewer sharp strain gradients caused by sharp transitions in properties of different phases after initial yielding. Sufficiently refined microstructure models in 3D without cohesive elements typically require between 5 and 30 hours to complete on a computing cluster at using 16 cpus, but may require as long as a week for instantiations with particularly sharp strain gradients. Extending the damage parameter to fully 3D volumes significantly reduces the amount of computational time required with respect to fully 3D cohesive zone models for a first order optimization of microstructure variation in Mo-Si-B alloys between the competing properties of strength, fatigue, and relative damage tolerance.

6.5 Temperature and Si Content Effects

Before the DIP can be used in a broad microstructure parametric study of triplex Mo-Si-B alloys, the damage initiation displacement, δ_i^0, for the α-Mo/intermetallic intergranular interfaces must be made a function of temperature and α-Mo Si content. This is achieved by making the material properties of for the damage law, specifically $T_{max|\alpha-Mo/A15}$ and $T_{max|\alpha-Mo/T2}$ shown in Table 6.3, functions of temperature and Si content. For the estimated effects of temperature and Si content on the interface strength of the α-Mo/intermetallic grain boundaries, the material properties in Table 6.3 are treated as the room temperature and Mo-0.00Si calibration and are scaled first by an α-Mo Si content scaling factor and then by a temperature scaling factor.

The mechanical behavior of the α-Mo phase is strongly dependent on the Si content of the phase. Further, Si tends to segregate at grain boundaries and reduce the grain boundary strength and, consequently, reduces the fracture toughness. The most complete study on the effects of Si content was previously discussed in Chapter 2 and

includes the effects of Si on the room temperature fracture toughness of polycrystalline α-Mo material [38]. Figure 6.15 presents the dependence of fracture toughness on Si content of the α-Mo phase [38]. This data provides a relatively smooth function for the Si content effects on fracture toughness. A log function fits the data quite well; however, due to the sharp difference in mechanical behavior and active deformation mechanisms between pure Mo and α-Mo with any small additions of Si, a second order polynomial is fit to the α-Mo data with non-zero Si content and the result is scaled by the pure Mo fracture toughness. The resulting scale factors for the Si content calibrations included in the final parametric study are included in Table 6.4.

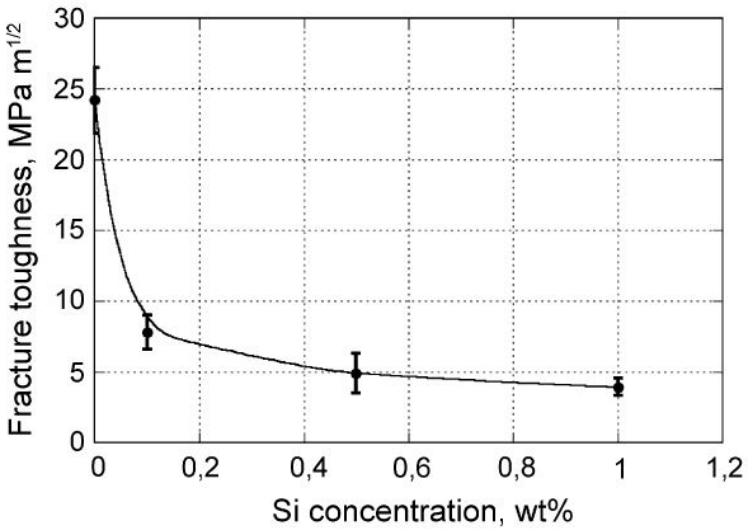

Figure 6.15: α-Mo room temperature fracture toughness as a function of Si content [38]

Table 6.4: Interfacial strength reduction factors as a function of α-Mo Si content

α-Mo Si content [wt.% Si]	0.00	0.10	0.25	0.50	0.75	1.00
Reduction Factor	1.00	0.322	0.268	0.202	0.167	0.161

There is no experimental data relating the chemical compositions of the intermetallics to changes in fracture toughness. While it is possible for either phase to

have small variations in Si content, and early approximation must be to assume that the fracture toughness of these phases do not change with variations in Si content. In the parametric study presented in Chapter 7, variations in chemical composition of the intermetallics is not addressed. Additionally, in the fully 3D simulations, the DIP does not account for cleavage of the intermetallics so no calibration of the intermetallic fracture toughness is pursued in this work.

The fracture toughness of the intermetallics, K_{A15} and K_{T2}, are already functions of temperature [118], but the interfacial strengths between the α-Mo phase and the intermetallics, $T_{max|\alpha\text{-}Mo/A15}$ and $T_{max|\alpha\text{-}Mo/T2}$, require a temperature calibration. The temperature dependence of the interfacial strengths cannot be estimated as smooth functions of temperature; however, differences in fracture toughness between room temperature and 1300°C are reported for several triplex Mo-Si-B alloys with a continuous α-Mo matrix [19]. Table 6.5 presents the fracture toughness of two similar triplex Mo-Si-B alloys with continuous α-Mo phase [19]. Therefore, the fracture toughness is expected to increase from approximately 7 MPa$\sqrt{\text{m}}$ at room temperature to approximately 24 MPa$\sqrt{\text{m}}$ at 1300°C. This represents of factor of three or four increase in the fracture toughness of triplex Mo-Si-B over this temperature range. The parametric study presented in Chapter 7 is conducted at room temperature and 1400°C, so a factor of three is chosen as an approximate increase in the interfacial strength from room temperature to 1400°C.

Table 6.5: Temperature dependent fracture toughness of two triplex Mo-Si-B alloys with a continuous α-Mo matrix [19]

Alloy	Fracture Toughness MPa$\sqrt{\text{m}}$	
	25°C	1300°C
ULTMAT [127]	7.8	22
Middlemas [203]	7.1	26

6.6 Summary

A novel damage indicator parameter (DIP) is developed that can be used as a surrogate for susceptibility to brittle microcrack formation in Mo-Si-B alloys without the use of cohesive elements. A validation study shows that the DIP indicates decreasing damage, and a corresponding increase in the strain at maximum tensile stress, with increasing volume fraction of the ductile matrix phase, which is shown to be consistent with the trends predicted by the more computationally expensive cohesive simulation predictions.

Finally, the calibration of the damage initiation displacement, δ_i^0, is presented as a function of α-Mo Si content and temperature for use in the 3D triplex Mo-Si-B parametric study presented in Chapter 7.

6.7 Significance

The novel reduced order DIP modeling approach facilitates the design of fully 3D microstructures using a quantitative measure for relative interface average damage as one of the targeted design objectives. This reduced order approach significantly reduces the computational cost in estimating susceptibility to microcracking from the cost of cohesive zone elements.

CHAPTER VII

PARAMETRIC STUDY OF TRIPLEX MO-SI-B

7.1 Introduction

Three modeling tools are required for microstructural modeling of polycrystalline metals at the grain scale: microstructure generators to re-create synthetic, statistically accurate microstructures, crystal viscoplasticity constitutive equations implemented for use with finite element solvers, and post-processing tools to evaluate important mechanical properties. This chapter presents the results of applying the microstructure-sensitive mechanical property modeling workflow, shown in Figure 7.1, to the mechanical property optimization of triplex Mo-Si-B alloys containing the α-Mo, A15, and T2 phases.

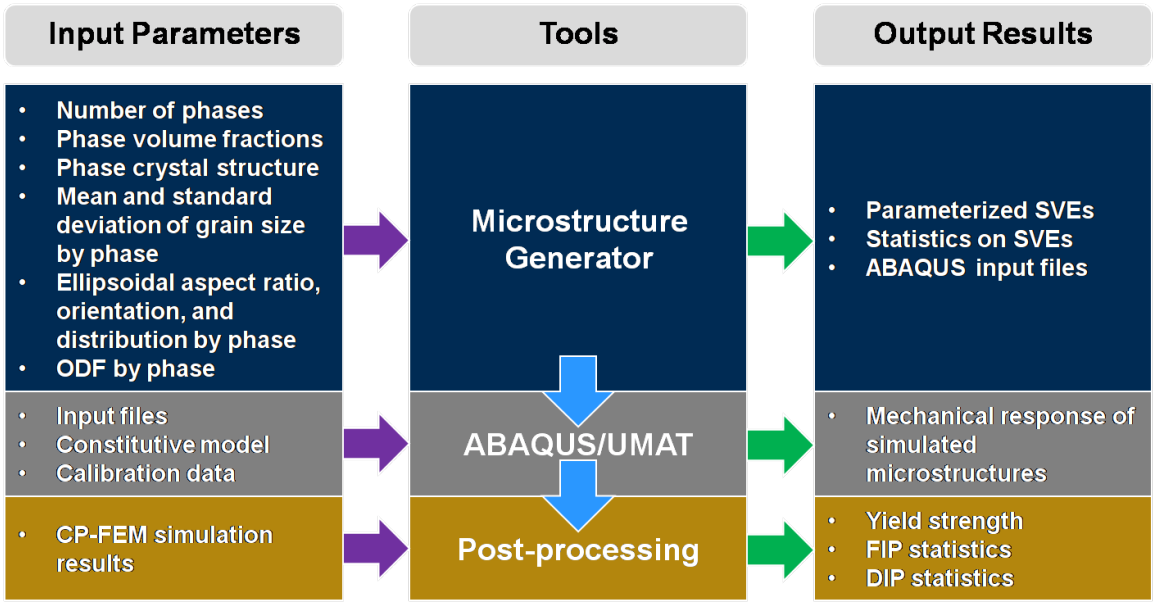

Figure 7.1: Microstructure-sensitive mechanical property modeling workflow

7.2 Scope of Study

The parametric study is designed to help determine an optimized triplex Mo-Si-B microstructure that balances strength, fatigue life, and susceptibility to microcracking. The volume fraction of the α-Mo phase varies from 0.45 to 0.8, with the intermetallic phases maintaining a constant ratio of 1:2 A15 to T2 phase to fill the remaining volume fraction. The Si content of the α-Mo varies from zero to one weight percent Si. Each microstructure has a random texture with randomly orientated grain shapes. Finally, the effects of grain size are evaluated with volume elements of differing mean grain sizes with 63% volume fraction α-Mo. In total, eight sets of volume elements are created according to the microstructure characteristics shown in Table 7.1, where SVE1 through SVE6 reflect the α-Mo volume fraction variation and SVE7 and SVE8 address the role of grain size.

To examine the effects of the volume element instantiations themselves, six separate synthetic volume element instantiations are created for each SVE. The full parametric study is carried out at both room temperature and 1400°C with the parameters given in Tables 7.2 and 7.3.

A baseline microstructure is taken from Jain and Kumar [29] and from sample material provided by the Pratt & Whitney to ensure the parametric study spans a promising and useful portion of the possible Mo-Si-B microstructures. In the Jain and Kumar microstructure, the α-Mo phase has an average grain diameter of 20 μm and a volume fraction of 0.511, while the intermetallic phases have grain diameter averages of 15 μm with 0.170 volume fraction Mo_3Si and the remainder made up of the T2 phase.

Table 7.1: Parametric study microstructure parameters

Parameter	**SVE1**	**SVE2**	**SVE3**	**SVE4**	**SVE5**	**SVE6**	**SVE7**	**SVE8**
Edge length $[mm]$	0.090	0.090	0.090	0.090	0.090	0.090	0.900	0.009
Number of elements per edge	33	33	33	33	33	33	33	33
Vv α-Mo	0.45	0.54	0.63	0.71	0.76	0.80	0.63	0.63
Vv A15	0.37	0.31	0.25	0.19	0.16	0.13	0.25	0.25
Vv T2	0.18	0.15	0.12	0.10	0.08	0.07	0.12	0.12
α-Mo mean dia. $[\mu m]$	10	10	10	10	10	10	100	1
α-Mo std. dev. dia. $[\mu m]$	2	2	2	2	2	2	20	0.02
A15 mean dia. $[\mu m]$	8	8	8	8	8	8	80	0.80
A15 std. dev. dia. $[\mu m]$	1	1	1	1	1	1	10	0.01
T2 mean dia. $[\mu m]$	8	8	8	8	8	8	80	0.80
T2 std. dev. dia. $[\mu m]$	1	1	1	1	1	1	10	0.01
α-Mo mean aspect ratio [-]	0.80	0.80	0.80	0.80	0.80	0.80	0.80	0.80
α-Mo std. dev. aspect ratio [-]	0.08	0.08	0.08	0.08	0.08	0.08	0.08	0.08
A15 mean aspect ratio [-]	0.80	0.80	0.80	0.80	0.80	0.80	0.80	0.80
A15 std. dev. aspect ratio [-]	0.08	0.08	0.08	0.08	0.08	0.08	0.08	0.08
T2 mean aspect ratio [-]	0.80	0.80	0.80	0.80	0.80	0.80	0.80	0.80
T2 std. dev. aspect ratio [-]	0.08	0.08	0.08	0.08	0.08	0.08	0.08	0.08

Table 7.2: Complete parametric study at room temperature with simulation nomenclature: SVEX-Y-Z. X is the volume element microstructural parameters. Y is the instantiation number. Z is the α-Mo CVP parameter set.

α-Mo volume fraction [-]	**Si content [wt.%]**					
	0.00	0.10	0.25	0.50	0.75	1.00
0.45	SVE1-Y-1	SVE1-Y-1b	SVE1-Y-2	SVE1-Y-3	SVE1-Y-4	SVE1-Y-5
0.54	SVE2-Y-1	SVE2-Y-1b	SVE2-Y-2	SVE2-Y-3	SVE2-Y-4	SVE2-Y-5
0.63	SVE3-Y-1	SVE3-Y-1b	SVE3-Y-2	SVE3-Y-3	SVE3-Y-4	SVE3-Y-5
0.71	SVE4-Y-1	SVE4-Y-1b	SVE4-Y-2	SVE4-Y-3	SVE4-Y-4	SVE4-Y-5
0.76	SVE5-Y-1	SVE5-Y-1b	SVE5-Y-2	SVE5-Y-3	SVE5-Y-4	SVE5-Y-5
0.80	SVE6-Y-1	SVE6-Y-1b	SVE6-Y-2	SVE6-Y-3	SVE6-Y-4	SVE6-Y-5

Table 7.3: Complete parametric study at 1400°C with simulation nomenclature: SVEX-Y-Z. X is the volume element microstructural parameters. Y is the instantiation number. Z is the α-Mo CVP parameter set.

α-Mo volume fraction [-]	**Si content [wt.%]**					
	0.00	0.10	0.25	0.50	0.75	1.00
0.45	SVE1-Y-6	SVE1-Y-6b	SVE1-Y-7	SVE1-Y-8	SVE1-Y-9	SVE1-Y-10
0.54	SVE2-Y-6	SVE2-Y-6b	SVE2-Y-7	SVE2-Y-8	SVE2-Y-9	SVE2-Y-10
0.63	SVE3-Y-6	SVE3-Y-6b	SVE3-Y-7	SVE3-Y-8	SVE3-Y-9	SVE3-Y-10
0.71	SVE4-Y-6	SVE4-Y-6b	SVE4-Y-7	SVE4-Y-8	SVE4-Y-9	SVE4-Y-10
0.76	SVE5-Y-6	SVE5-Y-6b	SVE5-Y-7	SVE5-Y-8	SVE5-Y-9	SVE5-Y-10
0.80	SVE6-Y-6	SVE6-Y-6b	SVE6-Y-7	SVE6-Y-8	SVE6-Y-9	SVE6-Y-10

7.3 Simulations

Figure 7.2 shows the example triplex Mo-Si-B SVE instantiation with 63% α-Mo volume fraction first shown in Chapter 4. The triplex Mo-Si-B SVEs have 33 elements

per edge and have an edge length of 90 μm. The grain size study SVEs differ in edge length by one order of magnitude corresponding to the order of magnitude change in grain size, where SVE7 has an edge length of 900 μm and SVE8 has an edge length of 9 μm. Each SVE contains approximately 300 grains in total.

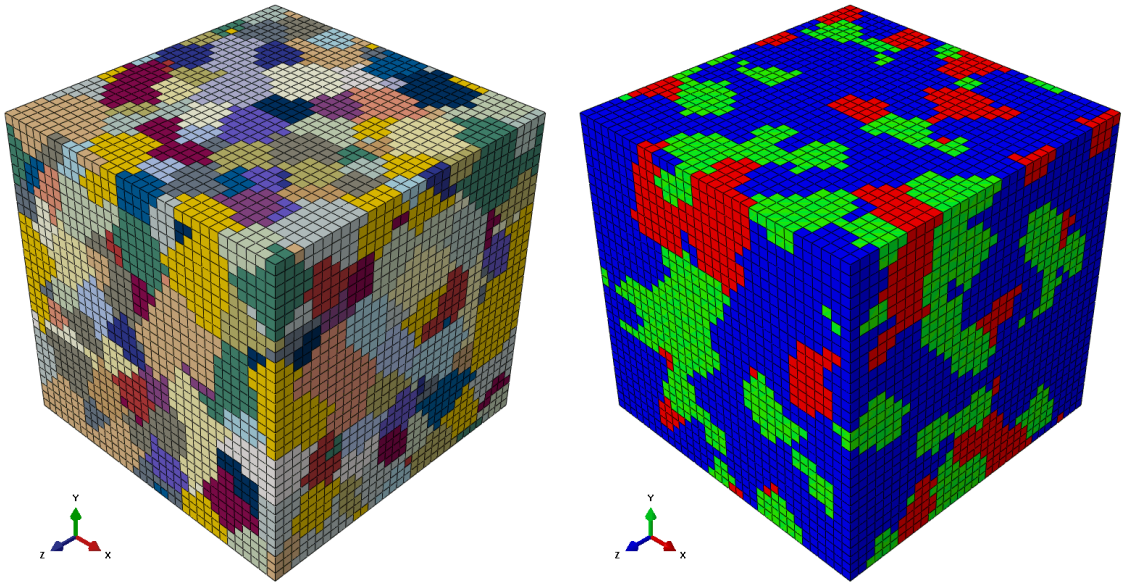

(a) Colors assigned by unique grains

(b) Colors assigned by phase. Blue: α-Mo. Green: A15. Red: T2.

Figure 7.2: Triplex Mo-Si-B synthetic microstructure with 63% volume fraction α-Mo.

The simulations consist of one fully reversed fatigue cycle with a mechanical strain amplitude of 0.5% strain applied along the Y-axis (vertical direction in Figure 7.2). Periodic boundary conditions are applied to all six faces of the SVE, consistent with the periodic packing of ellipsoids in the microstructure generator. Rigid body motion is eliminated by fixing the corner vertex node of the model that corresponds to the global coordinate system origin and application of restrictions on the remaining model vertex nodes consistent with periodic boundary conditions. Loading is applied through displacement along the global Y axis of the vertex node in the corner opposite from the origin.

An example simulation macroscopic stress-strain plot is shown in Figure 7.3 for

the 63% α-Mo SVE as function of Si content and temperature. The corresponding monotonic stress-strain curves are shown in Figure 7.4. These plots show the effects of solid solution softening of the α-Mo phase at room temperature, where the yield strength of the Mo-0.10Si α-Mo is lower than that of the Mo-0.00Si α-Mo. The extreme ranges of strength in this parametric study result in large variations in cyclic plastic strain at the fixed macroscopic strain amplitude of 0.5% mechanical strain.

A strain range including macroscopic plasticity is chosen to reflect the low cycle and thermomechanical fatigue conditions which typically drive life limiting fatigue crack initiation in gas turbine engine components and is the focus of Ni-base superalloy studies for applicability to the gas turbine engine environment [2, 204–211]. The constitutive law implementation from this work cannot currently handle thermomechanical simulations, but has been calibrated over a range of temperatures to facilitate future development for thermomechanical fatigue simulations, which are important to optimizing Mo-Si-B alloys for use in gas turbine engines. While large strain ranges are simulated in this parametric study, the tools and SVEs would be equally well suited for isothermal simulations of macroscopically elastic cycles with small amounts of local plasticity developing as a result of microstructure constraints.

The size and mesh density of the SVEs are chosen for a balance between converged elastic modulus and yield strength and efficient computation times. In total this work includes 576 simulations in the parametric study alone. Each simulation required between 8 and 30 hours to complete, with some extreme examples requiring as many as 48 hours and the majority of simulations requiring approximately 14 hours.

The simulations with higher α-Mo Si content and lower α-Mo volume fraction SVEs required the most time to complete. The difference in computation time is largely determined by the difficulty of solving the FE simulation during plastic deformation with large stress gradients between phases and the difference between plastically deforming grains next to elastically deforming grains. Simulations of one full

fatigue cycle at 1% macroscopic strain range take significantly longer than monotonic simulations or simulations without macroscopic plastic deformation.

Unlike the FE simulations, the time required for post-processing is quite consistent at about two minutes per simulation; and the full set of post-processing can be completed in less than 24 hours. Creating a full suite of plots based on the post-processed data can be accomplished in less than an hour after the post-processing is complete.

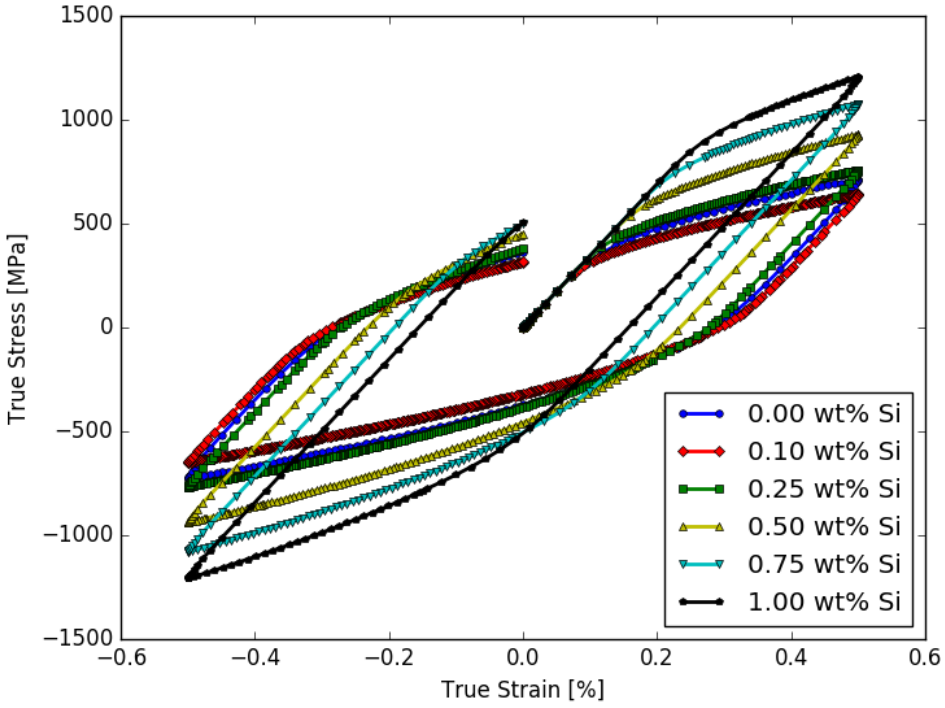

(a) Room temperature

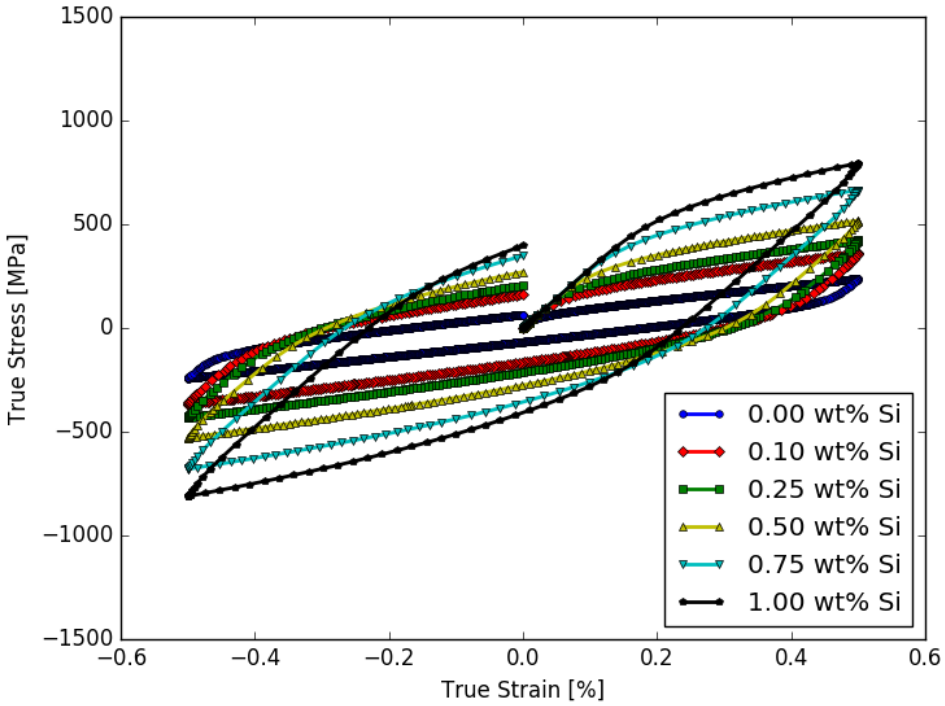

(b) 1400 °C

Figure 7.3: Cyclic stress-strain response of triplex Mo-Si-B SVE with 63% volume fraction α-Mo as a function of Si content and temperature

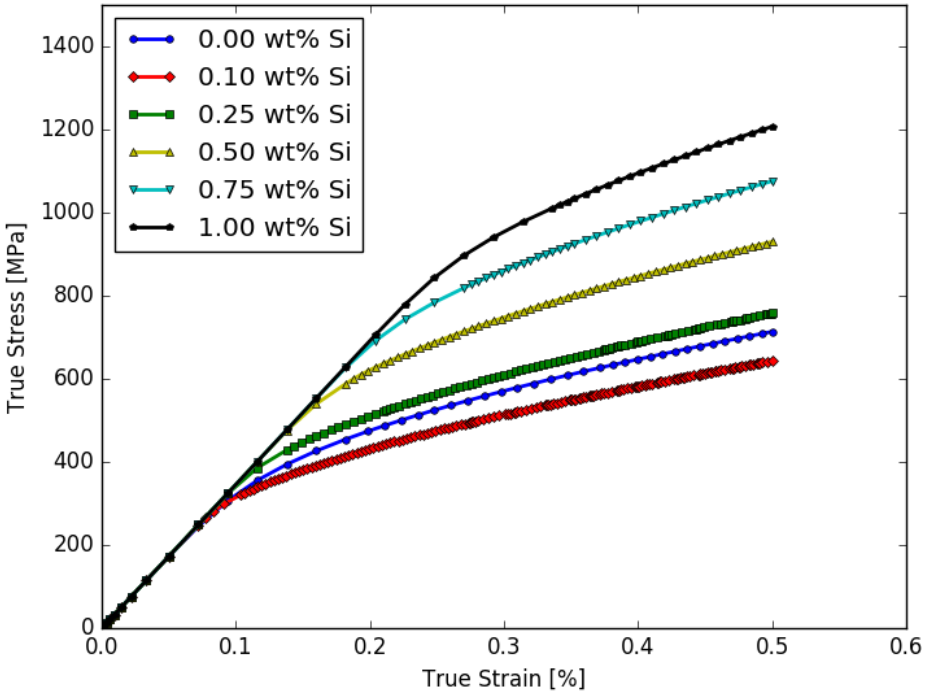

(a) Room temperature

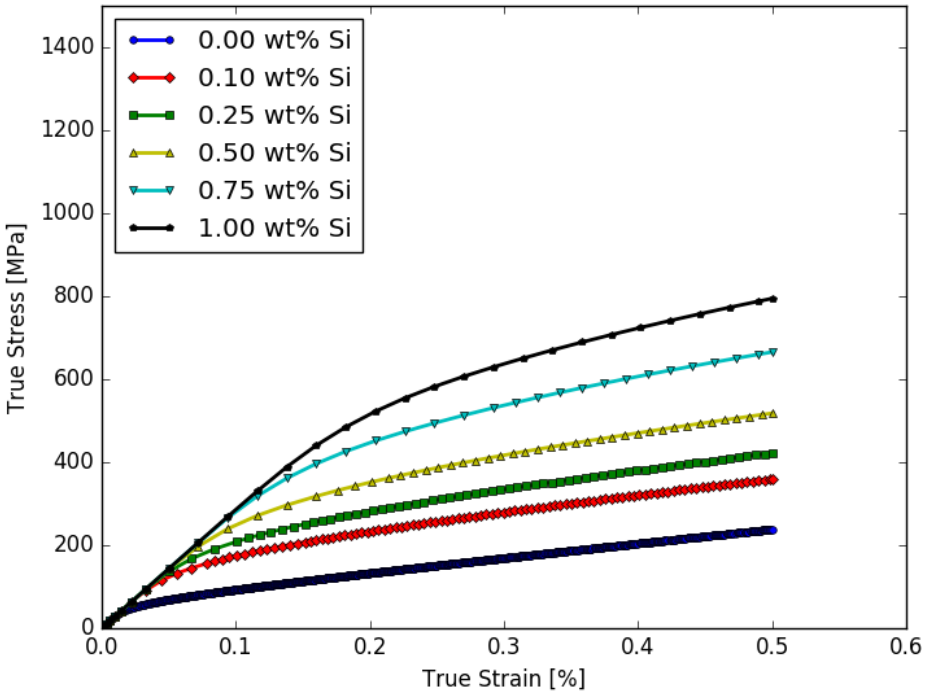

(b) 1400 °C

Figure 7.4: Monotonic tension stress-strain response of triplex Mo-Si-B SVE with 63% volume fraction α-Mo as a function of Si content and temperature

7.4 Results

7.4.1 Elastic Modulus

The elastic modulus is calculated from the volume averaged stress-strain response in the elastic portion of the initial loading, which is calculated most simply from the load and displacement of the controlling node and dividing by the model's cross-sectional area and edge length, respectively. Validation of this approach was performed by volume averaging the stress-strain response of each individual element. The elastic modulus predictions as a function of α-Mo volume fraction at both room temperature and 1400°C are presented in Figure 7.5. Because the elastic tensor properties of α-Mo are assumed to be invariant with α-Mo Si content, the elastic modulus predictions do not vary with α-Mo Si content, as shown in Figure 7.6 for an α-Mo volume fraction of 63%. Each data point in these plots represents the mean modulus calculated from six instantiations of the same microstructural parameters. The bars represent two standard deviations of the calculated elastic modulus.

These plots show that the volume averaged elastic modulus in the loading direction is consistent between SVE instantiations targeting the same α-Mo volume fraction, despite the relatively large variation in the final volume fraction of α-Mo which varies between instantiations. Better control over the variation in final α-Mo volume fractions is quite difficult without a significant increase in SVE volume. However, the variation in final volume fraction for any given instantiation lies within the separation of target volume fractions in the parametric study, and there is a clear and correct trend of decreasing modulus with increasing volume fraction α-Mo in the resulting modulus predictions. Therefore the volume element instantiations are considered to be sufficiently accurate to the target volume fraction for the purposes of this broad microstructure study. However, it is understood that some of the variation in predicted mechanical properties at fixed targeted α-Mo volume fractions is a result of the variation in the actual α-Mo volume fraction between instantiations.

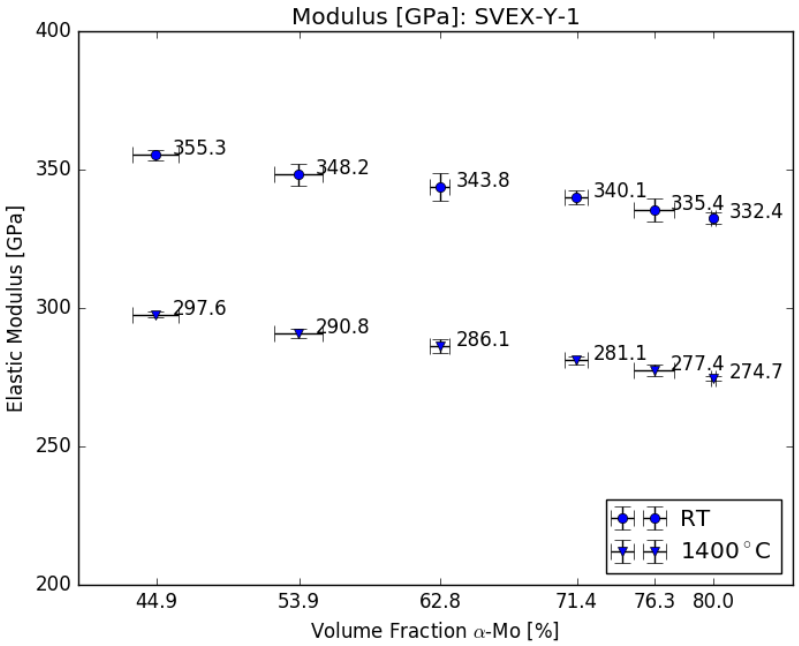

Figure 7.5: Predicted elastic modulus over six instantiations of SVEs for triplex Mo-Si-B with Mo-0.00Si α-Mo CVP parameter set. Bars represent two standard deviations.

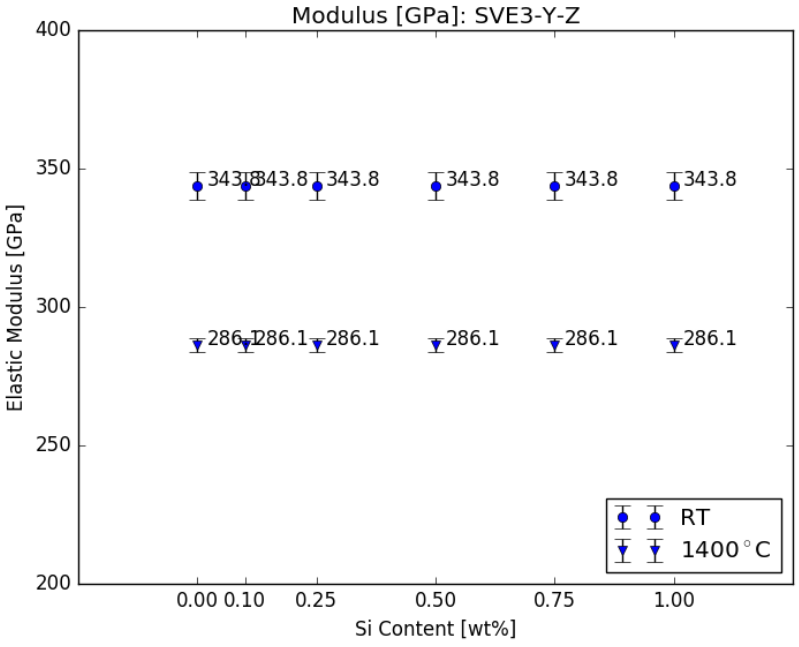

Figure 7.6: Variation in elastic modulus over six instantiations of SVEs with a Mo-1.00Si CVP parameter set. Bars represent two standard deviations.

The influence of α-Mo volume fraction and Si content on the elastic modulus are presented together as surface plots in Figure 7.7.

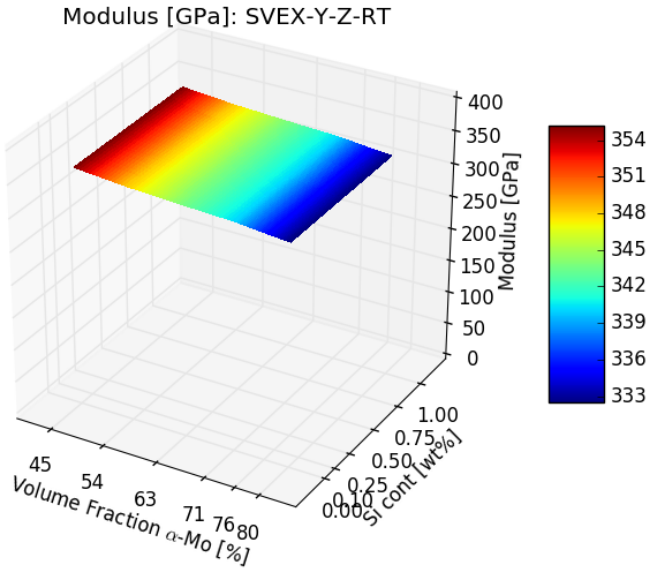

(a) Room temperature

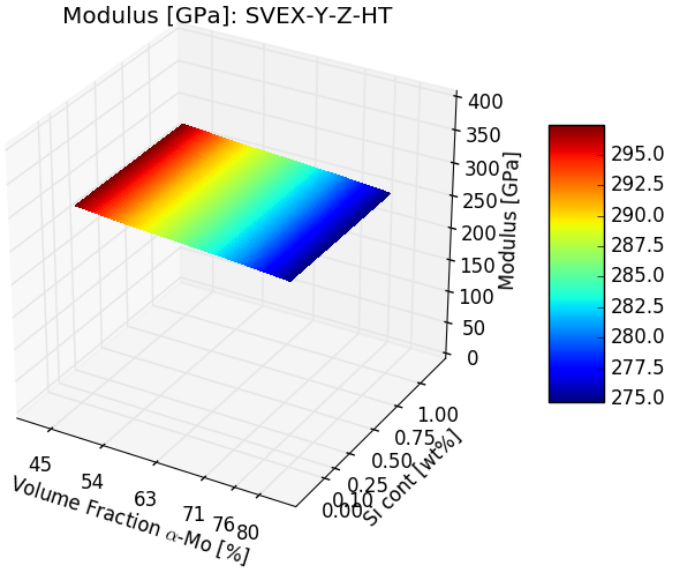

(b) 1400°C

Figure 7.7: Predicted elastic modulus as a function of α-Mo volume fraction and α-Mo Si content

7.4.2 Yield Strength

Yield strength is calculated as an 0.02% offset strength from the volume averaged stress-strain response of the monotonic initial loading step, where the volume average stress-strain response is calculated in the same manner as for the modulus calculations. Figures 7.8-7.13 present the uniaxial yield strength predictions as a function of α-Mo volume fraction and temperature for each α-Mo Si content. As with the elastic modulus predictions, the yield strength shows very little variation as a function of instantiation at each combination of α-Mo volume fraction and α-Mo Si content. The simulations also capture the expected trends of decreasing strength with increasing α-Mo volume fraction and decreasing strength with increasing temperature.

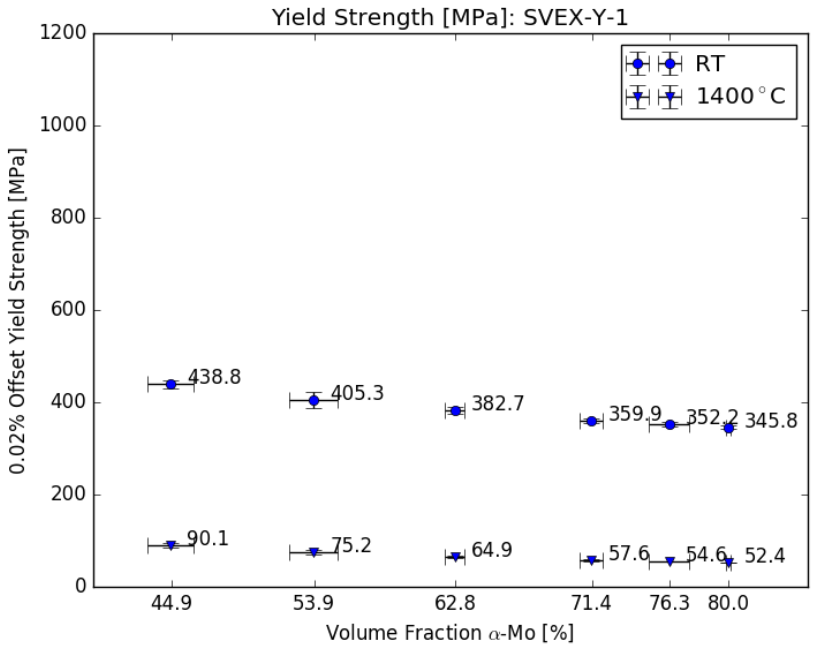

Figure 7.8: Predicted 0.02% offset yield strengths for triplex Mo-Si-B averaged over six instantiations of SVEs for each α-Mo volume fraction with a Mo-0.00Si CVP parameter set. Bars represent two standard deviations.

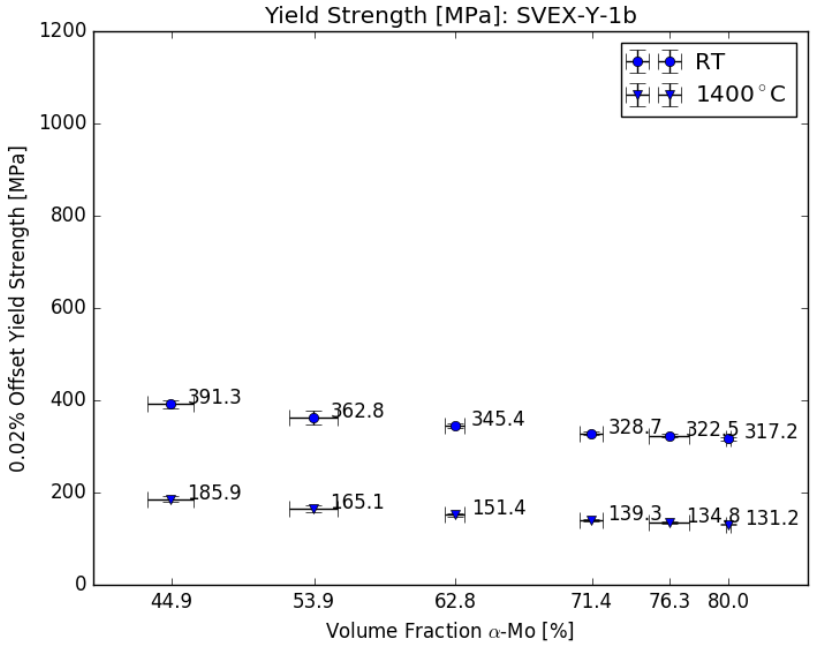

Figure 7.9: Predicted 0.02% offset yield strengths for triplex Mo-Si-B averaged over six instantiations of SVEs for each α-Mo volume fraction with a Mo-0.10Si CVP parameter set. Bars represent two standard deviations.

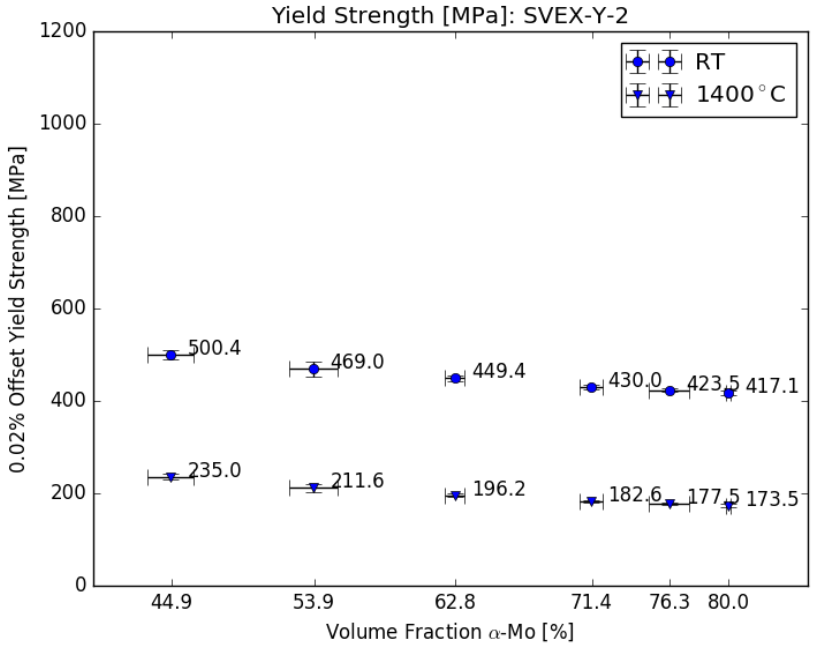

Figure 7.10: Predicted 0.02% offset yield strengths for triplex Mo-Si-B averaged over six instantiations of SVEs for each α-Mo volume fraction with a Mo-0.25Si CVP parameter set. Bars represent two standard deviations.

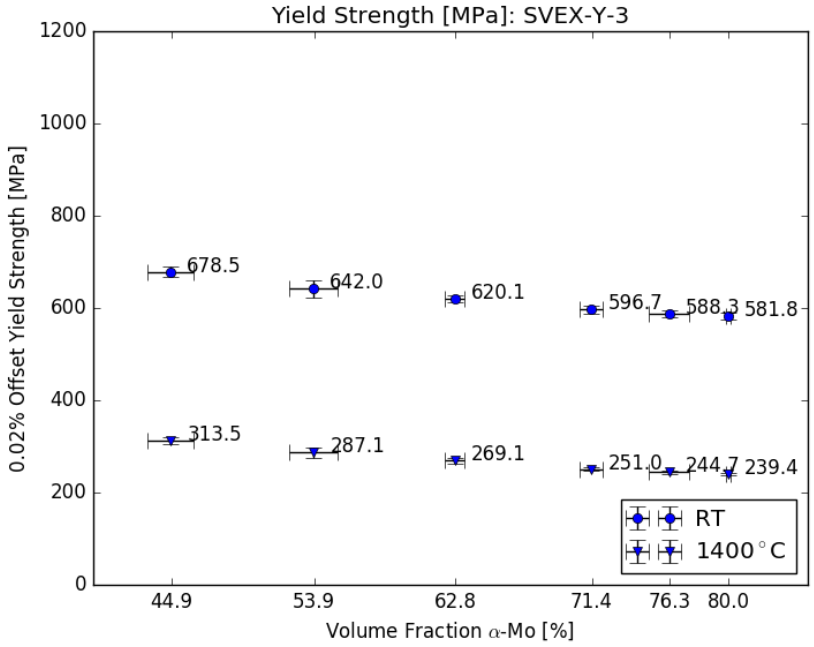

Figure 7.11: Predicted 0.02% offset yield strengths for triplex Mo-Si-B averaged over six instantiations of SVEs for each α-Mo volume fraction with a Mo-0.50Si CVP parameter set. Bars represent two standard deviations.

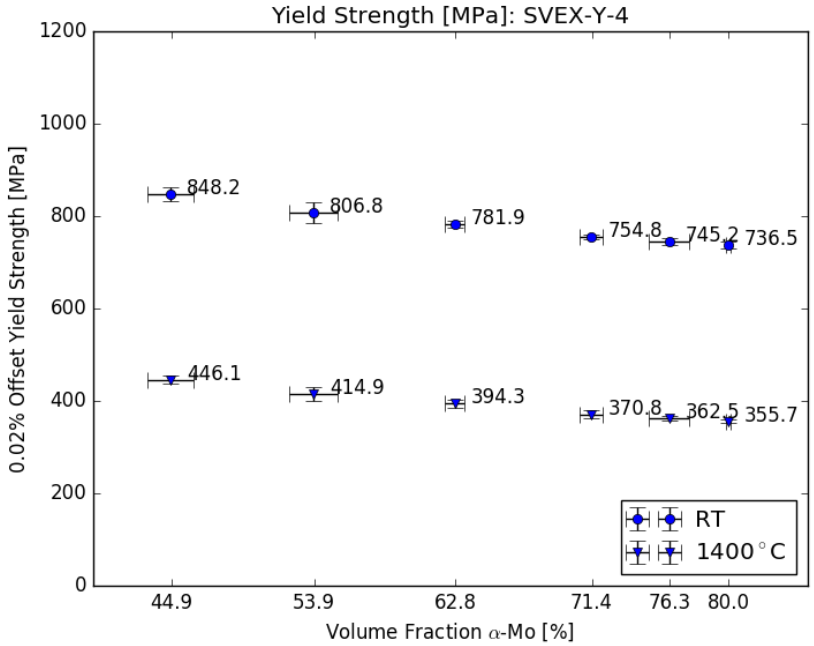

Figure 7.12: Predicted 0.02% offset yield strengths for triplex Mo-Si-B averaged over six instantiations of SVEs for each α-Mo volume fraction with a Mo-0.75Si CVP parameter set. Bars represent two standard deviations.

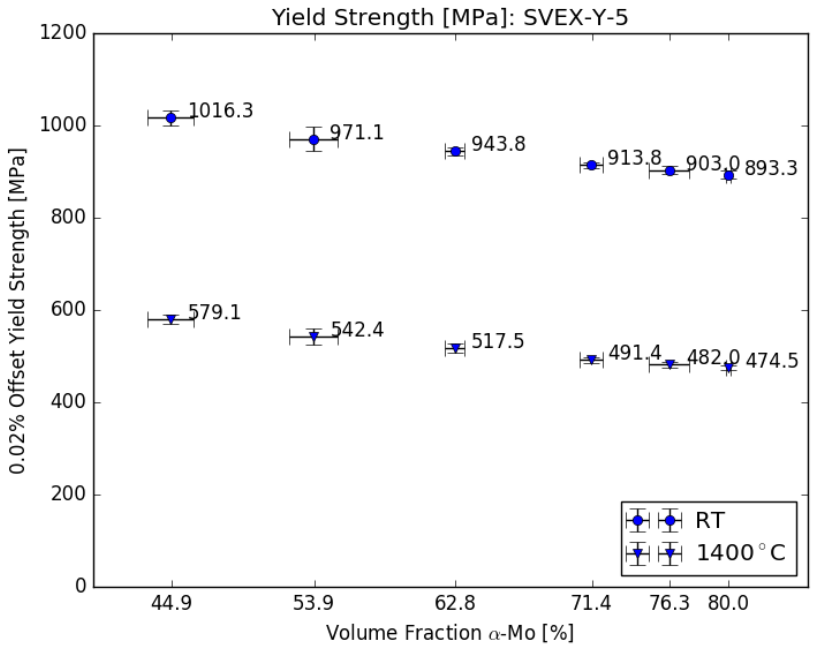

Figure 7.13: Predicted 0.02% offset yield strengths for triplex Mo-Si-B averaged over six instantiations of SVEs for each α-Mo volume fraction with a Mo-1.00Si CVP parameter set. Bars represent two standard deviations.

Figures 7.14-7.19 present the same yield strength predictions as a function of Si content and temperature at each α-Mo volume fraction. At 1400°C these plots more clearly show the expected trend of increasing strength with increasing Si content; however, at room temperature, they show the effects of solid solution softening between the Mo-0.00Si and Mo-0.10Si materials.

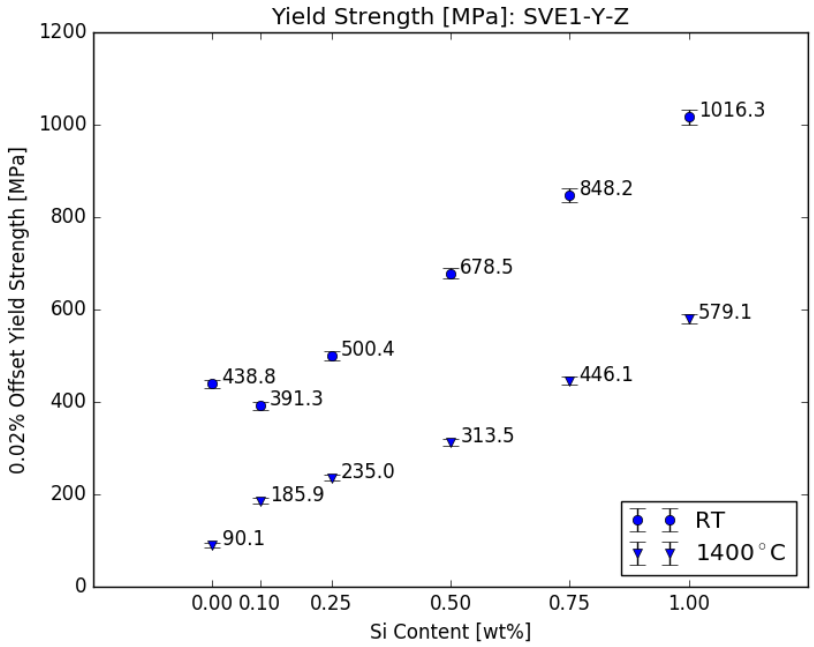

Figure 7.14: Predicted 0.02% offset yield strengths for triplex Mo-Si-B averaged over six instantiations of SVEs for each α-Mo Si content at 45% volume fraction α-Mo. Bars represent two standard deviations.

Finally, the influence of α-Mo volume fraction and Si content on yield strength are presented together as surface plots in Figure 7.20.

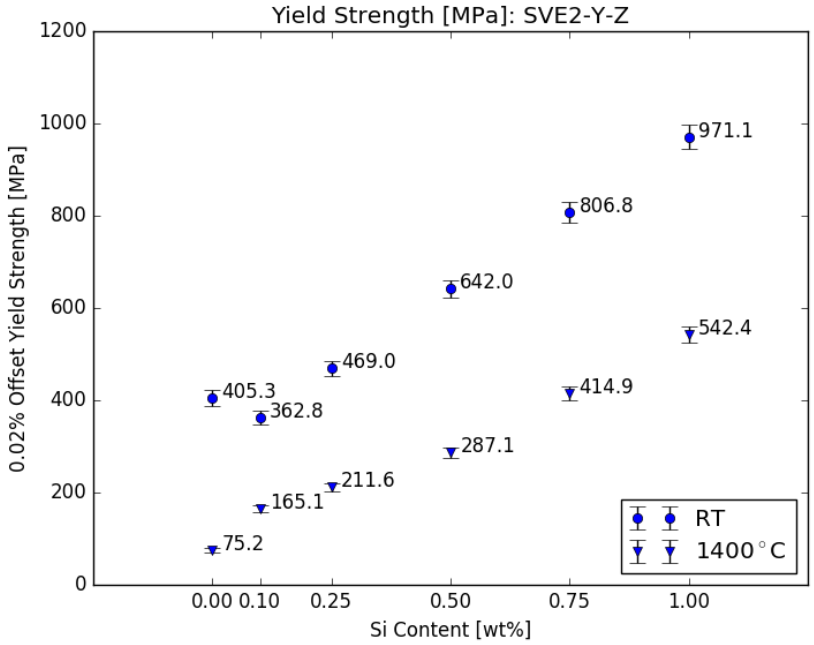

Figure 7.15: Predicted 0.02% offset yield strengths for triplex Mo-Si-B averaged over six instantiations of SVEs for each α-Mo Si content at 54% volume fraction α-Mo. Bars represent two standard deviations.

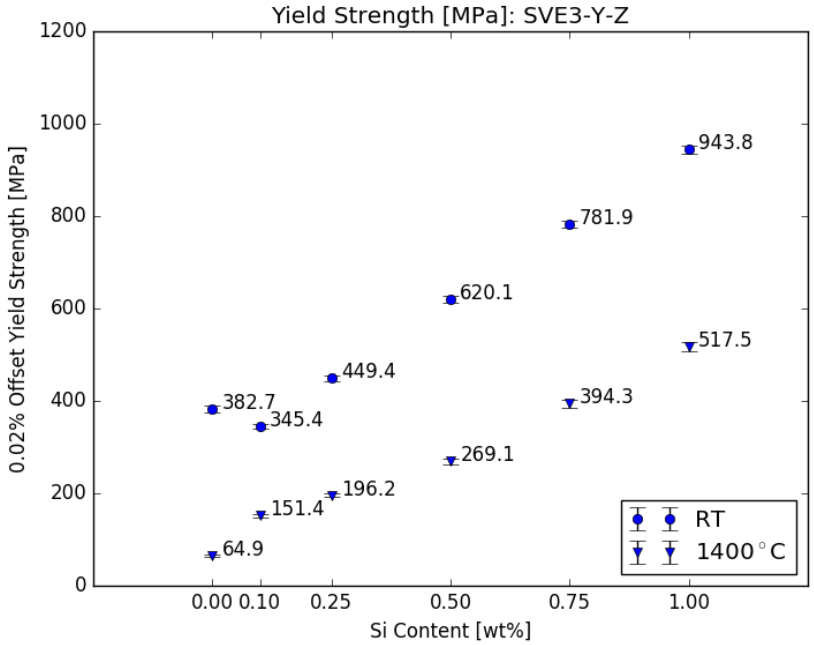

Figure 7.16: Predicted 0.02% offset yield strengths for triplex Mo-Si-B averaged over six instantiations of SVEs for each α-Mo Si content at 63% volume fraction α-Mo. Bars represent two standard deviations.

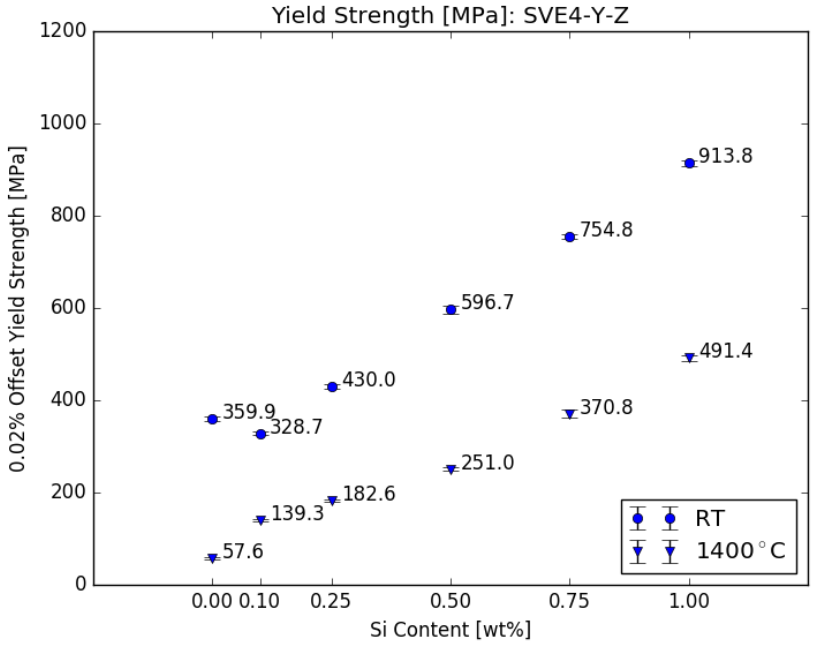

Figure 7.17: Predicted 0.02% offset yield strengths for triplex Mo-Si-B averaged over six instantiations of SVEs for each α-Mo Si content at 71% volume fraction α-Mo. Bars represent two standard deviations.

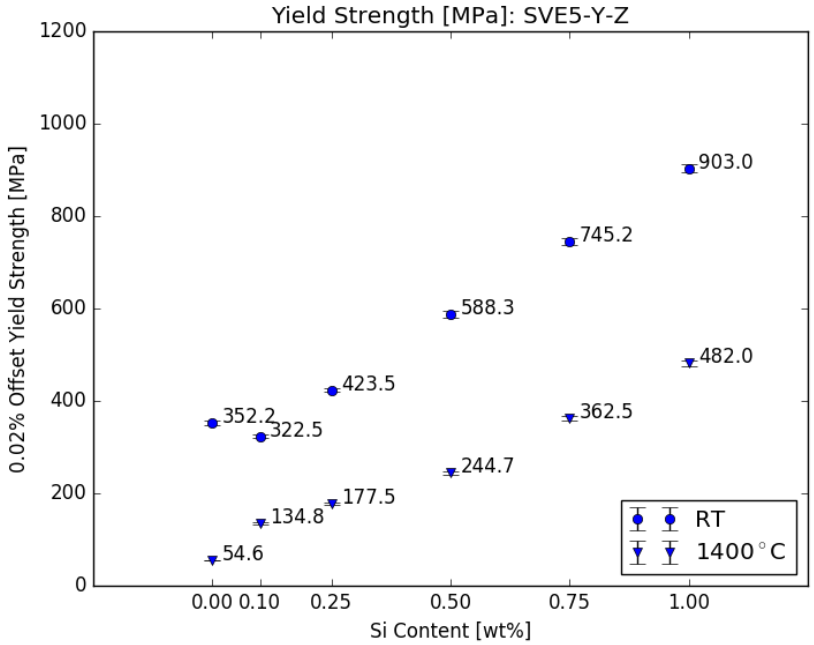

Figure 7.18: Predicted 0.02% offset yield strengths for triplex Mo-Si-B averaged over six instantiations of SVEs for each α-Mo Si content at 76% volume fraction α-Mo. Bars represent two standard deviations.

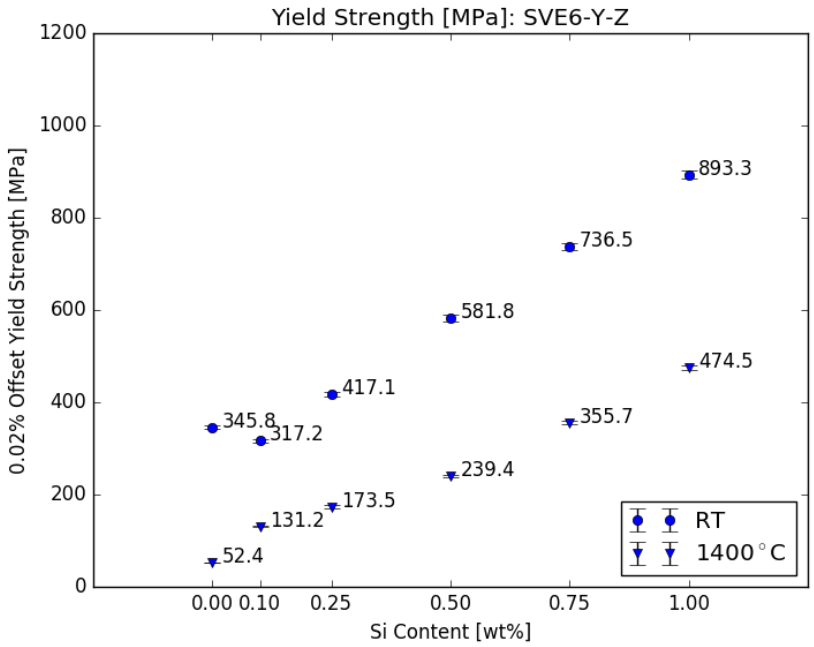

Figure 7.19: Predicted 0.02% offset yield strengths for triplex Mo-Si-B averaged over six instantiations of SVEs for each α-Mo Si content at 80% volume fraction α-Mo. Bars represent two standard deviations.

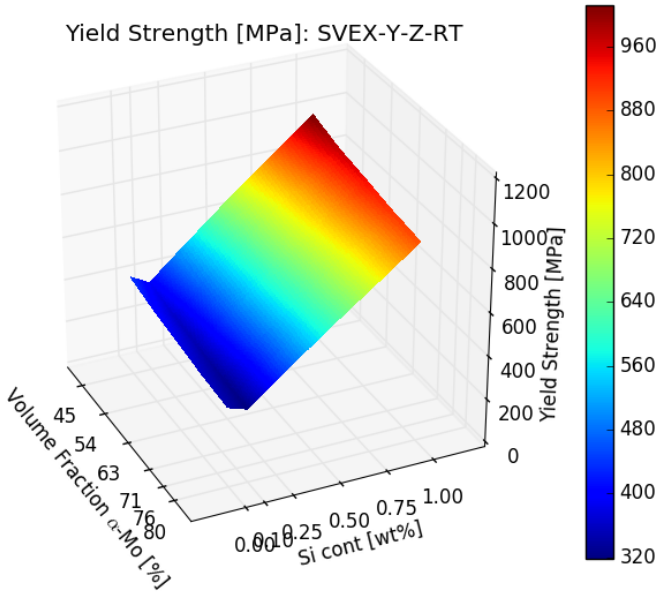

(a) Room temperature

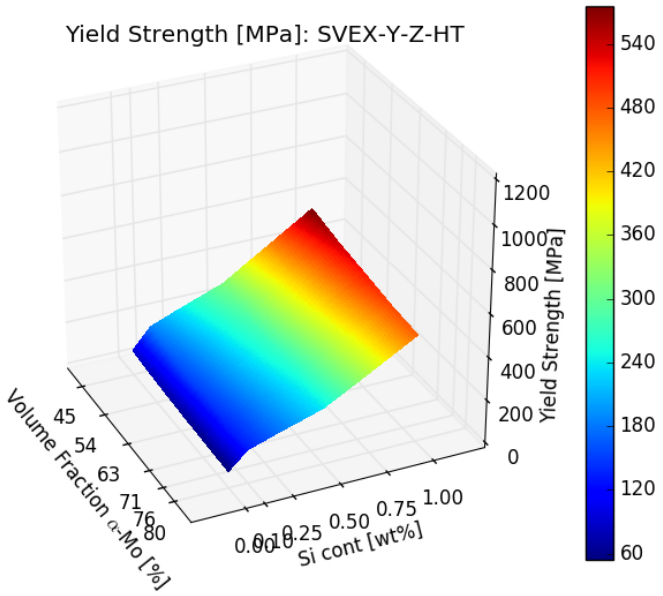

(b) 1400°C

Figure 7.20: Predicted 0.02% yield strengths as a function of temperature and α-Mo Si content

7.4.3 Fatigue Resistance

Having shown that the variation in volume average modulus and yield strength are small between SVE instantiations, the volume elements can be treated as RVEs for those properties. Because RVEs for fatigue and damage initiation are prohibitively large, these volume elements are treated as SVEs for the final two mechanical property predictions: fatigue resistance and relative susceptibility to microcracking.

The FIP calculation, which characterizes the magnitude of the driving force for fatigue crack formation, is carried out from a single fully reversed fatigue cycle simulation with a macroscopic mechanical strain amplitude of 0.5%. In this work, the local volume averaging is performed using a Gaussian filter where the length scale is adjusted by setting the standard deviation of the filter and is set to half of the mean α-Mo equivalent grain radius of $5\mu m$.

Before beginning the discussion of FIPs and the predicted results of this study, it is important to reiterate that FIPs only predict the driving force for fatigue crack initiation. The results of this study do not directly predict fatigue resistance, which also depends on the critical value of FIP required to form a fatigue crack. The critical driving force for fatigue crack formation is microstructure dependent and can change with local variations of microstructure within a volume element. Consequently, the results in this section can only be treated as direct comparisons of fatigue resistance under the assumption that the critical driving force for fatigue crack initiation is independent of microstructure.

Another important point is that fatigue life is a combination of resistance to fatigue crack initiation and resistance to fatigue crack propagation. These two portions of fatigue life span multiple crack lengths and the associated deformation mechanisms. Because the deformation mechanisms change as cracks grow, microstructures which resist fatigue crack initiation may not resist fatigue crack propagation very well [57]. Instead of approaching the problem of fatigue crack propagation, which requires linear

elastic fracture mechanics (LEFM) and crack growth models, this study only estimates fatigue resistance to crack initiation. This approximation can be justified by the very high crack growth rates seen in triplex Mo-Si-B alloys [25, 26, 31, 35, 96–98], which is expected in materials with quasi-brittle phases and indicates that total fatigue life is dominated by fatigue crack initiation.

As previously discussed in Chapter 2, due to the localization problem of fatigue crack initiation a proper treatment of fatigue requires several hundred SVE instantiations for each combination of microstructural parameters and α-Mo CVP parameter set [57]. In the extreme value approach, a FIP is calculated at each integration point and a local volume averaging scheme is applied. Each SVE then produces a single data point, the maximum valued FIP, for the fatigue analysis. The resulting distribution of the maximum FIP from each SVE can then be correlated to the distribution in fatigue life under a single loading condition, and the process must be repeated for every loading condition of interest. This distribution is assumed to converge as the number of SVEs increases.

Due to the breadth of the microstructures and α-Mo CVP parameter sets in this study, only a small number of SVEs can be simulated under a single loading condition for each combination of microstructure and CVP parameter set. Figure 7.21 shows the variation in the predicted maximum FIP as a result of the differences in microstructure between six instantiations for the 63% volume fraction α-Mo SVEs. Each data point represents the mean value from six instantiations and the bars represent two standard deviations. In this figure, the variation seen in ECPS for the Mo-0.00Si material is consistent with the variation that might be expected for a larger fatigue study. The relatively small variation at the higher Si contents, especially for the FS FIP, is an unexpected result. It would be expected that as more instantiations are simulated, the variation in predicted FIPs would actually increase as instantiations with greater variation in the 2^{nd} order microstructural features, such as misorientation distribution,

are introduced to the simulation data set.

Further conclusions about variation in the FIP predictions cannot be made because the data on this plot comes from only six instantiations. However, these results suggest that the trend of decreasing variation with increasing Si content might continue as additional instantiations are simulated. Such a trend could be explained by the decreased amount of plasticity occurring over the fixed mechanical loading as a result of the increase in strength of the α-Mo phase. The increasing strength of the α-Mo phase does not just reduce the amount of local plasticity development, but it also reduces the large stress discontinuities that develop between the α-Mo matrix and the intermetallic phases. Because the intermetallic phases are assumed to be elastic only, this further suggests that if the intermetallics are allowed to plastically deform any plasticity developed by the intermetallic phases would further reduce the stress discontinuities, and therefore the variation seen in FIP prediction. This would likely only affect the high temperature predictions, since the intermetallics show very little plasticity even at 1400°C.

Because the small number of instantiations is insufficient for conducting a proper fatigue study, the full set of plots presenting the maximum valued FIP by instantiation are not shown. Instead, a volume average is conducted over all of the integration points in each instantiation to obtain a volume average FIP value for individual instantiations. Figures 7.22-7.27 present the mean and standard deviation of the volume average FIPs as a function of α-Mo volume fraction for each α-Mo CVP parameter set.

In the FIP plots, a larger value represents greater damage per fatigue cycle. The effective cumulative plastic strain (ECPS) parameter accounts for cyclically accumulated plastic strain. The Fatemi-Socie (FS) parameter includes the effects of normal stress on at fatigue crack initiation sites. Consequently, these different FIPs account for different damage mechanisms and may not show similar levels of damage per cycle

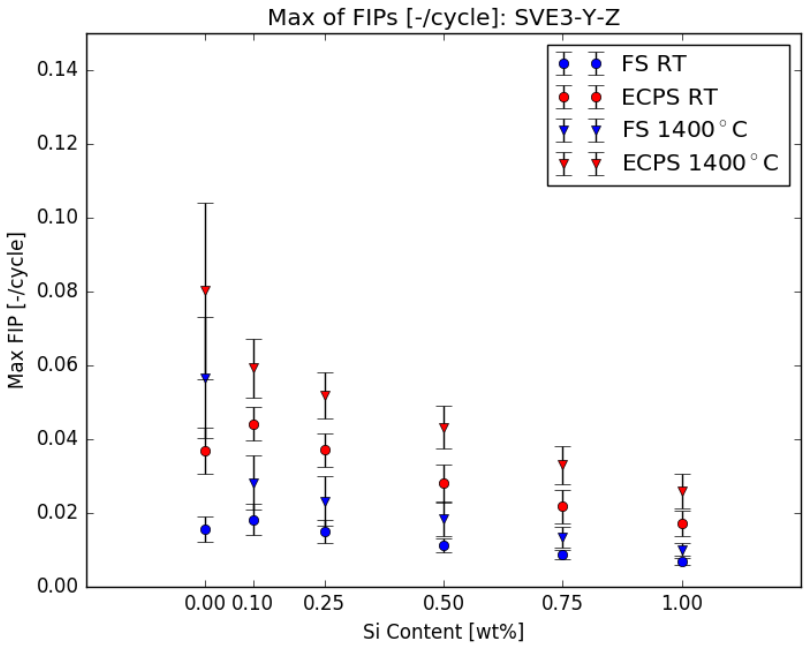

Figure 7.21: Predicted maximum FIPs averaged over six instantiations of SVEs for each α-Mo Si content with 63% volume fraction α-Mo. Bars represent two standard deviations.

or trends in damage accumulation per cycle.

In the case of the Mo-0.00Si shown in Figure 7.22, both parameters predict increasing damage per cycle with increasing α-Mo volume fraction at room temperature. This is explained by greater amounts of plasticity present in the volume with a larger volume fraction of α-Mo. At 1400°C both FIPs predict initial increasing damage per cycle with increasing α-Mo volume fraction, followed by decreasing damage per cycle after at higher α-Mo volume fractions. However, the predicted α-Mo volume fraction where the trend changes is 74% for ECPS and 54% for FS.

This indicates that there is a re-distribution in the strain fields at higher α-Mo volume fractions where plastic strain accumulation is more evenly distributed, resulting in lower FIP calculations across the SVE on average. The difference in the transition point for ECPS and FS is most likely related to the effects of normal stress and indicates that there are lower normal stresses present at crack initiation sites that

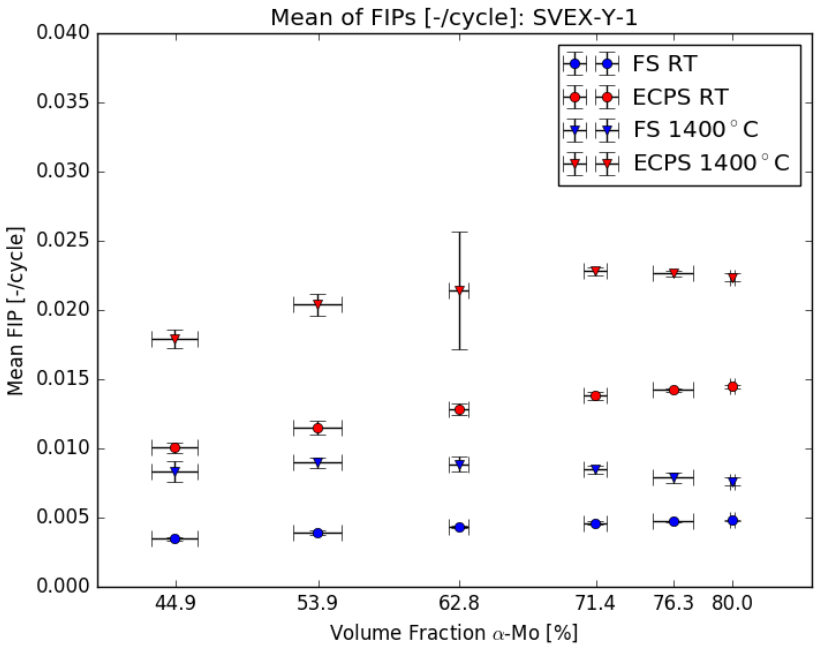

Figure 7.22: Predicted volume averaged FIPs averaged over six instantiations of SVEs for each α-Mo volume fraction with the Mo-0.00Si CVP parameter set. Bars represent two standard deviations.

decreases the damage per cycle earlier in the FS parameter.

In Figure 7.22, the unusually large variation of the mean volume average ECPS prediction for 63% α-Mo volume fraction is the result of a single instantiation with a much lower volume average ECPS than the other instantiations at this volume fraction. This large difference does not show up at room temperature, and if the instantiation is excluded from the mean and standard deviation calculations, the resulting standard deviation more closely resembles that of all the other predictions on this plot.

The change in variation from room temperature to 1400°C is accompanied by a shift in the location where the largest maximum valued ECPS is predicted within the outstanding instantiation. Most instantiations predict that the maximum valued FIPs remain in the same grain as a function of temperature, but in this case the grain with the maximum valued ECPS is different at room temperature and 1400°C.

A change in the location of the maximum predicted FIP suggests that the driving microstructural feature for fatigue damage has changed with changing temperature. In this case, it is speculated that the instantiation with an abnormally low volume average ECPS contains a favorable misorientation distribution that tends to more evenly distribute the accumulated plastic strain.

The ability to track such changes in FIP prediction as a function of microstructural features makes microstructure-sensitive modeling a powerful tool for studying fatigue; however, such a study is left to future work. An in depth study relating the microstructural features driving variation in fatigue damage requires a more detailed and complete fatigue study of a small sub set of microstructures. It is expected that this future work would require an experimental study including fatigue tests in order to perform a more rigorous calibration of the constitutive law for the material's mechanical behavior under cyclic loading. Perhaps more importantly, such a fatigue study would help correlate fatigue data to fatigue crack driving forces which would provide experimental evidence for how the critical fatigue crack driving force changes with microstructure. This would provide the necessary information to perform a complete fatigue resistance prediction without the assumption that the critical driving force is independent of microstructure.

In Figure 7.23, the Mo-0.10Si material only shows the increasing-decreasing FIP trend in the high temperature volume average FS predictions, and the transition point has shifted to a higher 71% α-Mo volume fraction. The volume average ECPS now shows only increasing damage per cycle with increasing α-Mo volume fraction, even at 1400°C. This suggests that the increasing strength introduced by a higher α-Mo Si content has removed the benefits of stress and strain distribution at higher α-Mo volume fractions. Instead, the higher volume fraction of α-Mo now leads to more wide spread plastic strain accumulation and larger ECPS on average in each SVE.

The remaining Figures 7.24-7.27 show the same plots for the Mo-0.25Si, Mo-0.50Si,

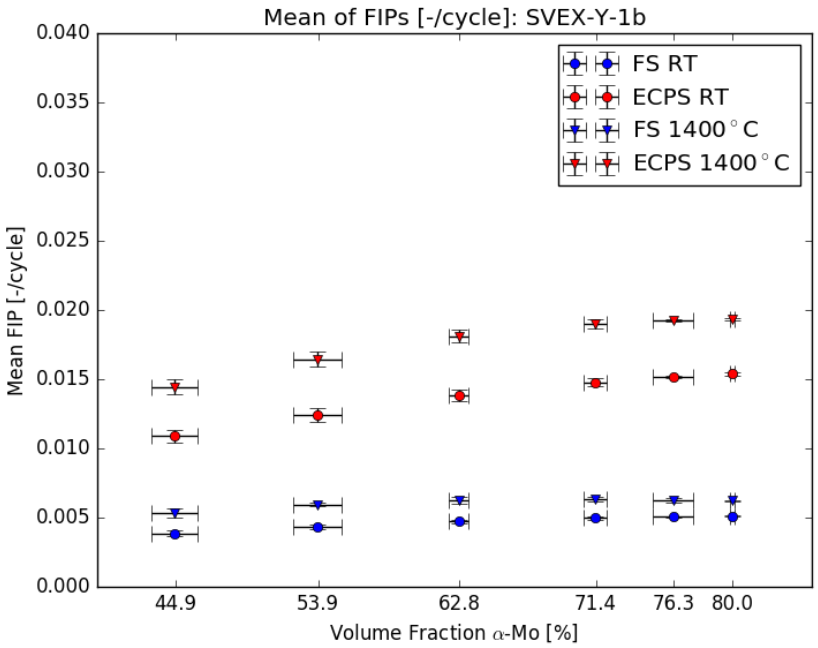

Figure 7.23: Predicted volume averaged FIPs averaged over six instantiations of SVEs for each α-Mo volume fraction with the Mo-0.10Si CVP parameter set. Bars represent two standard deviations.

and Mo-1.00Si α-Mo CVP parameter sets. These plots show only increasing damage with increasing α-Mo volume fraction. This is the expected result of adding a greater volume fraction of the ductile phase, because there is now more material allowed to accumulate plastic strain.

Allowing the intermetallic phases to plastically deform at high temperatures may relieve some of the accumulated plastic strain in the α-Mo matrix. This could result in lower average accumulated plastic strain throughout the SVE. Consequently, if the intermetallic phases are allowed to deform plastically, it might be expected that a transition from increasing to decreasing damage per cycle with increasing α-Mo volume fraction might be present at high temperatures for the higher α-Mo Si contents. Allowing the intermetallics to plastically deform might also decrease the maximum predicted FIP as a result of reducing the concentration of plastic deformation in the α-Mo phase, resulting in more uniformly distributed stress and strain fields.

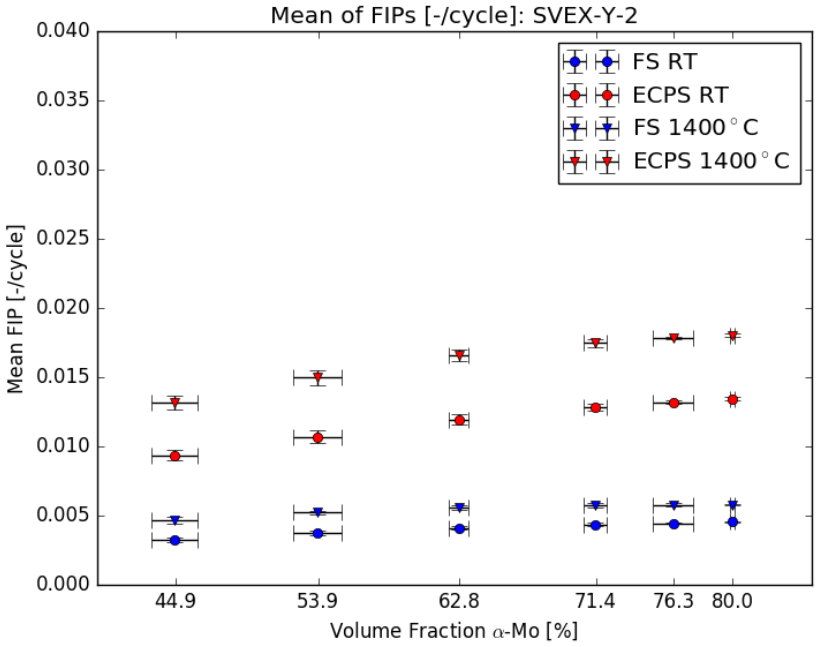

Figure 7.24: Predicted volume averaged FIPs averaged over six instantiations of SVEs for each α-Mo volume fraction with the Mo-0.25Si CVP parameter set. Bars represent two standard deviations.

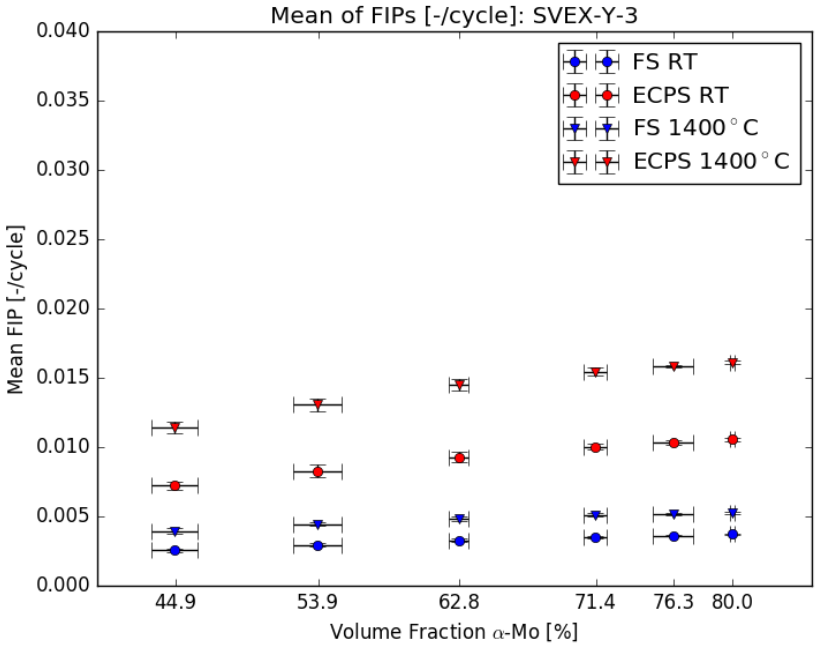

Figure 7.25: Predicted volume averaged FIPs averaged over six instantiations of SVEs for each α-Mo volume fraction with the Mo-0.50Si CVP parameter set. Bars represent two standard deviations.

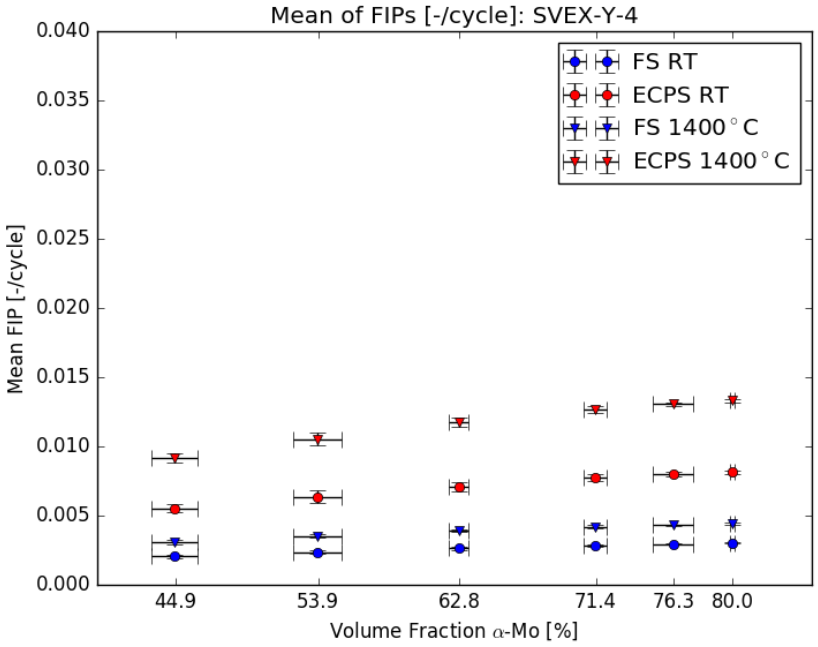

Figure 7.26: Predicted volume averaged FIPs averaged over six instantiations of SVEs for each α-Mo volume fraction with the Mo-0.75Si CVP parameter set. Bars represent two standard deviations.

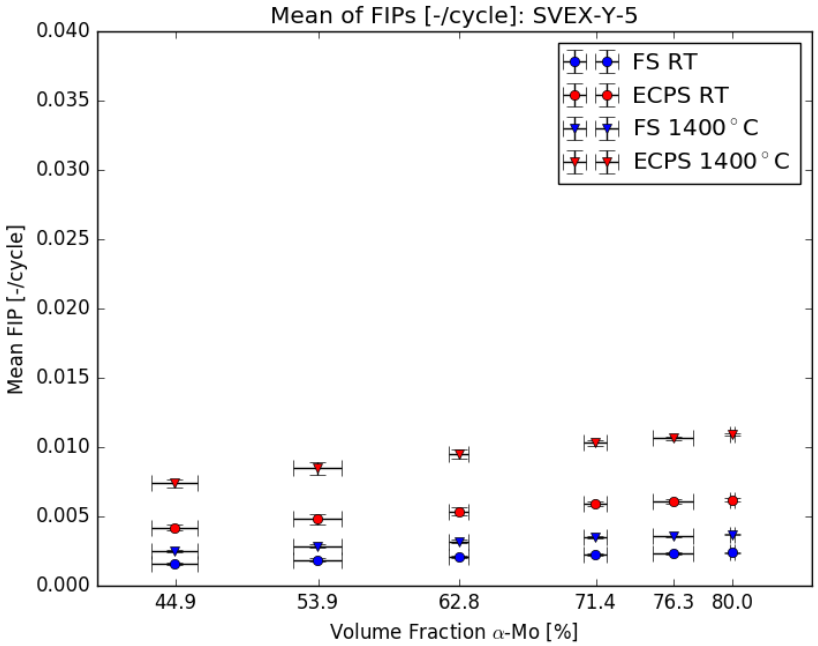

Figure 7.27: Predicted volume averaged FIPs averaged over six instantiations of SVEs for each α-Mo volume fraction with the Mo-1.00Si CVP parameter set. Bars represent two standard deviations.

Figures 7.28-7.33 present the same volume average FIP predictions as a function of Si content and temperature at each α-Mo volume fraction. At each α-Mo volume fraction, both FIPs show the same trends as a function of Si content. At room temperature, the solid solution softening demonstrated by α-Mo at 0.1 wt.% Si results in increased plasticity and an increase in FIP over pure Mo. Subsequent increases in Si content result in decreasing FIP, where the FIP at 0.25 wt% Si is slightly less than for pure Mo. At 1400°C, increasing Si content results in deceasing FIP.

The difference in trends as a function temperature is related to the presence of solid solution softening for small additions of Si at room temperature, whereas at higher temperatures, only solid solution strengthening is observed. The transition from solid solution softening to solid solution strengthening with increasing temperature is related to a transition temperature where the double kink mechanism no longer dominates plastic deformation and the mobilities of edge and screw dislocations become similar [38]. Consequently, solid solution softening is only observed near room temperature and lower temperatures. These sub-structure effects are homogenized in the Si content and temperature sensitive calibration of the parameters in the α-Mo flow rule and evolution equations.

When comparing the FIP trends as a function of Si content, it is important to remember that these predictions do not necessarily reflect changes in fatigue resistance. Particularly in the case of Mo-0.00Si, it is possible that the critical driving force required for fatigue crack formation is significantly larger than that for α-Mo containing Si. Before a proper characterization of fatigue resistance can be made, further experimental work is required to provide relative changes in the critical fatigue crack driving force as a function of microstructure.

Figure 7.30 again shows the large variation of the predicted ECPS at 1400°C for the Mo-0.00Si and 63% α-Mo. In this figure, we see that the variation is large with respect to the predicted ECPS, but still clearly show decreasing FIP with increasing

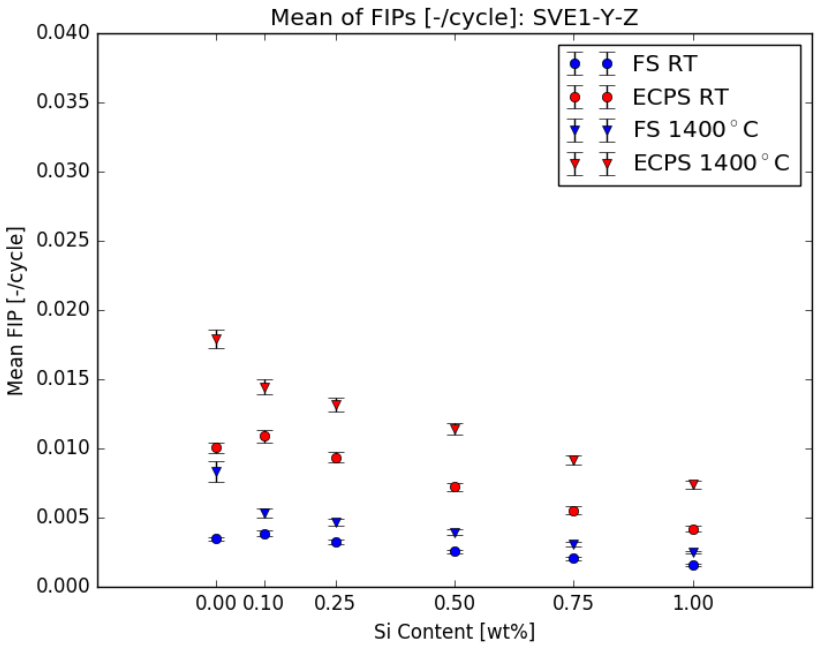

Figure 7.28: Predicted volume average FIPs averaged over six instantiations of SVEs for each α-Mo Si content at 45% volume fraction of α-Mo. Bars represent two standard deviations.

Si content.

Finally the influence of α-Mo volume fraction and Si content on the FIP predictions are presented together as surface plots for ECPS and FS in Figure 7.34 and Figure 7.35, respectively.

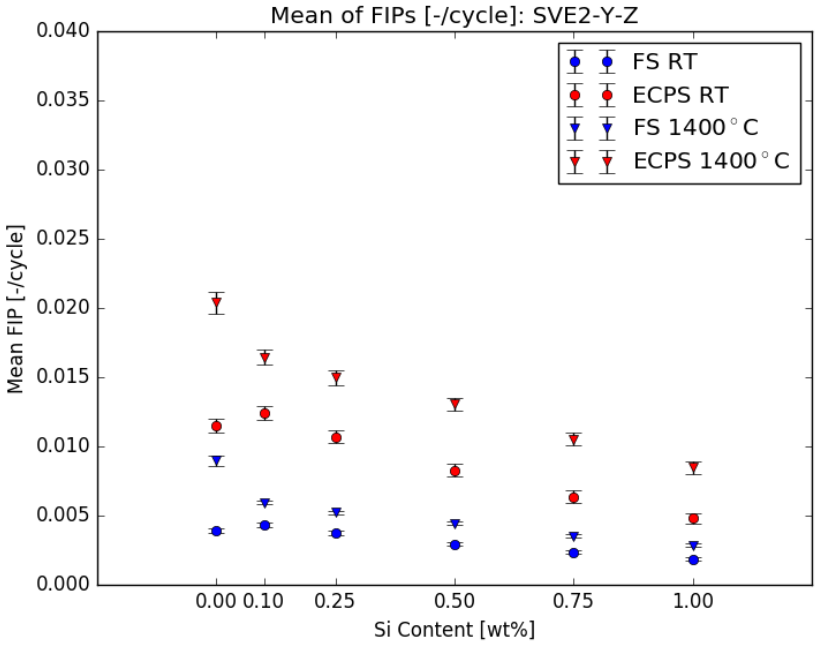

Figure 7.29: Predicted volume average FIPs averaged over six instantiations of SVEs for each α-Mo Si content at 54% volume fraction of α-Mo. Bars represent two standard deviations.

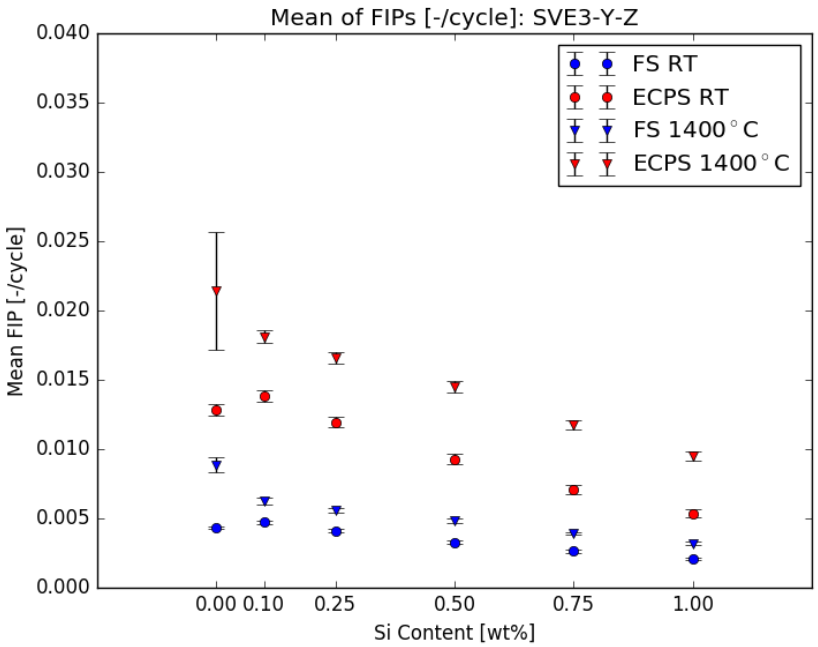

Figure 7.30: Predicted volume average FIPs averaged over six instantiations of SVEs for each α-Mo Si content at 63% volume fraction of α-Mo. Bars represent two standard deviations.

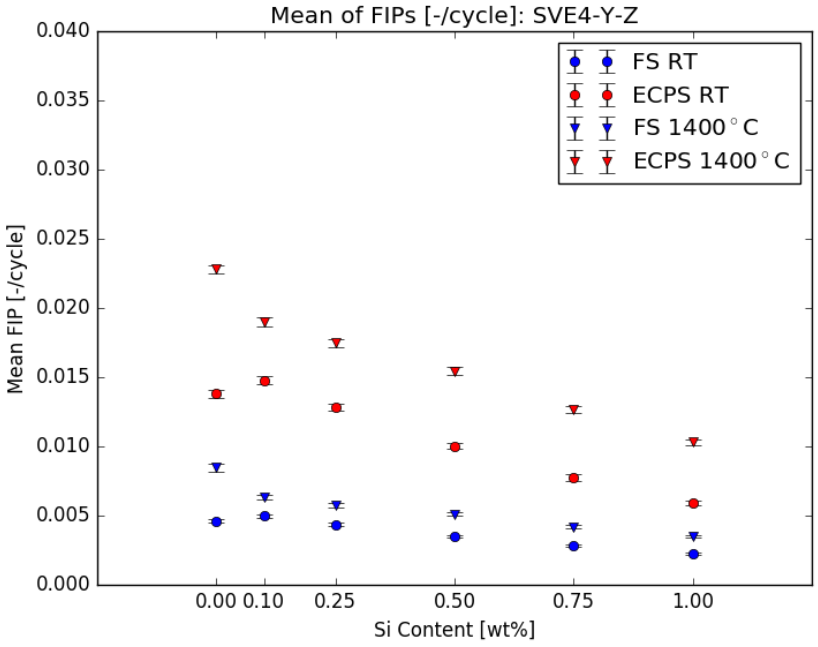

Figure 7.31: Predicted volume average FIPs averaged over six instantiations of SVEs for each α-Mo Si content at 71% volume fraction of α-Mo. Bars represent two standard deviations.

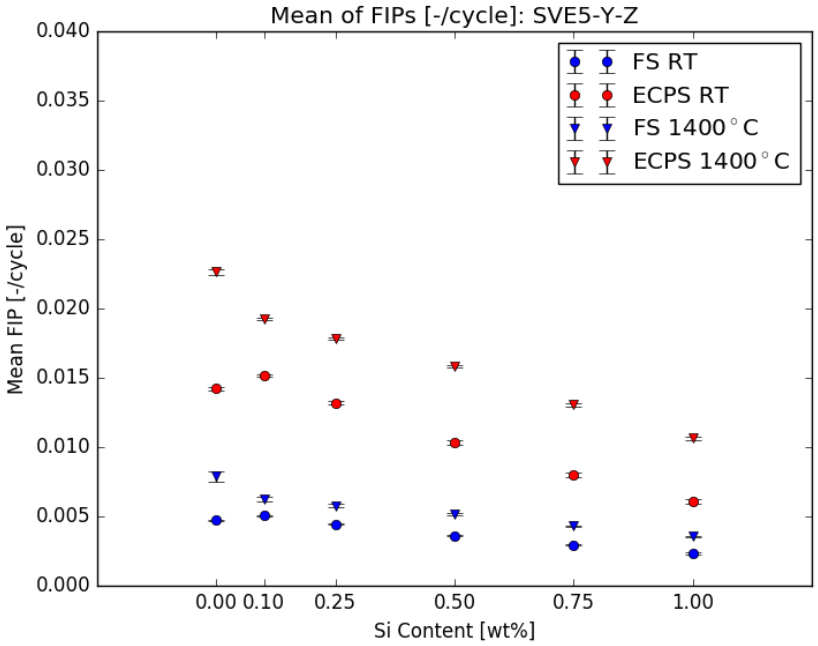

Figure 7.32: Predicted volume average FIPs averaged over six instantiations of SVEs for each α-Mo Si content at 76% volume fraction of α-Mo. Bars represent two standard deviations.

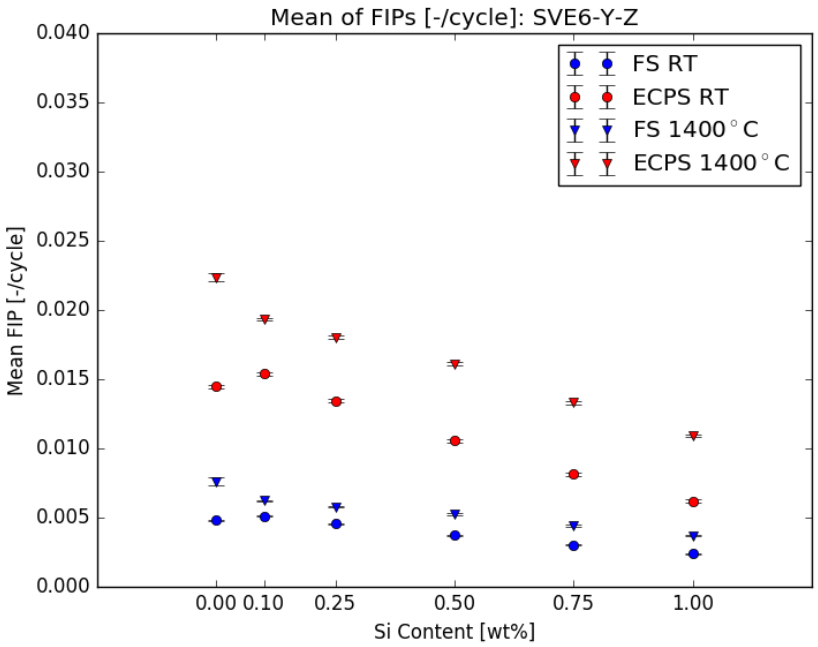

Figure 7.33: Predicted volume average FIPs averaged over six instantiations of SVEs for each α-Mo Si content at 80% volume fraction of α-Mo. Bars represent two standard deviations.

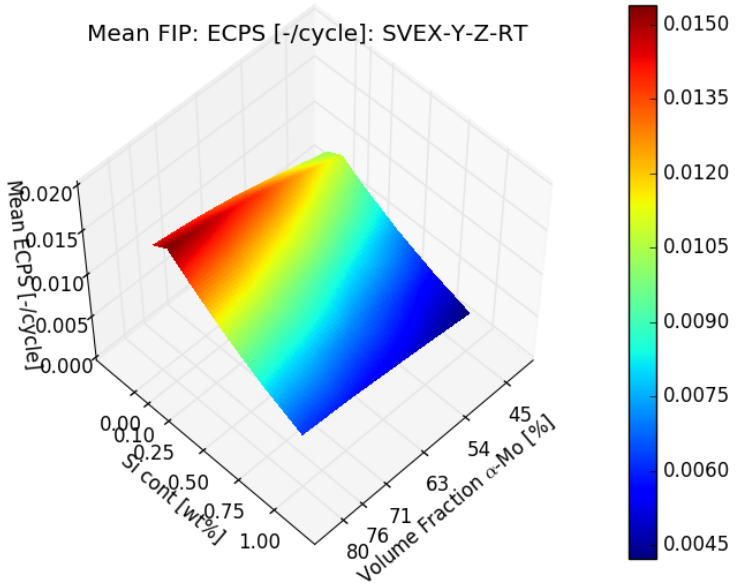

(a) Room temperature

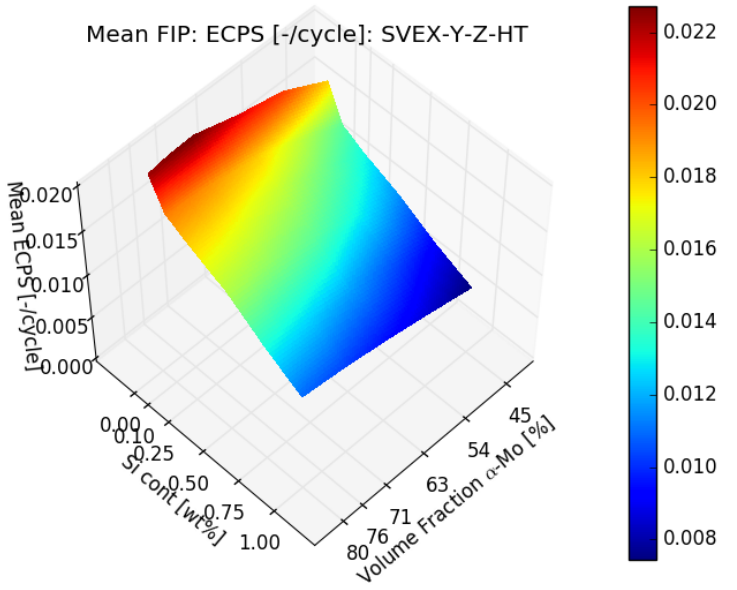

(b) 1400°C

Figure 7.34: Predicted volume averaged effective cumulative plastic strain (ECPS) as a function of temperature and α-Mo Si content

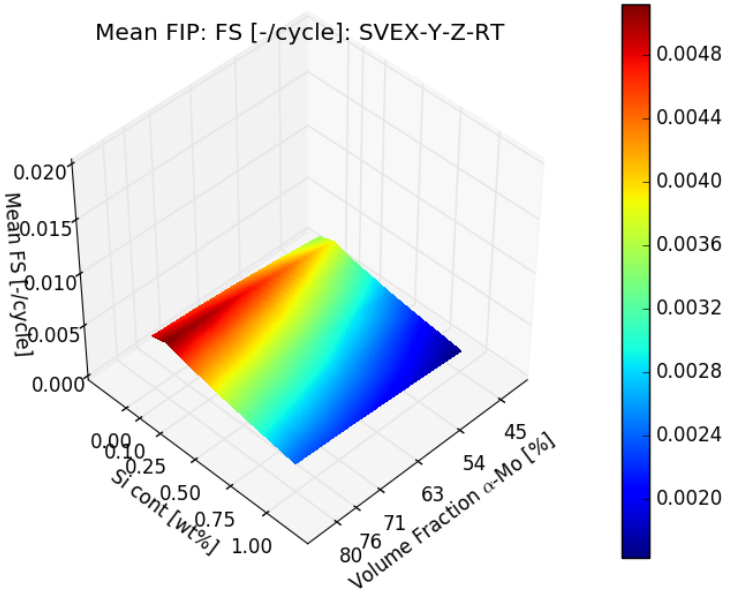

(a) Room temperature

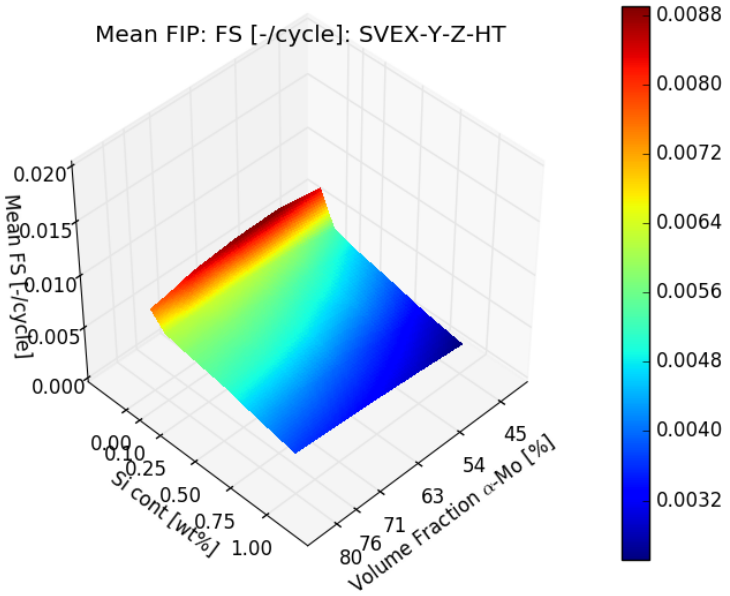

(b) 1400°C

Figure 7.35: Predicted volume averaged Fatemi-Socie (FS) as a function of temperature and α-Mo Si content

7.4.4 Susceptibility to Microcracking

The fourth mechanical property prediction is measured by the volume averaged DIP_{avg} introduced in Chapter 6. The volume averaged DIP_{avg} is calculated at 0.5% macroscopic uniaxial strain, which corresponds to the end of initial loading in the fatigue cycle. The DIP introduced in Chapter 6 is a measure of driving force for cracking under monotonic just as a FIP is a measure of driving force for fatigue crack formation. Although the dependence of critical driving force is addressed in the calibration of interface strengths as function of Si content, it is possible for the critical crack driving force to vary with other microstructural features. Therefore, comparing the susceptibility to microcracking with the DIP_{avg} metric requires the assumption that the critical driving force is independent of microstructure. Similar to the volume average FIP, a larger value for the volume average DIP_{avg} indicates greater susceptibility to damage formation.

As discussed in Chapter 6, a larger volume average DIP_{avg} is an indicator of a decrease in ductility and damage tolerance. Figures 7.36-7.41 present the volume average DIP_{avg} as a function of α-Mo volume fraction at room temperature and 1400°C for fixed α-Mo Si content.

Figure 7.36 most clearly shows the trends for volume average DIP_{avg} as a function of increasing α-Mo volume fraction, but the same trends are shown at each α-Mo Si content. The volume average DIP_{avg} is larger at room temperature than at 1400°C, which is expected since most materials demonstrate more ductility at high temperatures. At room temperature, the volume average demonstrates a shallowly decreasing damage with increasing α-Mo volume fraction. At 1400°C, the same trend is seen, but the decrease in damage is more significant with increasing α-Mo volume fraction. The only exception is at 76% volume fraction α-Mo where the volume average DIP_{avg} shows a slight increase over the volume average DIP_{avg} at 71%.

The cause of the slight increase in volume average DIP_{avg} between 71% and 76%

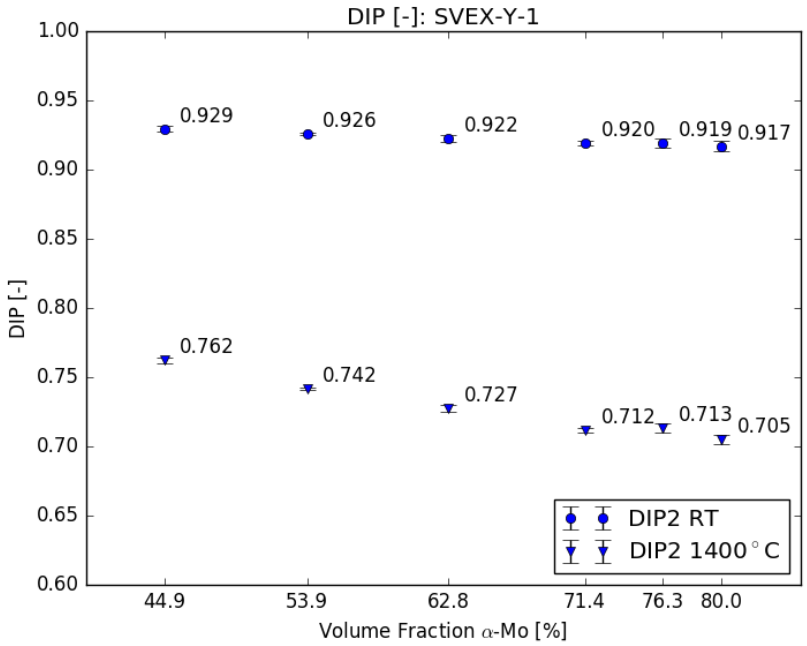

Figure 7.36: Predicted volume averaged DIP_{avg} averaged over six instantiations of SVEs for each α-Mo volume fraction with a Mo-0.00Si CVP parameter set. Bars represent two standard deviations.

α-Mo volume fraction is unknown. Generally it is expected that an increase in the volume fraction of the ductile α-Mo phase would increase the ductility of the material, and correspondingly decrease the volume average DIP_{avg}. The volume average DIP_{avg} is calculated in a similar manner to the volume average FIPs, and is just as susceptible to the uncontrolled variations in microstructural features. Therefore, it is possible that the small number of instantiations at 76% α-Mo volume fraction all contain microstructural features leading to greater susceptibility to microcracking and that a larger number of instantiations might change the trend. However, this possibility is contradicted by the surprisingly small standard deviation of the predicted volume average DIP_{avg}.

Figures 7.37-7.41 show the same general trends for the Mo-0.10Si through Mo-1.00Si α-Mo CVP parameter sets; however, with increasing Si content the decrease in damage with increasing α-Mo volume fraction becomes increasingly gradual. Note

that these figures are plotted on a different scale than Figure 7.36 to better show the differences between simulations with different α-Mo volume fractions.

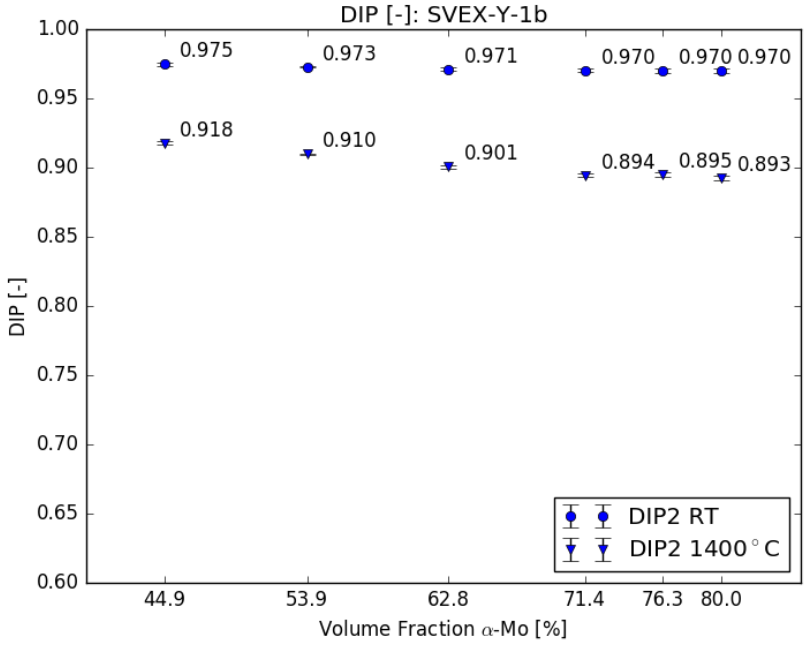

Figure 7.37: Predicted volume averaged DIP_{avg} averaged over six instantiations of SVEs for each α-Mo volume fraction with a Mo-0.10Si CVP parameter set. Bars represent two standard deviations.

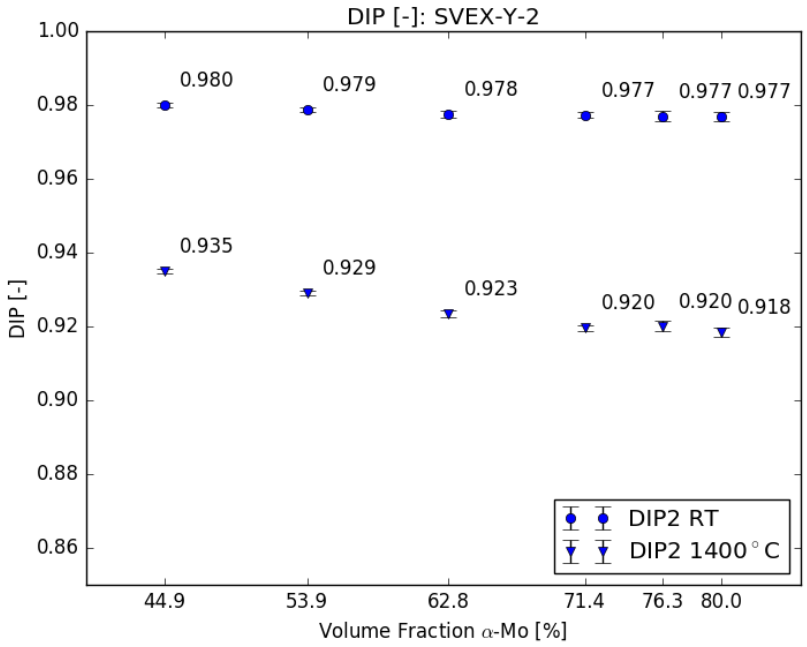

Figure 7.38: Predicted volume averaged DIP_{avg} averaged over six instantiations of SVEs for each α-Mo volume fraction with a Mo-0.25Si CVP parameter set. Bars represent two standard deviations.

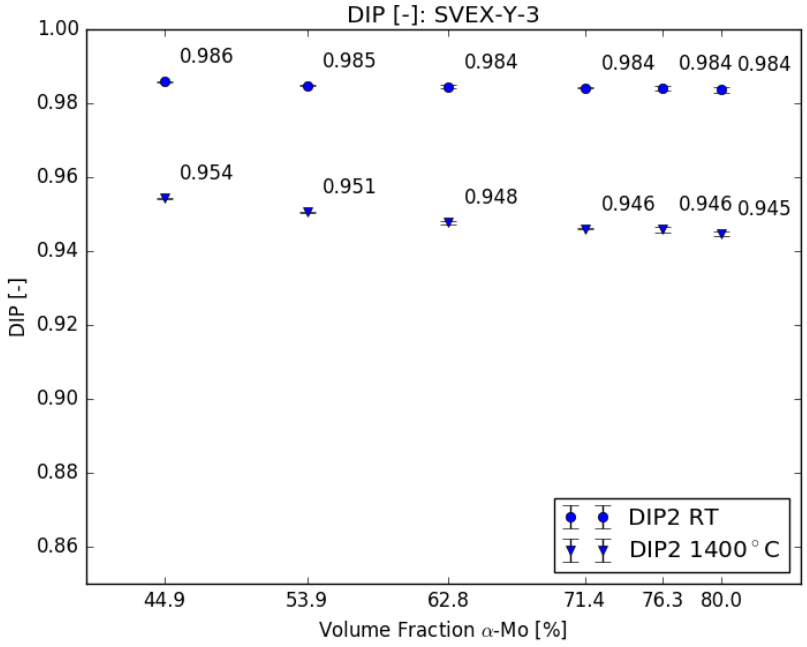

Figure 7.39: Predicted volume averaged DIP_{avg} averaged over six instantiations of SVEs for each α-Mo volume fraction with a Mo-0.50Si CVP parameter set. Bars represent two standard deviations.

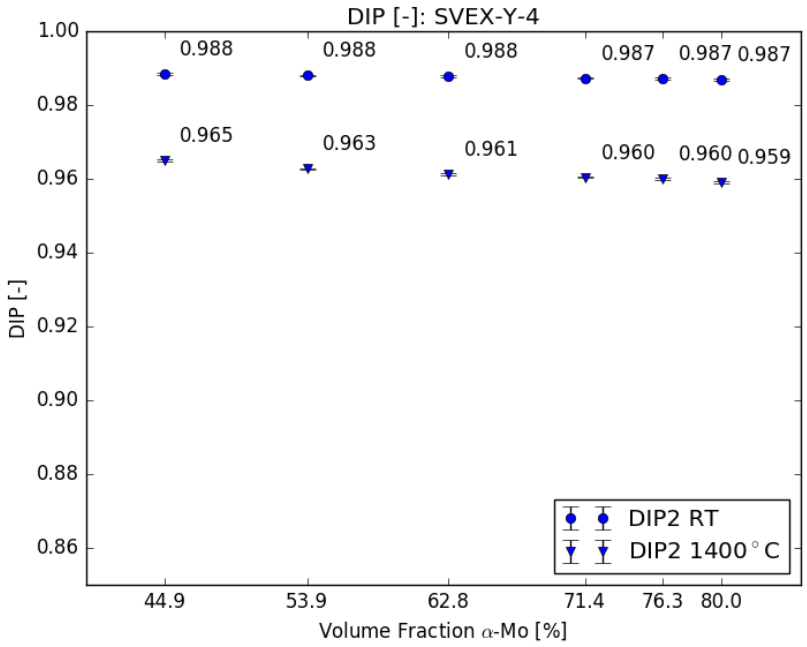

Figure 7.40: Predicted volume averaged DIP_{avg} averaged over six instantiations of SVEs for each α-Mo volume fraction with a Mo-0.75Si CVP parameter set. Bars represent two standard deviations.

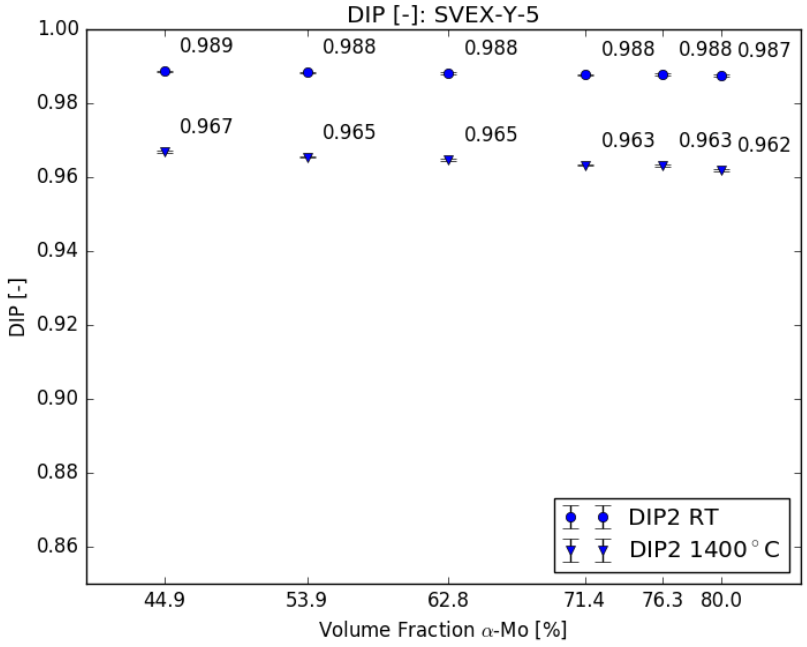

Figure 7.41: Predicted volume averaged DIP_{avg} averaged over six instantiations of SVEs for each α-Mo volume fraction with a Mo-1.00Si CVP parameter set. Bars represent two standard deviations.

Figures 7.42-7.47 presents the volume average DIP_{avg} results as a function of Si content and temperature at each α-Mo volume fraction. In these plots, the triplex materials with higher α-Mo Si content show decreasing variation as a function of instantiation.

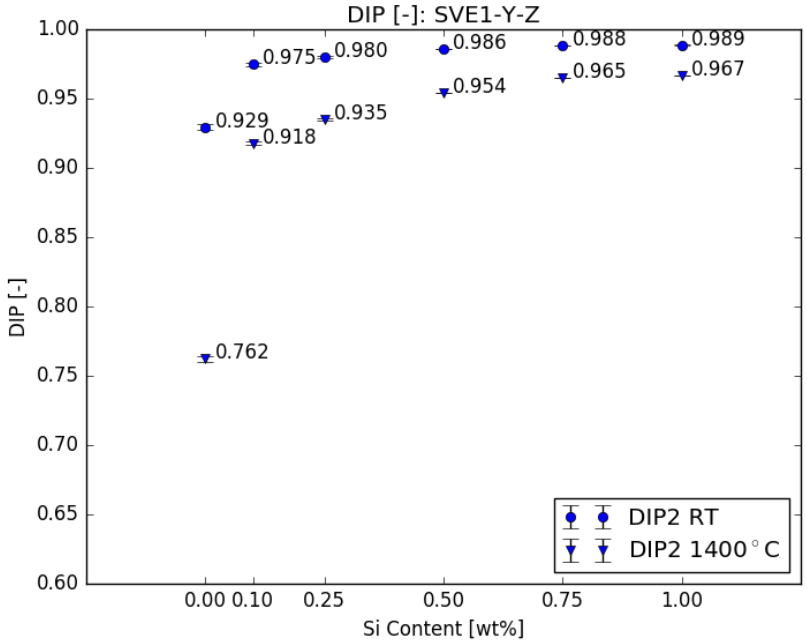

Figure 7.42: Predicted volume average DIP_{avg} averaged over six instantiations of SVEs for each α-Mo Si content at 45% volume fraction of α-Mo. Bars represent two standard deviations.

Figure 7.42 clearly shows the trends in volume average DIP_{avg} as a function of Si content at 45% α-Mo volume fraction, and these trends are consistent with changing α-Mo volume fraction. There is a steep increase in the volume average DIP_{avg} from pure Mo with the addition of 0.1 wt.% Si, corresponding to a steep decrease in relative ductility. This large jump in volume average DIP_{avg} is more severe at 1400°C than at room temperature. From 0.10 wt.% to 1.00 wt.% Si, the volume average DIP_{avg} steadily increases, with smaller increases between the higher Si content α-Mo CVP parameter sets. In fact, at room temperature, the volume average DIP_{avg} is nearly invariant between 0.50 wt.% and 1.00 wt.% Si in α-Mo.

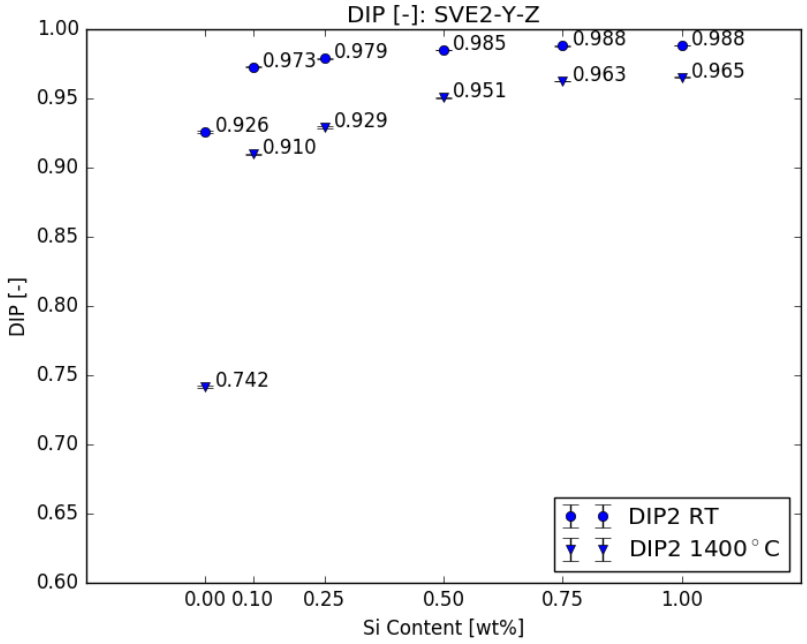

Figure 7.43: Predicted volume average DIP_{avg} averaged over six instantiations of SVEs for each α-Mo Si content at 54% volume fraction of α-Mo. Bars represent two standard deviations.

Finally, the influence of α-Mo volume fraction and Si content on the volume average DIP_{avg} predictions are presented together as surface plots in Figure 7.48.

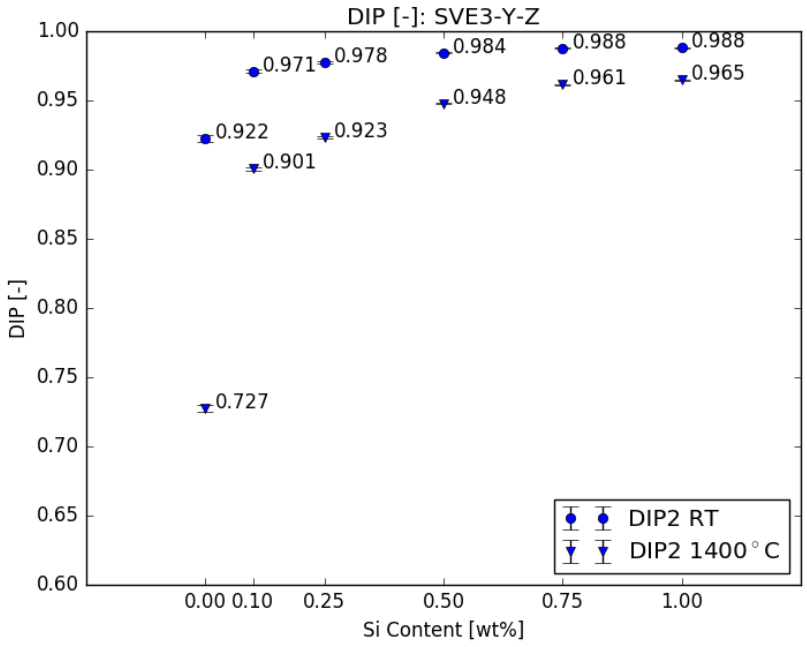

Figure 7.44: Predicted volume average DIP_{avg} averaged over six instantiations of SVEs for each α-Mo Si content at 63% volume fraction of α-Mo. Bars represent two standard deviations.

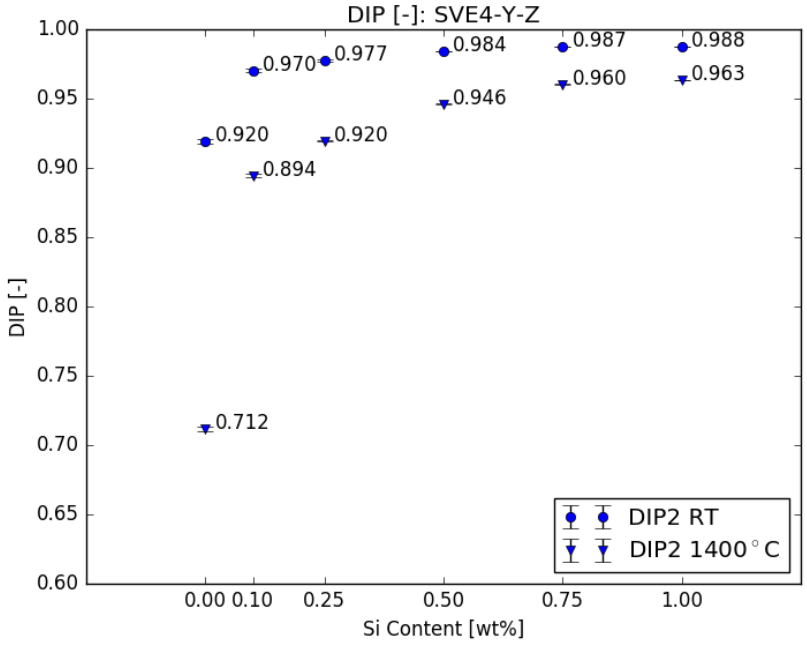

Figure 7.45: Predicted volume average DIP_{avg} averaged over six instantiations of SVEs for each α-Mo Si content at 71% volume fraction of α-Mo. Bars represent two standard deviations.

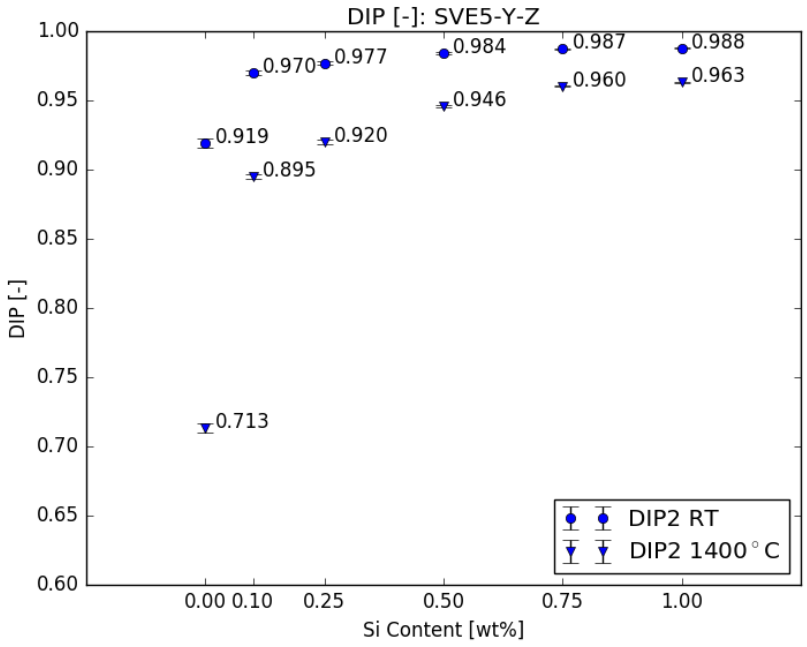

Figure 7.46: Predicted volume average DIP_{avg} averaged over six instantiations of SVEs for each α-Mo Si content at 76% volume fraction of α-Mo. Bars represent two standard deviations.

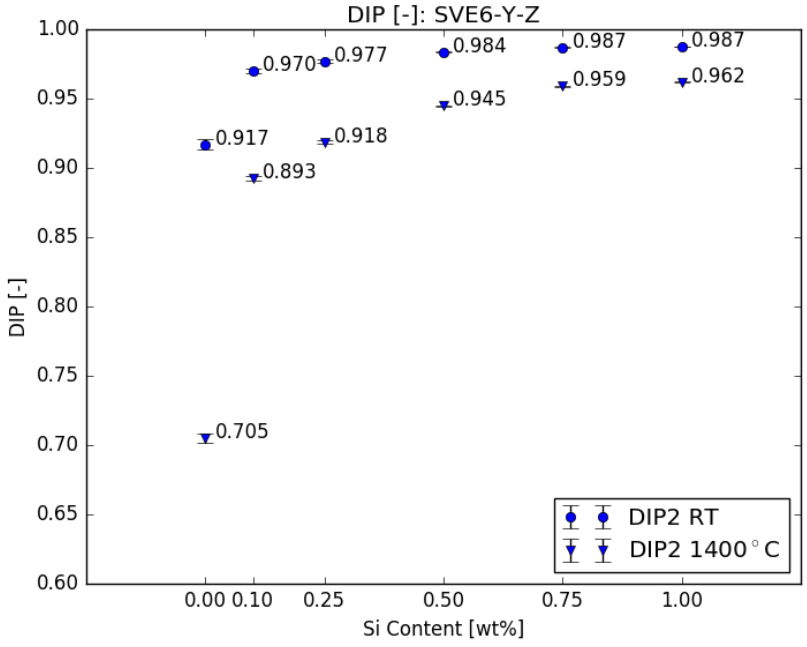

Figure 7.47: Predicted volume average DIP_{avg} averaged over six instantiations of SVEs for each α-Mo Si content at 80% volume fraction of α-Mo. Bars represent two standard deviations.

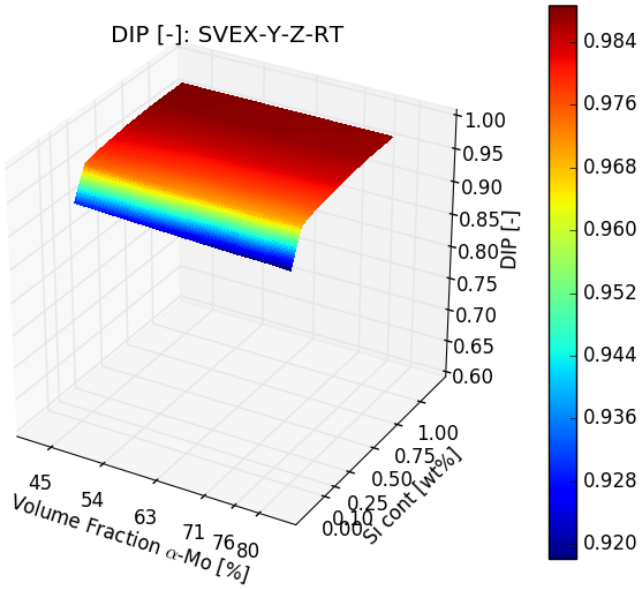

(a) Room temperature

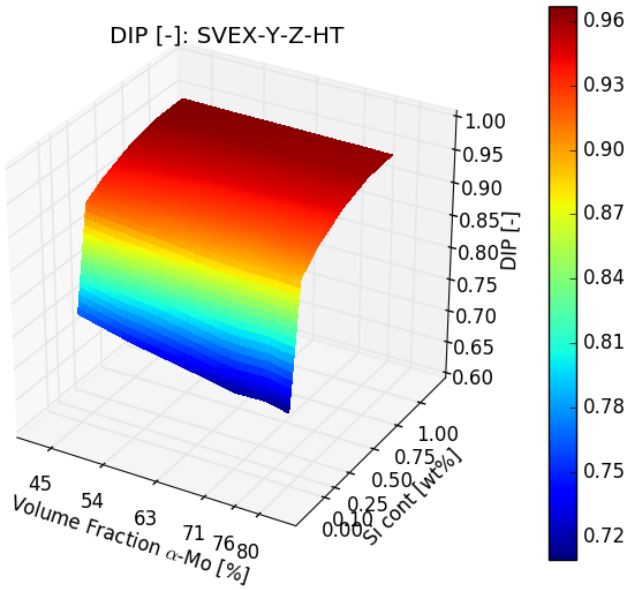

(b) 1400°C

Figure 7.48: Predicted volume averaged DIP_{avg} as a function of temperature and α-Mo Si content

7.4.5 Influence of Grain Size

The grain size study is carried out at 63% α-Mo volume fraction as a reasonable compromise between strength, fatigue resistance, and relative susceptibility to micro-cracking. At this volume fraction, the predicted properties of strength and fatigue are predicted to be roughly the mean value between the extreme predictions of these properties as a function of α-Mo volume fraction. Because changing the Si content is a simple re-assignment of α-Mo CVP model parameters, the grain size study is performed as a function of Si content. Figure 7.49-7.52 present the predicted changes in modulus, yield strength, the volume average FIPs, and the volume average DIP_{avg} at both room temperature and 1400°C.

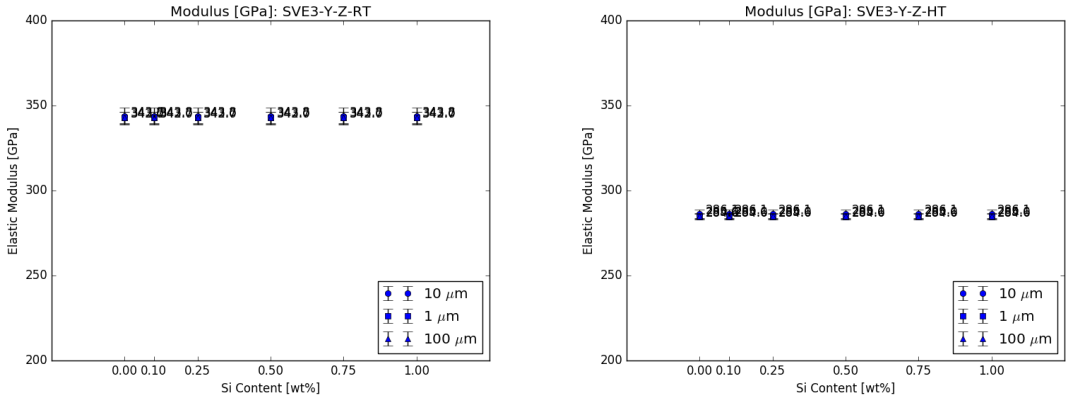

(a) Room temperature **(b)** 1400°C

Figure 7.49: Predicted elastic modulus at 63% α-Mo volume fraction as a function of mean equivalent grain diameter, temperature, and α-Mo Si content

These figures show overlapping predictions for all four mechanical properties for mean equivalent grain diameters spanning three orders of magnitude. Although this is not expected to be a realistic result, it is not surprising because the calibration of the constitutive law is invariant with grain size. In crystal plasticity, the only explicit method available to capture grain size effects is through the initial parameters and evolution parameters of the flow rule. Typically, grain size is only explicitly accounted for in a Hall-Petch term in the threshold stress calibration.

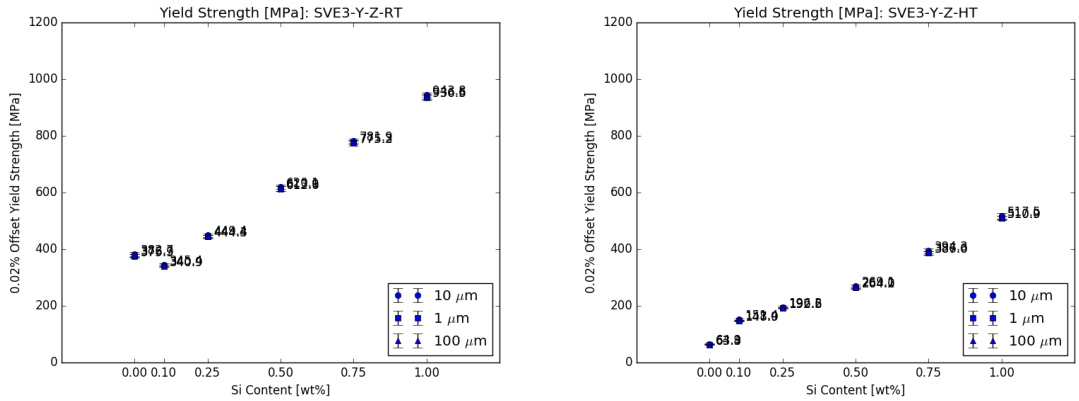

(a) Room temperature **(b)** 1400°C

Figure 7.50: Predicted 0.02% offset yield strength at 63% α-Mo volume fraction as a function of mean equivalent grain diameter, temperature, and α-Mo Si content

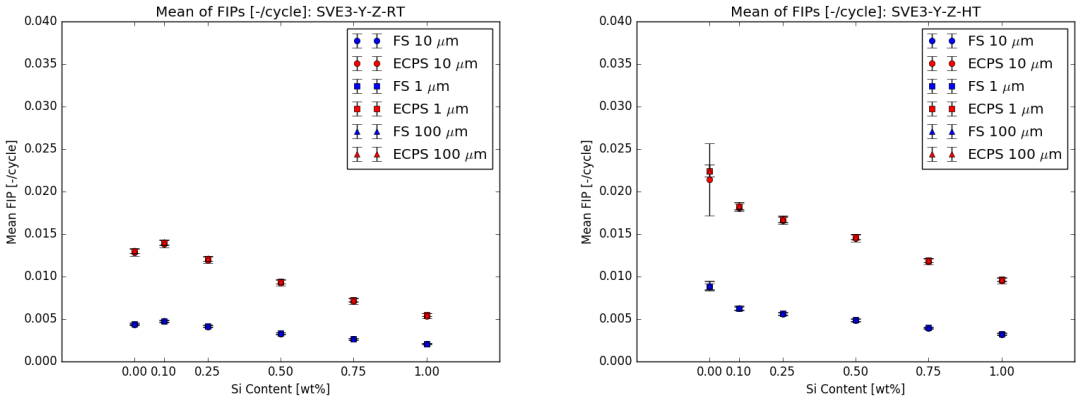

(a) Room temperature **(b)** 1400°C

Figure 7.51: Predicted volume average FIPs at 63% α-Mo volume fraction as a function of mean equivalent grain diameter, temperature, and α-Mo Si content

As discussed in Chapters 2 and 5, the Hall-Petch effect is assumed to be negligible in this work as a result of the reported constant yield strength of α-Mo as a function of grain size for mean grain sizes as small as 54 microns and the conflicting reports of any observable Hall-Petch behavior for smaller grain sizes [38]. It is possible and likely that Mo exhibits a Hall-Petch effect for smaller grain sizes, but the only two studies reporting a Hall-Petch effect report contradicting results from experiments on material from the same supplier [38]. Consequently, the only mechanisms for grain size effects in this work come from the absolute length scale of microstructure. In

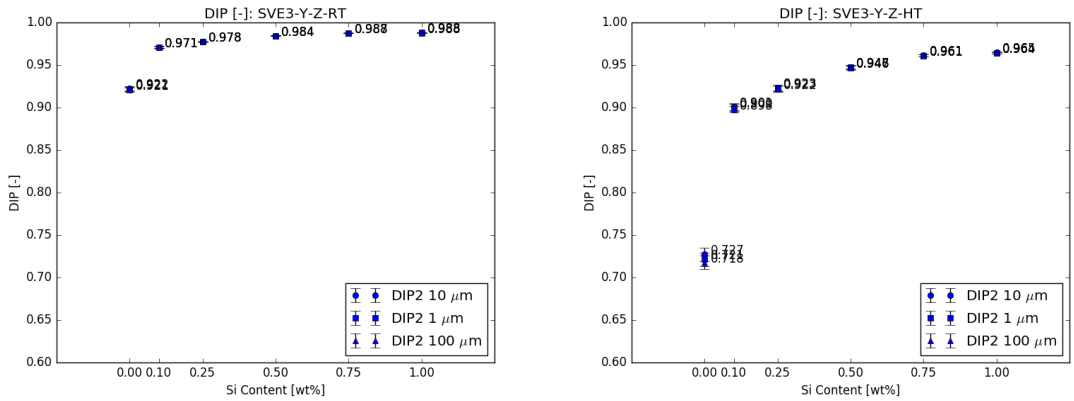

(a) Room temperature **(b)** 1400°C

Figure 7.52: Predicted volume average DIP_{avg} at 63% α-Mo volume fraction as a function of mean equivalent grain diameter, temperature, and α-Mo Si content

these volume elements, the mesh density is kept nearly constant with respect to mean grain size because volume elements with constant absolute length scale elements are too large to be computationally tractable for mean grain diameter changes of an order of magnitude. Instead, the meshes themselves only vary in the assigned element or voxel dimension. Consequently, without any indication of the volume element length scale, the volume elements would be indistinguishable. The result is that any absolute length scale microstructure constraints cannot be resolved in this study.

The last place grain size effects could make a difference is in the local volume averaging scheme performed as part of the FIP calculation. In the original parametric study, the local volume averaging is carried out over the length of the α-Mo mean grain radius. Without any information regarding the scale of volume affecting fatigue crack initiation, this is a required and reasonable assumption. In theory, the local volume averaging should take place over the same absolute length scale without regard for the mean grain diameter. However, with the mesh density of the current SVEs, one mean grain radius is on the order of several elements or voxels. This means that the local volume averaging cannot be varied easily with the large changes in grain size in the study. An extremely refined mesh would be required to perform local volume

averaging over the same absolute length scale smaller than the smallest grains in a study spanning several orders of magnitude in mean grain size. Instead, the local volume averaging is performed at the length of a the mean grain radius for each set of simulations, and not on an absolute length scale. It is anticipated that the grain size effect from such volume averaging would be small with respect to the effects expected with a calibrated Hall-Petch term for threshold stress.

Although any anticipated grain size effects are not represented in this second study, some sense for how a Hall-Petch relationship might affect the results can be obtained from the variations in material calibration according to α-Mo Si content. Although the Si content calibration is achieved by varying the initial drag stress and not the threshold stress, the resulting change in yield strength would be nearly identical under monotonic loading for either method. A more significant change in plastic hardening might be expected, but yield strength has the greatest impact on the resulting mechanical property predictions. Consequently, if the plots showing variation in properties as a function of Si content are re-plotted as a function of the initial drag stress and the Hall-Petch parameters are introduced as a term in the initial drag stress instead of threshold stress, one could relate the change in properties to grain size effects without performing additional simulations.

7.5 Summary

A parametric study of triplex Mo-Si-B alloys containing the α-Mo, A15, and T2 phases is presented to capture the microstructure-sensitive mechanical properties of yield strength, fatigue resistance, and susceptibility to microcracking which is inversely related to relative ductility. The parametric study includes the effects of α-Mo Si content and phase volume fraction, as well as grain size effects at a fixed α-Mo volume fraction.

Volume elements produced by the microstructure generator discussed in Chapter

4 are subjected to a fully reversed fatigue cycle with a mechanical strain amplitude of 0.5% strain. Simulations are conducted over the range of 45% to 80% α-Mo volume fraction with α-Mo constitutive CVP parameter sets ranging from 0.00 wt.% to 1.00 wt.% Si at room temperature and 1400°C. Convergence of the simulated elastic modulus and yield strength is demonstrated as function of SVE instantiation for each volume fraction and Si content combination. Yield strength of the triplex Mo-Si-B alloys demonstrates decreasing strength with increasing α-Mo volume fraction and generally increasing strength with increasing α-Mo Si content. However, at room temperature, an α-Mo Si content of 0.10 wt.% Si demonstrates the effects of the solid-solution softening of α-Mo with a lower yield strength than α-Mo with 0.00 wt.% Si. In all cases, the high temperature yield strength is predicted to be significantly less than that at room temperature.

A full fatigue study would require several hundred instantiations for each volume fraction and Si content combination. However, such a complete study is too large for the breadth of microstructure investigated in the parametric study. Instead the general trends in fatigue resistance are evaluated by studying the predicted instantiation volume average fatigue indicator parameters (FIPs) under the assumption that the critical driving force for fatigue crack formation is independent of microstructure. It is shown that the fatigue crack driving force generally increases with increasing α-Mo volume fraction, which can be associated with increasing cyclic plasticity in the fatigue stress-strain response. However, at low α-Mo Si contents, the fatigue crack driving force is actually predicted to decrease for the largest α-Mo volume fractions. This effect is most likely due to a more even distribution of plasticity across a volume element for larger α-Mo volume fractions with more localized and greater plastic accumulation at low α-Mo volume fractions. At higher α-Mo Si contents, this effect is significantly less pronounced and does not occur at any temperature for α-Mo Si content greater than 0.25 wt.% Si. In all cases, the effect of increasing temperature

is an increase in the fatigue crack driving force.

The susceptibility to microcracking is evaluated at the peak of the initial loading of the fatigue cycle. A complete study may require a similar approach as required for fatigue, but a similar volume average method is applied to rank order the broad microstructures of the parametric study. The susceptibility to microcracking, which is inversely related to relative ductility, is predicted to increase dramatically from 0.00 wt.% Si to 0.10 wt.% Si of the α-Mo phase; however, it increases more gradually with increasing Si content beyond 0.10 wt.% Si in the α-Mo phase. The susceptibility to microcracking demonstrates a slight decrease with increasing volume fraction α-Mo, and effect which becomes more gradual with increasing α-Mo Si content until it is almost negligible for 1.00 wt.% Si in α-Mo. In all cases, increasing temperature results in decreasing susceptibility to microcracking.

Finally, the results of the grain size study do not show any dependence of the mechanical properties on grain size. This is an unexpected and unrealistic result shown to be a result of the lack of an observable Hall-Petch effect in the experimental yield strength found in literature and reflected in the α-Mo calibration [38]. Although no Hall-Petch effect is observed for polycrystalline α-Mo with mean grain diameters as small as 50 μm, it is reasonable to assume that sufficiently small grains exhibit a Hall-Petch effect. In future work, further experimental evidence of a Hall-Petch effect can be easily incorporated into the calibration of the α-Mo constitutive law developed in this work. Additional grain size effects are expected for fatigue resistance and susceptibility to microcracking even in the absence of a Hall-Petch effect on yield strength; however, the grain size study in this work is limited by the computational cost of sufficiently resolved FE meshes capable of capturing the same absolute length scales for volume elements with orders of magnitude differences in mean grain size.

7.6 Significance

This chapter presents a unique, broad study of variations in microstructure-sensitive mechanical properties for triplex Mo-Si-B alloys containing the α-Mo, A15, and T2 phases. This study presents the first computational model for building the microstructure-property relationships in Mo-Si-B alloys, and uses a novel reduced order technique to include relative ductility as a fourth mechanical property for optimization in addition to elastic modulus, yield strength, and fatigue resistance. The results of this parametric study demonstrate the ability of the modeling tools to capture spatial distributions of Si content and phase clustering, which can be included in future work. Further, these modeling tools are general and can be adapted to model similar quasi-brittle material systems.

CHAPTER VIII

CONCLUSIONS

8.1 Summary

Research into Mo-Si-B alloys has begun to yield promising results towards using these alloys in gas turbine engines. However, little work has been done to model the mechanical properties of Mo-Si-B alloys. This research advances the understanding of the microstructure-property relationships of Mo-Si-B alloys by developing and exercising a novel computational approach to microstructure-sensitive mechanical property modeling for Mo-Si-B alloys.

Three novel modeling tools are developed, calibrated, and exercised for triplex Mo-Si-B alloys: a microstructure generator, a crystal-viscoplastic constitutive law, and post-processing algorithms for evaluating mechanical properties. To calibrate and provide input for these modeling tools, samples of polycrystalline α-Mo and representative triplex Mo-Si-B alloys containing the α-Mo, A15, and T2 phases are obtained and characterized. An experimental study of the stress-strain response of polycrystalline α-Mo is conducted to determine variations in mechanical response of α-Mo as a function of temperature and composition.

Chapter 3 introduces the necessary material characterization to fully capture microstructure-sensitivities for the mechanical properties of yield strength, fatigue resistance, and susceptibility to microcracking. Orientation imaging microscopy (OIM) is performed with EBSD mapping of α-Mo material with varying Si content to capture the large inhomogeneity of the experimental monotonic compression specimens. Optical microscopy is used to partially characterize a representative triplex Mo-Si-B microstructure and guide a parametric study of triplex Mo-Si-B microstructures.

Chapter 4 introduces the development of a custom microstructure generator capable of capturing the large spatial inhomogeneity of the α-Mo material used in the experimental compression specimens. The microstructure generator is used to build synthetic volume elements of polycrystalline α-Mo material for use in calibrating the α-Mo constitutive law. This same microstructure generator is used to build the synthetic volume elements used in the parametric study of triplex Mo-Si-B microstructure-sensitive mechanical properties.

In Chapter 5, the crystal-viscoplastic constitutive law is presented and calibrated for α-Mo. Although the intermetallic phases are not treated with a calibrated CVP constitutive law, the ability to include plastic deformation in these phases is retained in the constitutive model implementation. The anisotropic elastic and relevant thermal properties of each phase are taken from literature as a function of temperature. The elasticity tensor is assigned as a function of phase crystal structure, but the coefficient of thermal expansion is assumed to be isotropic for all phases.

A reduced order damage indicator parameter is developed and validated against 2D cohesive zone simulations of triplex Mo-Si-B in Chapter 6. Here the reduced order damage indicator parameter is formulated following the constitutive law for damage in a bilinear traction-separation cohesive zone model. An interface area averaged DIP_{avg} is shown to capture initial microcracking up to the limit where the corresponding 2D cohesive simulations show widespread crack propagation. This reduced order approach facilitates the mechanical property prediction of susceptibility to microcracking in 3D simulations for which full cohesive simulations are computationally intractable.

Finally, the full results of a broad parametric study of triplex Mo-Si-B microstructures is presented in Chapter 7. This study explores the microstructure effects of α-Mo volume fraction and Si content on the mechanical properties of yield strength, fatigue resistance under isothermal low cycle fatigue conditions, and susceptibility

to microcracking. The study shows the expected trends of increasing yield strength with increasing α-Mo Si content and decreasing yield strength with increasing α-Mo volume fraction; however, it also includes the solid-solution softening between pure Mo and α-Mo with small additions of Si content. The fatigue crack driving forces generally decrease with increasing α-Mo Si content and increase with increasing α-Mo volume fractions; however, at low α-Mo Si contents, the fatigue crack driving forces change trends to decreasing driving force with increasing α-Mo volume fraction after a certain α-Mo volume fraction is reached. This threshold in α-Mo volume fraction increases with increasing α-Mo Si content, until it surpasses the 80% α-Mo volume fraction at an α-Mo Si content of 0.25 wt.% Si. The susceptibility to microcracking is predicted to increase significantly from pure Mo to α-Mo with only 0.10 wt.% Si, and increase gradually with additional increases in Si content. With increasing α-Mo volume fraction, a decrease in susceptibility to microcracking is observed; however, this effect is very gradual with respect to the variation predicted for Si content variations and all but disappears for α-Mo Si content of 0.75 wt.% or greater.

8.2 Significance

The novel modeling tools developed in this work include a microstructure generator capable of seamlessly capturing material inhomogeneity with regions of distinct microstructures and up to three separate phases, a crystal-viscoplastic constitutive law calibrated for α-Mo that captures the effects of Si content and temperature, and a quantitative reduced order damage indicator parameter for estimating susceptibility to microcracking as a function of microstructure.

The α-Mo experimental study conducted to calibrate the α-Mo CVP law contains additional evidence of changing deformation mechanisms between pure Mo and α-Mo with even small additions of Si. This change in deformation mechanisms is observed in the changing strain rate sensitivity behavior as a function of temperature.

The novel reduced order damage indicator parameter (DIP) is introduced as a surrogate for cohesive zone models in order to evaluate microstructure-sensitive changes in relative ductility related to susceptibility to widespread brittle microcrack formation in quasi-brittle materials without the need for computationally expensive cohesive zone elements. This reduced order modeling approach facilitates the design of fully 3D microstructures using a quantitative measure for relative interface average damage indicator as one of the targeted design objectives.

The parametric study exercising these modeling tools provides insight into the relationship between α-Mo Si content and α-Mo volume fraction and the mechanical properties of yield strength, fatigue resistance, and susceptibility to microcracking at both room temperature and 1400°C. A short study on the effects of grain size demonstrates the need for high resolution FE models in order to capture grains sizes spanning several orders of magnitude at the same absolute length scales. The parametric study examining these properties also helps build a database of microstructure-property relationships capable of guiding the optimization process for Mo-Si-B alloys for many different applications including for use in gas turbine engines.

In addition to the advances in understanding Mo-Si-B alloys, this research builds the modeling tools and establishes the workflow required to optimize similar material systems including both ductile and quasi-brittle phases for a variety of applications. This helps further establish a framework to rapidly deploy Integrated Computational Materials Engineering (ICME) modeling tools for the optimization of new alloy systems beyond that of Mo-Si-B alloys.

8.3 Future Work

There are many aspects of this work that would benefit from continuing projects. Now that the microstructure-sensitive modeling tools have been developed for Mo-Si-B and been applied over a broad range of microstructures, a more detailed study can be

conducted on a targeted subset of microstructures. The modeling tools developed in this work can also be extended to similar multi-phase materials containing a mixture of quasi-brittle and ductile phases.

A more detailed Mo-Si-B study would benefit from improvements to the constitutive law calibration, such as including variations in the calibration of slip system types and calibrating to cyclic loading data, and by refining the reduced order DIP. Improvements could be made to the constitutive model, both by conducting an experimental study of material more closely matching the microstructures of interest and by including sub-structure mechanism details in the evolution equations. The reduced order DIP could be improved by developing a method to determine an estimated location and size for intermetallic cracking. Both the reduced order DIP and cohesive zone simulations could be improved with targeted experiments for separately calibrating the cohesive element constitutive law based on location in the microstructure and fractography to quantitatively determine the changing role of intergranular and transgranular cleavage as a function of both temperature and Si content. Finally, if the CVP constitutive law is re-written for use with Abaqus\Explicit, a more detailed microstructure-sensitive study could be conducted with the 2D cohesive simulations that retain the ability to allow microcrack formation and propagation.

8.3.1 Experimental Work

In the calibration of the CVP constitutive law for α-Mo of this work, each of the 24 included slip systems is treated identically. To properly calibrate a CVP model on a slip system basis, single crystal experiments are required so that slip systems can be isolated and calibrated separately. If single crystal material cannot be tested, micro-indentation or nano-indentation could provide relative differences in slip system strength and possibly plastic hardening rates, as well. Without additional experimental work to separately calibrate individual slip systems, the CVP constitutive law may

still be improved by distinguishing between types or families of slip systems; however, this requires additional assumptions about the differences in slip resistance or hardening rates on different families of slip system.

Regardless of the ability to separately calibrate individual or families of slip systems, a better calibration of the CVP model could be made with a more thorough experimental schedule. The first improvement would come from α-Mo calibration material with a homogeneous microstructure. Single crystals would be preferred, but fine grained polycrystalline material could still provide good data for improvements of the CVP calibration. Polycrystalline material should contain equiaxed, randomly textured microstructures with a typical log-normal distribution of grain diameter and small enough grains to treat experimental specimens as RVEs for modulus and yield strength. The material should also have a spatially homogeneous distribution of Si content, or at least a sufficiently large volume that the spatial distribution does not significantly effect the volume averaged experimental stress-strain results. While this first step would greatly improve the compression test schedule presented in this work, adding multiple tests at each point in the test schedule would help quantify the variation resulting from specimen variation.

The next easiest improvement to the α-Mo calibration would come from a more complete test schedule including both tension and compression test specimens. If the test schedule is also expanded to include a greater refinement of Si content between pure Mo and Mo with 0.1 wt.% Si, the steep changes in yield strength and volume average DIP_{avg} could be refined and explored.

Very little is known about the cyclic behavior of α-Mo and Mo-Si-B alloys. The final goal for experimental improvements should be test specimens for fatigue calibration, both for isothermal calibration of the constitutive law at multiple temperatures and for thermomechanical fatigue validation of the temperature dependent constitutive law. Starting with a cyclic mechanical response calibration of the α-Mo would

be the easiest way to start improving the constitutive model for fatigue predictions. Eventually, a properly calibrated constitutive model for the mechanical response under fatigue loading could help begin linking FIP predictions to fatigue life.

Combining these experimental studies with quantitative fractography and spatial composition characterization to distinguish the relative amounts of intergranular and transgranular cleavage as a function of Si content would help refine the cohesive zone constitutive law, and by extension the volume average DIP_{avg} calculations. Distinguishing between the relative strengths of the intermetallic phases or the grain boundary strength as a function of Si content would allow for more quantitative crack formation and propagation studies with the potential to predict changing damage mechanisms as a function of microstructural changes.

While this experimental work would greatly improve the mechanical property predictions using the microstructure-sensitive modeling tools developed in this work, a thorough experimental program is time consuming and expensive. Consequently, it is easier to start by refining the modeling tools while the experimental work is progress.

8.3.2 Computational Work

Perhaps the most straight forward continuing work would be to use the same modeling tools developed in this work to explore additional microstructure effects. The microstructure generator, constitutive model implementation, and post-processing tools can be directly applied to study the influence of texture, spatial distributions of α-Mo Si content, and spatial distributions of each phase such as the clustering of intermetallics. Texture effects in both polycrystalline α-Mo and triplex Mo-Si-B would benefit understanding potential processing effects when creating engineering parts from these materials. Differences in α-Mo Si content could easily be implemented on a grain-by-grain basis in both the polycrystalline α-Mo and in the α-Mo

phase of triplex Mo-Si-B alloys by assigning different α-Mo calibrations to each grain; however, understanding spatial variation of Si content within individual α-Mo grains would require a microstructure generator targeted at modeling a smaller number of grains in highly resolved meshes and assigning constitutive model calibrations on an element by element basis. Clustering of the intermetallic phases can have a significant effect on the strength, fracture toughness, and ductility of triplex Mo-Si-B alloys through the effects of the percolation threshold of crack formation, propagation, and coalescence. Relatively small updates to the microstructure generator's ellipsoidal packing algorithm would be required to populate a volume element with ellipsoids defining intermetallic clusters prior to packing the volume with ellipsoids representing individual grains. Intermetallic clustering would be achieved by restricting all or some volume fraction of the intermetallics to the intermetallic cluster ellipsoids when placing individual grains.

Another project that would continue quite naturally from the modeling tools presented in this work is to perform a microstructure-sensitive parametric study with the 2D cohesive simulations. A good study examining the effects of intermetallic clustering and Si content has already been performed [118], but could be improved by implementing the CVP model of this work for use in Abaqus\Explicit to explore spatial distribution of Si content and temperature effects on susceptibility to and propagation of microcracking at room temperature. Such a study would require rewriting the constitutive law for the differences in the user material subroutines used by Abaqus\Standard and Abaqus\Explicit and accounting for 2D slip systems instead of the fully 3D slip systems calibrated in this work. The remaining post-processing modeling tools require minor changes accompanying the differences in output between 2D and 3D simulations.

The next computational tool improvement would come from including transgranular cleavage in the volume average DIP_{avg} calculations. Transgranular cleavage is left

out of this work due to the difficulties of defining an accurate and consistent method of estimating transgranular crack location and size without cohesive elements. In comparison to intergranular cleavage with well defined spatial locations and orientations, it is difficult to predict transgranular cleavage location and orientation without cohesive elements. It is anticipated that implementing transgranular cleavage without cohesive elements would require examining the spatial distributions of stress and strain within each grain. An estimate for location could be predicted if there is sufficient variation in the local stress or strain field and orientation may be estimated from the principal stress or principal strain directions. The final difficulty is predicting the size of affected surface area. The simplest approach would be to calculate damage within or between every element in the grain, but this would likely overestimate the damage driving microcrack formation and eliminate any benefits from predicting crack location and orientation. A more difficult process would be to first estimate the location and orientation of microcrack formation and then calculate damage only along those elements in the plane of the microcrack across the entire grain. Such a process would be the closest analogue to the estimation of microcrack formation along grain boundaries and probably produce the best results.

Including transgranular cleavage with such an approach would significantly increase the computational resources required in post-processing. The intergranular microcrack formation can be performed without separating the stress-strain field into and examining individual grain responses. Instead, each element can be investigated individually and the intergranular damage parameter is calculated between elements of the desired different phases. Including microcracking between grains of the same phase would be equally inexpensive, instead performing the calculations whenever adjacent elements have separate grain IDs. The only additional computational expense would come from determining which material properties to use as a function of the phases of each element, which is a small additional cost with respect to the detailed

individual grain analysis required for transgranular cleavage. An early attempt at separating individual grain stress-strain responses suggests that including transgranular cleavage could increase the post-processing computation time from several minutes to several hours or even an entire day for a single SVE instantiation, depending on the calibration of the constitutive law.

With the inclusion of transgranular cleavage, improvements could be made to the evaluation of the DIP. In this work, a volume average DIP_{avg} is used to rank microstructures. This approach neglects the effects both the extreme value distribution and spatial distribution of microcracks, which effect the relative susceptibility to microcracking and relative damage tolerance of microstructures. While the extreme value statistics simply requires a more detailed set of simulations at each point in a parametric study, understanding and quantifying the effects of spatial distribution in microcracks requires further development from a 2D cohesive study similar to that presented in Chapter 6.

With the availability of increased computational power or for a more focused microstructure study, the microstructure-sensitive mechanical property predictions could be further refined with larger, more refined FE simulations. Relating microstructural features such as misorientation or intermetallic clustering to drivers of minimum fatigue life or more extensive microcrack formation would require larger, more refined FE models than used in this work. Evaluating the effects of voxellated meshes on artificial stress concentrations, FIPs, and DIP would require a microstructure generator capable of meshing smooth grain boundaries and significant mesh refinements over the SVEs used in this work.

Finally, a complete optimization of Mo-Si-B alloys for use in a gas turbine engine environment must include creep and oxidation resistance. Incorporating microstructure-sensitive creep and oxidation modeling tools with the tools developed in this work would allow additional mechanical properties to be considered in future property

optimization work.

REFERENCES

[1] Munroe, R., "xkcd." `https://xkcd.com/722/`.

[2] Pineau, A. and Antolovich, S. D., "High temperature fatigue of nickel-base superalloys - a review with special emphasis on deformation modes and oxidation," *Engineering Failure Analysis*, vol. 16(8), pp. 2668–2697, 2010.

[3] Reed, R. C., *The Superalloys: Fundamentals and Applications*. Cambridge University Press, 2008.

[4] Dimiduk, D. M. and Perepezko, J. H., "Mo-Si-B alloys: Developing a revolutionary turbine-engine material," *Materials Research Society Bulletin*, pp. 639–645, September 2003.

[5] U.S. Department of Energy, "How gas turbine power plants work." `http://energy.gov/fe/how-gas-turbine-power-plants-work`, October 2013.

[6] Bewlay, B. P., Jackson, M. R., Zhao, J. C., and Subramanian, P. R., "A review of very-high-temperature Nb-silicide-based composites," *Metallurgical and Materials Transactions A*, vol. 34A, pp. 2043–2052, October 2003.

[7] Perepezko, J. H., "The hotter the engine, the better," *Science*, vol. 326, pp. 1068–1069, November 2009.

[8] Lemberg, J. A. and Ritchie, R. O., "Mo-Si-B alloys for ultrahigh-temperature structural applications," *Advanced Materials*, vol. 24, pp. 3445–3480, 2012.

[9] Alur, A. P., Sakidja, R., Wang, P., Jain, P., Perepezko, J. H., and Kumar, K. S., "Deformation behavior of a quaternary Mo-Nb-Si-B alloy," in *Materials Research Society Symposium Proceedings*, vol. 1295, pp. 355–360, Materials Research Society, 2011.

[10] Mitra, R., "Mechanical behaviour and oxidation resistance of structural silicides," *International Materials Reviews*, vol. 51, no. 1, pp. 13–64, 2006.

[11] Aryal, S., Gao, M. C., Ouyang, L., Rulis, P., and Ching, W. Y., "*Ab initio* studies of Mo-based alloys: Mechanical, elastic, and vibrational properties," *Intermetallics*, vol. 38, pp. 116–125, 2013.

[12] Schneibel, J. H., Kramer, M. J., Ünal, O., and Wright, R. N., "Processing and mechanical properties of a molybdenum silicide with the composition Mo-12Si-8.5B (at. %)," *Intermetallics*, vol. 9, pp. 25–31, 2001.

[13] Parthasarathy, T. A., Mendiratta, M. G., and Dimiduk, D. M., "Oxidation mechanisms in Mo-reinforced Mo_5SiB_2 (T2) - Mo_3Si alloys," *Acta Materialia*, vol. 50, pp. 1857–1868, 2002.

[14] Allison, J., Backman, D., and Christodoulou, L., "Integrated computational materials engineering: A new paradigm for the global materials profession," *JOM*, pp. 25–27, November 2006.

[15] Committee on Integrated Computational Materials Engineering, N. R. C., *Integrated Computational Materials Engineering: A Transformational Discipline for Improved Competitiveness and National Security*. The National Academies Press, 2008.

[16] Nowotny, H., Dimakopoulou, E., and Kudielka, H., "Untersuchungen in den dreistoffsystemen: Molybdä-silizium-bor, wolfram-silizium-bor und in dem system: VSi_2-$TaSi_2$," *Monatshefte für Chemie*, vol. 88, no. 2, pp. 180–192, 1957. in German.

[17] Aronsson, B., "The crystal structure of Mo_5SiB_2," *Acta Chemica Scandinavica*, vol. 12, no. 1, pp. 31–37, 1958.

[18] Nunes, C. A., Sakidja, R., Dong, Z., and Perepezko, J. H., "Liquidus projection for the Mo-rich portion of the Mo-Si-B ternary system," *Intermetallics*, vol. 8, pp. 327–337, 2000.

[19] Lemberg, J. A., Middlemas, M. R., Weingärtner, T., Gludovatz, B., Cochran, J. K., and Ritchie, R. O., "On the fracture toughness of fine-grained Mo-3Si-1B (wt. %) alloys at ambient to elevated (1300 °C) temperatures," *Intermetallics*, vol. 20, pp. 141–154, 2012.

[20] Featherston, F. H. and Neighbours, J. R., "Elastic constants of tantalum, tungsten, and molybdenum," *Physical Review*, vol. 130, pp. 1324–1333, May 1963.

[21] Dickinson, J. M. and Armstrong, P. E., "Temperature dependence of the elastic constants of molybdenum," *Journal of Applied Physics*, vol. 38, pp. 602–606, February 1967.

[22] Swadener, J. G., Rosales, I., and Schneibel, J. H., "Elastic and plastic properties of Mo_3Si measured by nanoindentation," in *Materials Research Society Symposium Proceedings*, vol. 646, Materials Research Society, 2001.

[23] Ito, K., Ihara, K., Tanaka, K., Fujikura, M., and Yamaguchi, M., "Physical and mechanical properties of single crystals of the T_2 phase in the Mo-Si-B system," *Intermetallics*, vol. 9, pp. 591–602, 2001.

[24] Alur, A. P., Chollacoop, N., and Kumar, K. S., "High-temperature compression behavior of Mo-Si-B alloys," *Acta Materialia*, vol. 52, pp. 5571–5587, 2004.

[25] Choe, H., Chen, D., Schneibel, J. H., and Ritchie, R. O., "Ambient to high temperature fracture toughness and fatigue-crack propagation behavior in a Mo-12Si-8.5B (at. %) intermetallic," *Intermetallics*, vol. 9, pp. 319–329, 2001.

[26] Choe, H., Schneibel, J. H., and Ritchie, R. O., "On the fracture and fatigue properties of Mo-Mo_3Si-Mo_5SiB_2 refractory intermetallic alloys at ambient to elevated temperatures (25°c to 1300°c)," *Metallurgical and Materials Transactions*, vol. 34A, no. 2, p. 225, 2003.

[27] Jain, P., Alur, A. P., and Kumar, K. S., "High temperature compressive flow behavior of a Mo-Si-B solid solution alloy," *Scripta Materialia*, vol. 54, pp. 13–17, 2006.

[28] Jéhanno, P., Heilmaier, M., Saage, H., Böning, M., Kestler, H., Freudenberger, J., and Drawin, S., "Assessment of the high temperature deformation behavior of molybdenum silicide alloys," *Materials Science and Engineering A*, vol. 463, pp. 216–223, 2007.

[29] Jain, P. and Kumar, K. S., "Tensile creep of Mo-Si-B alloys," *Acta Materialia*, vol. 58, pp. 2124–2142, 2010.

[30] Jéhanno, P., Heilmaier, M., Saage, H., Heyse, H., Böning, M., Kestler, H., and Schneibel, J. H., "Superplasticity of a multiphase refractory Mo-Si-B alloy," *Scripta Materialia*, vol. 55, pp. 525–528, 2006.

[31] Kumar, K. S. and Alur, A. P., "Deformation behavior of a two-phase Mo-Si-B alloy," *Intermetallics*, vol. 15, pp. 687–693, 2007.

[32] Liu, C. T., Schneibel, J. H., and Heatherly, L., "Processing, microstructure, and properties of multiphase Mo silicide alloys," in *Materials Research Society Symposium Proceedings*, vol. 552, Materials Research Society, 1999.

[33] Nieh, T. G., Wang, J. G., and Liu, C. T., "Deformation of a multiphase Mo-9.4Si-13.8B alloy at elevated temperatures," *Intermetallics*, vol. 9, pp. 73–79, 2001.

[34] Schneibel, J. H., Kramer, M. J., and Easton, D. S., "A Mo-Si-B intermetallic alloy with a continuous α-Mo matrix," *Scripta Materialia*, vol. 46, pp. 217–221, 2002.

[35] Kruzic, J. J., Schneibel, J. H., and Ritchie, R. O., "Ambient- to elevated-temperature fracture and fatigue properties of Mo-Si-B alloys: Role of microstructure," *Metallurgical and Materials Transactions*, vol. 36A, pp. 2393–2402, September 2005.

[36] Middlemas, M. R., *Fabrication, Strength and Oxidation of Molybdenum-Silicon-Boron Alloys from Reaction Synthesis*. PhD thesis, Georgia Institute of Technology, May 2009.

[37] Gokhale, A. B. and Abbaschian, G. J., "The Mo-Si (molybdenum-silicon) system," *Journal of Phase Equilibria*, vol. 12, no. 4, pp. 493–498, 1991.

[38] Sturm, D., Heilmaier, M., Schneibel, J. H., Jéhanno, P., Skrotzki, B., and Saage, H., "The influence of silicon on the strength and fracture toughness of molybdenum," *Materials Science and Engineering A*, vol. 463, pp. 107–114, 2007.

[39] Floquet, N., Bertrand, O., and Heizmann, J. J., "Structural and morphological studies of the growth of MoO_3 scales during high-temperature oxidation of molybdenum," *Oxidation of Metals*, vol. 37, pp. 253–280, April 1992.

[40] Pink, E. and Arsenault, R. J. *Progress in Materials Science*, vol. 24, 1979.

[41] Promisel, N. E., ed., *The Science and Technology of Tungsten, Tantalum, Molybdenum, Niobium and Their Alloys*. New York: Pergamon Press, 1964.

[42] Petukhov, B. V., "Effect of solid-solution softening of crystalline materials: Review," *Crystallography Reports*, vol. 52, no. 1, pp. 112–122, 2007.

[43] Wronski, A. S. and Johnson, A. A. *Philosophical Magazine*, vol. 7, p. 213, 1962.

[44] Orava, R. N. *Transactions of the Metallurgical Society of AIME*, vol. 230, p. 1614, 1964.

[45] Bruckart, W. L., LaChance, M. H., Craighead, C. M., and Jaffee, R. I. *Transactions of the American Society of Metals*, vol. 45, no. 286, 1953.

[46] Northcott, L., *Molybdenum*. New York: Academic Press Inc., 1956.

[47] Rosales, I. and Schneibel, J. H., "Stoichiometry and mechanical properties of Mo_3Si," *Intermetallics*, vol. 8, pp. 885–889, 2000.

[48] Rioult, F. A., Imhoff, S. D., Sakidja, R., and Perepezko, J. H., "Transient oxidation of Mo-Si-B alloys: Effect of the microstructure size scale," *Acta Materialia*, vol. 57, pp. 4600–4613, 2009.

[49] Rawn, C. J., Scheibel, J. H., Hoffmann, C. M., and Hubbard, C. R., "The crystal structure and thermal expansion of Mo_5SiB_2," *Intermetallics*, vol. 9, pp. 209–216, 2001.

[50] Daloz, W. L., *Developing a High Temperature, Oxidation Resistant Molybdenum-Silica Composite*. PhD thesis, Georgia Institute of Technology, December 2015.

[51] Kumar, K. S., "Fatigue response of Mo-Si-B alloys," tech. rep., Brown University, 2005.

[52] Marshall, P. E., *Development of Oxidation Resistant Molybdenum-Silicon-Boron Composites*. PhD thesis, Georgia Institute of Technology, December 2015.

[53] Schneibel, J. H., Liu, C. T., Easton, D. S., and Carmichael, C. A., "Microstructure and mechanical properties of Mo-Mo_3Si-Mo_5SiB_2 silicides," *Materials Science and Engineering A*, vol. 261, pp. 78–83, 1999.

[54] Przybyla, C. P., *Microstructure-sensitive Extreme Value Probabilities of Fatigue in Advance Engineering Alloys*. PhD thesis, Georgia Institute of Technology, August 2010.

[55] Hill, R., "Elastic properties of reinforced solids: Some theoretical principles," *Journal of the Mechanics and Physics of Solids*, vol. 11, no. 5, pp. 357–372, 1963.

[56] Qu, J. and Cherkaoui, M., *Fundamentlas of Micromechanics of Solids*. John Wiley & Sons, Inc., 2006.

[57] McDowell, D. L. and Dunne, F. P. E., "Microstructure-sensitive computational modeling of fatigue crack formation," *International Journal of Fatigue*, vol. 32, pp. 1521–1542, 2010.

[58] Kanit, T., Forest, S., Galliet, I., Mounoury, V., and Jeulin, D., "Determination of the size of the representative volume element for random composites: Statistical and numerical approach," *International Journal of Solids and Structures*, vol. 40, pp. 3647–3679, 2003.

[59] Ostoja-Starzewski, M., "Material spatial randomness: From statistical to representative volume element," *Probabilistic Engineering Mechanics*, vol. 21, pp. 112–132, 2004.

[60] Ostoja-Starzewski, M., Du, X., Khisaeva, Z. F., and Li, W., "On the size of representative volume element in elastic, plastic, thermoelastic and permeable random microstructures," *Materials Science Forum*, vol. 539-543, pp. 201–206, 2007.

[61] Saylor, D. M., Fridy, J., El-Dasher, B. S., Jung, K.-Y., and Rollet, A. D., "Statistically representative three-dimensional microstructures based on orthogonal observation sections," *Metallurgical and Materials Transactions*, vol. 35A, pp. 1969–1979, 2004.

[62] Gross, D. and Li, M., "Constructing microstructures of poly- and noncrystalline materials for numerical modeling and simulation," *Applied Physics Letters*, vol. 80, pp. 746–748, 2002.

[63] Brahme, A., Alvi, M. H., Saylor, D., Fridy, J., and Rollett, A. D., "3d reconstruction of microstructure in a commercial purity aluminum," *Scripta Materialia*, vol. 55, pp. 75–80, 2006.

[64] Groeber, M., Ghosh, S., Uchic, M. D., and Dimiduk, D. M., "A framework for automated analysis and simulation of 3d polycrystalline microstructures. part 1: Statistical characterization," *Acta Materialia*, vol. 56, pp. 1257–1273, 2008.

[65] Groeber, M., Ghosh, S., Uchic, M. D., and Dimiduk, D. M., "A framework for automated analysis and simulation of 3d polycrystalline microstructures. part 2: Synthetic structure generation," *Acta Materialia*, vol. 56, pp. 1274–1287, 2008.

[66] Jiang, L., Chawla, N., Pachero, M., and Noveski, V., "Three-dimensional (3d) micostructural characterization and quantification of reflow porosity in sn-rich alloy/copper joints by x-ray tomography," *Materials Characterization*, vol. 62, pp. 970–975, 2011.

[67] Horálek, V., "ASTM grain-size model and related random tesselation models," *Materials Characterization*, vol. 25, pp. 263–284, 1990.

[68] Aurenhammer, F., "Voronoi diagrams – a survey of a fundamental geometric data structure," *ACM Computing Surveys*, vol. 23, no. 3, pp. 345–405, 1991.

[69] Barbe, F., Decker, L., Jeulin, D., and Cailletaud, G., "Intergranular and intragranular behavior of polycrystalline aggregates. par 1: F.e. model," *International Journal of Plasticity*, vol. 17, pp. 513–536, 2001.

[70] Groeber, M. A. and Jackson, M. A., "DREAM.3D: A digital representation environment for the analysis of microstructure in 3d," *Integrating Materials and Manufacturing Innovation*, vol. 3, no. 5, 2014.

[71] "DREAM.3D." `http://dream3d.bluequartz.net/`, February 2017.

[72] Hill, R., "Generalized constitutive relations for incremental deformation of metal crystals by multislip," *Journal of the Mechanics and Physics of Solids*, vol. 14, no. 2, p. 95, 1966.

[73] Lee, E. H., "Elastic-plastic deformation at finite strains," *Journal of Applied Mechanics*, vol. 36, no. 1, p. 1, 1969.

[74] Rice, J. R., "Inelastic constitutive relations for solid: An internal-variable theory and its application to metal plasticity," *Journal of the Mechanics and Physics of Solids*, vol. 19, no. 6, p. 433, 1971.

[75] Hill, R. and Rice, J. R., "Constitutive analysis of elastic-plastic crystals at arbitrary strain," *Journal of the Mechanics and Physics of Solids*, vol. 20, no. 6, p. 401, 1972.

[76] Asaro, R. J. and Rice, J. R., "Strain localization in ductile single-crystals," *Journal of the Mechanics and Physics of Solids*, vol. 25, no. 5, pp. 309–338, 1977.

[77] Hill, R. and Havner, K. S., "Perspectives in the mechanics of elastoplastic crystals," *Journal of the Mechanics and Physics of Solids*, vol. 30, no. 1, pp. 5–22, 1982.

[78] Asaro, R. J., "Crystal plasticity," *Journal of Applied Mechanics*, vol. 50, pp. 921–934, December 1983.

[79] Peirce, D., Asaro, R. J., and Needleman, A., "Material rate dependence and localized deformation in crystalline solids," *Acta Metallurgica*, vol. 31, no. 12, pp. 1951–1976, 1983.

[80] Asaro, R. J., "Large strain plasticity in crystalline materials," *Journal of Metals*, vol. 35, no. 8, p. A28, 1983.

[81] Asaro, R. J., "Micromechanics of crystals and polycrystals," *Advances in Applied Mechanics*, vol. 23, pp. 1–115, 1983.

[82] Needleman, A., Asaro, R. J., Lemonds, J., and Peirce, D., "Finite-element analysis of crystalline solids," *Computer Methods in Applied Mechanics and Engineering*, vol. 52, no. 1, pp. 689–708, 1985.

[83] Kalidindi, S. R., Bronkhorst, C. A., and Anand, L., "Crystallographic texture evolution in bulk deformation processing of fcc metals," *Journal of the Mechanics and Physics of Solids*, vol. 40, no. 3, pp. 537–569, 1992.

[84] McDowell, D. L., *Internal State Variable Theory*, vol. 3, pp. 1151–1170. Springer, 2005.

[85] Coleman, B. D. and Gurtin, M. E., "Thermodynamics with internal state variables," *Journal of Chemical Physics*, vol. 47, pp. 597–613, 1967.

[86] Kestin, J. and Rice, J. R., *A Critical Review of Thermodynamics*, ch. Paradoxes in the Application of Thermodynamics to Strained Solids, pp. 275–298. Baltimore: Mono-Book Corp., 1970.

[87] Germain, P., Nguyen, Q. S., and Suquet, P., "Continuum thermodynamics," *Journal of Applied Mechanics*, vol. 50, p. 1010, 1983.

[88] Kestin, J., "Local equilibrium formalism applied to mechanics of solids," *International Journal of Solids and Structures*, vol. 29, no. 14-15, pp. 1827–1836, 1992.

[89] Khan, A. S. and Huang, S., *Continuum Theory of Plasticity*. John Wiley and Sons, Inc., 1995.

[90] McGinty, R. D., *Multiscale Representation of Polycrystalline Inelasticity*. PhD thesis, Georgia Institute of Technology, 2001.

[91] Zambaldi, C., Roters, F., and Raabe, D., "Analysis of the plastic anisotropy and pre-yielding of (γ/α_2)-phase titanium aluminide microstructures by crystal plasticity simulation," *Intermetallics*, vol. 19, pp. 820–827, 2011.

[92] Mayeur, J. R. and McDowell, D. L., "A three-dimensional crystal plasticity model for duplex ti-6al-4v," *International Journal of Plasticity*, vol. 23, pp. 1457–1485, 2007.

[93] Grujicic, M. and Batchu, S., "A crystal plasticity materials constitutive model for polysynthetically-twinned γ-TiAl+α_2-Ti_3Al single crystals," *Journal of Materials Science*, vol. 36, pp. 2851–2863, 2001.

[94] Zhang, M., Zhang, J., and McDowell, D. L., "Microstructure-based crystal plasticity modeling of cyclic deformation of ti-6al-4v," *International Journal of Plasticity*, vol. 23, no. 8, pp. 1328–1348, 2007.

[95] Kern, P. C., "Improvements to the computational pipeline in crystal plasticity estimates of high cycle fatigue of microstructures," Master's thesis, Georgia Institute of Technology, May 2016.

[96] Kruzic, J. J., Scheibel, J. H., and Ritchie, R. O., "Fracture and fatigue resistance of Mo-Si-B alloys for ultrahigh-temperature structural applications," *Scripta Materialia*, vol. 50, no. 4, pp. 459–464, 2004.

[97] Kruzic, J. J., Schneibel, J. H., and Ritchie, R. O., "Role of microstructure in promoting fracture and fatigue resistance in Mo-Si-B alloys," in *Materials Research Society Symposium Proceedings*, vol. 842, 2005.

[98] Kumar, S. and Alur, A. P., "Crack growth behavior in a two-phase Mo-Si-B alloy," vol. 980 of *Materials Research Society Symposia Proceedings*, Materials Research Society, Cambridge University Press, 2007.

[99] Fatemi, A. and Socie, D. F., "A critical plane approach to multiaxial fatigue damage including out-of-phase loading," *Fatigue & Fracture of Engineering Materials & Structures*, vol. 11, no. 3, pp. 149–165, 1988.

[100] Hochhalter, J. D., Littlewood, D. J., Jr., R. J. C., Veilleux, M. G., Bozek, J. E., Ingraffea, A. R., and Maniatty, A. M., "A geometric approach to modeling microstructurally small fatigue crack formation: Ii. physically based modeling of microstructure-dependent slip localization and actuation of the crack nucleation mechanism in aa 7075-t651," *Modelling and Simulation in Materials Science and Engineering*, vol. 18, 2010.

[101] Bennett, V. P. and McDowell, D. L., "Polycrystal orientation distribution effects on microslip in high cycle fatigue," *International Journal of Fatigue*, vol. 25, pp. 27–39, 2003.

[102] Suresh, S., *Fatigue of Materials*. Cambridge University Press, 2 ed., 1998.

[103] Manonukul, A. and Dunne, F. P. E., "High- and low-cycle fatigue crack initiation using polycrystal plasticity," *The Royal Society*, vol. 460, pp. 1881–1903, April 2004.

[104] Dune, F. P. E., Wilkinson, A. J., and Allen, R., "Experimental and computational studies of low cycle fatigue crack nucleation in a polycrystal," *International Journal of Plasticity*, vol. 23, pp. 273–295, February 2007.

[105] Socie, D., "Critical plane approaches for multiaxial fatigue damage assessment," in *Advances in Multiaxial Fatigue, ASTM STP 1191* (McDowell, D. L. and Ellis, R., eds.), no. ASTM STP 1191, (Philadelphia), pp. 7–36, American Society for Testing and Materials, 1993.

[106] Elices, M., Guinea, G. V., Gómez, J., and Planas, J., "The cohesive zone model: Advantages, limitations and challenges," *Engineering Fracture Mechanics*, vol. 69, pp. 137–163, January 2002.

[107] Planas, J., Elices, M., Guinea, G. V., Gómez, F. J., Cendón, D. A., and Arbilla, I., "Generalizations and specializations of cohesive crack models," *Engineering Fracture Mechanics*, vol. 70, pp. 1759–1776, September 2003.

[108] Moës, N. and Belytschko, T., "Extended finite element method for cohesive crack growth," *Engineering Fracture Mechanics*, vol. 69, pp. 813–833, May 2002.

[109] Chandra, N., Li, H., Shet, C., and Ghonem, H., "Some issues in the application of cohesive zone models for metal-ceramic interfaces," *International Journal of Solids and Structures*, vol. 39, pp. 2827–2855, 2002.

[110] Park, K. and Paulino, G. H., "Cohesive zone models: A critical review of traction-separation relationships across fracture surfaces," *Applied Mechanics Reivews*, vol. 64, November 2011.

[111] Hillerborg, A., Modéer, M., and Petersson, P. E., "Analysis of crack formation and crack growth in concrete by means of fracture mechanics and finite elements," *Cement and Concrete Research*, vol. 6, pp. 773–782, 1976.

[112] Mai, Y.-W. and Lawn, B. R., "Crack-interface bridging as a fracture resistance mechanism in ceramics: Ii theoretical fracture mechanics model," *Journal of the American Ceramic Society*, vol. 70, pp. 289–294, April 1987.

[113] Tijssens, M. G. A., van der Giessen, E., and Sluys, L. J., "Modeling of crazing using a cohesive surface methodology," *Mechanics of Materials*, vol. 32, pp. 19–35, January 2000.

[114] Tvergaard, V. and Hutchinson, J. W., "The relation between crack growth resistance and fracture process parameters in elastic-plastic solids," *Journal of the Mechanics and Physics of Solids*, vol. 40, pp. 1377–1397, 1992.

[115] Needleman, A., "A continuum model for void nucleation by inclusion debonding," *Journal of Applied Mechanics*, vol. 54, pp. 525–531, 1987.

[116] Needleman, A., "Analysis of tensile decohesion along an interface," *Journal of the Mechanics and Physics of Solids*, vol. 38, pp. 289–324, 1990.

[117] Tomar, V., Zhai, J., and Zhou, M., "Bounds for element size in a variable stiffness cohesive finite element model," *International Journal for Numerical Methods in Engineering*, vol. 61, pp. 1894–1920, October 2004.

[118] Patra, A., Priddy, M. W., and McDowell, D. L., "Modeling the effects of microstructure on the tensile properties and micro-fracture behavior of Mo-Si-B alloys at elevated temperatures," *Intermetallics*, vol. 64, pp. 6–17, 2015.

[119] Turon, A., Dávila, C. G., Camanho, P. P., and Costa, J., "An engineering solution for mesh size effects in the simulation of delamination using cohesive zone models," *Engineering Fracture Mechanics*, vol. 74, pp. 1665–1682, July 2007.

[120] Saucedo-Mora, L. and Marrow, T. J., "FEMME: A multi-scale finite element microstructure meshfree fracture model for quasi-brittle materials with complex microstructures," *Engineering Fracture Mechanics*, vol. 147, pp. 355–372, October 2015.

[121] Anderson, T. L., *Fracture Mechanics: Fundamentals and Applications*. Boca Raton, FL: CRC Press, 2005.

[122] Evans, A. G., "The new high-toughness ceramics," in *Fracture Mechanics: Perspectives and Directions (Twentieth Symposium)* (Wei, R. P. and Gangloff, R. P., eds.), no. ASTM STP 1020, (Philadelphia), pp. 267–291, American Society for Testing and Materials, 1989.

[123] Budiansky, B., Hutchinson, J. W., and Evans, A. G., "Matrix fracture in fiber-reinforced ceramics," *Journal of the Mechanics and Physics of Solids*, vol. 34, pp. 167–189, 1986.

[124] Evans, A. G., "Perspective on the development of high-toughness ceramics," *Journal of the American Ceramic Society*, vol. 73, no. 2, pp. 187–206, 1990.

[125] Li, V. C., Stang, H., and Krenchel, H., "Mircomechanics of crack bridging in fiber reinforced concrete," *Materials and Structures*, vol. 26, pp. 486–494, October 1993.

[126] Awaji, H., Ebisudani, M., Choi, S.-M., and Ohashi, T., "Crack deflection toughening mechanism in brittle materials," in *Fracture Resistance Testing of Monolithic and Composite Brittle Materials* (Salem, J. A., Quinn, G. D., and Jenkins, M. G., eds.), no. ASTM STp 1409, (West Conshochocken, PA), American Society for Testing and Materials, 2002.

[127] Krüger, M., Franz, S., Saage, H., Heilmaier, M., Schneibel, J. H., Jéhanno, P., Möning, M., and Kestler, H., "Mechanically alloyed mo-si-b alloys with a continuous α-mo matrix and improved mechanical properties," *Intermetallics*, vol. 16, pp. 933–941, 2008.

[128] Clemens, H. and Mayer, S., "Design, processing, microstructure, properties, and applications of advanced intermetallic tial alloys," *Advanced Engineering Materials*, vol. 15, no. 4, pp. 191–215, 2013.

[129] Kalidindi, S. R., "Incorporation of deformation twinning in crystal plasticity models," *Journal of the Mechanics and Physics of Solids*, vol. 46, no. 2, pp. 267–290, 1998.

[130] Barenblatt, G. I., "The formation of equilibrium cracks during brittle fracture. general ideas and hypotheses. axially-symmetric cracks," *Prikl Mat Mekh*, vol. 23, pp. 434–444, 1959.

[131] Barenblatt, G. I., *Advances in Applied Mechanics*, vol. VII, ch. Mathematical Theory of Equilibrium Cracks in Brittle Fracture, pp. 55–125. Academic Press, New York, 1962.

[132] Dugdale, D. S., "Yielding of steel sheets containing slits," *Journal of the Mechanics and Physics of Solids*, vol. 8, pp. 100–104, May 1960.

[133] Dassault Systemés Simulia Corporation, "Abaqus v. 6.10," 2010. Providence, RI, USA.

[134] Camacho, G. T. and Ortiz, M., "Computational modelling of impact damage in brittle materials," *International Journal of Solids and Structures*, vol. 33, no. 20-22, pp. 2899–2938, 1996.

[135] Ortiz, M. and Pandolfi, A., "Finite-deformation irresversible cohesive elements for three-dimensional crack-propagation analysis," *International Journal for Numerical Methods in Engineering*, vol. 44, pp. 1267–1282, 1999.

[136] Espinosa, H. D., Dwivedi, S., and Lu, H.-C., "Modeling impact induced delamination of woven fiber reinforced composites with contact/cohesive laws," *Computer Method in Applied Mechanics and Engineering*, vol. 183, pp. 259–290, 2000.

[137] Camanho, P. P. and Dávila, C. G., "Mixed-mode decohesion finite elements for the simulation of delamination in composite materials," Tech. Rep. TM-2002-211737, NASA, 2002.

[138] Xu, X. P. and Needleman, A., "Numerical simulations of fast crack growth in brittle solids," *Journal of the Mechanics and Physics of Solids*, vol. 42, pp. 1397–1434, 1994.

[139] Chen, J., Crisfield, M. A., A. J. Kinloch, E. P. B., Matthews, F. L., and Qiu, Y., "Predicting progressive delamination of composite material specimens via interface elements," *Mechanics of Composite Materials and Structures*, vol. 6, pp. 301–317, 1999.

[140] Alfano, G. and Crisfield, M. A., "Finite element interface models for the delamination analysis of laminated composites: Mechanical and compuational issues," *International Journal for Numerical Methods in Engineering*, vol. 50, pp. 1701–1736, 2001.

[141] Dávila, C. G., Camanho, P. P., and Moura, M. F., "Mixed-mode decohesion elements for analyses with progressive delamination," in *42nd AIAA/ASME/ASCE/AHS/ASC Structures, Structural Dynamics and Materials Conference*, (Seattle, Washington, U.S.A), 2001.

[142] Cui, W., Wisnom, M. R., and Jones, M., "A comparison of failure criteria to predict delamination of unidirectional galss/epoxy specimens waisted through the thickness," *Composites*, vol. 23, no. 3, pp. 158–166, 1992.

[143] Camanho, P. P. and Matthews, F. L., "Delamination onset prediction in mechanically fastened joints in composite laminates," *Journal of Composite Materials*, vol. 33, pp. 906–927, 1999.

[144] Dávila, C. G. and Johnson, E. R., "Analysis of delamination initiation in postbuckled dropped-ply laminates," *AIAA Journal*, vol. 31, no. 4, pp. 721–727, 1993.

[145] Falk, M. A., Needleman, A., and Rice, J. R., "A critical evaluation of dynamic fracture simulations using cohesive surfaces," *Journal de Physique IV*, vol. 4, no. 11, pp. 43–52, 2001.

[146] Klein, P., Foulk, J., , Chen, E., Wimmer, S., and Gao, H., "Physics-based modeling of brittle fracture: Cohesive formulations and the application of meshfree methods," Tech. Rep. SAND2001-8099, Sandia National Laboratories, USA, 2000.

[147] Geubell, P. and Baylor, J., "Impact-induced delamination of composites: a 2-d simulation," *Composites Part B: Engineering*, vol. 29, pp. 589–602, 1998.

[148] Gomez, F. J. and Elices, M., "Fracture of components with v-shaped notches," *Engineering Fracture Mechanics*, vol. 70, pp. 1913–1927, 2003.

[149] Pandolfi, A. and Ortiz, M., "An efficient adaptive procedure for three-dimensional fragmentation simulations," *Engineering with Computers*, vol. 18, pp. 148–159, 2002.

[150] Pandolfi, A. and Ortiz, M., "Solid modeling aspects of three-dimensional fragmentation," *Engineering with Computers*, vol. 14, no. 4, pp. 287–308, 1998.

[151] Silling, S. A., "Reformulation of elasticity theory for discontinuities and long-range forces," *Journal of the Mechanics and Physics of Solids*, vol. 48, no. 1, pp. 175–209, 2000.

[152] Silling, S. A. and Lehoucq, R. B., "Peridynamic theory of solid mechanics," *Advances in Applied Mechanics*, vol. 44, pp. 73–168, 2010.

[153] Silling, S. A., Epton, M., Weckner, O., Xu, J., and Askari, E., "Peridynamic states and constitutive modeling," *Journal of Elasticity*, vol. 88, pp. 151–184, 2007.

[154] Kilic, B. and Madenci, E., "Peridynamic theory for thermomechanical analysis," *IEEE Transactions on Advanced Packaging*, vol. 33, pp. 97–105, 2010.

[155] Xu, J., Askari, A., Weckner, O., and Silling, S. A., "Peridynamic analysis of impact damage in composite laminates," *Journal of Aerospace Engineering*, vol. 21, pp. 187–194, 2008.

[156] Silling, S. A., Zimmerman, M., and Abeyaratne, R., "Deformation of a peridynamic bar," *Journal of Elasticity*, vol. 73, pp. 173–190, 2003.

[157] Zimmerman, M., *A Continuum Theory with Long-range Forces for Solids*. Department of mecahnical engineering, Massachusetts Institute of Technology, 2005.

[158] Weckner, O. and Emmrich, E., "Numerical simulation of the dynamics of a nonlocal, inhomogeneous, infinite bar," *Journal of Computational and Applied Mechanics*, vol. 6, pp. 311–319, 2005.

[159] Weckner, O., Brunk, G., Epton, M. A., Silling, S. A., and Askari, E., "Green's functions in non-local three-dimensional linear elasticity," *Proceedings of the Royal Society A*, vol. 465, pp. 3463–3487, 2009.

[160] Alali, B. and Lipton, R., "Multiscale analysis of heterogeneous media in the peridynamic formulation," Technical Report IMA Preprint Series 2241, Institute for Mathematics and Its Applications, Minneapolis, Minnesota, USA, 2009.

[161] Du, Q. and Zhou, K., "Mathematical analysis for the peridynamic nonlocal continuum theory," *Mathematical Modelling and Numerical Analysis*, vol. 45, no. 2, pp. 217–234, 2011.

[162] Du, Q. and Zhou, K., "Mathematical and numerical analysis of linear peridynamic models with nonlocal boundary conditions," *SIAM Journal on Numerical Analysis*, vol. 45, no. 5, pp. 1759–1780, 2010.

[163] Emmrich, E. and Weckner, O., "Analysis and numerical approximation of an integro-differential equation modeling non-local effects in linear elasticity," *Mathematics and Mechanics of Solids*, vol. 12, pp. 363–384, 2007.

[164] Emmerich, E. and Weckner, O., "On the well-posedness of the linear peridynamic model and its convergence towards the navier equation of linear elasticity," *Communications in Mathematical Sciences*, vol. 5, pp. 851–864, 2007.

[165] Gunzburger, M. and Lehoucq, R. B., "A nonlocal vector calculus with application to nonlocal boundary value problems," Technical Report SAND2009-4666J, Sandia National Laboratories, Albuquerque, New Mexico 87185 and Livermore, California 94550, 2010.

[166] Warren, T. L., Silling, S. A., Askari, A., Weckner, O., Epton, M. A., and Xu, J., "A non-ordinary sate-based peridynamic method to model solid material deformation and fracture," *International Journal of Solids and Structures*, vol. 46, pp. 1186–1195, 2009.

[167] Foster, J. T., Silling, S. A., and Chen, W. W., "Viscoplasticity using peridynamics," *International Journal for Numerical Methods in Engineering*, vol. 81, pp. 1242–1258, 2010.

[168] Silling, S. A. and Lehoucq, R. B., "Convergence of peridynamics to classical elasticity theory," *Journal of Elasticity*, vol. 93, pp. 13–37, 2008.

[169] Macek, R. W. and Silling, S. A., "Peridynamics via finite element analysis," *Finite Elements in Analysis and Design*, vol. 43, pp. 1169–1178, 2007.

[170] Chen, X. and Gunzburger, M., "Continuous and discontinuous finite element methods for a peridynamics model of mechanics," technical report, Florida State University, 2010.

[171] Bobaru, F., "Influence of van der waals forces on increasing the strength and toughness in dynamic fracture of nanofibre networks: A peridynamic approach," *Modelling and Simulation in Materials Science and Engineering*, vol. 15, pp. 397–417, 2007.

[172] Bobaru, F. and Silling, S. A., "Peridynamic 3d models of nanofiber networks and carbon nanotube-reinforced composites," in *NUMIFORM 2004 - Proceedings of the 8th International Conference on Numerical Methods in Industrial Forming Processes, AIP Conference Proceedings*, vol. 712, pp. 16565–1570, 2004.

[173] Silling, S. A. and Bobaru, F., "Peridynamic modeling of membranes and fibers," *International Journal of Non-Linear Mechanics*, vol. 40, pp. 395–409, 2005.

[174] Agwai, A., Guven, I., and Madenci, E., "Peridynamic theory for failure prediction in multilayer thin-film structures of electronic packages," in *Proceedings of 58th Electronic Components and Technology Conference (ECTC)*, pp. 1614–1619, IEEE, 2008.

[175] Agwai, A., Guven, I., and Madenci, E., "Peridynamic theory for impact damage prediction and propagation in electronic packages due to drop," in *Proceeding of 58th Electronic Components and Technology Conference (ECTC)*, pp. 1048–1053, IEEE, 2008.

[176] Askari, E., Bobaru, F., Lehoucq, R. B., Parks, M. L., Silling, S. A., and Weckner, O., "Peridynamics for multiscale materials modeling," in *Journal of Physics: Conference Series*, vol. 125, 2008.

[177] Gerstle, W. H., Sau, N., and Silling, S. A., "Peridynamic modeling of plain and reinforced concrete structures," in *18th International Conference on Structural Mechanics in Reactor Technology*, vol. SMIRT 18, (Beijing, China), pp. 54–68, 2005.

[178] Gerstle, W., Sau, N., and Silling, S. A., "Peridynamics modeling of concrete structures," *Nuclear Engineering and Design*, vol. 237, pp. 1250–1258, 2007.

[179] Gerstle, W. H., Sau, N., and Sakhavand, N., "On peridynamic computational simulation of concrete structures," Technical Report SP265-11, American Concrete Institute, 2009.

[180] Kilic, B., Agwai, A., and Madenci, E., "Peridynamic theory for progressive damage prediction in center-cracked composite laminates," *Composites Structures*, vol. 90, pp. 141–151, 2009.

[181] Foster, J. T., *Dynamic Crack Initiation Toughness: Experiments and Peridynamic Modeling*. Ph.d. dissertation, Purdue University, 2009.

[182] Geers, M. G. D. and Yvonnet, J., "Mulstiscale modeling of microstructure-property relations," *Materials Research Society Bulletin*, vol. 41, pp. 610–616, August 2016.

[183] McDowell, D., "Metal plasticity at multiple scales." Georgia Institute of Techology, ME7203 Lecture Notes, November 2010.

[184] McDowell, D., "Hierarchical multiscale modeling." Georgia Institute of Technology, ME7203 Lecture Notes, 2010.

[185] Chakraborty, A. and Rahman, S., "Sochastic multiscale models for fracture analysis of functionally graded materials," *Engineering Fracture Mechanics*, vol. 75, pp. 2062–2086, 2008.

[186] Park, H. S., Karpov, E. G., Klein, P. A., and Liu, W. K., "Three-dimensional bridging scale analysis of dynamic fracture," *Journal of Computational Physics*, vol. 207, pp. 588–609, 2005.

[187] Gumbsch, P., "An atomistic study of brittle fracture: Toward explicit failure criteria from atomistic modeling," *Journal of Materials Research*, vol. 10, no. 11, pp. 2897–2907, 1995.

[188] Orive, L.-M. C., "Particle size-shape distributions: the general spheroid problem," *Journal of Microscopy*, vol. 107, pp. 235–253, August 1976.

[189] Bachmann, F., Hielscher, R., and Schaeben, H., "Texture analysis with MTEX - free and open source software toolbox," *Solid State Phenomena*, vol. 160, pp. 63–68, February 2010.

[190] Kopf, J., Fu, C.-W., Cohen-Or, D., Deussen, O., Lischinski, D., and Wong, T.-T., "Solid texture synthesis from 2d exemplars," *ACM Transactions on Graphics*, vol. 26, no. 3, p. 2, 2007.

[191] Chen, J. and Wang, B., "High quality solid texture synthesis using position and index histogram matching," *The Visual Computer*, vol. 26, no. 4, pp. 253–262, 2010.

[192] Paget, R. and Longstaff, I. D., "Texture synthesis via a noncausal nonparametric multiscale markov random field. image processing.," *IEEE Transactions*, vol. 7, no. 6, pp. 925–931, 1998.

[193] Sundararaghavan, V., "Reconstruction of three-dimensional anisotropic microstructures from two-dimensional micrographs imaged on orthogonal planes," *Intergrated Materials and Manufacturing Innovation*, vol. 3, no. 1, p. 19, 2014.

[194] Turner, D. M. and Kalidindi, S. R., "Statistical construction of 3-d microstructures from 2-d exemplars collected on oblique sections," *Acat Materialia*, vol. 102, pp. 136–148, 2016.

[195] Armstrong, P. J. and Frederick, C. O., "A mathematical representation of the multiaxial bauschinger effect," Tech. Rep. GEGB Report, RD/B/N731, Berkeley Nuclear Laboratories, 1966.

[196] Dassault Systemes, "Abaqus v. 6.11-1. 2011." Providence, RI, USA.

[197] Brindley, K. A. and Neu, R. W., "Progress in structure-property modeling tools for γ-TiAl," in *TMS 2015 Annual Meeting Supplemental Proceedings*, pp. 1173–1183, The Minerals, Metals, and Materials Society, Wiley, March 2015.

[198] Biragoni, P. G. and Heilmaier, M., "FEM-simulation of real and artificial microstructures of Mo-Si-B alloys for elastic properties and comparison with analytical methods," *Advanced Engineering Materials*, vol. 9, no. 10, pp. 882–887, 2007.

[199] Jain, P. and Kumar, K. S., "Dissolved Si in Mo and its effects on the properties of Mo-Si-B alloys," *Scripta Materialia*, vol. 62, pp. 1–4, 2010.

[200] Zhang, L., Pan, K., and Lin, J., "Fracture toughness and fracture mechanisms in Mo_5SiB_2 at ambient to elevated temperatures," *Intermetallics*, vol. 38, pp. 49–54, 2013.

[201] Yu, J. L., Li, Z. K., Zheng, X., Zhang, J. J., Liu, H., Bai, R., and Wang, H., "Tensile properties of multiphase Mo-Si-B refractory alloys at elevated temperatures," *Materials Science and Engineering A*, vol. 532, pp. 392–395, 2012.

[202] Alur, A. P. and Kumar, K. S., "Monotonic and cyclic crack growth response of a Mo-Si-B alloy," *Acta Materiala*, vol. 54, pp. 385–400, 2006.

[203] Middlemas, M. R., Cochran, J. K., Jain, P., and Kumar, K. S., "Strength and oxidation resistance of Mo-Si-B alloys produced by reaction synthesis," in *Materials Processing and Properties 2010*, vol. 1 of *TMS 2010 139th Annual Meeting & Exhibition - Supplemental Proceedings*, pp. 859–866, The Minerals, Metals, and Materials Society, 2010.

[204] Kirka, M. M., Brindley, K. A., Neu, R. W., Antolovich, S. D., Shinde, S. R., and Gravett, P. W., "Parameters influencing thermomechanical fatigue of a directionally-solidified ni-base superalloy," *International Journal of Fatigue*, vol. 81, pp. 48–60, 2015.

[205] Kirka, M. M., Brindley, K. A., Neu, R. W., Antolovich, S. D., Shinde, S. R., and Gravett, P. W., "Influence of coarsened and rafted microstructures on the thermomechanical fatigue of a ni-base superalloy," *International Journal of Fatigue*, vol. 81, pp. 191–201, 2015.

[206] Brindley, K. A., Kirka, M. M., Fenandez-Zelaia, P., and Neu, R. W., "Thermomechanical fatigue of mar-m247: Extension of a unified constitutive and life model to higher temperatures," *Journal of Engineering Material and Technology*, vol. 137, July 2015.

[207] Boismier, D. A. and Sehitoglu, H., "Thermo-mechanical fatigue of mar-m247: Part 1—experiments," *Journal of Engineering Materials and Technology*, vol. 112, pp. 68–79, January 1990.

[208] Antolovich, S. D., Liu, S., and Baur, R., "Low-cycle fatigue behavior of rene 80 at elevated temperature," *Metallurgical Transactions, A*, vol. 12A, pp. 473–481, 1981.

[209] Amaro, R. L., *Thermomechanical Fatigue Crack Formation In A Single Crystal Ni-base Superalloy.* PhD thesis, Georgia Institute of Technology, December 2010.

[210] Vasseur, E. and Rémy, L., "High temperature low cycle fatigue and thermalmechanical fatigue behaviour of an oxide-dispersion-strengthened nickel-base superalloy," *Materials Science and Engineering A*, vol. 184, no. 1, pp. 1–5, 1994.

[211] Wright, P. K., "Oxidation-fatigue interactions in a single-crystal superalloy," in *Low Cycle Fatigue* (Solomon, H. D., ed.), no. ASTM STP 942, (Philadelphia), pp. 558–575, American Society for Testing and Materials, 1988.